

Operation of  
CdZnTe Semiconductor Detectors  
in Liquid Scintillator  
for the COBRA Experiment

Dissertation  
zur Erlangung der Doktorgrades  
des Department Physik  
der Universität Hamburg

vorgelegt von  
Christian Oldorf  
aus Hamburg

Hamburg  
2015

Gutachterin/Gutachter der Dissertation: Prof. Dr. Caren Hagner  
Prof. Dr. Kai Zuber

Gutachterin/Gutachter der Disputation: Prof. Dr. Caren Hagner  
Prof. Dr. Michael Wurm

Datum der Disputation: 23.07.2015

Vorsitzender des Prüfungsausschusses: Dr. Georg Steinbrück

Vorsitzender des Promotionsausschusses: Prof. Dr. Jan Louis

Dekan der MIN-Fakultät Prof. Dr. Heinrich Graener

## Operation of CdZnTe Semiconductor Detectors in Liquid Scintillator for the COBRA Experiment

### Abstract

COBRA, the *Cadmium-Zinc-Telluride O-neutrino double-Beta Research Apparatus*, is an experiment aiming for the measurement of the neutrinoless double beta decay with several isotopes, in particular  $^{116}\text{Cd}$ ,  $^{106}\text{Cd}$  and  $^{130}\text{Te}$ . A highly granular large scale experiment with about 400 kg of CdZnTe semiconductor detectors is currently under development. To provide evidence for the neutrinoless double beta decay of  $^{116}\text{Cd}$ , a background rate in the order of  $10^{-3}$  counts/keV/kg/a is needed to achieve the required half-life sensitivity of at least  $2 \cdot 10^{26}$  years. To reach this target, the detectors have to be operated in a highly pure environment, shielded from external radiation. Liquid scintillator is a promising candidate as a circumfluent replacement for the currently used lacquer. Next to the function as highly pure passivation material, liquid scintillator also acts as a neutron shield and active veto for external gammas. Within this thesis, the design, construction and assembly of a test set-up is described. The operation of four CdZnTe detectors after several years of storage in liquid scintillator is demonstrated. Next to extensive material compatibility tests prior to the assembly, the commissioning of the set-up and the characterization of the detectors are shown. Finally, results concerning the background reduction capability of liquid scintillator and the detection of cosmic muons are presented and compared to a Monte Carlo simulation.

## **Betrieb von CdZnTe-Halbleiterdetektoren in Flüssigszintillator für das COBRA Experiment**

### **Zusammenfassung**

Ziel des Experiments COBRA (*Cadmium-Zinc-Telluride O-neutrino double-Beta Research Apparatus*) ist der Nachweis des neutrinolosen Doppelbetazerfalls mit mehreren Isotopen, hauptsächlich  $^{116}\text{Cd}$ ,  $^{106}\text{Cd}$  und  $^{130}\text{Te}$ . Ein hochgranulares Großexperiment bestehend aus etwa 400 kg CdZnTe-Halbleiterdetektoren ist momentan in Vorbereitung. Um den Nachweis des neutrinolosen Doppelbetazerfalls mit dem Isotop  $^{116}\text{Cd}$  erbringen zu können, wird eine Untergrundrate von  $10^{-3}$  counts/keV/kg/a benötigt um die erforderliche Sensitivität auf eine Halbwertszeit von mindestens  $2 \cdot 10^{26}$  Jahren zu erlangen. Um dieses Ziel zu erreichen, müssen die Detektoren in einer hochreinen Umgebung betrieben werden, abgeschirmt von externen Strahlungsquellen. Flüssigszintillator als umgebendes Medium ist ein vielversprechender Ersatz für den momentan genutzten Schutzlack der Detektoren. Zusätzlich zu seiner Eigenschaft als hochreines Passivierungsmaterial fungiert Flüssigszintillator außerdem als Abschirmung gegen Neutronen und als aktives Veto gegen externe Gammastrahlung. Die vorliegende Arbeit beschreibt die Planung, die Konstruktion und den Zusammenbau eines Teststandes. Der Betrieb von vier CdZnTe Detektoren, die mehrere Jahre in Flüssigszintillator gelagert wurden, wird gezeigt. Umfangreiche Materialverträglichkeitsuntersuchungen vor dem Zusammenbau werden ebenso dargelegt wie die Inbetriebnahme des Teststands und die Charakterisierung der Detektoren. Schließlich werden Ergebnisse der Leistungsfähigkeit des Flüssigszintillators bezüglich der Untergrundunterdrückung und der Nachweis von kosmischen Myonen vorgestellt. Diese Ergebnisse werden mit Monte Carlo Simulationen verglichen.

# Contents

<b>1</b>	<b>Introduction</b>	<b>1</b>
<b>2</b>	<b>Neutrino Physics</b>	<b>3</b>
2.1	Dirac and Majorana Particles . . . . .	3
2.2	Theory of Neutrino Masses . . . . .	6
2.3	Neutrino Mixing and Mass Hierarchy . . . . .	11
2.4	Electromagnetic Properties of Neutrinos . . . . .	14
2.5	Double Beta Decay . . . . .	16
2.5.1	The $2\nu\beta\beta$ Decay . . . . .	17
2.5.2	The $0\nu\beta\beta$ Decay . . . . .	19
2.5.3	The $0\nu\beta^+\beta^+$ Decay and Resonant $0\nu\text{EC}/\text{EC}$ . . . . .	26
2.6	Current Status and Future Perspective of $0\nu\beta\beta$ . . . . .	27
2.7	Determination of Neutrino Masses other than $0\nu\beta\beta$ . . . . .	31
<b>3</b>	<b>Liquid Scintillator Detectors for the Search of <math>0\nu\beta\beta</math> Decay</b>	<b>35</b>
3.1	Scintillators in General . . . . .	36
3.1.1	Principal Mechanism of Scintillation in Organic Scintillators	37
3.1.2	Multi-Component Liquid Scintillators . . . . .	39
3.1.3	Chemical and Optical Properties of Scintillator Components	40
3.1.4	Achievable Purification Levels . . . . .	45
3.1.5	Neutron Attenuation and Capture . . . . .	47
3.2	The $0\nu\beta\beta$ Decay Experiment KamLAND-Zen . . . . .	48
3.3	The $0\nu\beta\beta$ Decay Experiment SNO+ . . . . .	50
<b>4</b>	<b>The COBRA Experiment</b>	<b>53</b>
4.1	Isotopes under Investigation . . . . .	53
4.2	Background Sources . . . . .	55
4.2.1	Natural Decay Chains and $^{40}\text{K}$ . . . . .	55
4.2.2	Neutron Induced Background and Neutron Detection . . . . .	58
4.2.3	Cosmogenic Radioisotopes . . . . .	62
4.2.4	Neutrino Accompanied Double Beta Decay . . . . .	62
4.3	CdZnTe as Material for Semiconductor Detectors . . . . .	62
4.3.1	Semiconductor Properties . . . . .	63

4.3.2	Intrinsic Charge Carriers . . . . .	64
4.3.3	Charge Transport and Trapping . . . . .	65
4.3.4	Pulse Formation . . . . .	65
4.4	COBRA Demonstrator at the LNGS . . . . .	71
4.4.1	Detector Build-up . . . . .	71
4.4.2	Radiation Shield . . . . .	72
4.4.3	EMI Shield . . . . .	74
4.4.4	Readout Electronics . . . . .	74
4.4.5	Preamplifier Cooling Unit . . . . .	75
4.4.6	Current Status . . . . .	76
4.5	Toward a Large Scale COBRA Experiment . . . . .	78
<b>5</b>	<b>Design, Construction and Simulation of the Set-Up</b>	<b>81</b>
5.1	Material Compatibility Tests . . . . .	82
5.1.1	Choice of Liquid Scintillators . . . . .	82
5.1.2	Choice of Materials . . . . .	83
5.1.3	Results . . . . .	84
5.2	Design of Mechanical Components . . . . .	85
5.2.1	Operation Vessel . . . . .	85
5.2.2	Cable Feedthroughs . . . . .	87
5.2.3	PMT Support Structure . . . . .	88
5.2.4	Storage Vessel and Liquid Handling . . . . .	88
5.2.5	Detector Holder . . . . .	89
5.3	EMI Shield . . . . .	89
5.4	Readout Electronics, DAQ and Data Processing . . . . .	90
5.4.1	Data Cleaning Cuts and Pulse Shape Analysis . . . . .	93
5.5	Photomultiplier Tubes . . . . .	94
5.6	Calibration Sources . . . . .	94
5.7	Monte Carlo Simulation . . . . .	96
5.7.1	Geant4 and VENOM . . . . .	97
5.7.2	Implementation of the Set-Up . . . . .	97
<b>6</b>	<b>Measurements and Comparison to Simulations</b>	<b>99</b>
6.1	Detector Working Points . . . . .	99
6.2	Calibration and Time Stability . . . . .	101
6.2.1	Calibration Parameters . . . . .	101
6.2.2	Data Rate . . . . .	102
6.3	Coincidence Time for Veto . . . . .	103
6.4	Comparison of $^{137}\text{Cs}$ Measurement and Simulation . . . . .	106
6.5	Veto Performance in the ROI of COBRA . . . . .	110
6.6	Characterization of Scintillator Veto Events . . . . .	114
<b>7</b>	<b>Summary and Outlook</b>	<b>129</b>

<b>Appendices</b>	<b>132</b>
<b>A Uranium Decay Chain</b>	<b>132</b>
<b>B Thorium Decay Chain</b>	<b>135</b>
<b>C ET Enterprise 9829B Photomultiplier Tube</b>	<b>137</b>
<b>D Technical CAD Drawings</b>	<b>140</b>
<b>E Veto Time</b>	<b>145</b>
<b>List of Figures</b>	<b>147</b>
<b>List of Tables</b>	<b>149</b>
<b>Bibliography</b>	<b>151</b>





# Chapter 1

## Introduction

Over the last decades the knowledge in the field of neutrino physics has rapidly grown. Neutrino oscillations are an experimentally proven framework today and helped to finally solve the solar neutrino problem. At the same time it is proven that neutrinos possess a mass. The precise determination of the neutrino mixing parameters in the PMNS matrix is still being conducted by several experiments.

However, many questions concerning the properties of neutrinos are unanswered so far. Next to the question of CP violation in the neutrino sector, their electromagnetic properties, the unknown absolute values for neutrino masses and their ordering in the mass hierarchy, the neutrino nature being Dirac or Majorana particle is of great interest. Except for neutrinos, all other fermions in the Standard Model possess a charge leading to a distinction between particles and antiparticles. Hence, they are Dirac particles.

The possibility of neutrinos being Majorana particles offers an explanation by the Seesaw mechanism for their small mass values compared to their corresponding leptons. Also, other interesting questions in cosmology, particle and astroparticle physics are affected by the fundamental nature of neutrinos, e.g. the explanation of baryon asymmetry in the universe by the assumption of a previous lepton asymmetry (leptogenesis).

The best way known today to clarify the nature of the neutrino is the detection of the neutrinoless double beta decay. Although the underlying physics process would be unknown, the evidence of the neutrinoless double beta decay is equivalent to the fact that neutrinos are Majorana particles. The observation of the neutrinoless double beta decay in  $^{76}\text{Ge}$  was reported by a part of the Heidelberg-Moscow experiment in 2004 and 2006, but has recently been refuted by the GERDA experiment in 2013.

As one of the next-generation experiments, COBRA aims for the discovery of the neutrinoless double beta decay by using CdZnTe semiconductor detectors. The targeted half-life sensitivity is in the order of  $10^{26}$  years, corresponding to an effective Majorana mass of 50 meV. Beside a large source mass and a very good energy

resolution, an extremely low background rate in the order of  $10^{-3}$  counts/keV/kg/a is necessary to achieve this goal. This is only achievable, if the detectors are operated in a very radiopure environment and shielded from external radiation. A large part of the background in the current COBRA demonstrator at the LNGS underground laboratory originates from the passivation lacquer of the detectors. The replacement of the lacquer with a liquid scintillator environment is an excellent option, as it is a highly pure material, a very good neutron shield and acts as an active veto for external radiation.

To study the operation of CdZnTe detectors in liquid scintillator, a test set-up was planned, constructed and operated at the Universität Hamburg. During the planning phase detailed compatibility tests for the construction materials were performed with respect to the stability and performance in liquid scintillator. To allow for comparison with the results from the COBRA demonstrator, a similar read-out chain was implemented. To better understand the measured data, a Monte Carlo simulation was also performed.

Following this introduction, an overview of neutrino physics with the emphasis on neutrinoless double beta decay is given in Chapter 2. In addition, the theory and determination of neutrino masses are examined. Recent results and the perspectives of other neutrinoless double beta decay experiments are also summarized.

The importance of liquid scintillator as a detection material for the search of neutrinoless double beta decay is explained in Chapter 3. Next to the fundamental processes leading to scintillation, chemical and optical properties of selected scintillator compounds are presented. With respect to the achievable background reduction for COBRA, purity levels and neutron attenuation in liquid scintillators are described. Finally, the two liquid scintillator experiments KamLAND-ZEN and SNO+ are introduced.

The COBRA experiment and the properties of CdZnTe detectors are described in Chapter 4. Next to a future large scale experiment, the current demonstrator at the LNGS laboratory is presented. The general discussion of background sources for the COBRA experiment are an important part in the course of this thesis.

The description of the test set-up in Hamburg follows in Chapter 5. Initially, the material compatibility tests and the choice of liquid scintillators are presented. The design of the mechanical components, the EMI shield and the read-out chain follow. To better understand the measurements of the test set-up, a Monte Carlo simulation campaign was conducted.

The measurements performed with the test set-up and comparisons with the performed Monte Carlo simulations are presented in Chapter 6. Next to the operation parameters and the performance of the CdZnTe detectors, the identification of cosmic muons and the background reduction capabilities of liquid scintillator are described.

To conclude, a summary and outlook are given in Chapter 7.

## Chapter 2

# Neutrino Physics

The knowledge about neutrino physics has rapidly grown over the past years since the confirmation of neutrino oscillations by Super-Kamiokande in 1998 [1] and the solution of the solar neutrino problem by SNO in 2002 [2]. These discoveries are equivalent to the fact, that neutrinos possess a rest mass. Although neutrinos are described as massless particles in the Standard Model (SM), neutrino masses do not violate any fundamental gauge symmetry of that theory.

The confirmation of neutrino masses results in other unresolved issues of neutrino physics. Two of them, the absolute neutrino mass scale as well as the probe of the fundamental character of neutrinos, being a Majorana or Dirac particle, can be addressed by the observation of neutrinoless double beta decay.

This chapter gives an introduction to neutrino physics, especially on the distinction between Dirac and Majorana particles, neutrino oscillations and double beta decays. An overview of the current experimental status in the field of neutrinoless double beta decay and the search for neutrino masses is also presented.

### 2.1 Dirac and Majorana Particles

Within the SM, neutrinos are fundamental spin- $\frac{1}{2}$  fermions. The relativistic wavefunction  $\Psi(x)$  of spin- $\frac{1}{2}$  particles is generally given by the Dirac equation<sup>1</sup>:

$$\left(\gamma_\alpha \frac{\partial}{\partial x_\alpha} + m\right) \Psi(x) = 0 \quad (2.1)$$

The four independent components of the spinor  $\Psi$  represent the four possibilities 'particle' and 'antiparticle' each with the two spins  $J_z = +\frac{1}{2}$  and  $J_z = -\frac{1}{2}$ .  $\gamma_\alpha$  are the  $4 \times 4$  Hermitian Dirac matrices:

$$\gamma_\alpha = \begin{pmatrix} 0 & -i\sigma_k \\ i\sigma_k & 0 \end{pmatrix} \text{ for } \alpha = 1, 2, 3 \quad \text{and} \quad \gamma_4 = \begin{pmatrix} I & 0 \\ 0 & I \end{pmatrix}. \quad (2.2)$$

---

<sup>1</sup>Following the convention used in [3], the Dirac-Pauli representation is used in this chapter. Other conventions are also commonly used in literature, leading to slightly different forms for the following expressions.

$\sigma_k$  are the  $2 \times 2$  Pauli spin matrices and  $I$  is the  $2 \times 2$  unitary matrix.

The  $4 \times 4$  Hermitian matrix  $\gamma_5$  is important to describe projection operators and is given by

$$\gamma_5 = \gamma_1 \gamma_2 \gamma_3 \gamma_4 = \begin{pmatrix} 0 & -I \\ -I & 0 \end{pmatrix} = \begin{pmatrix} 0 & 0 & -1 & 0 \\ 0 & 0 & 0 & -1 \\ -1 & 0 & 0 & 0 \\ 0 & -1 & 0 & 0 \end{pmatrix}, \quad \gamma_5^2 = 1. \quad (2.3)$$

Two projection operators  $P_L$  and  $P_R$  are defined as

$$P_L = \frac{1}{2}(1 + \gamma_5) \quad (2.4)$$

$$P_R = \frac{1}{2}(1 - \gamma_5) \quad (2.5)$$

with the properties

$$P_L^2 = P_L, \quad P_R^2 = P_R, \quad P_R P_L = P_L P_R = 0. \quad (2.6)$$

Using these projection operators, any arbitrary spinor  $\Psi$  can be separated in a so-called left-handed component  $\Psi_L$  and a right-handed component  $\Psi_R$ :

$$\Psi_L = \frac{1}{2}(1 + \gamma_5)\Psi = P_L \Psi \quad (2.7)$$

$$\Psi_R = \frac{1}{2}(1 - \gamma_5)\Psi = P_R \Psi \quad (2.8)$$

$$\Psi = \Psi_L + \Psi_R \quad (2.9)$$

and it applies

$$\gamma_5 \Psi_R = -\Psi_R \quad \text{and} \quad \gamma_5 \Psi_L = \Psi_L. \quad (2.10)$$

The eigenvalues  $\pm 1$  to  $\gamma_5$  are called chirality and every  $\Psi$  can be separated in  $\Psi_L$  and  $\Psi_R$

$$\Psi = \Psi_L + \Psi_R = \frac{1}{2}(1 + \gamma_5)\Psi + \frac{1}{2}(1 - \gamma_5)\Psi, \quad (2.11)$$

and the Dirac equation ends in

$$\frac{\partial}{\partial x_4} \Psi_{L,R} \pm i \sigma_k \frac{\partial}{\partial x_k} \Psi_{L,R} = -m \gamma_4 \Psi_{R,L}. \quad (2.12)$$

For  $m = 0$  this system decouples and one finds two independent equations for  $\Psi_L$  and  $\Psi_R$ :

$$\frac{\partial}{\partial x_4} \Psi_{L,R} = \mp i \sigma_k \frac{\partial}{\partial x_k} \Psi_{L,R}. \quad (2.13)$$

The latter implies, that  $\Psi_{L,R}$  are also eigenfunctions to the helicity  $H$ , which is defined as the projection of the spin to the direction of the momentum  $\hat{p} = \vec{p}/|\vec{p}|$ :

$$H = \vec{J}_z \cdot \hat{p} \quad (2.14)$$

The operators  $P_L$  and  $P_R$  project the component with  $H = -1$  respectively  $H = +1$  from the spinor  $\Psi$  for particles and vice versa for antiparticles. Thus, for  $m = 0$  the chirality is contrarily equal to the helicity. For  $m > 0$  the decoupling in Equation 2.12 is no longer possible and the chirality eigenspinors  $\Psi_L$  and  $\Psi_R$  do not describe particles with a fixed helicity.

### Two Component Theory

Another way to describe massless spin- $\frac{1}{2}$  particles is the two-component theory by H. Weyl [4]. The Weyl equation is equivalent to the Dirac equation and the neutrino spinor  $\Psi_{\nu}$  always has the following form in weak interactions:

$$\Psi_{\nu} = \frac{1}{2}(1 + \gamma_5)\Psi_{\nu} = \Psi_L \quad \text{and} \quad \Psi_{\bar{\nu}} = \frac{1}{2}(1 - \gamma_5)\Psi_{\bar{\nu}} = 0 \quad (2.15)$$

Thus, an interacting neutrino  $\nu$  is always left-handed and an interacting antineutrino  $\bar{\nu}$  is always right-handed. This is equivalent to the case, that  $\nu$  always has  $H = -1$  and  $\bar{\nu}$  always  $H = +1$  for  $m = 0$ . Each Dirac spinor  $\Psi_L$  and  $\Psi_R$  has now only two independent components. The Dirac spinors are then expressed by the two-component Weyl spinors  $\Phi$  and  $\chi$ :

$$\Psi_L = \begin{pmatrix} \Phi \\ -\Phi \end{pmatrix} \quad \text{and} \quad \Psi_R = \begin{pmatrix} \chi \\ \chi \end{pmatrix} \quad (2.16)$$

The four-component Dirac spinors  $\Psi_L$  and  $\Psi_R$  are equivalent to the two-component Weyl spinors  $\Phi$  and  $\chi$  and thus a Dirac field can be expressed by the sum of two Weyl fields.

### The Theory of Majorana Neutrinos

All fundamental fermions of the SM beside the neutrinos carry a charge and hence a discrimination between particle and antiparticle is simple. For massive neutral fermions, E. Majorana proposed in 1937 a theory for particles being their own antiparticles [5]. As the neutrino does not carry a charge, it can in principle be identical to its own antiparticle. If  $\nu$  does not equal  $\bar{\nu}$ , the neutrino is called Dirac neutrino  $\nu^D$  ( $\nu \neq \bar{\nu}$ ), which has four independent components in  $\Psi$ . Otherwise it is called Majorana neutrino  $\nu^M$  ( $\nu = \bar{\nu}$ ) and a two-component spinor  $\Psi_{\nu}$  is sufficient to describe the neutrino.

As there is proof for massive neutrinos (see Chapter 2.3), the question arises, if there is an additive quantum number (called lepton number  $L$ ), in which the sign discriminates between  $\nu$  and  $\bar{\nu}$  in weak interactions. For Dirac neutrinos  $\nu^D$  the lepton number is conserved and for Majorana neutrinos  $\nu^M$  it is violated in particle processes.

Within the SM, neutrinos are produced in weak interactions as pure weak flavor eigenstates. By definition, the flavor and the lepton number of a neutrino is given by the charged lepton  $l_i^-$  or antilepton  $l_i^+$  involved in the interaction.

In processes like the inverse beta decay, the violation of lepton number conservation could not be found. For instance, the inverse beta decay of reactor electron antineutrinos [6] was not observed:

$$\begin{aligned}\bar{\nu}_e + n &\not\rightarrow p + e^- \\ L &= -1 + 0 \neq 0 + 1 \\ \bar{\nu}_e + {}^{37}\text{Cl} &\not\rightarrow {}^{37}\text{Ar} + e^-. \end{aligned} \quad (2.17)$$

On the other hand, the search for electron neutrinos produced in the Sun was successful [7]:

$$\begin{aligned}\nu_e + n &\rightarrow p + e^- \\ L &= 1 + 0 = 0 + 1 \\ \nu_e + {}^{37}\text{Cl} &\rightarrow {}^{37}\text{Ar} + e^-. \end{aligned} \quad (2.18)$$

If neutrinos and antineutrinos were identical particles, the reactions in Equation 2.17 and 2.18 should occur with the same cross section. Anyhow, these results do not prove that  $\nu_e$  is different to  $\bar{\nu}_e$ . As the mass of neutrinos is very small (see Chapter 2.3 and 2.7), the sensitivity of inverse beta decay experiments is not sufficient to decide whether the observed differences between  $\nu_e$  and  $\bar{\nu}_e$  are due to opposite helicities of  $\nu^M$  or due to the non-identity of  $\nu_e$  (with  $H = -1$ ) and  $\bar{\nu}_e$  (with  $H = +1$ ).

The best practical way known today to decide whether the neutrino is a Dirac or Majorana particle, is the observation of the neutrinoless double beta decay, in detail explained in Chapter 2.5. This process violates the lepton number conservation by two units:

$$\begin{aligned}2n &\rightarrow 2p + 2e^- \\ L &= 0 \neq 0 + 2 \end{aligned} \quad (2.19)$$

## 2.2 Theory of Neutrino Masses

In this section the Dirac and Majorana mass terms for free particles without interactions with other particles are derived. The mechanisms are shown for only one neutrino flavor, the generalization to  $n$  neutrino flavors can be found in [8].

### The Dirac Mass

The Dirac equation can be derived with the help of the Euler-Lagrange equation from a Lagrangian:

$$-\mathcal{L} = \bar{\Psi} \left( \gamma_\alpha \frac{\partial}{\partial x_\alpha} + m_D \right) \Psi. \quad (2.20)$$

The first term corresponds to the kinetic energy. The interesting part is the mass term with the Dirac mass  $m_D$

$$- \mathcal{L}_D = m_D \bar{\Psi} \Psi, \quad (2.21)$$

where  $\bar{\Psi} \Psi$  is Lorentz invariant and Hermitian. Requiring  $\mathcal{L}_D$  to be Hermitian too,  $m_D$  must be real ( $m_D^* = m_D$ ). With Equation 2.11, the Dirac mass term can be written as Weyl spinors or chiral components:

$$- \mathcal{L}_D = m_D (\bar{\Psi}_L \Psi_R + \bar{\Psi}_R \Psi_L). \quad (2.22)$$

As can be seen, it requires both left- and right-handed Dirac neutrinos to produce such a mass term. As only left-handed neutrinos are observable in experiments, they have to be massless ( $m_D = 0$ ) within the Standard Model. The fact that neutrinos are massive is proved by the existence of neutrino oscillation, see Section 2.3. This requires an extension of the simple Standard Model.

### The Majorana Mass

In a more general treatment, neutrinos are not constraint to Dirac neutrinos anymore. If the charged conjugated spinor  $\Psi^c$  is added, three more Lorentz scalars next to  $\bar{\Psi} \Psi$  are produced:  $\bar{\Psi}^c \Psi^c$ ,  $\bar{\Psi} \Psi^c$  and  $\bar{\Psi}^c \Psi$ .

$\bar{\Psi}^c \Psi^c$  is equivalent to  $\bar{\Psi} \Psi$  and also Hermitian.  $\bar{\Psi} \Psi^c$  and  $\bar{\Psi}^c \Psi$  are Hermitian conjugates and next to the Dirac mass term  $\mathcal{L}_D$  an additional Hermitian Majorana mass term  $\mathcal{L}_M$  with the Majorana mass  $m_M$  arises:

$$- \mathcal{L}_M = \frac{1}{2} (m_M \bar{\Psi} \Psi^c + m_M \bar{\Psi}^c \Psi) = \frac{1}{2} m_M \bar{\Psi} \Psi^c + \text{h.c.}^2 \quad (2.23)$$

Using chiral projections with the notation

$$\Psi_{L,R}^c = (\Psi^c)_{L,R} = (\Psi_{R,L})^c, \quad (2.24)$$

two Hermitian Majorana mass terms with real masses  $m_{L,R}$  show up:

$$- \mathcal{L}_M^L = \frac{1}{2} m_L (\bar{\Psi}_L \Psi_R^c + \bar{\Psi}_R^c \Psi_L) = \frac{1}{2} m_L \bar{\Psi}_L \Psi_R^c + \text{h.c.} \quad (2.25)$$

$$- \mathcal{L}_M^R = \frac{1}{2} m_R (\bar{\Psi}_L^c \Psi_R + \bar{\Psi}_R \Psi_L^c) = \frac{1}{2} m_R \bar{\Psi}_L^c \Psi_R + \text{h.c.} \quad (2.26)$$

The masses  $m_{L,R}$  are real, because for both first terms the Hermitian conjugate second terms follow.

The most general mass term for neutrinos is a combination of Equations 2.22 and 2.26 and called the Dirac-Majorana mass term  $\mathcal{L}_{DM}$ :

$$-2\mathcal{L}_{DM} = m_D (\bar{\Psi}_L \Psi_R + \bar{\Psi}_R \Psi_L) + m_L \bar{\Psi}_L \Psi_R^c + m_R \bar{\Psi}_L^c \Psi_R + \text{h.c.} \quad (2.27)$$

$$= (\bar{\Psi}_L, \bar{\Psi}_L^c) \begin{pmatrix} m_L & m_D \\ m_D & m_R \end{pmatrix} \begin{pmatrix} \Psi_R^c \\ \Psi_R \end{pmatrix} + \text{h.c.} \quad (2.28)$$

$$= \bar{\Psi}_L M \Psi_R^c + \bar{\Psi}_R^c M \Psi_L, \quad (2.29)$$

<sup>2</sup>h.c. means Hermitian conjugate

with

$$M = \begin{pmatrix} m_L & m_D \\ m_D & m_R \end{pmatrix}, \quad (2.30)$$

$$\Psi_L = \begin{pmatrix} \Psi_L \\ \Psi_L^c \end{pmatrix} = \begin{pmatrix} \Psi_L \\ (\Psi_R)^c \end{pmatrix}, \quad (2.31)$$

$$(\Psi_L)^c = \begin{pmatrix} (\Psi_L)^c \\ \Psi_R \end{pmatrix} = \begin{pmatrix} \Psi_R^c \\ \Psi_R \end{pmatrix} = \Psi_R^c. \quad (2.32)$$

In case of combined charge ( $C$ ) and parity ( $P$ ) conservation ( $CP$ -conservation) the elements of the mass matrix  $M$  are real. In the observable neutrino interactions only  $\Psi_L$  and  $\Psi_R^c$  are present, they are called active neutrinos. In contrast, the fields  $\Psi_R$  and  $\Psi_L^c$  are not participating in weak interactions within the Standard Model and thus they are called sterile neutrinos. To emphasize this distinction, the following notation is often used:

$$\Psi_L = \nu_L; \quad \Psi_R^c = \nu_R^c = \bar{\nu}_R; \quad \Psi_R = N_R; \quad \Psi_L^c = N_L^c \quad (2.33)$$

With this notation, Equation 2.27 becomes:

$$-2\mathcal{L}_{DM} = m_D (\bar{\nu}_L N_R + \bar{N}_L^c \nu_R^c) + m_L \bar{\nu}_L \nu_R^c + m_R \bar{N}_L^c N_R + \text{h.c.} \quad (2.34)$$

$$= (\bar{\nu}_L, \bar{N}_L^c) \begin{pmatrix} m_L & m_D \\ m_D & m_R \end{pmatrix} \begin{pmatrix} \nu_R^c \\ N_R \end{pmatrix} + \text{h.c.} \quad (2.35)$$

To obtain the mass eigenstates, the matrix  $M$  has to be diagonalized. This method is described e.g. in [3] and the eigenvalues are

$$\Psi_{1L} = \cos \theta \cdot \Psi_L - \sin \theta \cdot \Psi_L^c, \quad (2.36)$$

$$\Psi_{1R}^c = \cos \theta \cdot \Psi_R^c - \sin \theta \cdot \Psi_R, \quad (2.37)$$

$$\Psi_{2L} = \sin \theta \cdot \Psi_L + \cos \theta \cdot \Psi_L^c, \quad (2.38)$$

$$\Psi_{2R}^c = \sin \theta \cdot \Psi_R^c + \cos \theta \cdot \Psi_R, \quad (2.39)$$

with a mixing angle  $\theta$  given by

$$\tan 2\theta = \frac{2m_D}{m_R - m_L}. \quad (2.40)$$

To get a more clearly arranged expression, two independent Majorana fields with positive masses  $m_1$  and  $m_2$  are introduced, see [3, 9]:

$$\phi_1 = \Psi_{1L} + \epsilon_1 \Psi_{1R}^c, \quad (2.41)$$

$$\phi_2 = \Psi_{2L} + \epsilon_2 \Psi_{2R}^c. \quad (2.42)$$

$$(2.43)$$



$\epsilon_k = \pm 1$  ( $k = 1, 2$ ) is the  $CP$  eigenvalue of the Majorana neutrino  $\phi_k$  and the following expression is obtained:

$$-2\mathcal{L}_{DM} = m_1\bar{\phi}_1\phi_1 + m_2\bar{\phi}_2\phi_2. \quad (2.44)$$

From this general discussion one can select four interesting special aspects:

- $m_L = m_R = 0$  ( $\theta = 45^\circ$ ):

This results in  $m_{1,2} = m_D$  and  $\epsilon_{1,2} = \mp 1$  with two degenerated Majorana states

$$\phi_1 = \frac{1}{\sqrt{2}}(\Psi_L - \Psi_R^c - \Psi_L^c + \Psi_R) = \frac{1}{\sqrt{2}}(\Psi - \Psi^c), \quad (2.45)$$

$$\phi_2 = \frac{1}{\sqrt{2}}(\Psi_L + \Psi_R^c + \Psi_L^c + \Psi_R) = \frac{1}{\sqrt{2}}(\Psi + \Psi^c). \quad (2.46)$$

These two states can be used to construct a Dirac field  $\Psi$ :

$$\frac{1}{\sqrt{2}}(\phi_1 + \phi_2) = \Psi_L + \Psi_R = \Psi. \quad (2.47)$$

Because of  $\bar{\phi}_1\phi_2 + \bar{\phi}_2\phi_1 = 0$ , the corresponding mass term from Equation 2.44 is

$$\mathcal{L}_{DM} = -\frac{1}{2}m_D(\bar{\phi}_1 + \bar{\phi}_2)(\phi_1 + \phi_2) = -m_D\bar{\Psi}\Psi = \mathcal{L}_D. \quad (2.48)$$

Hence, a Dirac field is a composition of two degenerated Majorana fields, i.e. a Dirac  $\nu^D$  can be seen as a pair of Majorana  $\nu^M$ . Therefore, the Dirac case is a special solution of the more general Majorana case.

- $m_D \gg m_L, m_R$  ( $\theta \approx 45^\circ$ ):

In this case the two states  $\phi_1$  and  $\phi_2$  are almost degenerated with  $m_{1,2} \approx m_D$ . This is called a pseudo-Dirac neutrino.

- $m_D = 0$  ( $\theta = 0^\circ$ ):

In this case  $m_{1,2} = m_{L,R}$  and  $\epsilon_{1,2} = 1$ . This results in

$$\phi_1 = \Psi_L + \Psi_R^c, \quad (2.49)$$

$$\phi_2 = \Psi_R + \Psi_L^c. \quad (2.50)$$

This is called the pure Majorana case.

- $m_R \gg m_D, m_L = 0$  ( $\theta = \frac{m_D}{m_R} \ll 1$ ):

One obtains  $\epsilon_{1,2} = \mp 1$  and two mass eigenvalues:

$$m_\nu = m_1 = \frac{m_D^2}{m_R} \quad (2.51)$$

$$m_N = m_2 = m_R \frac{m_D^2}{m_R^2} \approx m_R \quad (2.52)$$

The corresponding fields are

$$\phi_1 \approx \Psi_L - \Psi_R^c \quad (2.53)$$

$$\phi_2 \approx \Psi_L^c + \Psi_R \quad (2.54)$$

This case is very popular to explain the generation of neutrino masses within the Seesaw Model.

### The Seesaw Mechanism

The case for  $m_R \gg m_D$  and  $m_L = 0$  in the previous section can explain the light weight of neutrino masses compared to the masses of the charged leptons. Within the Seesaw Model, for every light left-handed neutrino  $\nu_L$  ( $m \approx 0$ ) a heavy right-handed Majorana neutrino  $N_R$  ( $m_R \gg m_D$ ) is introduced. The Lagrangian is then

$$-\mathcal{L}_{DM} = -(\mathcal{L}_D + \mathcal{L}_M) = m_D \bar{\nu}_L N_R + \frac{1}{2} m_R \bar{N}_L^c N_R + \text{h.c.}, \quad (2.55)$$

$$= \frac{1}{2} (\bar{\nu}_L, \bar{N}_L^c) \begin{pmatrix} 0 & m_D \\ m_D & m_R \end{pmatrix} \begin{pmatrix} \nu_R^c \\ N_R \end{pmatrix} + \text{h.c.} \quad (2.56)$$

The diagonalization of the mass matrix in Equation 2.56 yields again the two mass eigenstates for a light neutrino  $\nu$  and a heavy Majorana neutrino  $N$  as already depicted in Equation 2.52:

$$m_\nu = \frac{m_D^2}{m_R} \quad (2.57)$$

$$m_N \approx m_R \quad (2.58)$$

The value of  $m_\nu$  is reduced by a factor of  $m_D/m_R \ll 1$  compared to the mass of fermions  $m_D$ . For a fixed value of  $m_D$ , this mechanism produces a lighter  $m_\nu$ , as the hypothetical Majorana neutrino gets heavier. This is why its called Seesaw Mechanism.

To generalize this formalism to three lepton flavors, in many grand unified theories (GUTs)  $m_R$  is set to the same value for every flavor. This produces a

quadratic scaling behavior of the neutrino masses with the quark masses or charged lepton masses [3]:

$$m_{\nu_e} : m_{\nu_\mu} : m_{\nu_\tau} \sim m_u^2 : m_c^2 : m_t^2 \quad \text{or} \quad (2.59)$$

$$m_{\nu_e} : m_{\nu_\mu} : m_{\nu_\tau} \sim m_e^2 : m_\mu^2 : m_\tau^2. \quad (2.60)$$

In alternative models,  $m_R$  is assumed to be proportional to  $m_D$  and a linear scaling behavior results:

$$m_{\nu_e} : m_{\nu_\mu} : m_{\nu_\tau} \sim m_u : m_c : m_t \quad (2.61)$$

Thus, predictions for neutrino masses within the Seesaw Mechanism are model-dependent.

However, the Seesaw Mechanism forms the basis for many models to account for neutrino masses and oscillations. For example the neutrino minimal Standard Model ( $\nu$ MSM) [10, 11] predicts the existence of three heavy neutral leptons (HNLs) being Dark Matter candidates and explains the excess of matter over anti-matter in the Universe by baryogenesis. Having a mass below 2 MeV, these HNLs could be produced in decays of  $D$  and  $D_S$  mesons. A physics and technical proposal has recently been prepared for an experiment called SHiP (Search for Hidden Particles), detecting NHLs produced at the SPS (Super Proton Synchrotron) at CERN [12, 13].

## 2.3 Neutrino Mixing and Mass Hierarchy

As mentioned in Section 2.1, neutrinos are produced and absorbed in weak interactions as pure weak flavor eigenstates  $|\nu_l\rangle$  with  $l = e, \mu, \tau$ . The flavor of the charged lepton  $l_l^-$  or antilepton  $l_l^+$  defines the flavor of the neutrino  $\nu_l$  in a charged current interaction. For non-vanishing rest masses of neutrinos, flavor and mass eigenstates don't have to be identical. Mass eigenstates  $|\nu_i\rangle$  with  $i = 1, 2, 3$  and flavor eigenstates  $|\nu_l\rangle$  are connected via a  $n \times n$  matrix  $U$ :

$$|\nu_l\rangle = \sum_i U_{li} |\nu_i\rangle, \quad |\nu_i\rangle = \sum_l U_{il}^\dagger |\nu_l\rangle = \sum_l U_{li}^* |\nu_l\rangle \quad (2.62)$$

$U$  is a unitary matrix for which

$$U^\dagger U = 1, \quad \sum_i U_{li} U_{l'i}^* = \delta_{ll'}, \quad \sum_l U_{li} U_{lj}^* = \delta_{ij}, \quad (2.63)$$

is true. In the case of antineutrinos, the matrix  $U$  has to be replaced by its conjugate matrix  $U^*$ :

$$|\bar{\nu}_l\rangle = \sum_i U_{li}^* |\bar{\nu}_i\rangle \quad (2.64)$$

In the rest frame of a neutrino mass eigenstate, the time evolution of  $|\nu_i\rangle$  with a rest mass  $m_i$  is described by the Schrödinger equation, which is solved by:

$$|\nu_i(\tau_i)\rangle = e^{-im_i\tau_i} |\nu_i(0)\rangle. \quad (2.65)$$

The phase  $m_i\tau_i$  in the  $\nu_i$  propagator can be transformed into the laboratory frame by using Lorentz invariance:

$$m_i\tau_i = E_it - p_iL \quad (2.66)$$

$t$  is the time in the laboratory frame between the production of a neutrino and its detection at a distance  $L$ .  $t$  and  $L$  are defined by the experiment and are thus common to all  $\nu_i$ . Furthermore,  $t$  equals  $L$  (in natural units) for ultrarelativistic neutrinos. Assuming, that every eigenstate  $|\nu_i\rangle$  has the same energy  $E_i = E$  and a mass  $m_i \approx 0$ , the momentum  $p_i$  is given by

$$p_i = \sqrt{E_i^2 - m_i^2} \quad (2.67)$$

$$\approx E - \frac{m_i^2}{2E}. \quad (2.68)$$

and thus with Equation 2.66

$$m_i\tau_i \approx E(t - L) + \frac{m_i^2}{2E}L = m_i^2 \frac{L}{2E}. \quad (2.69)$$

The time evolution of a flavor state can then be written as

$$|\nu_l(t)\rangle = \sum_i U_{li} e^{-im_i^2 \frac{L}{2E}} |\nu_i(0)\rangle. \quad (2.70)$$

The time dependent transition amplitude  $A$  for the process  $\nu_l \rightarrow \nu_{l'}$  is given by

$$A(\nu_l \rightarrow \nu_{l'}, L) \equiv \langle \nu_{l'}(L) | \nu_l(0) \rangle \quad (2.71)$$

$$= \sum_i U_{li} U_{l'i}^* e^{-im_i^2 \frac{L}{2E}}. \quad (2.72)$$

The transition probability for a neutrino produced with the initial flavor  $l$  and detected with the oscillated flavor  $l'$  after traveling the distance  $L$  in the lab frame is called oscillation probability  $P$  and given by

$$P(\nu_l \rightarrow \nu_{l'}, L) \equiv |A(\nu_l \rightarrow \nu_{l'}, L)|^2 \quad (2.73)$$

$$= \left| \sum_i U_{li} U_{l'i}^* e^{-im_i^2 \frac{L}{2E}} \right|^2 \quad (2.74)$$

$$= \sum_i \sum_j U_{li} U_{l'i}^* U_{l'j}^* U_{lj} e^{-i\Delta m_{ij}^2 \frac{L}{2E}}, \quad (2.75)$$

with  $\Delta m_{ij}^2 = m_i^2 - m_j^2$ . By separating the real and imaginary parts, this can be rewritten to

$$\begin{aligned} P(\nu_l \rightarrow \nu_{l'}, L) &= \delta_{ll'} - 4 \sum_{i>j} \Re(U_{li} U_{l'i}^* U_{l'j}^* U_{lj}) \sin^2(\Delta m_{ij}^2 \frac{L}{4E}) \\ &\quad + 2 \sum_{i>j} \Im(U_{li} U_{l'i}^* U_{l'j}^* U_{lj}) \sin(\Delta m_{ij}^2 \frac{L}{4E}). \end{aligned} \quad (2.76)$$

In case of antineutrinos, the sign of the third term changes:

$$\begin{aligned}
P(\bar{\nu}_l \rightarrow \bar{\nu}_{l'}, L) &= \delta_{ll'} - 4 \sum_{i>j} \Re(U_{li}U_{l'i}^*U_{lj}^*U_{l'j}) \sin^2(\Delta m_{ij}^2 \frac{L}{4E}) \\
&\quad - 2 \sum_{i>j} \Im(U_{li}U_{l'i}^*U_{lj}^*U_{l'j}) \sin(\Delta m_{ij}^2 \frac{L}{4E}).
\end{aligned} \tag{2.77}$$

A  $n \times n$  unitary matrix is completely described by  $n^2$  parameters, with  $n$  being the number of lepton generations in this case. The  $2n - 1$  relative phases of the  $2n$  neutrino states can be defined in a way, that  $(n - 1)^2$  independent parameters remain in case of Dirac neutrinos. It is convenient to describe the  $n$ -dimensional rotational matrix with  $\frac{1}{2}n(n - 1)$  weak mixing angles together with  $\frac{1}{2}(n - 1)(n - 2)$  complex phases [8].

The Matrix  $U$  is generally called PMNS-matrix, named after B. Pontecorvo, Z. Maki, M. Nakagawa, and S. Sakata. Setting the lepton number to three, the PMNS matrix is parametrized by 3 angles and, in case of Dirac neutrinos with 1 complex phase, respectively in case of Majorana neutrinos with 3 complex phases. Except for the neutrino oscillation experiments LSND [14] and Miniboone [15], which measured a  $\bar{\nu}_\mu \rightarrow \bar{\nu}_e$  oscillation with a  $\Delta m^2$  in the region of 0.1 to 1 eV<sup>2</sup>, all experiments are perfectly described by the minimal scheme of three-neutrino mixing. The PMNS matrix is often written in the form

$$\begin{aligned}
U &= \begin{bmatrix} U_{e1} & U_{e2} & U_{e3} \\ U_{\mu1} & U_{\mu2} & U_{\mu3} \\ U_{\tau1} & U_{\tau2} & U_{\tau3} \end{bmatrix} \\
&= \begin{bmatrix} 1 & 0 & 0 \\ 0 & c_{23} & s_{23} \\ 0 & -s_{23} & c_{23} \end{bmatrix} \begin{bmatrix} c_{13} & 0 & s_{13} e^{-i\delta} \\ 0 & 1 & 0 \\ s_{13} e^{i\delta} & 0 & c_{13} \end{bmatrix} \begin{bmatrix} c_{12} & s_{12} & 0 \\ -s_{12} & c_{12} & 0 \\ 0 & 0 & 1 \end{bmatrix} \begin{bmatrix} e^{\frac{i\alpha_1}{2}} & 0 & 0 \\ 0 & e^{\frac{i\alpha_2}{2}} & 0 \\ 0 & 0 & 1 \end{bmatrix}
\end{aligned} \tag{2.78}$$

with  $s_{ij} = \sin(\theta_{ij})$  and  $c_{ij} = \cos(\theta_{ij})$ . Equations 2.76 and 2.77 show that  $P(\nu_l \rightarrow \nu_{l'})$  does not equal  $P(\bar{\nu}_l \rightarrow \bar{\nu}_{l'})$  if the combined charge and parity symmetry conjugation is violated, so  $CP$ -violation occurs. In equation 2.78 a possible  $CP$ -violation is expressed by the so-called Dirac phase  $\delta$  which is commonly multiplied by the angle  $\theta_{13}$ .

$\alpha_{1,2}$  are also  $CP$ -violating phases, called Majorana phases. The Majorana phases are zero if neutrinos are Dirac particles. In any case, these phases have no effect on neutrino oscillations, as they are located on the diagonal in Equation 2.78 and thus vanish when the transition amplitude  $A$  is squared to obtain the oscillation probability  $P$  in Equation 2.73. Neutrino oscillations are therefore completely insensitive to whether neutrinos are Dirac or Majorana particles.

All three angles  $\theta_{12}$ ,  $\theta_{13}$ ,  $\theta_{23}$ , the phase  $\delta$  and the mass squared differences  $\Delta m_{21}^2$  and  $\Delta m_{32}^2$  are physical constants and have to be determined experimentally. An overview about the current status is given in Table 2.1.

As Equation 2.75 shows, the oscillation frequencies measured by neutrino oscillation experiments only depend on squared-mass differences and not on the squared neutrino masses themselves. Hence, only the squared-mass spectral pattern is measurable, not the absolute neutrino masses.

The three squared-mass differences are not independent, since

$$\Delta m_{21}^2 + \Delta m_{32}^2 - \Delta m_{31}^2 = 0. \quad (2.79)$$

The labeling of the mass eigenstates  $m_i$  can be picked at random, but are commonly chosen such that the squared-mass difference observed in solar neutrino oscillation experiments is  $\Delta m_{\text{sol}}^2 = \Delta m_{21}^2$  with  $m_2^2 > m_1^2$ . The sign of the squared-mass difference observed in atmospheric oscillation  $\Delta m_{\text{atm}}^2 \approx |\Delta m_{32}^2| \approx |\Delta m_{31}^2|$  is unknown, which leads to the question of the neutrino mass hierarchy. The three possibilities of the neutrino mass hierarchy are called normal (Equation 2.80), inverted (Equation 2.81) or quasi-degenerate (Equation 2.82):

$$\text{NH:} \quad m_1 < m_2 < m_3 \quad (2.80)$$

$$\text{IH:} \quad m_3 < m_1 < m_2 \quad (2.81)$$

$$\text{QDH:} \quad m_1 \approx m_2 \approx m_3 \quad (2.82)$$

The answer to this question by future neutrino oscillation experiments is of great importance for the search of neutrinoless double beta decay. This is exemplified in Section 2.5.

**Table 2.1:** Neutrino oscillation parameters for normal hierarchy, all values taken from [16]. For  $\Delta m_{31}^2$ ,  $\sin^2(\theta_{23})$ ,  $\sin^2(\theta_{13})$  and  $\delta$  the given values vary slightly in case of inverted hierarchy and are not listed here.

Parameter	best fit	$1\sigma$ range	$3\sigma$ range
$\sin^2(\theta_{12})$	0.323	0.307-0.339	0.278-0.375
$\sin^2(\theta_{23})$	0.567	0.439-0.599	0.392-0.643
$\sin^2(\theta_{13})/10^{-2}$	2.34	2.14-2.54	1.77-2.94
$\Delta m_{21}^2$ [ $10^{-5}$ eV <sup>2</sup> ]	7.60	7.42-7.79	7.11-8.18
$\Delta m_{31}^2$ [ $10^{-3}$ eV <sup>2</sup> ]	2.48	2.41-2.53	2.30-2.65
$\delta/\pi$	1.34	0.96-1.98	0-2

## 2.4 Electromagnetic Properties of Neutrinos

Within the SM, neutrinos are massless and left-handed Dirac particles, which cannot possess an electromagnetic dipole moment. This is due to the fact, that for  $m_\nu = 0$  the helicity is fixed  $H = -1$  for  $\nu$  (and  $H = +1$  for  $\bar{\nu}$ ). If the neutrino

had a magnetic moment, an external magnetic field could flip the spin and thereby the helicity into  $H = +1$ . This is not possible in the Standard model.

Within a minimal extension of the SM with small Dirac masses  $m_\nu$ , neutrinos gain a magnetic dipole moment by coupling with photons via loop diagrams [3]. The magnetic dipole moment  $\mu_\nu$  is then [17]

$$\mu_\nu = \frac{3G_f e}{8\sqrt{2}\pi^2} m_\nu = 3.2 \cdot 10^{-19} \frac{m_\nu}{\text{eV}} \mu_B. \quad (2.83)$$

Here  $G_f$  is the Fermi coupling constant,  $e$  the charge of an electron and  $\mu_B$  the Bohr magneton:

$$\mu_B = \frac{e\hbar}{2m_e} \approx 9.274 \cdot 10^{-24} \frac{\text{J}}{\text{T}}. \quad (2.84)$$

Assuming  $CPT^3$  invariance, a Majorana neutrino cannot possess a magnetic dipole moment  $\mu_\nu$  or an electric dipole moment  $d_\nu$ . In a magnetic field  $\vec{B}$  and an electric field  $\vec{E}$  a neutrino with spin direction  $\vec{\sigma}$  has an electromagnetic energy  $E_{em}$ :

$$E_{em} = -\mu_\nu \vec{\sigma} \cdot \vec{B} - d_\nu \vec{\sigma} \cdot \vec{E} \quad (2.85)$$

Applying  $CPT$  results in  $\vec{B} \rightarrow \vec{B}$ ,  $\vec{E} \rightarrow \vec{E}$ ,  $\vec{\sigma} \rightarrow -\vec{\sigma}$  and thus  $E_{em} \rightarrow -E_{em}$ . As  $CPT$  transforms a Majorana neutrino into itself ( $\nu = \bar{\nu}$ ), no change in  $E_{em}$  is allowed. Hence,  $E_{em}$  has to equal zero which is only possible with  $\mu_\nu = d_\nu = 0$ .

Applying  $CPT$  invariance to Dirac neutrinos leads to the finding, that Dirac neutrinos have a vanishing electric dipole moment  $d_\nu$ . Therefore, the distinction between Dirac and Majorana neutrinos is in principle possible by investigating the magnetic dipole moment. Applying upper bounds on neutrino masses from Equations 2.125 - 2.127, the following upper bounds on  $\mu_\nu$  are set to:

$$\mu_{\nu_e}^{\text{SM}} < 6.4 \cdot 10^{-19} \mu_B \quad (2.86)$$

$$\mu_{\nu_\mu}^{\text{SM}} < 6.08 \cdot 10^{-14} \mu_B \quad (2.87)$$

$$\mu_{\nu_\tau}^{\text{SM}} < 5.82 \cdot 10^{-12} \mu_B \quad (2.88)$$

Currently, the magnetic dipole moment is far too small to be observed or to have any measurable effect in astrophysics. Reference [18] quotes the following experimental upper limits:

$$\mu_{\nu_e} < 0.32 \cdot 10^{-10} \mu_B \quad (2.89)$$

$$\mu_{\nu_\mu} < 6.8 \cdot 10^{-10} \mu_B \quad (2.90)$$

$$\mu_{\nu_\tau} < 3900 \cdot 10^{-10} \mu_B \quad (2.91)$$

<sup>3</sup> $CPT$  is the combined charge ( $C$ ), parity ( $P$ ) and time ( $T$ ) symmetry conjugation.

## 2.5 Double Beta Decay

Double beta decay in general is a nuclear process among isobaric isotopes changing the nuclear charge  $Z$  by two units while leaving the atomic mass  $A$  unchanged. The mass  $m(Z, A)$  of an atom is given by the semi-empirical Weizsäcker's formula [19, 20]

$$m(Z, A) = Nm_n + Zm_p + Zm_e - a_v A + a_s A^{2/3} + a_c \frac{Z^2}{A^{1/3}} + a_a \frac{(N - Z)^2}{4A} + \frac{\delta}{A^{1/2}}, \quad (2.92)$$

where  $N = A - Z$  is the number of neutrons,  $m_n$  the neutron mass,  $m_p$  the proton mass and  $m_e$  the electron mass. The values for the parameters  $a_v, a_s, a_c, a_a$  and  $\delta$  vary, depending on the mass range under consideration. Some coefficients are insensitive to mass, but are affected by other effects like the necessary energy for producing fission. A set of values often used is [21]:

$$\begin{aligned} a_v &= 15.67 \text{ MeV} \\ a_s &= 17.23 \text{ MeV} \\ a_c &= 0.714 \text{ MeV} \\ a_a &= 93.15 \text{ MeV} \\ \delta &= \begin{cases} -11.2 \text{ MeV} & \text{for even } Z \text{ and } N \\ 0 \text{ MeV} & \text{for odd } A \\ 11.2 \text{ MeV} & \text{for odd } Z \text{ and } N \end{cases} \end{aligned} \quad (2.93)$$

For considering isobars in double beta decay, Equation 2.92 can be simplified to

$$m(Z, A = \text{const.}) \propto a + b \cdot Z + c \cdot Z^2 + \frac{\delta}{A^{1/2}}. \quad (2.94)$$

The term including  $\delta$  is called the pairing energy, which vanishes in case for odd  $A$ . In contrast, for even  $A$  the mass  $m(Z, A)$  splits into two parabolas separated by  $2 \cdot \delta \cdot \sqrt{A}$ .

The splitting into two parabolas allows double beta decay to occur, at which all double beta decay candidate isotopes are even-even nuclei. In this process, the double beta decay nuclei with  $m(Z, A)$  decays into the next lighter even-even nuclei on the same mass parabola with  $m(Z + 2, A)$ . Thus, the compelling requirement for double beta decay to occur is

$$m(Z, A) > m(Z + 2, A). \quad (2.95)$$

The decay into the interim odd-odd nuclei with  $m(Z + 1, A)$  has to be energetically forbidden or strongly suppressed for experimental reasons:

$$m(Z, A) < m(Z + 1, A). \quad (2.96)$$



In Figure 2.1 an example is given for  $A = 116$ , where the double beta decay of  $^{116}\text{Cd}$  is illustrated. A selection of double beta decay isotopes under experimental consideration together with their decay energies (called Q-values) and natural abundances is given in Table 2.2.

**Table 2.2:** A selection of double beta decay isotopes under experimental consideration. All values taken from [22], except for the Q-value and the natural abundance of  $^{116}\text{Cd}$  [23].

Transition	Q-value [keV]	nat. ab. [%]
$^{76}\text{Ge} \rightarrow ^{76}\text{Se}$	2039.1	7.8
$^{82}\text{Se} \rightarrow ^{82}\text{Kr}$	2995.5	9.2
$^{116}\text{Cd} \rightarrow ^{116}\text{Sn}$	2813.5	7.5
$^{130}\text{Te} \rightarrow ^{130}\text{Xe}$	2530.3	34.5
$^{136}\text{Xe} \rightarrow ^{136}\text{Ba}$	2457.8	8.9

### 2.5.1 The $2\nu\beta\beta$ Decay

Double beta decay was first discussed by M. Goeppert-Mayer [25] in the form

$$(Z, A) \rightarrow (Z + 2, A) + 2e^- + 2\bar{\nu}_e \quad (2.97)$$

$$2n \rightarrow 2p + 2e^- + 2\bar{\nu}_e \quad (2.98)$$

and in the following is referred to as neutrino accompanied double beta decay or  $2\nu\beta\beta$ . A Feynman diagram is shown in Figure 2.2. This decay mode conserves lepton number and is therefore allowed in the standard model.  $2\nu\beta\beta$  decay is among the rarest processes observed, with half-lives in the order of  $10^{20}$  years. An incomplete compilation of measured half-lives is given in Table 2.3. These half-lives are important for the development of neutrinoless double beta decay experiments, as  $2\nu\beta\beta$  decays are an unavoidable background (see Chapter 4.2.4).

An equivalent decay mode is the  $\beta^+\beta^+$  decay, which is always accompanied by electron capture (EC) in the form of  $\beta^+/\text{EC}$  or  $\text{EC}/\text{EC}$ :

$$(Z, A) \rightarrow (Z - 2, A) + 2\nu_e + 2e^+ \quad (\beta^+\beta^+) \quad (2.99)$$

$$e^- + (Z, A) \rightarrow (Z - 2, A) + 2\nu_e + e^+ \quad (\beta^+/\text{EC}) \quad (2.100)$$

$$2e^- + (Z, A) \rightarrow (Z - 2, A) + 2\nu_e \quad (\text{EC}/\text{EC}) \quad (2.101)$$

Compared to double electron capture, the Q-value of  $\beta^+\beta^+$  decay is reduced due to the Coulomb barrier by  $4m_e = 2044$  keV and thus is only possible for six nuclides (see Table 2.4). Half-lives for  $2\nu\beta^+\beta^+$  are predicted in the order of  $10^{26}$  years,

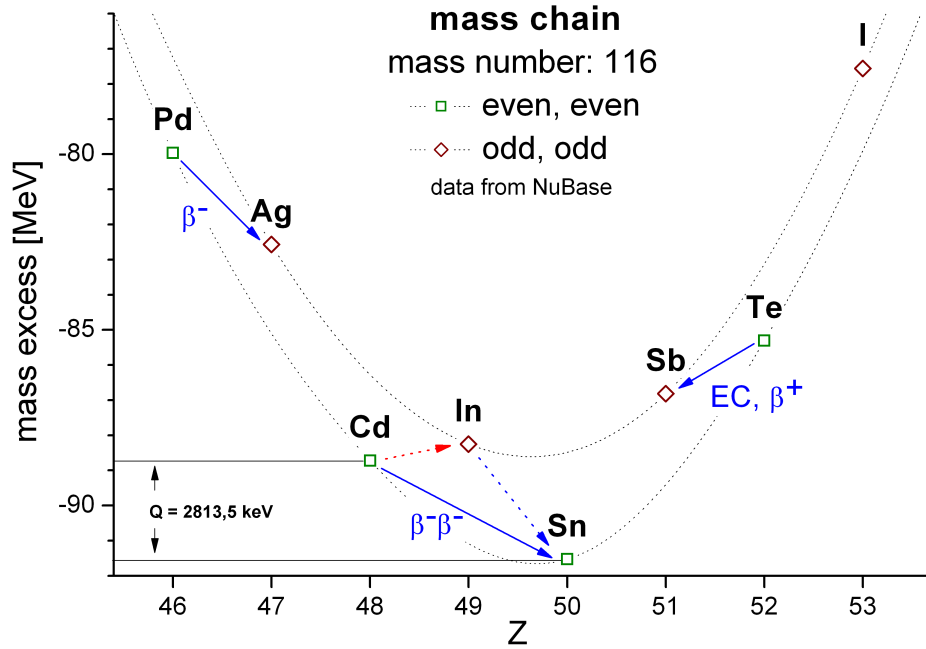


**Figure 2.1:** Mass chain for  $A = 116$ . The mass parabolas are separated for even-even and odd-odd nuclei. As the beta decay from  $^{116}\text{Cd}$  to  $^{116}\text{In}$  is energetically forbidden, the double beta decay to  $^{116}\text{Sn}$  with a  $Q$ -value of 2813.5 keV is observable. Taken from [24].

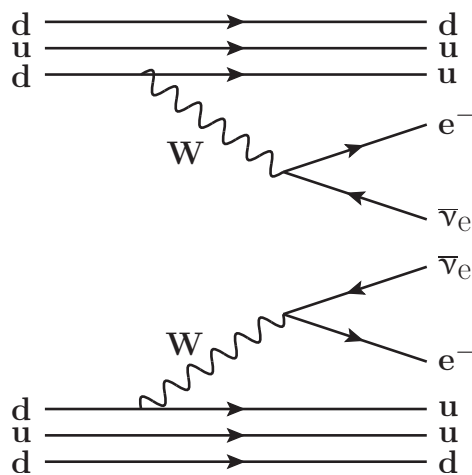


**Figure 2.2:** Feynman diagram for  $2\nu\beta\beta$  decay.

**Table 2.3:** A compilation of  $2\nu\beta\beta$  decay half-lives  $T_{1/2}$ . All values are given with 68 % C.L. [18].

Transition	$T_{1/2}$ [ $10^{21}$ y]	Experiment
$^{76}\text{Ge} \rightarrow ^{76}\text{Se}$	$1.74 \pm 0.01^{+0.18}_{-0.16}$	Heidelberg-Moscow
$^{82}\text{Se} \rightarrow ^{82}\text{Kr}$	$(9.6 \pm 0.3 \pm 0.1) \cdot 10^{-2}$	NEMO-3
$^{116}\text{Cd} \rightarrow ^{116}\text{Sn}$	$(2.8 \pm 0.1 \pm 0.3) \cdot 10^{-2}$	NEMO-3
$^{130}\text{Te} \rightarrow ^{130}\text{Xe}$	$0.7 \pm 0.09 \pm 0.11$	NEMO-3
$^{136}\text{Xe} \rightarrow ^{136}\text{Ba}$	$2.38 \pm 0.02 \pm 0.14$	KamLAND-ZEN
$^{136}\text{Xe} \rightarrow ^{136}\text{Ba}$	$2.11 \pm 0.04 \pm 0.21$	EXO-200

while half-lives in the order of  $10^{23}$  years for  $2\nu\beta^+/\text{EC}$  are more realistic for experimental detection [9]. Although having the lowest expected half-life,  $2\nu\text{EC}/\text{EC}$  decay can hardly be detected, as there are only two electron neutrinos in the final state. Up to now, only the observation of  $2\nu\text{EC}/\text{EC}$  of  $^{130}\text{Ba}$  has been claimed, using a geochemical technique [26]. The search for neutrinoless double electron capture ( $0\nu\text{EC}/\text{EC}$ ) is discussed in Section 2.5.3.

**Table 2.4:** Compilation of six known double  $\beta^+$  decay isotopes along with their Q-values and natural abundances [27].

Transition	Q-value [keV]	nat. ab. [%]
$^{78}\text{Kr} \rightarrow ^{78}\text{Se}$	838	0.35
$^{96}\text{Se} \rightarrow ^{96}\text{Kr}$	676	5.5
$^{106}\text{Cd} \rightarrow ^{106}\text{Pd}$	738	1.25
$^{124}\text{Xe} \rightarrow ^{124}\text{Te}$	822	0.10
$^{130}\text{Ba} \rightarrow ^{130}\text{Xe}$	534	0.11
$^{136}\text{Ce} \rightarrow ^{136}\text{Ba}$	362	0.19

## 2.5.2 The $0\nu\beta\beta$ Decay

After the proposal of a neutrino with a two-component spinor by E. Majorana, the neutrinoless double beta decay ( $0\nu\beta\beta$ ) was suggested by G. Racah [28] and W. Furry [29]:

$$(Z + A) \rightarrow (Z + 2, A) + 2e^- \quad (2.102)$$

$$2n \rightarrow 2p + 2e^- \quad (2.103)$$

This process violates lepton number conservation by two units and is therefore forbidden in the standard model.

An elementary approach for this process is the so-called light-neutrino-exchange. It can be understood as two subsequent steps, the Racah sequence:

$$\begin{aligned} (Z + A) &\rightarrow (Z + 1, A) + \bar{\nu}_e + e^- \\ (Z + 1, A) + \nu_e &\rightarrow (Z + 2, A) + e^- \end{aligned} \quad (2.104)$$

In the first step, a neutron decays under emission of a right-handed  $\bar{\nu}_e$  and an electron. In the second step, this antineutrino is absorbed by a second neutron in the same nucleus as a left-handed  $\nu_e$  and another electron is emitted. A Feynman diagram for this process is shown in Figure 2.3. Two conditions for the occurrence of this process have to be realized:

1. Neutrino and antineutrino are identical and hence a Majorana particle
2. To allow for helicity matching, neutrinos are massive

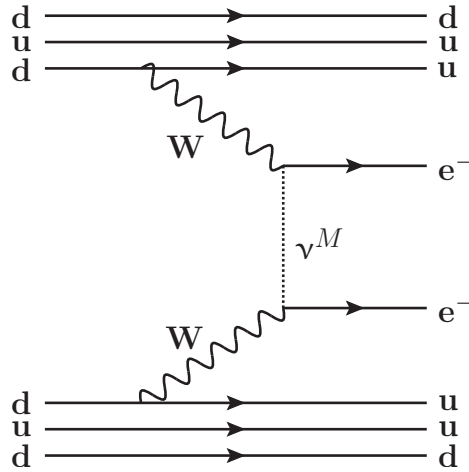


**Figure 2.3:** Feynman diagram for  $0\nu\beta\beta$  decay. In this case, the exchange of a light Majorana neutrino  $\nu^M$  is depicted.

In contrast to  $2\nu\beta\beta$ , no neutrinos are present in the final state of the  $0\nu\beta\beta$  decay. Hence the proof for  $0\nu\beta\beta$  decay is the observation of a peak at the  $Q$ -value in the sum spectrum of the electrons.

The exchange of a light neutrino in the Racah sequence is not the only possible mechanism leading to the occurrence of  $0\nu\beta\beta$  decay. A variety of mechanisms is conceivable, i. g. the helicity matching could be due to  $V + A$  interactions allowing for right-handed charged currents. An overview on other active mechanism can be found in [30]. Nonetheless, the observation of neutrinoless double beta decay guarantees the Majorana nature of neutrinos. The Schechter-Valle theorem [31]

relates the effective  $0\nu\beta\beta$  decay operator to a non-zero effective Majorana electron neutrino mass. On the other hand, the physical neutrino masses can also depend on Dirac mass terms and not only on Majorana mass terms. As the underlying mechanism is not distinguishable by observing the  $0\nu\beta\beta$  decay in current and future neutrinoless double beta decay experiments, the Schechter-Valle theorem is often referred as the Black Box theorem (see Figure 2.4).

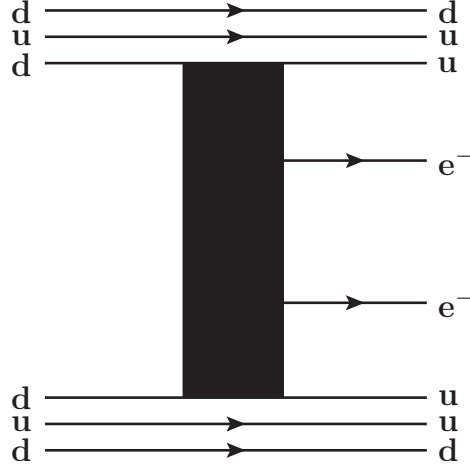


**Figure 2.4:** Black box diagram for  $0\nu\beta\beta$  decay. The underlying mechanism is not visible in current and upcoming  $0\nu\beta\beta$  experiments, only the two electrons of the final state are detectable.

For  $0\nu\beta\beta$  decay half-life calculations, one has to consider different nuclear matrix elements associated with different decay mechanism. For light-neutrino-exchange, the half-life of  $0\nu\beta\beta$  is given by [9]

$$\frac{1}{T_{1/2}^{0\nu}} = G^{0\nu}(Q, Z) \cdot |M^{0\nu}|^2 \cdot \frac{m_{\beta\beta}^2}{m_e^2}. \quad (2.105)$$

$G^{0\nu}(Q, Z)$  is the known phase-space factor and  $M^{0\nu}$  the nuclear matrix element (NME), which depends on the nuclear structure of the participating isotopes  $(Z, A)$ ,  $(Z + 1, A)$  and  $(Z + 2, A)$ . The quantity  $m_{\beta\beta}$  is called effective Majorana neutrino mass.

### Effective Majorana Neutrino Mass

The effective Majorana neutrino mass  $m_{\beta\beta}$  is given by

$$\begin{aligned} m_{\beta\beta} &= \left| \sum_i U_{ei}^2 m_i \right| = |U_{e1}^2 m_1 \pm U_{e2}^2 m_2 \pm U_{e3}^2 m_3| \\ &= |c_{12}^2 c_{13}^2 e^{i\alpha_1} m_1 \pm s_{12}^2 c_{13}^2 e^{i\alpha_2} m_2 \pm s_{13}^2 m_3| \end{aligned} \quad (2.106)$$

with  $U$  being the PMNS matrix introduced in Section 2.3. The full expression for  $m_{\beta\beta}$  is

$$\begin{aligned} m_{\beta\beta}^2 &= c_{12}^4 c_{13}^4 m_1^2 + s_{12}^4 c_{13}^4 m_2^2 + s_{13}^4 m_3^2 \\ &+ 2c_{12}^2 s_{12}^2 c_{13}^4 m_1 m_2 \cos(\alpha_1 - \alpha_2) \\ &+ 2c_{12}^2 c_{13}^2 s_{13}^2 m_1 m_3 \cos(\alpha_1) \\ &+ 2s_{12}^2 c_{13}^2 s_{13}^2 m_2 m_3 \cos(\alpha_2). \end{aligned} \quad (2.107)$$

From this equation follows that the effective Majorana neutrino mass depends on the neutrino mass spectrum and three unknown parameters: the lightest neutrino mass  $m_{min}$  and the two Majorana phases  $\alpha_1$  and  $\alpha_2$ . With some simplifications, upper and lower limits for  $m_{\beta\beta}$  can be calculated [32]:

For normal hierarchy  $m_1$  is the lightest mass and one finds:

$$\Delta m_{12}^2 \ll \Delta m_{23}^2, \quad (2.108)$$

$$m_{min} = m_1 \ll m_2 \ll m_3, \quad (2.109)$$

$$m_2 \simeq \sqrt{\Delta m_{sol}^2}, \quad (2.110)$$

$$m_3 \simeq \sqrt{\Delta m_{atm}^2}. \quad (2.111)$$

By neglecting the small contribution of  $m_1$  the following range for  $m_{\beta\beta}^{NH}$  is then:

$$\left| s_{12}^2 c_{12}^2 \sqrt{\Delta m_{sol}^2} - s_{13}^2 \sqrt{\Delta m_{atm}^2} \right| \leq m_{\beta\beta}^{NH} \leq s_{12}^2 c_{13}^2 \sqrt{\Delta m_{sol}^2} + s_{13}^2 \sqrt{\Delta m_{atm}^2}. \quad (2.112)$$

Using the best fit values from [33] one finds

$$1.5 \text{ meV} \leq m_{\beta\beta}^{NH} \leq 3.8 \text{ meV}. \quad (2.113)$$

In contrast, for the inverted hierarchy  $m_3$  is the lightest mass:

$$\Delta m_{12}^2 \ll |\Delta m_{13}^2|, \quad (2.114)$$

$$m_{min} = m_3 \ll m_1 < m_2, \quad (2.115)$$

$$m_3 \ll \sqrt{\Delta m_{atm}^2}, \quad (2.116)$$

$$m_1 \simeq m_2 \simeq \sqrt{\Delta m_{atm}^2}. \quad (2.117)$$

The range for  $m_{\beta\beta}^{IH}$  is in this case:

$$|\cos(2\theta_{12})| c_{13}^2 \sqrt{\Delta m_{atm}^2} \leq m_{\beta\beta}^{IH} \leq c_{13}^2 \sqrt{\Delta m_{atm}^2} \quad (2.118)$$

And again using the best fit values from [33] one finds

$$18 \text{ meV} \leq m_{\beta\beta}^{IH} \leq 48 \text{ meV}. \quad (2.119)$$

The ranges for  $m_{\beta\beta}^{NH}$  and  $m_{\beta\beta}^{IH}$  are given by the Majorana phases  $\alpha_1$  and  $\alpha_2$  in Equation 2.107 and are not due to uncertainties in the measured mixing parameters. They have to be taken into account separately and are considered in Figure 2.5.

Current lower limits for  $m_{\beta\beta}$  obtained with different isotopes are examined in Section 2.6. However, one can conclude that even next-generation experiments will not be sensitive enough to reach the normal mass hierarchy. Thus, the goal for next-generation experiments is a sensitivity on  $m_{\beta\beta}$  of 50 meV. The knowledge of the mass hierarchy being normal, inverted or quasi-degenerated, would be very helpful for the development of future experiments.

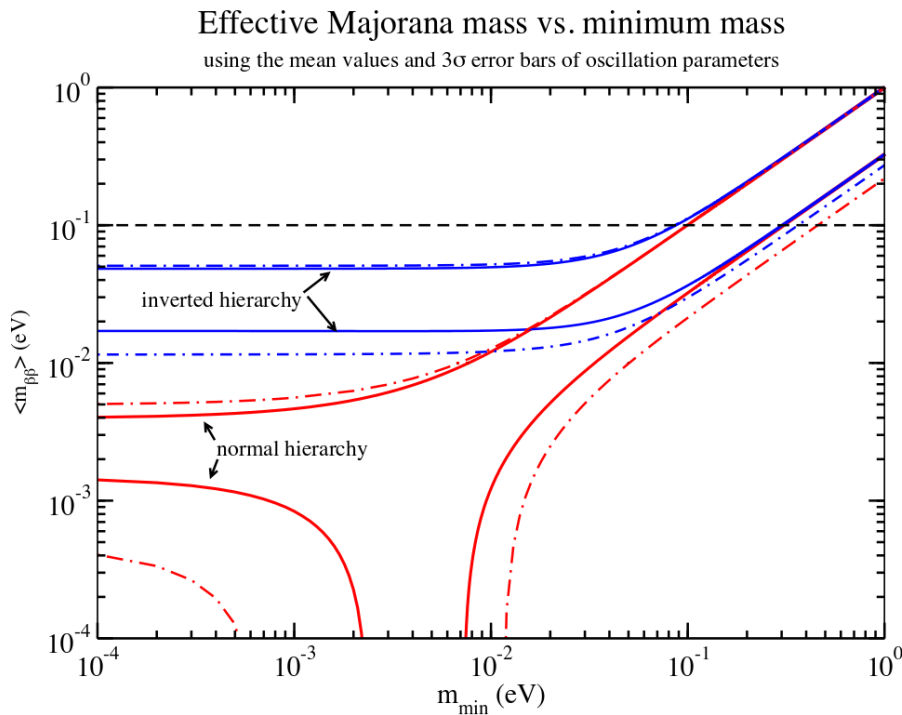


**Figure 2.5:** Allowed regions for  $m_{\beta\beta}$  as a function of the lightest neutrino mass  $m_{\min}$  for the inverted and normal hierarchies. Taken from [34]. The regions defined by the solid curves correspond to the best fit neutrino mixing parameters from [33] and account for the degeneracy due to the unknown Majorana phases. The regions defined by the dashed-dotted curves correspond to the maximal allowed regions including mixing parameter uncertainties as evaluated in [33]. The dashed line shows expected sensitivity of next-generation 100 kg class experiments and the dotted line shows potential reach of multi-ton scale future experiments.

### Nuclear Matrix Elements

The nuclear matrix elements  $M^{0\nu}$  of neutrinoless double beta decay have to be calculated using nuclear structure theory. As there are no observables linked to the

magnitude of  $0\nu\beta\beta$  NMEs, they can not be determined in a model independent way. Furthermore, the calculations are difficult due to many excited states of openshell nuclei with complicated nuclear structure under consideration. There are a number of methods used for the calculation of  $M^{0\nu}$ , some of them are:

- The Interacting Shell Model (ISM)
- The Quasiparticle Random Phase Approximation (QRPA)
- The Interacting Boson Model (IBM)
- The Projected Hartree-Fock-Boboliubov Method (PHFB)
- The Energy Density Functional Method (EDF)
- The Generator Coordinate Method (GCM)
- The Large Scale Shell Model (LSSM)

A compilation of NMEs calculated with different approaches is listed in Table 2.5, a more comprehensive collection of NMEs is given in Figure 2.6.

**Table 2.5:** Nuclear matrix elements  $M^{0\nu}$  calculated with different approaches [32]. The PHFB method is not listed here, as there is only a value for  $^{130}\text{Te}$  available. The different values for the QRPA method were calculated by different groups.

Transition	ISM	QRPA	IBM-2	EDF
$^{76}\text{Ge} \rightarrow ^{76}\text{Se}$	2.30	4.92, 4.72	5.47	3.70
$^{82}\text{Se} \rightarrow ^{82}\text{Kr}$	2.18	4.39, 2.77	4.41	3.39
$^{116}\text{Cd} \rightarrow ^{116}\text{Sn}$		2.99, 3.17		3.80
$^{130}\text{Te} \rightarrow ^{130}\text{Xe}$	2.12	3.56, 3.28	4.06	4.12
$^{136}\text{Xe} \rightarrow ^{136}\text{Ba}$	1.76	2.30, 2.54		3.38

Considering a specific value  $M^{0\nu}$  for a given isotope, one can now use Equation 2.105 to calculate the required half-life to reach a specific value of  $m_{\beta\beta}$ . To reach the inverted hierarchy a minimum sensitivity to achieve  $m_{\beta\beta} = 50$  meV is needed. The corresponding half-lives for different isotopes and NME approaches are shown in Figure 2.7. This diagram shows that the COBRA experiment has to aim for a half-life sensitivity of at least  $2 \cdot 10^{26}$  years for the decay of  $^{116}\text{Cd}$  to reach the effective Majorana neutrino mass of 50 meV.

As there are large discrepancies between different NME approaches for a given isotope,  $m_{\beta\beta}$  can only be calculated with big uncertainties for a measured  $0\nu\beta\beta$  half-life. These uncertainties can only be reduced by measuring  $T_{1/2}^{0\nu}$  for as many different  $0\nu\beta\beta$  decay isotopes as possible.



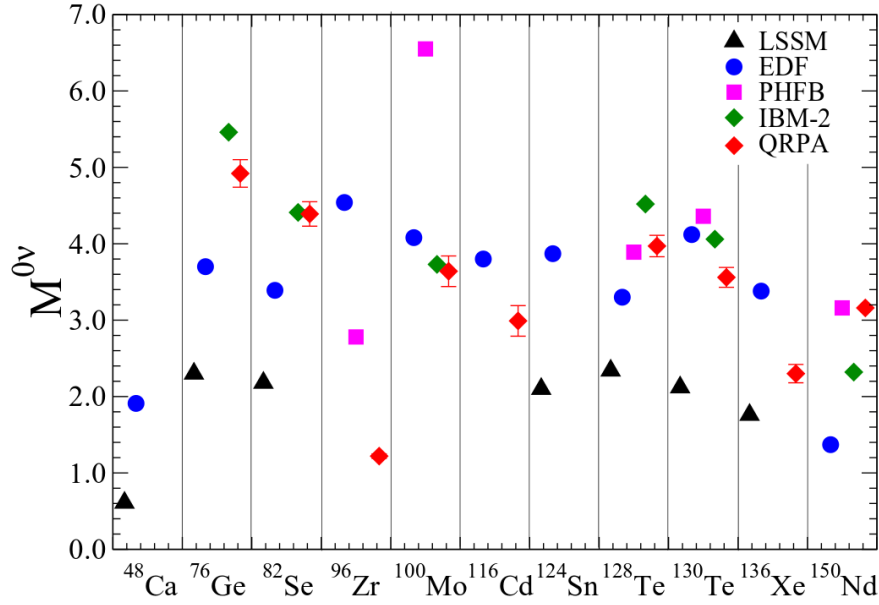


**Figure 2.6:** Nuclear matrix elements  $M^{0\nu}$  for  $0\nu\beta\beta$  isotopes calculated with different nuclear structure approaches [35].

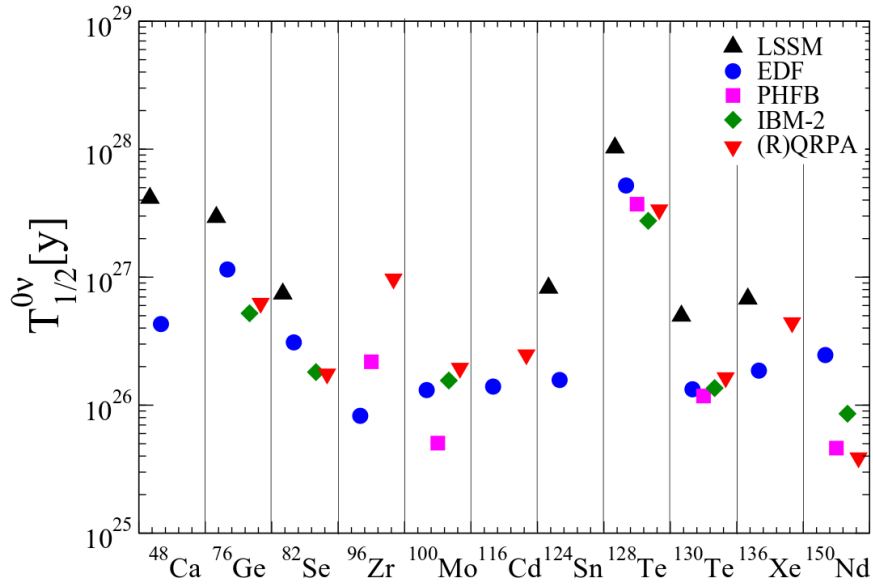


**Figure 2.7:** Half-lives  $T_{1/2}^{0\nu}$  calculated with different nuclear structure approaches for  $m_{\beta\beta} = 50$  meV [35].

### Experimental Half-Life Sensitivity

As described in Section 2.6, only one experiment so far claimed the observation of  $0\nu\beta\beta$ . For all other experiments the detected number of events in the region of interest (ROI) around the Q-value of the decay is consistent with the background expectation  $n_{bkg}$ . This number can be approximated by [22]

$$n_{bkg} = M \cdot t \cdot B \cdot \Delta E, \quad (2.120)$$

where  $M$  is the detector mass,  $t$  the measuring time,  $B$  the background index normally given in counts/keV/kg/a and  $\Delta E$  the energy resolution dependent search window around the Q-value. This approximation does not account for the normally non-linear shape of the background spectrum.

The half-life  $T_{1/2}^{0\nu}$  is related to the upper limit on the number of signal events  $n_{sig}$  if  $0\nu\beta\beta$  is not observed:

$$n_{sig} = \ln 2 \cdot N_A \cdot \epsilon \cdot a \cdot M \cdot t / (m_A \cdot T_{1/2}^{0\nu}) \quad (2.121)$$

Here  $N_A$  is the Avogadro constant,  $m_A$  the molar mass of the isotope,  $\epsilon$  the signal detection efficiency and  $a$  the fraction of  $0\nu\beta\beta$  candidate isotope in the detector mass.

For  $n_{bkg} < 1$  the experimental half-life sensitivity scales with  $M \cdot t$ , while for present and next-generation experiments  $n_{bkg} \gg 1$ . This means, that the background is dominant in the expected signal region. Considering the absence of a  $0\nu\beta\beta$  signal, the 90% C.L. limit on the half-life is then given by

$$T_{1/2}^{0\nu} (90\% \text{ C.L.}) > \frac{\ln 2}{1.64} \frac{N_A}{m_A} \cdot \epsilon \cdot a \cdot \sqrt{\frac{M \cdot t}{B \cdot \Delta E}}. \quad (2.122)$$

Equation 2.122 summarizes the most important aspects for the development of a  $0\nu\beta\beta$  decay experiment. The choice of an isotope not only defines the molar mass, but also restricts the choice of detector technology and has thus a huge impact on the achievable detection efficiency and energy resolution. Furthermore, isotopic abundance and enrichment costs vary among different isotopes and have to be taken into account to reach a satisfactory detector mass.

An unavoidable background for every experiment is the  $2\nu\beta\beta$  decay, therefore an isotope with a high  $T_{1/2}^{2\nu}$  and a detector concept with a very good energy resolution are preferred to separate  $2\nu\beta\beta$  and  $0\nu\beta\beta$  decay events. The Q-value of the chosen isotope is also very important with respect to the achievable background index  $B$ . These two aspects regarding the background are explained with more details in Section 4.2.

### 2.5.3 The $0\nu\beta^+\beta^+$ Decay and Resonant $0\nu\text{EC}/\text{EC}$

In analogy to the  $2\nu\beta^+\beta^+$  decay, discussed in Section 2.5.1, the neutrinoless  $\beta^+\beta^+$  decay is also under investigation and can occur as  $0\nu\beta^+\beta^+$ ,  $0\nu\beta^+/\text{EC}$  or

$0\nu\text{EC}/\text{EC}$ . The observation of one of the three decay modes would also imply violation of lepton number conservation by two units and proof the Majorana nature of neutrinos.

In contrast to neutrino accompanied  $\beta^-\beta^-$  decay, none of the three possible decay modes neither of neutrino accompanied nor neutrinoless  $\beta^+\beta^+$  decay has ever been observed, except the claim for measuring the  $2\nu\text{EC}/\text{EC}$  of  $^{130}\text{Ba}$  [26]. In addition, the natural abundances for  $\beta^+\beta^+$  decay candidate isotopes are comparatively small (see Table 2.4) and thus large source masses are not easily achievable.

The  $0\nu\text{EC}/\text{EC}$  was first considered by R. G. Winter in 1955 [36]:

$$(Z, A) + e_b^- + e_b^- \rightarrow (Z - 2, A)^{**} \quad (2.123)$$

Here two bound electrons from the atomic shell are captured by two protons, potentially leaving the system in an excited nuclear or atomic state. The energy excess due to the Q-value of the decay has to be carried away by a photon, whose energy is

$$E_{h\nu} = Q - E_{atom}^x - E_{nucl}^x. \quad (2.124)$$

Here  $E_{atom}^x$  is the energy of X-rays or Auger electrons emitted from the excited electron shell and  $E_{nucl}^x$  is the energy of the electromagnetic decay of the excited nucleus in case of non-ground-state transition.

The signature of  $0\nu\text{EC}/\text{EC}$  is different from the signature of  $0\nu\beta\beta$  decay and coincident detection techniques for photons and/or X-rays have to be applied. The coupling to an extra photon makes the half-life of  $0\nu\text{EC}/\text{EC}$  comparatively long, e.g. for  $^{106}\text{Cd}$  above  $10^{30}$  y for  $m_{\beta\beta} = 1$  eV. Thus, this decay mode has not been experimentally considered for a long time.

The situation however changes, if the energy difference in Equation 2.124 converges to 0 and an extra photon is not required for the decay. This decay mode is called resonant enhanced neutrinoless double electron capture ( $\text{R}0\nu\text{EC}/\text{EC}$ ). Half-lives are predicted to be as low as  $10^{22}$  y for the Majorana neutrino of 1 eV [37]. To accurately predict  $\text{R}0\nu\text{EC}/\text{EC}$  half-lives, precision mass measurements of the involved atoms in the range of 10 eV have to be performed, e.g. by using Penning Traps.

## 2.6 Current Status and Future Perspective of $0\nu\beta\beta$

Up to now, only a part of the Heidelberg-Moscow collaboration claimed the observation of a  $0\nu\beta\beta$  signal. This result and the experiment are explained in more detail in this section. Thereafter an incomplete overview on past, current and next-generation  $0\nu\beta\beta$  experiments is given, separated by the isotopes under investigation. As the experiments KamLAND-Zen and SNO+ use liquid scintillator as active detector mass for the search of neutrinoless double beta decay, they are explained in more detail in Chapter 3.

### Heidelberg-Moscow

Between 1990 and 2003 the Heidelberg-Moscow experiment operated five germanium detectors with a total mass of 11 kg. The detector material was enriched in  $^{76}\text{Ge}$  to an average level of 86%. The germanium diodes were mounted in a copper cryostat and shielded by copper, lead and Polyethylene. A total exposure of 71.7 kg·a was collected.

In 2004 a part of the Heidelberg-Moscow collaboration published the observation of  $0\nu\beta\beta$  with a half-life of  $T_{1/2}^{0\nu} = 1.19_{-0.23}^{+0.37} \cdot 10^{25}$  a (only statistical error quoted) [38].

In 2006 this claim was extended in another publication [39]. Background originating from gamma events was rejected using a pulse shape analysis. A half-life of  $T_{1/2}^{0\nu} = 2.23_{-0.31}^{+0.44} \cdot 10^{25}$  a is reported. This analysis is controversially discussed, e.g. in [22].

### $^{76}\text{Ge}$ : GERDA and MAJORANA

GERDA is a phased stage experiment using germanium detectors with a new shielding approach. The detectors are operated in a 4 m cryostat filled with liquid Argon. The cryostat is surrounded by a water tank instrumented with photomultiplier tubes (PMTs) acting as a muon veto.

In the first phase, detectors from Heidelberg-Moscow and IGEX with a total double beta emitter mass of about 13 kg are used. Commissioning of the detector started in 2010 and data-taking began in November 2011. Until May 2013 21.6 kg·a data was collected with a background index of about  $10^{-2}$  counts/keV/kg/a. No signal is observed and the lower half-life limit for  $0\nu\beta\beta$  is given by  $T_{1/2}^{0\nu} = 2.1 \cdot 10^{25}$  a (90% C.L.) [40]. This value nearly completely excludes the published observation of  $0\nu\beta\beta$  by a part of the Heidelberg-Moscow collaboration.

In the second phase, newly developed detectors with a mass of 18 kg of  $^{76}\text{Ge}$  are added and the liquid Argon is instrumented to further reduce the background.

A third stage would be the combination with the MAJORANA experiment. MAJORANA [41] also operates germanium detectors, but with a shielding approach similar to the former Heidelberg-Moscow experiment. The detectors with a mass of about 27 kg of  $^{76}\text{Ge}$  are operated in a vacuum cryostat made of electroformed copper, which is self-made in an underground laboratory. This ultra-clean copper is expected to have at least a factor 100 smaller content of Thorium, Uranium and Radium contamination than commercial available copper. In addition, the production of cosmogenic radioisotopes is largely suppressed, compared to production and storage at the earth's surface (see Section 4.2).

### $^{130}\text{Te}$ : Cuoricino, CUORE and SNO+

With its very high natural abundance of about 34%,  $^{130}\text{Te}$  is a very cost-efficient isotope for the search of  $0\nu\beta\beta$ . In ongoing and proposed experiments, the enrich-

ment of  $^{130}\text{Te}$  is not planned.

The experiment CUORE [42] uses 988 bolometric  $\text{TeO}_2$  crystals, assembled in 20 towers. Each detector weighs 750 g, so in total about 206 kg of  $^{130}\text{Te}$  are used. The detector towers are cooled in a dilution refrigerator to  $\sim 10$  mK, at which point the small heat capacity allows for the measurement of deposited energy by the rise of temperature. The first tower containing 52 crystals with a mass of 11 kg of  $^{130}\text{Te}$ , called CUORE-0, is currently under operation. First results with an exposure of 9.8 kg·a yield a background index of approximately 0.058 counts/keV/kg/a and a lower bound on the  $^{130}\text{Te}$  half-life of  $T_{1/2}^{0\nu} > 2.7 \cdot 10^{24}$  a with 90% C.L. [43]. The remaining 19 towers are already assembled and the experiment will be fully operational in 2015.

The predecessor experiment Cuoricino operated 62  $\text{TeO}_2$  detectors between 2003 and 2008. The total mass was 40.7 kg, corresponding to 11.3 kg of  $^{130}\text{Te}$ . With a total exposure of 19.75 kg·a a lower limit for the  $0\nu\beta\beta$  half-life was set to  $T_{1/2}^{0\nu} > 2.8 \cdot 10^{24}$  a with 90% C.L. [44].

Another experiment investigating  $^{130}\text{Te}$  is SNO+ [45], which uses most of the infrastructure from the former SNO experiment and is located in the same underground laboratory. SNO+ has a manifold neutrino physics program, including the observation of low energy solar neutrinos, supernova neutrinos and geo-neutrinos [46]. By loading 800 t of liquid scintillator with  $^{130}\text{Te}$ , SNO+ converts into a  $0\nu\beta\beta$  experiment. In a first step, SNO+ will load the liquid scintillator with 0.3% natural Te, which corresponds to 800 kg of  $^{130}\text{Te}$ . In a second step, the loading can be increased to 3%, corresponding to 8 t of  $^{130}\text{Te}$ . The SNO+ experiment is explained in more detail in Section 3.3.

### $^{136}\text{Xe}$ : KamLAND-ZEN, EXO and NEXT

From all  $0\nu\beta\beta$  candidate isotopes,  $^{136}\text{Xe}$  is the by far easiest to enrich. Since  $^{136}\text{Xe}$  is already a noble gas, enrichment with gas centrifuges is comparatively easy. Thus,  $^{136}\text{Xe}$  is the isotope with the highest amount of enriched source material available and is investigated in different experimental approaches.

The KamLAND-ZEN experiment [47] applies a similar approach like the SNO+ experiment. The detector consists of a 13 m diameter nylon balloon filled with 1000 t liquid scintillator. To convert KamLAND into a  $0\nu\beta\beta$  experiment, a 3 m diameter inner balloon was inserted into the center of the detector. This balloon contains a mixture made of Xenon and liquid scintillator with a total mass of 13 t. Xenon is enriched to 91% in  $^{136}\text{Xe}$ , corresponding to about 320 kg double beta source mass. Data-taking started in 2011. The half-life of the  $2\nu\beta\beta$  in  $^{136}\text{Xe}$  was measured [47] and with an exposure of 108.8 kg·a a lower limit on the  $0\nu\beta\beta$  half-life was set to  $T_{1/2}^{0\nu} > 2.6 \cdot 10^{25}$  a at 90% C.L. [48]. The KamLAND-Zen experiment is explained in more details in Section 3.2.

Xenon is also used in the EXO experiment [49], enriched to 80.6% in  $^{136}\text{Xe}$ .

Exo-200 is a time projection chamber (TPC) with a length of 40 cm and 40 cm diameter. 175 kg liquid Xenon is used, whereof 110 kg remains in the active detector volume. The small amount of source mass compared to KamLAND-ZEN is compensated by a better energy resolution and a lower background index. EXO-200 was the first experiment measuring the half-life of the  $2\nu\beta\beta$  in  $^{136}\text{Xe}$  [50, 51]. With an exposure of 32.5 kg·a and a background index of about  $1.5 \cdot 10^{-3}$  counts/keV/kg/a a lower limit on the  $0\nu\beta\beta$  half-life was set to  $T_{1/2}^{0\nu} > 1.6 \cdot 10^{25}$  a at 90% C.L. [52].

EXO-200 will continue data-taking until 2016. In the meantime, the development of a 5 kt  $^{136}\text{Xe}$  TPC called nEXO is ongoing. Also the direct identification of the resulting  $^{136}\text{Ba}$  daughter atoms using laser tagging [53] or a radio-frequency funnel [54] is under development.

A third approach to use  $^{136}\text{Xe}$  is a high pressure gas TPC. The NEXT experiment [55] constructs such a TPC with 1.4 m length and 1.1 m diameter. Depending on the pressure (10–15 bar), the source mass will be 10–15 kg of  $^{136}\text{Xe}$ . The approach of a gaseous TPC allows for a better energy resolution compared to a liquid Xenon TPC ( $\approx 1\%$  vs.  $\approx 4\%$  FWHM). In addition, the observation of event topologies allows for a very efficient background reduction by direct particle identification.

### $^{82}\text{Se}$ : NEMO-3 and SuperNEMO

The SuperNEMO experiment [56] is the only approach presented in this section where the source mass does not equal the detection volume. On one hand, this complicates the efforts towards a large source mass. On the other hand, topological event reconstruction reduces backgrounds not originating from the source mass. In addition, the measurement of the opening angle between both electrons from  $0\nu\beta\beta$  allows for the drawing of conclusions regarding the decay mechanism.

The SuperNEMO experiment currently constructs a demonstrator module with a thin foil containing 7 kg  $^{82}\text{Se}$ . The foil is located in a drift chamber with a magnetic field to track the path of the electrons. The electrons energy is measured outside the drift region in plastic scintillator blocks instrumented with PMTs. The beginning of data-taking is planned for 2015 [57].

The predecessor experiment NEMO-3 used thin foils made of different isotopes with a total mass of about 10 kg. Data-taking lasted from 2003 to 2011. The most promising isotopes were  $^{100}\text{Mo}$  and  $^{82}\text{Se}$  because of the available sample mass and the high Q-values around 3 MeV. Lower half-life limits with 90% C.L. are  $T_{1/2}^{0\nu} > 1.0 \cdot 10^{24}$  a for  $^{100}\text{Mo}$  respectively  $T_{1/2}^{0\nu} > 3.2 \cdot 10^{23}$  a for  $^{82}\text{Se}$  [58].

## 2.7 Determination of Neutrino Masses other than $0\nu\beta\beta$

In addition to neutrinoless double beta decay, information on absolute values of neutrino masses can be obtained by cosmological observations and direct determination of the neutrino mass by kinematics. Reference [18] quotes the following values for the masses of electron, muon and tau neutrinos:

$$m_{\nu_e} = \sqrt{\sum_i |U_{ei}|^2 m_i^2} < 2 \text{ eV} \quad (2.125)$$

$$m_{\nu_\mu} = \sqrt{\sum_i |U_{\mu i}|^2 m_i^2} < 0.19 \text{ MeV} \quad (2.126)$$

$$m_{\nu_\tau} = \sqrt{\sum_i |U_{\tau i}|^2 m_i^2} < 18.2 \text{ MeV} \quad (2.127)$$

### Investigation of $\beta$ Decay Spectra Endpoints

The classical way to investigate kinematics to search for neutrino masses is the study of the effective electron antineutrino mass in  $\beta$  decay. In this decay mode the ordering number  $Z$  of the nucleus changes by one unit, while the mass number  $A$  stays the same:

$$(Z, A) \rightarrow (Z + 1, A) + \bar{\nu}_e + e^- \quad (\beta^- \text{ decay}) \quad (2.128)$$

$$(Z, A) \rightarrow (Z - 1, A) + \nu_e + e^+ \quad (\beta^+ \text{ decay}) \quad (2.129)$$

$$e^- + (Z, A) \rightarrow (Z - 1, A) + \nu_e \quad (\text{electron capture}) \quad (2.130)$$

The number of beta decay nuclides under consideration for current and future experiments is mostly limited to three:  ${}^3\text{H}$  (or T for Tritium),  ${}^{187}\text{Re}$  and  ${}^{163}\text{Ho}$ . They meet the experimental requirements of low Q-values and reasonable low half-lives.

In case for the decay  ${}^3\text{H} \rightarrow {}^3\text{He} + e^- + \bar{\nu}_e$  the electron energy spectrum has the form

$$\frac{dN}{dE} \propto F(Z, E)p(E + m_e)(Q - E)\sqrt{(Q - E)^2 - m_\nu^2}. \quad (2.131)$$

where  $p$ ,  $E$  are the electron momentum and energy,  $Q$  is the Q-value of the decay and  $F(Z, E)$  is the Fermi function. Without taking sterile neutrinos into account, the flavor state  $\nu_e$  is an admixture of the three mass eigenstates  $\nu_1$ ,  $\nu_2$  and  $\nu_3$ . Thus, a beta decay generates a superposition of three different spectra, each with a different endpoint shape and cutoff. If the energy resolution of the detector is not sufficient to resolve the three cutoffs, the beta spectrum can be well approximated by a single neutrino spectrum with an effective mass  $m_\beta$ :

$$m_\beta = \sqrt{\sum_i |U_{ei}|^2 m_i^2} = m_{\nu_e}. \quad (2.132)$$

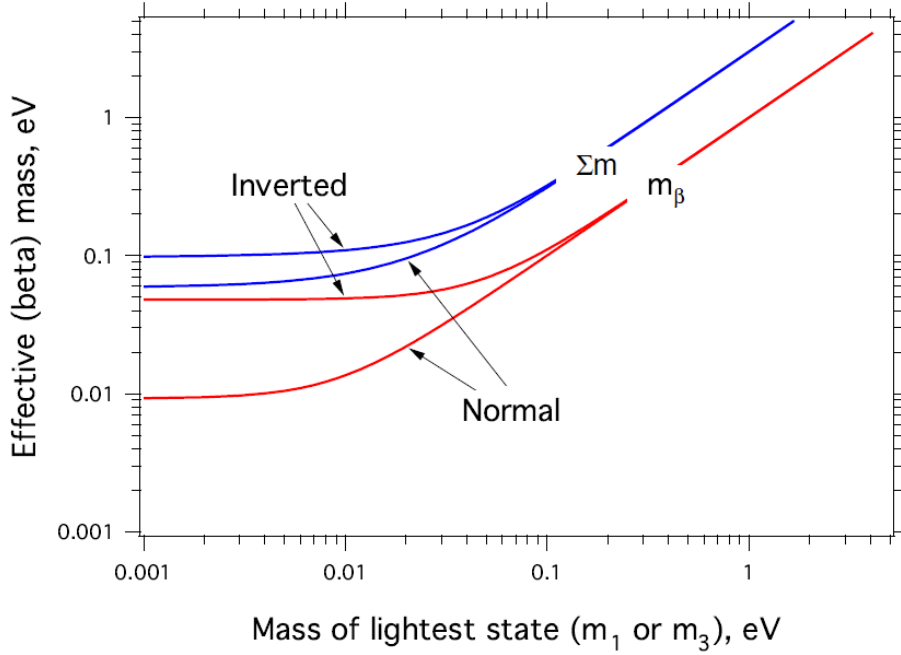


**Figure 2.8:** Allowed regions of  $m_\beta$  as a function of the lightest neutrino mass  $m_{min}$  for the inverted and normal hierarchies. Taken from [34]. The allowed regions for the total neutrino mass  $\sum m_i$  are also shown.

Here  $m_\beta$  is the incoherent and unresolved sum of  $\beta$ -spectra each leading with probability  $|U_{ei}|^2$  to a mass eigenstate  $m_i$ .  $\beta$  decay is not responsive to the distinction between Dirac and Majorana neutrinos and independent from nuclear matrix element calculations. Analogous to Figure 2.5, the allowed regions for  $m_\beta$  are depicted in Figure 2.8.

If neutrinos were massless, the beta spectrum near the endpoint would approximately be parabolic around  $Q$ .  $m_\beta$  has a small but potentially measurable effect on the phase space in low-energy beta decays and a finite neutrino mass changes the shape of the parabola and cuts it off before the zero-mass endpoint. Therefore, experiments investigating the kinematics of beta decay must have a high energy resolution with a well-known spectrometer resolution. In order to collect sufficient statistics at the beta spectrum endpoint, a very large number of decays has to be observed.

The current best limits on  $m_\beta$  are obtained from the Mainz and Troitsk experiments:

$$m_\beta \leq 2.3 \text{ eV at 95\% C.L. from Mainz [59]} \quad (2.133)$$

$$m_\beta \leq 2.05 \text{ eV at 95\% C.L. from Troitsk [60]} \quad (2.134)$$

A comprehensive summary of past experiments searching for the effective electron antineutrino mass in  $\beta$  decay can be found in [61].



The future KATRIN experiment [62] aims for a sensitivity limit down to  $m_\beta < 0.2$  eV. It will use a gaseous  $T_2$  source with a decay rate in the order of  $10^{11}$  Bq. The high energy resolution will be achieved by using a MAC-E (Magnetic Adiabatic Collimation-Electrostatic) filter with 10 m diameter. Start of data-taking is expected to begin in 2016.

A recent development to measure the energy spectrum of tritium decay electrons is Project 8 [63]. The decay electrons are stored in a magnetic bottle and undergo cyclotron motion with a frequency

$$\omega = \frac{\omega_0}{\gamma} = \frac{qB}{m + E}, \quad (2.135)$$

where  $E$  is the kinetic energy,  $B$  the magnetic field and  $q$  and  $m$  the electrons charge and mass.  $\omega_0$  is the unshifted cyclotron frequency and  $\gamma$  the Lorentz factor. The cyclotron radiation emitted by the electrons is detected by a sensitive array of microwave antennae and is used to reconstruct the electron's kinetic energy. This technique is complementary to MAC-E filter experiments like KATRIN, because the experimental systematic errors are very different.

An alternative experimental approach are microcalorimeters to study beta decays of  $^{187}\text{Re}$  or  $^{163}\text{Ho}$  electron capture decays. The main advantage is the 'source = detector' approach that allows to measure the complete decay energy and not only the kinetic energy of the decay electrons. However, large arrays of small calorimeter crystals have to be used to avoid pile-up effects in individual detectors. Experiments studying techniques for these decays are MARE [64] and ECHO [65].

### Cosmological Observations

The most stringent limits on the total neutrino mass  $\sum m_i$  are given by the measurements on the cosmic microwave background (CMB) by satellite experiments. The primary CMB power spectra of cosmological models are dependent on the neutrino mass and hence a fit to measured data can provide upper limits on the total neutrino mass. However, these upper limits are strongly depending on the considered cosmological model.

As shown in Figure 2.8, the total neutrino mass  $\sum m_i$  converges to 0.1 eV in case of inverted hierarchy and to 0.06 eV in case of normal hierarchy for a vanishing mass of the lightest eigenstate  $m_1$  or  $m_3$ . The Planck collaboration quotes for its 2015 cosmological parameters results an upper limit of  $\sum m_i < 0.23$  eV (95% C.L.) using also the dataset from the WMAP experiment and considering the high-resolution CMB data (highL) and baryon acoustic oscillations (BAO) [66].

With this method also the number of effective neutrinos  $N_{eff}$  can be measured.  $N_{eff}$  specifies the number of neutrino-like relativistic degrees of freedom and is 3.046 in the Standard Model [67]. The Planck collaboration quotes  $N_{eff} = 3.15 \pm 0.23$  (95% C.L.) and hence disfavors the existence of sterile neutrinos contributing

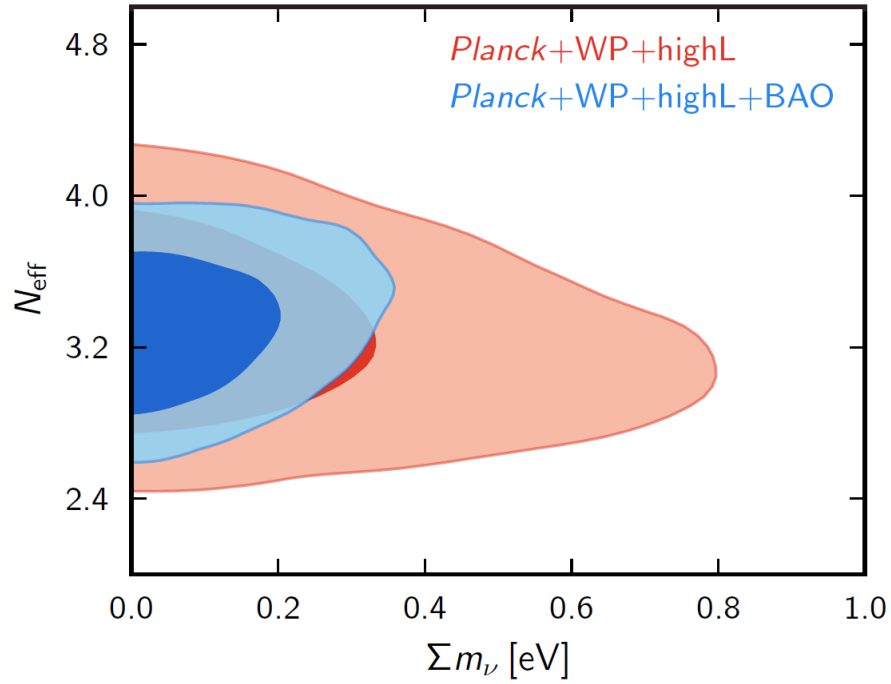


**Figure 2.9:** 2D distribution of the number of effective neutrinos  $N_{\text{eff}}$  and total neutrino mass  $\Sigma m_i$  using Planck and WMAP data under consideration of the high-resolution CMB data (highL) and baryon acoustic oscillations (BAO). Taken from the Planck 2013 cosmological parameters results [68].

to the CMB. Both results are summarized in Figure 2.9 from the Planck 2013 cosmological parameters results.

## Chapter 3

# Liquid Scintillator Detectors for the Search of $0\nu\beta\beta$ Decay

Scintillation detectors are one of the most often used detection devices in particle and nuclear physics today. In general, the detection material can be divided into two groups: Inorganic and organic scintillators. The latter can have the form of crystals, plastics or liquids. Large volume liquid scintillator detectors have contributed to recent results in the field of neutrino physics, e.g. the evidence for neutrino oscillation by KamLAND [69], the precise measurement of  $\theta_{13}$  by Double CHOOZ [70], Daya Bay [71] and Reno [72] or the detection of  ${}^7\text{Be}$ ,  ${}^8\text{B}$ , CNO,  $pep$  and  $pp$  solar neutrinos by Borexino [73, 74]. With NO $\nu$ A [75], a highly segmented liquid scintillator detector measuring  $\theta_{13}$  and searching for the mass hierarchy and the  $CP$  violating phase  $\delta$  has started data-taking in 2014.

Also, in the field of neutrinoless double beta decay several experiments take advantage of the excellent performance of liquid scintillator detectors regarding background reduction, e.g. KamLAND-Zen at the Kamioka Observatory in Japan and SNO+ at the Sudbury Neutrino Observatory in Canada. Liquid scintillator can be produced and purified to very low impurities regarding isotopes from the natural decay chains, which is explicitly demonstrated by the Borexino experiment at the LNGS underground laboratory in Italy. Due to its high content of Hydrogen, liquid scintillator is also a very good moderator and detector for neutrons.

In the framework of this thesis, a hybrid solution for the COBRA experiment is investigated, taking advantage of the low background and neutron shielding properties of liquid scintillator and the benefits of CdZnTe semiconductor detectors regarding energy resolution. The passivation lacquer needed to prevent CdZnTe from degradation and to suppress leakage currents on the surface is a potential source for a large amount of background events. Besides to the function as highly pure passivation material, liquid scintillator also acts as active veto for external gammas and neutrons. Therefore, liquid scintillator can be an ideal substitute for the currently used Glyptal lacquer.

### 3.1 Scintillators in General

On the one hand, both inorganic and organic scintillators in general are capable to provide a multitude of information when energy is deposited by an ionizing particle. Above a certain energy threshold, the light output of most scintillators is linear to the exciting energy of a specific particle. As the often used photomultiplier detectors are also linear devices, the electrical signal is proportional to this energy. Furthermore, the response and recovery times of scintillators are relatively short compared to some other types of detectors. Hence, high count rates and low dead times are feasible with scintillation detectors. At last, certain scintillators offer the ability to distinguish between different types of ionizing particles by analyzing the shape of the recorded PMT signal. This method is called pulse shape discrimination.

On the other hand, inorganic and organic scintillators differ in many characteristics and the choice of detector material is dependent on the operation purpose. Inorganic scintillators, of which sodium iodide is the mostly used, tend to have better light output and linearity. Furthermore inorganic alkali halide crystals have generally a higher  $Z$ -value than organic compounds and are therefore more suitable for gamma-ray spectroscopy.

In contrast, organic scintillators are preferred for electron and neutron detection, due to their high content of Hydrogen. They also have a commonly faster time response, making them appropriate for large count rates or as trigger for other detector components. Organic scintillators are mostly used as liquids or plastics, but also organic crystals are deployed. The highest light yield of all organic scintillators has the crystal Anthracene ( $C_{14}H_{10}$ ), which is chosen as the reference to which the light outputs of other scintillators are compared. A drawback of many organic scintillators is their partial intransparency to the wavelength of their own emitted light. For a good light collection at the photon sensors, wavelength shifting compounds have to be added.

The prompt emission of visible radiation from a material following its excitation or absorption of electromagnetic radiation is called fluorescence. This is the fundamental functionality of all scintillator detectors. But also several other processes can lead to the emission of visible light. Phosphorescent material does not immediately re-emit the absorbed energy, but with a characteristic time that is much slower than prompt fluorescence. This phosphorescence light is of longer wavelength than fluorescence light. In addition, delayed fluorescence can occur. This process is characterized with the same emission spectrum than prompt fluorescence, but again with a longer emission time following excitation. A material converting as large a fraction as possible of incident radiation energy to prompt fluorescence is desirable for scintillation detectors.

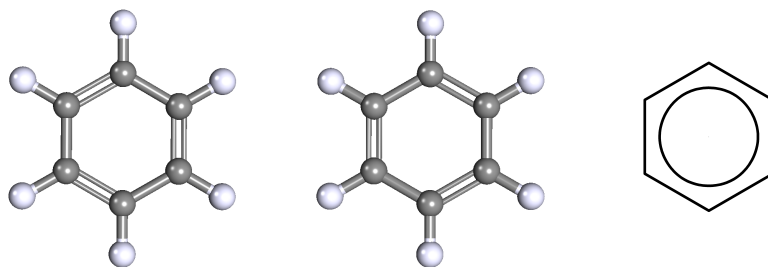


**Figure 3.1:** The two mesomerism of Cyclohexa-1,3,5-triene (left and middle) are shown as 3D view, produced with the PubChem 3D Viewer v2.0 from the PubChem Open Chemistry Database [76]. In fact, the electrons for the bonding between Carbon atoms are distributed equally between each atom. To indicate the delocalized structure of the bonding, Benzene is usually depicted with a circle inside a hexagonal structure of Carbon atoms (right). Due to the mesomerism, Benzene with its delocalized bonding is more stable than the hypothetical Cyclohexatriene with three double bonds.

### 3.1.1 Principal Mechanism of Scintillation in Organic Scintillators

The prompt fluorescence light of organic scintillators is due to the functionality of benzene-ring structures, which are linked or condensed in Hydrocarbon compounds. These compounds are called aromatic compounds. The free valence electrons of the Carbon atoms in the Benzene rings are delocalized and not associated with any particular atom or molecule. The delocalization leads to an advantageous energy of the Benzene molecule compared to its aromatic mesomerism, see Figure 3.1. The free electrons occupy the so called  $\pi$ -molecular orbital and are often called  $\pi$ -electrons.

In Figure 3.2 typical  $\pi$ -electronic energy levels of an aromatic molecule are depicted. The states with spin 0 (spin singlet states) are labeled  $S_0$ ,  $S_1$ ,  $S_2$ , and so on, while the states with spin 1 (spin triplet states) are labeled  $T_0$ ,  $T_1$ ,  $T_2$ , and so forth. The energy spacing between  $S_0$  and the first excited state  $S_1$  is in the order of 3 to 4eV for liquid scintillator materials. The spacing between higher-lying singlet states is usually smaller. To each electron level a fine structure labeled  $S_{xy}$  or  $T_{xy}$  is associated which corresponds to excited vibrational modes of the molecule. The energy spacing between these states is in the order of 0.1 eV.

As the average thermal energies (0.025 eV) are small compared to spacing between vibrational states, mostly all molecules are in the  $S_{00}$  state at room temperature. The absorption of kinetic energy from passing charged particles is depicted with solid upgoing arrows in Figure 3.2. If higher singlet states are excited, they decay within picoseconds to the  $S_1$  state. Also higher vibrational states quickly lose their energy and de-excite to the  $S_1$  state, as they are not in thermal equilibrium with their neighbors. Summarized, the excitation process leads to a population of molecules in the  $S_1$  state.

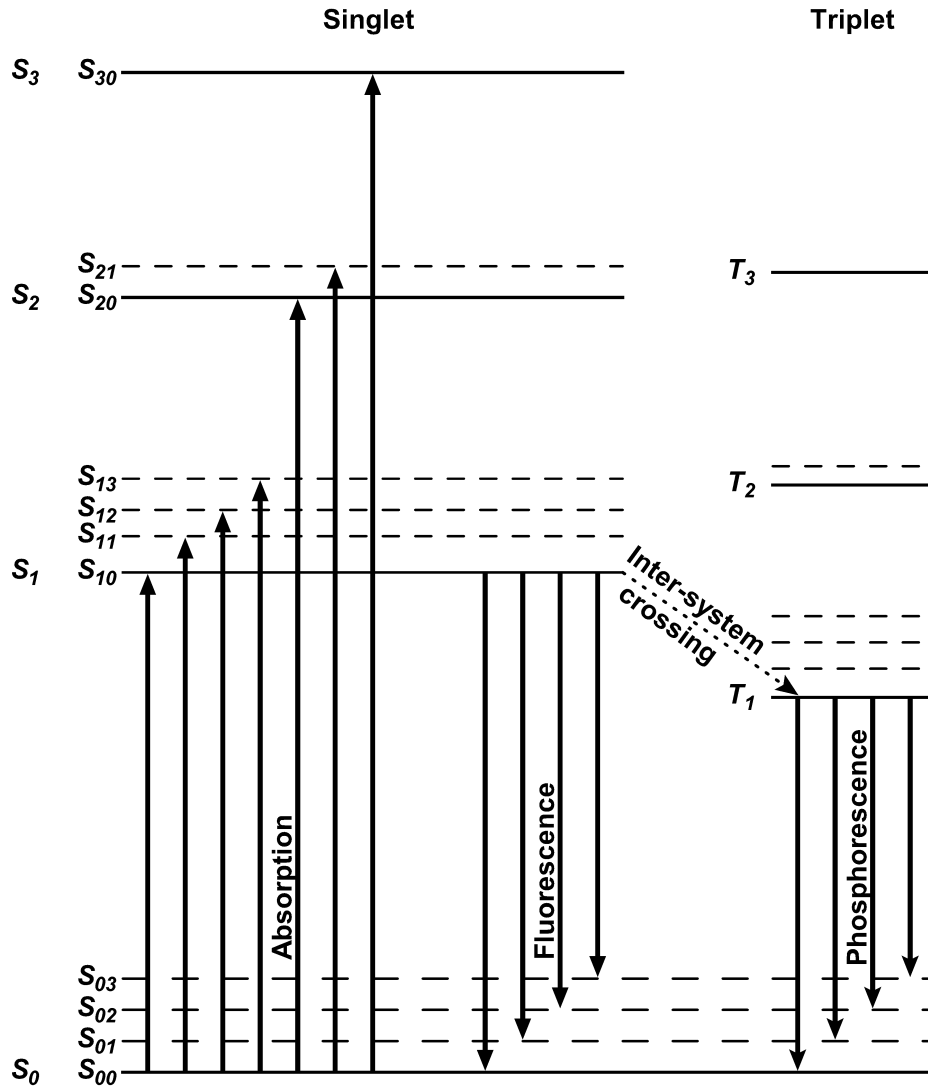


**Figure 3.2:** Typical  $\pi$ -electronic energy levels of an aromatic molecule. Adapted from [77]. Singlet states are labeled  $S_0, S_1, S_2, \dots$  and triplet states are labeled  $T_0, T_1, T_2, \dots$ . Vibrational states are labeled  $S_{xy}$  and  $T_{xy}$  respectively. Absorption is depicted by upgoing arrows from the  $S_{00}$  state to excited singlet states. Fluorescence light is depicted by downgoing arrows from the  $S_{10}$  to the  $S_{0y}$  ground states, while phosphorescence light is depicted by downgoing arrows from the  $T_1$  triplet state to the  $S_{0y}$  ground states.

The prompt fluorescence or scintillation light is emitted in transitions between the  $S_1$  state and the vibrational states  $S_{0y}$  or the ground state  $S_0$ . The decay time is usually a few nanoseconds and the prompt scintillation light is therefore relatively fast compared to other types of detectors. If the de-excitation from  $S_1$  takes place to a vibrational state  $S_{0y}$ , the emitted radiation does not have enough energy to re-excite the transition  $S_0 \rightarrow S_1$  and the scintillator is then transparent to its own radiation. The property of separated absorption and emission spectra in scintillators is often called Stokes shift. Only with the transition  $S_1 \rightarrow S_0$  an undesirable overlap in the absorption and emission spectra is produced.

Instead of decaying into the ground states, excited singlet states may convert into triplet states. This process is called intersystem crossing. Compared to the  $S_1$  state, the first triplet state  $T_1$  has a much longer lifetime in the order of milliseconds, as the transitions from  $T_1$  to the  $S_{0y}$  states are highly forbidden by multipole selection rules. As the energy of the  $T_1$  state lies below the  $S_1$  state, the emitted light has a longer wavelength than fluorescence and is characterized as phosphorescence. Usually the first triplet state decays by interaction with another excited  $T_1$  molecule in the form:



The light emitted by the  $S_1$  state is called delayed fluorescence or slow component of the scintillation light.

As there are alternate de-excitation modes than the emission of visible light possible for excited molecules, some incident particle energy is always not detectable in liquid scintillators. These excitations are mainly converted into heat and all radiationless de-excitation are grouped under the term quenching. Especially impurities like dissolved oxygen in scintillators provide alternate quenching mechanisms for the excitation energy. The purification of liquid scintillators by bubbling with pure nitrogen is important to remove oxygen and other impurities.

### 3.1.2 Multi-Component Liquid Scintillators

As the emission spectra of single-component organic scintillators have an undesirable overlap with their own absorption spectra, an important part of the information about the primary process of excitation is lost. To prevent these losses, a second or even third organic compound is added. These solutes are called wavelength-shifter or fluors. Their duty is to absorb the fluorescence light emitted by the primary scintillator, the solvent, and re-emit it at a higher wavelength where the solvent is transparent. Another goal of adding wavelength shifters is the emission of a fluorescence spectrum which fits the absorption spectrum of the used photon sensor as good as possible. The concentration of the primary wavelength-shifting compound is usually in the order of a few grams per liter solvent in the case of liquid scintillators. These mixtures are called binary scintillators. If a second

wavelength shifter is also added, its concentration is in the order of 10 mg/l and the mixtures are called ternary scintillators.

In the case of a binary scintillator system, the aromatic molecules of the solute are chosen such that their first singlet excitation energy of the  $\pi$ -electrons is lower than the first singlet excitation energy  $S_1$  of the solvent. The absorption spectrum of the wavelength shifter then overlaps with the emission spectrum of the solvent. If the lifetime of the first excited state  $S_1$  of the solvent is comparatively large in the order of 10 ns, its energy is mainly transferred via non-radiative dipole-dipole interaction to the first excited state of the solute. This populated state then decays into the ground state of the solute by emission of fluorescence light.

The concentration of the solute is chosen such that the non-radiative energy transfer between the first excited states of the solvent and the solute happens as fast as possible after the incident excitation. Therefore a high concentration is desirable on the one hand. On the other hand, a high concentration leads to the re-absorption of the solutes emission spectrum by its own molecules. This process is called concentration quenching and may lead to the loss of fluorescence light. The best concentration of the solute has to be determined experimentally by light yield measurements of the scintillator mixtures.

The addition of a second fluor to a binary scintillator leads to similar energy transfer processes and further shifts the emission spectrum to longer wavelengths. A more detailed explanation of the processes in binary and ternary scintillator mixtures is given in [77].

A way to produce large amounts of liquid scintillator detection material is to add a non-scintillating solvent to the primary scintillator. In most cases, alkanes like dodecane are used for this purpose, as their absorption length for visible light is comparatively long. For almost all organic materials like alkanes the excitation energy is transferred from molecule to molecule in the solvent before de-excitation occurs. If an efficient scintillator is added, the energy absorbed by the non-scintillating solvent will find its way to the scintillation molecules and cause light emission at that point.

### 3.1.3 Chemical and Optical Properties of Scintillator Components

In this section, an overview over selected solvents and solutes used in past, present and future liquid scintillator experiments is presented. This selection makes no claim to be complete. All of these materials are mentioned later in this Chapter in the context of detailed descriptions of neutrino experiments or in the context of the material compatibility tests performed in the course of this work.

For safety reasons, flammability, reactivity and health risks have to be taken serious for the work with Hydrocarbon compounds in the laboratory. The Hazardous Materials Identification System (HMIS), developed by the American Coatings As-



sociation, classifies the danger of material handling with color-coded bars. The four bars cover the level of health hazard (blue), flammability (red), physical hazard (orange), and for personal protection (white). In many material safety data sheets (MSDS), the numerical values ranging from 0 (safe) to 4 (very dangerous) for health hazard, flammability and physical hazard are listed. For the material compatibility tests in Section 5.1, scintillators with a health hazard or flammability rating higher than 1 were not considered. The HMIS rating is similar to the fire diamond, created by the National Fire Protection Association (NFPA), but conveys broader health warning information.

To avoid misunderstanding and ambiguities from the often used short names and the nomenclature of the International Union of Pure and Applied Chemistry (IUPAC), the registry numbers assigned by the Chemical Abstracts Service (CAS) are given in this section. All graphical representations are made with the PubChem 3D Viewer v2.0 from the PubChem Open Chemistry Database [76]. Values for absorption and emission spectra are peak values.

### Solvents

The liquid scintillator 1,2,4-trimethylbenzene (Pseudocumene, PC) was used in the KamLAND and Borexino experiments. Due to its high toxicity and comparatively low flash point of 48 °C, special care has to be taken during liquid handling. Due to the risks connected with the handling of PC, it was not considered for material compatibility tests.

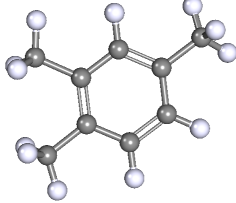
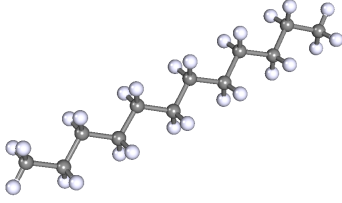
PC was often mixed with the mineral oil Dodecane to produce large amounts of liquid scintillator. Dodecane is a colorless, clear liquid with high transparency and increases the total number of free protons in the mixture when added to PC. As mineral oils don't produce scintillation light, the light yield of scintillator mixtures decreases when Dodecane is added. Dodecane has a flash point of 85 °C and is classified as harmful to health. Chemical and physical properties of Dodecane and Pseudocumene are summarized in Table 3.1.

In recent liquid scintillator experiments mostly 4-(1-Phenylethyl)-o-xylene (PXE) and (C10-C16)Alkylbenzene (Linear Alkylbenzene, LAB) are used. Both have the advantages of being non-hazardous liquids and having high flash points well above 100 °C. Chemical and physical properties of PXE and LAB are summarized in Table 3.2.

### Solutes

As described in Section 3.1.2, so-called wavelength-shifter or fluors are added to the liquid scintillator to prevent self-absorption of the fluorescence light and to shift the emission spectrum to fit as good as possible the absorption spectrum of the used photon sensor. Most of these solutes are powders and have to be thoroughly dissolved in the liquid solvent.

**Table 3.1:** Chemical and physical properties of Pseudocumene and Dodecane. Values for density and flash point taken from material safety data sheets [78, 79]. Value for the peak emission wavelength of Pseudocumene from [80].

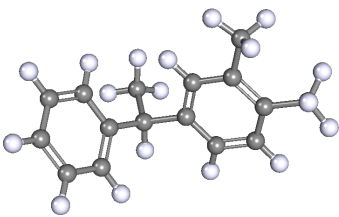
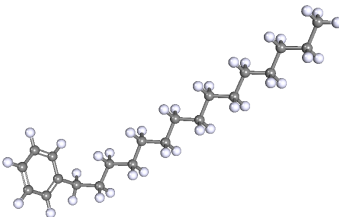
		
Name	1,2,4-trimethylbenzene	n-Dodecane
Short name	Pseudocumene, PC	Dodecane
Formula	C <sub>9</sub> H <sub>12</sub>	C <sub>12</sub> H <sub>26</sub>
CAS	95-63-6	112-40-3
Density	0.88 kg/l	0.75 kg/l
Flash point	48 °C	85 °C
Emission	290 nm	–
HMIS Rating		
Health hazard	2	2
Flammability	2	2
Physical hazard	0	0

2,5-Diphenyloxazole (PPO) and p-Terphenyl (pTP) are often used as primary wavelength shifters, as their absorption spectra fit well to the emission spectra of PXE and LAB. Both have a Stokes shift of approximately 60 nm and especially PPO is widely used and its properties are well known. Chemical and optical properties of PPO and pTP are summarized in Table 3.3.

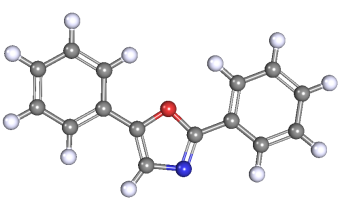
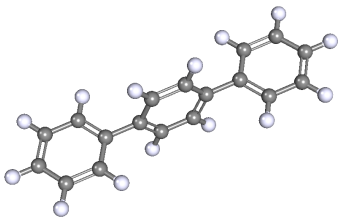
To further shift the emission spectrum, secondary wavelength shifter in addition to primary shifter can be added. To avoid self-absorption, they are added only in small quantities. Among this solutes, 1,4-Bis(2-methylstyryl)benzene (bis-MSB) is often used in liquid scintillator experiments. It has a Stokes shift of approximately 60 nm. Also 1,4-Bis(5-phenyloxazol-2-yl)benzene (POPOP) can be used, but it has a longer decay time than bis-MSB. Chemical and optical properties of bis-MSB and POPOP are summarized in Table 3.4.

An interesting fluor with a Stokes shift of 120 nm is 1-Phenyl-3-(2,4,6-trimethylphenyl)-2-pyrazoline (PMP). Due to the large shift from absorption to emission spectrum, self-absorption is very small. PMP can be used as substitute for the often used combination of PPO and bis-MSB. Chemical and optical properties of PMP are summarized in Table 3.5.

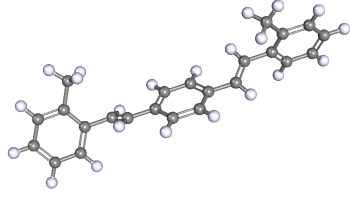
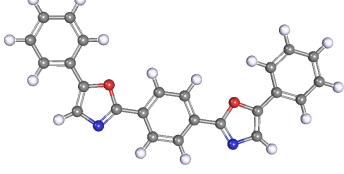
**Table 3.2:** Chemical and physical properties of PXE and LAB. Values for density and flash point taken from material safety data sheets [81, 82]. Value for the peak emission wavelength of PXE from [80].

		
Name	4-(1-Phenylethyl)-o-xylene	(C10-C16)Alkylbenzene
Short name	PXE	Linear Alkylbenzene, LAB
Formula	$C_{16}H_{18}$	$C_6H_5C_nH_{2n+1}$ , $n = 10 - 16$
CAS	6196-95-8	68890-99-3
Density	0.985 kg/l	0.86 kg/l
Flash point	167.1 °C	140 °C
Emission	290 nm	283 nm
HMIS Rating		
Health hazard	1	1
Flammability	1	1
Physical hazard	0	0

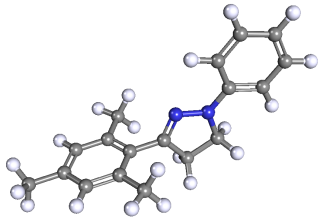
**Table 3.3:** Chemical and optical properties of PPO and pTP. Values for the peak absorption and emission wavelengths of PPO from [80], of pTP from [83].

		
Name	2,5-Diphenyloxazole	p-Terphenyl
Short name	PPO	pTP
Formula	$C_{15}H_{11}NO$	$C_{18}H_{14}$
CAS	92-71-7	92-94-4
Absorption	305 nm	275 nm
Emission	365 nm	340 nm

**Table 3.4:** Chemical and optical properties of bis-MSB and POPOP. Values for the peak absorption and emission wavelengths from [84].

		
Name	1,4-Bis(2-methylstyryl)-benzene	1,4-Bis(5-phenyloxazol-2-yl)-benzene
Short name	bis-MSB	POPOP
Formula	$C_{24}H_{22}NO$	$C_{24}H_{16}N_2O_2$
CAS	13280-61-0	1806-34-4
Absorption	367 nm	360 nm
Emission	425 nm	415 nm

**Table 3.5:** Chemical and optical properties of PMP. Values for the peak absorption and emission wavelengths from [85].

	
Name	1-Phenyl-3-(2,4,6-trimethylphenyl)-2-pyrazoline
Short name	PMP
Formula	$C_{18}H_{20}N_2$
CAS	60078-97-9
Absorption	294 nm
Emission	415 nm

### 3.1.4 Achievable Purification Levels

To achieve a half-life sensitivity for the  $0\nu\beta\beta$  decay in the order of  $10^{26}$  years, the reduction of background events in the region of interest is essential for the COBRA experiment. Important background sources are natural decay chains and events produced by neutrons. The most critical background sources for the COBRA experiment are explained in more detail in Section 4.2.

In a future large-scale COBRA experiment, liquid scintillator can act as an active veto as well as passivation. Liquid scintillator is an intrinsic clean material with respect to background originating from natural decay chains, as the raw material mineral oil was stored underground for millions of years. At the moment, the CdZnTe detectors are passivated with a Glyptal 1201 lacquer of  $\sim 10\ \mu\text{m}$  thickness to prevent them from damages and degradation. This lacquer is a potential background source for the COBRA experiment [86].

The liquid scintillator of the Borexino Experiment at the Laboratori Nazionali del Gran Sasso (LNGS) laboratory in Italy is characterized by unprecedented low levels of intrinsic radioactivity [73]. Running since 2007, the experiment is optimized for the study of low energy solar neutrinos.

The inner part of the Borexino detector consists of  $\sim 278\ \text{t}$  Pseudocumene contained in a  $125\ \mu\text{m}$  thick spherical nylon vessel with a diameter of 8.5 m. The fluor PPO is added with a concentration of 1.5 g/l as wavelength shifter. A second 11.0 m nylon vessel surrounds the inner vessel, acting as a barrier against contamination from outside. A 13.7 m diameter stainless steel sphere encloses the two nylon vessels and serves as support structure for 2212 photomultiplier tubes.

The outer vessel and the stainless steel sphere act as a passive shield and contain Pseudocumene mixed with a small amount of Dimethylphthalate (DMP), which quenches the residual scintillation light of Pseudocumene. Therefore, the scintillation signals in Borexino mainly arise from events in the inner vessel. The stainless steel sphere itself is contained in a tank with 18 m base diameter and 16.9 m height, filled with ultrapure water. Next to the function as passive shield, the water tank is equipped with 208 PMTs and serves as active Cherenkov detector.

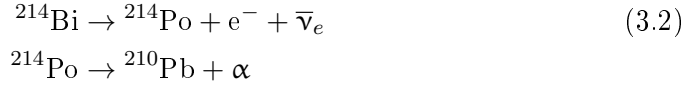
Prior to the assembly of the Borexino detector, the selection of low radioactivity materials as well as the liquid handling and purification strategies have been tested at the Counting Test Facility (CTF). Collecting data from 1995 until 2011, the CTF vessel was filled with  $5\ \text{m}^3$  organic liquid scintillator and equipped with 100 PMTs [87].

The Pseudocumene for Borexino was delivered to the LNGS underground laboratory in custom-built transport tanks and then transferred into four big reservoir tanks. Before mixing with PPO or DMP, the Pseudocumene was purified by distillation. For the crucial manipulation of the liquids, a plant providing purified nitrogen was set up. For cleaning operations and the filling of the outer water tank, ultrapure water was produced by a special system. More details about the

liquid handling system of Borexino can be found in [88].

The most dangerous background for the COBRA experiment with respect to radioactive impurities arises from alpha and gamma radiation produced by isotopes of the Uranium or Thorium decay chain. With a natural abundance of 99.3 %,  $^{238}\text{U}$  is the most common isotope of Uranium.  $^{238}\text{U}$  has a half-life of 4.468 billion years and its decay chain contains eight alpha and six beta decay isotopes, ending with the stable isotope  $^{206}\text{Pb}$ , see Appendix A.

Assuming secular equilibrium, the concentration of contaminants of the  $^{238}\text{U}$  chain can be measured by the  $^{214}\text{Bi}$ - $^{214}\text{Po}$  coincidence,



with a  $^{214}\text{Po}$  half-life of 164.3  $\mu\text{s}$ , an alpha energy of 7.687 MeV and a Q-value for the  $^{214}\text{Bi}$  decay of 3.272 MeV. Borexino measured  $(0.57 \pm 0.05)$   $^{214}\text{Bi}$ - $^{214}\text{Po}$  coincidence events per day and 100 t target mass, resulting in a  $^{238}\text{U}$  contamination of  $(5.3 \pm 0.5) \cdot 10^{-18}$  g/g [73]. This corresponds to a total activity of  $(6.5 \pm 0.6) \cdot 10^{-4}$  mBq/kg. However, as  $^{214}\text{Bi}$  and  $^{214}\text{Po}$  are  $^{222}\text{Rn}$  progenies, the assumption of secular equilibrium is often invalid due to radon diffusion or contamination of the scintillator with airborne radon.

Within the rear part of the  $^{238}\text{U}$  decay chain,  $^{210}\text{Pb}$  is often found to be out of equilibrium with the  $^{222}\text{Rn}$  part of the series, due to its long half-life of 22.3 years and its tendency to adsorb on to surfaces. While  $^{210}\text{Pb}$  and its daughter  $^{210}\text{Bi}$  are no major sources of background for the COBRA experiment, its granddaughter  $^{210}\text{Po}$  is an alpha emitter with an energy of 5.305 MeV and a half-life of 138.4 days. In the Borexino experiment, a high rate of  $^{210}\text{Po}$  decays out of equilibrium with  $^{210}\text{Bi}$  and the rest of the  $^{238}\text{U}$  series was found. This may be due to  $^{210}\text{Po}$  washing off the surfaces of storage tanks and pipes during purification and refilling operations.

The Thorium decay series starts with  $^{232}\text{Th}$ , which has a half-life of 14.05 billion years and a natural abundance of 100 %. The decay chain contains six alpha and four beta decay isotopes, ending with the stable isotope  $^{208}\text{Pb}$ , see Appendix B.

Assuming again secular equilibrium, the  $^{323}\text{Th}$  contamination can be inferred by the  $^{212}\text{Bi}$ - $^{212}\text{Po}$  coincidence at the end of the series,



with a  $^{212}\text{Po}$  half-life of 0.298  $\mu\text{s}$ , an alpha energy of 8.785 MeV and a Q-value for the  $^{212}\text{Bi}$  decay of 2.252 MeV. Borexino measured  $(0.13 \pm 0.03)$   $^{212}\text{Bi}$ - $^{212}\text{Po}$  coincidence events per day and 100 t target mass, resulting in a  $^{232}\text{Th}$  scintillator contamination of  $(3.8 \pm 0.8) \cdot 10^{-18}$  g/g [73]. This corresponds to a total activity of  $(1.5 \pm 0.3) \cdot 10^{-4}$  mBq/kg. Again, the assumption of secular equilibrium may be invalid, as  $^{212}\text{Bi}$  and  $^{212}\text{Po}$  are progenies of the noble gas  $^{220}\text{Rn}$ .

The activities of  $^{323}\text{Th}$  and  $^{238}\text{U}$  measured in Borexino are well below the requirements for an ultra pure environment for CdZnTe detectors in COBRA. This is illustrated in Section 4.2.1.

### 3.1.5 Neutron Attenuation and Capture

Neutrons are a potentially dangerous source of background for the COBRA experiment, mainly due to the 9 MeV gamma cascade after the capture of thermal neutrons on  $^{113}\text{Cd}$ . The  $^{113}\text{Cd}(n, \gamma)^{114}\text{Cd}$  reaction, neutron moderation, absorption and detection in general as well as the design for a conventional neutron shield based on Polyethylene are discussed in more detail in Section 4.2.2. In a very simple perception, neutrons are divided into slow neutrons and fast neutrons on the basis of their energy being below or above 0.5 eV. Slow neutrons with an energy of 0.025 eV are called thermal neutrons [89].

Due to its high content of Hydrogen, liquid scintillator is an ideal material to moderate fast neutrons. With a cross section of 0.332 barns, thermal neutrons are captured after a typical time of  $\sim 200 \mu\text{s}$  on free protons, emitting a gamma with an energy of 2.2 MeV.

In case of liquid scintillator detectors, an efficient neutron tagging is especially important for experiments measuring electron antineutrinos through the inverse beta decay,



To improve the neutron detection, in experiments like Double CHOOZ and Daya Bay Gadolinium is added to the scintillator mixture. Natural Gd has a cross section of 49 000 barns for the capture of thermal neutrons, with main contributions from  $^{157}\text{Gd}$  and  $^{155}\text{Gd}$ , see Figure 3.3. With natural abundances of 15.65 % for  $^{157}\text{Gd}$  and 14.80 % for  $^{155}\text{Gd}$  respectively, a concentration by mass of natural Gd in the order of 0.1 % in liquid scintillator is sufficient for an efficient neutron capture. Leading to a shorter attenuation length of visible light, higher concentrations of Gd are not desirable. In Gd-loaded scintillator the neutron-capture time is shortened to  $\sim 28 \mu\text{s}$  and a cascade of three to four gamma-rays with a total energy of 8 MeV is released [90].

For the Double CHOOZ experiment, the MPI Heidelberg developed a loading of PXE scintillator with natural Gd. Gd(III)-tris-(2,2,6,6-tetramethyl-heptane-3,5-dionate) ( $\text{Gd}(\text{thd})_3$ ) is added with a concentration of 4.5 g/l to the scintillator mixture made of 80 %<sub>vol</sub> Dodecane and 20 %<sub>vol</sub> PXE. This corresponds to a Gd concentration of 0.123 %<sub>wt</sub> [92].

For the Gd-loading of the liquid scintillator at the Daya Bay experiment, Gadolinium Chloride ( $\text{GdCl}_3 \cdot x\text{H}_2\text{O}$ ) was first purified and then combined with *trans*-3-Methyl-2-hexenoic acid (TMHA) to a moist Gd-TMHA solid. This solid was then dissolved in the LAB scintillator to a final concentration of 0.100 %<sub>wt</sub> [90]. By monitoring the attenuation length with calibration data, a degradation of

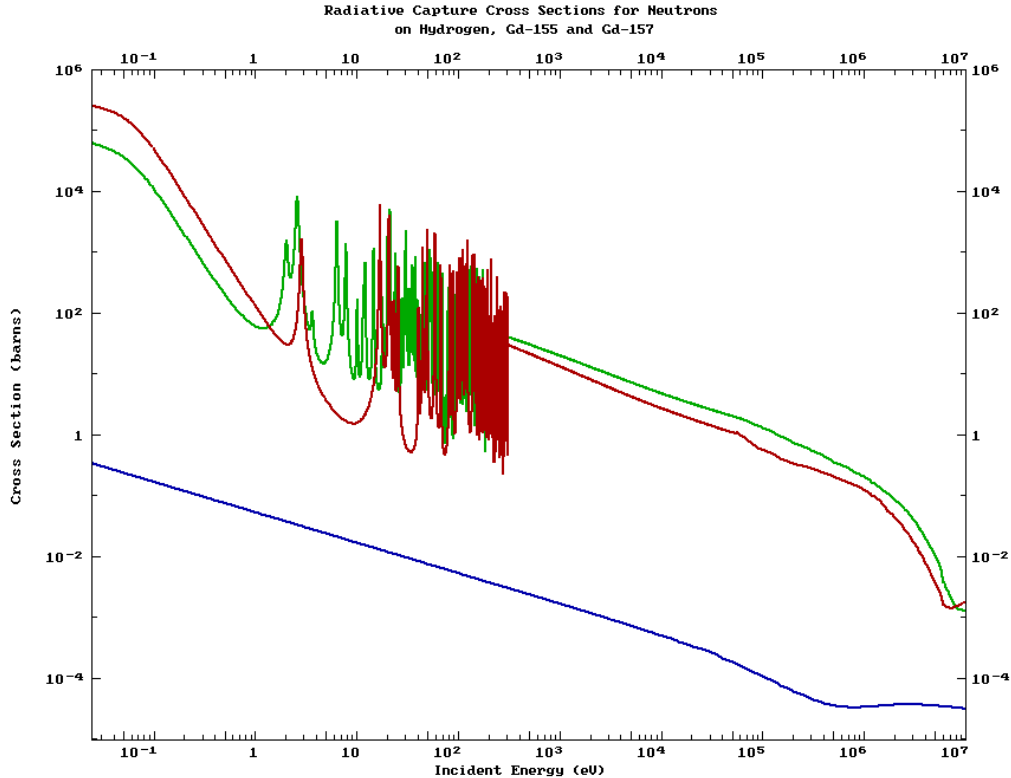


**Figure 3.3:** Cross sections for radiative neutron capture on  $^{157}\text{Gd}$  (red),  $^{155}\text{Gd}$  (green) and Hydrogen (blue). Generated with data from the ENDF/B-VII.1 database [91]. Due to the high cross sections for thermal neutron capture on  $^{157}\text{Gd}$  and  $^{155}\text{Gd}$ , Gadolinium is often used to enhance neutron detection in liquid scintillator experiments.

the scintillator of 1.3% per year in terms of photoelectrons per MeV was observed [93].

### 3.2 The $0\nu\beta\beta$ Decay Experiment KamLAND-Zen

The Kamioka Liquid scintillator Anti-Neutrino Detector (KamLAND), located at the Kamioka mine, Gifu, Japan, investigated neutrino oscillation parameters by observing antineutrinos from distant nuclear power plants. The  $\bar{\nu}_e$  flux was dominated by 56 Japanese nuclear power reactors at a flux-weighted average distance of approximately 180 km. The contribution from Korean reactors was estimated to 3.4%.

The KamLAND detector was situated at a depth of  $\sim 2700$  meters water equivalent and took data from 2002 to 2009. The inner part of the detector consisted of a nylon balloon filled with 1 kt liquid scintillator. The nylon balloon was suspended inside a 18 m diameter stainless steel sphere filled with purified mineral oil. An array of 1879 photomultiplier tubes was installed on the inner surface of



the sphere. The sphere was surrounded by a cylindrical tank filled with 3.2 kt water and equipped with photomultiplier tubes, acting as an active cosmic-ray veto detector and shield against external radiation.

The liquid scintillator consisted of 80 % Dodecane and 20 % Pseudocumene. As wavelength shifter PPO was added with a concentration of 1.36 g/l.

As already mentioned in Section 3.1.5, in detectors like KamLAND the electron antineutrinos are detected via the so called inverse  $\beta$  decay,

$$\bar{\nu}_e + p \rightarrow e^+ + n, \quad (3.5)$$

with a threshold of 1.8 MeV. With the prompt scintillation light of the positron, the  $\bar{\nu}_e$  energy  $E_{\bar{\nu}_e}$  can be derived:

$$E_{\bar{\nu}_e} \simeq E_p + \bar{E}_n + 0.8 \text{ MeV}, \quad (3.6)$$

where  $\bar{E}_n$  is the average neutron recoil energy and  $E_p$  the prompt event energy including annihilation and kinetic energy of the positron. With a probability of 99 % the neutron is captured on a free proton with a mean capture time of  $(207.5 \pm 2.8) \mu\text{s}$ , producing a gamma-ray with an energy of 2.2 MeV [94].

The latest three-flavor analysis from KamLAND in combination with solar neutrino experiments and without any constraints from other oscillation experiments yields the following best-fit values [69]:

$$\begin{aligned} \Delta m_{12}^2 &= (7.5^{+0.19}_{-0.20}) \cdot 10^{-5} \text{ eV}^2, \\ \tan^2 \theta_{12} &= 0.452^{+0.035}_{-0.033}, \\ \sin^2 \theta_{13} &= 0.020^{+0.016}_{-0.016}. \end{aligned} \quad (3.7)$$

To convert KamLAND into a neutrinoless double beta decay experiment, a second nylon balloon with a thickness of 25  $\mu\text{m}$  is inserted into the experiment. The 3.08 m diameter inner balloon of the KamLAND Zero-Neutrino Double-Beta Decay (KamLAND-ZEN) experiment contains 13 t of Xenon-loaded liquid scintillator and is surrounded by the 13 m diameter outer balloon containing 1 kt of liquid scintillator.

The Xenon-loaded liquid scintillator consists of 82 % Decane and 18 % Pseudocumene by volume, the wavelength shifter PPO is added with a concentration of 2.0 g/l. By weight 2.52 % of enriched Xenon gas are added for Phase 1 of the experiment. The isotopic abundances in the enriched Xenon were measured to be 90.9 %  $^{136}\text{Xe}$  and 8.9 %  $^{134}\text{Xe}$ . Other Xenon isotopes are negligible [47].

KamLAND-ZEN started data-taking in October 2011 and Phase 1 ended in June 2012. Based on 213.4 days of measurement, a lower limit on the  $0\nu\beta\beta$  half-life was set to  $T_{1/2}^{0\nu} > 1.9 \cdot 10^{25} \text{ a}$  at 90% C.L. [95].

As the  $0\nu\beta\beta$  decay search sensitivity was limited by a background peak arising from  $^{110m}\text{Ag}$ , a purification campaign for the liquid scintillator was set up. The

extracted Xenon was purified by distillation and adsorption by a getter material. The liquid scintillator was purified through water extraction and distillation. A reduction of  $^{110m}\text{Ag}$  by more than a factor of 10 was achieved and data-taking with 346 kg of  $^{136}\text{Xe}$  started in December 2013 (Phase 2).

With Phase 1 data and additional 114.8 days of Phase 2, a lower limit on the  $0\nu\beta\beta$  half-life was set to [48]:

$$T_{1/2}^{0\nu} > 2.6 \cdot 10^{25} \text{ a at 90 \% C.L.} \quad (3.8)$$

An upgrade with a bigger inner balloon containing up to 600 kg of Xenon is planned, aiming for a sensitivity close to  $2 \cdot 10^{26}$  a. To achieve a sensitivity for  $0\nu\beta\beta$  decay covering the inverted hierarchy, the KamLAND2-ZEN detector upgrade is planned. With light collective mirrors, high quantum efficiency PMTs and a new brighter liquid scintillator, the energy resolution is expected to improve from 4 % to less than 2.5 % at the Q-value of  $^{136}\text{Xe}$ . With an amount of 1 t of enriched Xenon and a five year measurement, a sensitivity of 20 meV for  $m_{\beta\beta}$  will be achieved [48].

### 3.3 The $0\nu\beta\beta$ Decay Experiment SNO+

From 1999 to 2006 the Sudbury Neutrino Observatory (SNO) measured the flux of neutrinos produced by  $^8\text{B}$  decays in the Sun, so called  $^8\text{B}$  neutrinos, and studied neutrino oscillations. SNO helped to solve the so called Solar Neutrino Problem, where solar neutrino experiments observed fewer neutrinos than predicted by models of the Sun, see e.g [96].

The SNO detector was located in Vale's Creighton mine near Sudbury, Ontario, Canada at a depth of 2100 m or nearly 5900 meters water equivalent. The detector consisted of a 12 m diameter transparent acrylic vessel filled with 1 kt of 99.92 % isotopically pure heavy water ( $^2\text{H}_2\text{O}$  or  $\text{D}_2\text{O}$ ). The acrylic vessel was held up by a series of ropes in a bath of 7 kt ultra pure water, acting as a shield against external radioactive backgrounds [97]. 9456 PMTs installed on a 17.8 m diameter stainless steel structure detected Cherenkov radiation produced in both the  $\text{D}_2\text{O}$  and  $\text{H}_2\text{O}$ .

The  $^8\text{B}$  neutrinos were detected via three different reactions. The rate of neutral current (NC) reactions,

$$\nu_x + \text{d} \rightarrow \text{p} + \text{n} + \nu_x, \quad (3.9)$$

is equally sensitive to all three active neutrino flavors ( $\nu_x = \nu_e, \nu_\mu, \nu_\tau$ ). By comparing the NC reaction rate to the rate of charged current (CC) reactions,

$$\nu_e + \text{d} \rightarrow \text{p} + \text{p} + \text{e}^-, \quad (3.10)$$

which is only sensitive to  $\nu_e$ , it was possible to determine the neutrino survival probability as a function of energy. In addition, SNO also measured the rate of elastic scattering (ES) reactions,

$$\nu_x + \text{e}^- \rightarrow \nu_x + \text{e}^-, \quad (3.11)$$

which is also sensitive to all three active neutrino flavors, but with a cross section for  $\nu_e$ 's being approximately six times larger than that for  $\nu_\mu$  and  $\nu_\tau$ .

The recoil electrons from both the CC and ES reactions were detected by their production of Cherenkov light. The energy of the interacting neutrino was correlated to the total amount of light detected by the PMTs.

The neutrons from the NC reactions were detected in several ways, so the SNO detector operated in three phases. In Phase 1, the neutrons were observed by their capture on deuterons in the D<sub>2</sub>O, releasing a 6.25 MeV gamma ray. The gamma ray was detected by the Cherenkov light of secondary Compton electrons or by  $e^+e^-$  pairs. In Phase 2, 2 t of NaCl were added to the D<sub>2</sub>O. The neutrons captured predominantly on <sup>35</sup>Cl, which has a much higher neutron capture cross section than deuterons. Neutron capture on <sup>35</sup>Cl releases multiple gamma rays with an energy of 8.6 MeV. In Phase 3, proportional counters made of high purity nickel tubes with a length of 2 m were welded to form 40 strings. 36 strings were filled with <sup>3</sup>He and the neutrons were detected via the reaction



where the Tritium and the proton have a kinetic energy of 0.76 MeV. Four additional strings were filled with <sup>4</sup>He to study backgrounds.

By combining the data from all three phases, the SNO experiment measured a total flux of active neutrino flavors from <sup>8</sup>B decays in the Sun of  $(5.25 \pm 0.16(\text{stat.})_{-0.13}^{+0.11}(\text{syst.})) \cdot 10^6 \text{ cm}^{-2}\text{s}^{-1}$ . This is consistent with solar model predictions [97]. Using only SNO data, a two-flavor neutrino oscillation analysis yields [97]

$$\begin{aligned} \Delta m_{12}^2 &= (5.6_{-1.4}^{+1.9}) \cdot 10^{-5} \text{eV}^2, \\ \tan^2 \theta_{12} &= 0.427_{-0.029}^{+0.033}. \end{aligned} \quad (3.13)$$

The main change between SNO and SNO+ is the substitution of the D<sub>2</sub>O with liquid scintillator. As solvent, LAB is filled in the same acrylic vessel used for SNO, containing 2 g/l PPO as fluor. To compensate the buoyant force due to the lower density of LAB compared to D<sub>2</sub>O, the acrylic vessel is hold in place inside the water shield with a rope net.

Because of the higher light yield and lower energy threshold, SNO+ will have a higher event rate and more signals from the PMTs to process. Therefore, electronics and data acquisition have been upgraded and all damaged PMTs are replaced. In addition, a new calibration system and processing and purification systems for both the water and scintillator are installed.

SNO+ has a broad physics program, including the measurement of supernova and solar neutrinos, as well as reactor and geo antineutrinos. However, the main goal is the search for the neutrinoless double beta decay [45]. The original plan was to load the liquid scintillator with <sup>150</sup>Nd, but now <sup>130</sup>Te is used as it has several

possible advantages [98]:  $^{130}\text{Te}$  has a high abundance of 34 % in natural Tellurium and is relatively inexpensive. The background remaining from  $2\nu\beta\beta$  decays is of a factor  $\sim 100$  smaller compared to  $^{150}\text{Nd}$  and Tellurium has no inherent atomic absorption in the optical range of the PMTs.

To load the liquid scintillator with Tellurium, initially telluric acid is dissolved in water, in which it is highly soluble. Using an amine-based surfactant, this mixture is then combined at the percent-level with LAB. The resulting liquid is clear and stable. As the scintillator mixture has no strong absorption lines in the region where the PMTs are sensitive, the scintillator can be loaded with high concentration of Tellurium without suffering from a loss in optical clarity.

In a first step, the liquid scintillator will be loaded with 0.3 % of Te, corresponding to approximately 800 kg of  $^{130}\text{Te}$  in the detector. With a 54 % effective photocathode coverage and a light yield of nearly 9400 photons/MeV an energy resolution of approximately 4.5 % at 2.5 MeV will be reached. A future loading level up to 3 % of Te, corresponding to approximately 8 t of  $^{130}\text{Te}$ , is under investigation.

In the commissioning phase, the SNO+ detector is filled with water. The filling with liquid scintillator will take place in 2015. By the end of 2015 or beginning 2016 the loading with Tellurium will take place [98].

## Chapter 4

# The COBRA Experiment

The field of neutrinoless double beta decay experiments greatly evolved recently, with new experimental approaches and the investigation of different promising isotopes. COBRA is the only experiment examining the isotopes  $^{116}\text{Cd}$  and  $^{106}\text{Cd}$ , while the interesting isotope  $^{130}\text{Te}$  can also be addressed. With its unique features the COBRA experiment intends to be a strong competitor to other next-generation neutrinoless double beta decay experiments.

COBRA is a Research and Development (R&D) project for a large-scale neutrinoless double beta decay experiment using Cadmium Zinc Telluride (CdZnTe) semiconductor detectors. CdZnTe contains nine double beta decay isotopes and therefore the detector acts as its own source mass. With a sensitivity of  $2 \cdot 10^{26}$  years to the half-life of  $^{116}\text{Cd}$ , the large scale set-up will be competitive to other experiments in this field. To reach this goal, the reduction of background events to a level of  $10^{-3}$  counts/keV/kg/a in the region of interest (ROI) around the Q-value of  $^{116}\text{Cd}$  is essential.

Currently, the COBRA experiment is in the prototyping stage with a 64 detectors demonstrator at the LNGS underground laboratory. The detectors with a size of  $1 \text{ cm}^3$  are arranged in a  $4 \times 4 \times 4$  array and shielded against external radiation. The background is mainly composed of  $\alpha$ - and  $\gamma$ -radiation generated inside or on the surfaces of the detector's holder or lacquer. Also background events induced by neutrons are a major concern for the development of a large scale experiment.

### 4.1 Isotopes under Investigation

CdZnTe contains overall nine double beta decay isotopes with  $^{116}\text{Cd}$ ,  $^{106}\text{Cd}$  and  $^{130}\text{Te}$  being the most interesting. All nine isotopes are listed in Table 4.1.

$^{116}\text{Cd}$  is the most important isotope for the COBRA experiment since its relatively high Q-value of 2813.5 keV is well beyond the prominent  $\gamma$ -line at 2614 keV from  $^{208}\text{Tl}$ . This is a big advantage compared to isotopes with a Q-value below 2.6 MeV and helps to reduce the intrinsic background caused by natural radioac-

**Table 4.1:** Decay modes, natural abundance and Q-values of all nine double beta decay candidate isotopes contained in CdZnTe. Values taken from [23].

Isotope	Decay mode	nat. ab. [%]	Q-value [keV]
$^{64}\text{Zn}$	$\beta^+/\text{EC}, \text{EC}/\text{EC}$	48.6	1096
$^{70}\text{Zn}$	$\beta^-\beta^-$	0.62	1001
$^{106}\text{Cd}$	$\beta^+\beta^+, \beta^+/\text{EC}, \text{EC}/\text{EC}$	1.21	2771
$^{108}\text{Cd}$	$\text{EC}/\text{EC}$	0.9	231
$^{114}\text{Cd}$	$\beta^-\beta^-$	28.7	534
$^{116}\text{Cd}$	$\beta^-\beta^-$	7.5	2814
$^{120}\text{Te}$	$\beta^+/\text{EC}, \text{EC}/\text{EC}$	0.1	1722
$^{128}\text{Te}$	$\beta^-\beta^-$	31.7	868
$^{130}\text{Te}$	$\beta^-\beta^-$	33.8	2527

tivity (see Section 4.2).

A shortcoming of  $^{116}\text{Cd}$  is its comparatively low  $2\nu\beta\beta$  decay half-life and therefore a very good energy resolution is needed to discriminate the  $0\nu\beta\beta$  decay and the  $2\nu\beta\beta$  decay. In addition, the high  $2\nu\beta\beta$  decay rate limits the sensitivity for decays in ground states of other double beta decay isotopes, in particular  $^{130}\text{Te}$ . In contrast, the search for  $\beta^+$  emitters or for decays in excited states is less affected, as COBRA is designed as an array of thousands of detectors. With a coincidence analysis, the search for the simultaneous energy deposition of electrons in one detector and for gammas in another is possible. This is an important feature of the COBRA design. As the natural abundance of  $^{116}\text{Cd}$  is 7.5 %, an enrichment for this isotope is needed in order to gain a sufficient amount of source atoms.

On the contrary,  $^{130}\text{Te}$  has a very high natural abundance of 33.8%. Enrichment is therefore cheaper compared to other isotopes or can be omitted completely. Another advantage of  $^{130}\text{Te}$  is its high  $2\nu\beta\beta$  decay half-life, which results in less  $2\nu\beta\beta$  decay background events in the  $0\nu\beta\beta$  decay signal-region. Thus, it is under investigation by various experiments, see Section 2.6. However, its Q-value of 2529 keV is between the full-energy peak and the Compton edge of the 2.6 MeV  $\gamma$ -line from  $^{208}\text{Tl}$ . This  $\gamma$ -background has to be shielded from the experiment.

Another interesting isotope is  $^{106}\text{Cd}$ , one of the most promising isotopes for the discovery of the  $0\nu\beta^+\beta^+$  decay. Three different decay modes are possible:  $0\nu\beta^+\beta^+$ ,  $0\nu\beta^+/\text{EC}$  and  $0\nu\text{EC}/\text{EC}$ , see Section 2.5.3. The Q-value of this decay is relatively large with 2775.4 keV. Longer half-lives compared to the  $0\nu\beta^-\beta^-$  decay are expected, especially for the  $0\nu\beta^+\beta^+$  mode. This is due to the reduction of the phase space by  $4 \cdot m_e = 2044$  keV due to the emission of two positrons. On the other hand, this decay generates a very distinct signature in a highly granular detector like COBRA and is easy to detect. The  $0\nu\beta^+/\text{EC}$  mode is of special

interest for the study of right-handed currents [99]. A lower half-life limit for resonant neutrinoless double electron capture to the 2741 keV  $^{106}\text{Pd}$  excited state has recently been given with  $T_{1/2}^{R0\nu EC/EC} > 1.1 \cdot 10^{20}$  a [100]. For a long time the spin value of the final state was unknown. As a new value for the spin is  $J = 4^+$ , this transition is disfavored due to selection rules [35].

## 4.2 Background Sources

To achieve a half-life sensitivity in the order of  $10^{26}$  years, the reduction of background events in the region of interest down to a level of  $10^{-3}$  counts/keV/kg/a is essential for the COBRA experiment. To study other interesting decay modes like  $2\nu\beta\beta$  decay the background has to be kept as low as possible throughout the entire measurement range. The emphasis in this section is placed on background in the detector's lacquer occurring from natural decay chains and background induced by neutrons.

### 4.2.1 Natural Decay Chains and $^{40}\text{K}$

Gamma radiation mainly originates from the natural decay chains of  $^{232}\text{Th}$  (Thorium series),  $^{238}\text{U}$  (Uranium series) and the decay of  $^{40}\text{K}$ .

From the Uranium series, especially decays from Radon daughters can deposit energy in the ROI of the COBRA experiment. The noble gas  $^{222}\text{Rn}$  has a half-life of nearly four days and escapes by diffusion from solid rocks. About 1300 Bq/m<sup>3</sup>/day of  $^{222}\text{Rn}$  are released into the Earth's atmosphere [101]. Its long-living progeny  $^{210}\text{Pb}$  with a half-life of over 23 years can be deposited on surfaces by washout and dry deposition. Especially statically charged surfaces like plastics and glass and high voltages attract Radon and its progenies.

For the ROI in the COBRA experiment mainly one  $\gamma$ -emitter is important:  $^{214}\text{Bi}$  from the Uranium series mostly decays into  $^{214}\text{Po}$ , emitting a  $\beta$ -particle with an energy up to 3.28 MeV and gammas with energies up to 3.27 MeV. Although these lines have a small probability, eight lines appear in the region between 2.7 MeV and 2.9 MeV. As the progenies of  $^{222}\text{Rn}$  decay within a half-life of several hours into the long-living  $^{210}\text{Pb}$ , the diffusion of Radon into the set-up has to be prevented in order to reduce the background originating from  $^{214}\text{Bi}$ . In addition, two  $\alpha$ -emitters in the Radium series have to be taken into account:  $^{214}\text{Po}$  emits alphas with an energy of 7.69 MeV and  $^{210}\text{Po}$  emits alphas with an energy of 5.31 MeV. A detailed overview of the Uranium series is given in Appendix A.

The Thorium series also has an intermediate Radon member,  $^{220}\text{Rn}$ . Due to the short half-life of 55.6 s, the abundance of  $^{220}\text{Rn}$  is normally below the percent level of  $^{222}\text{Rn}$  in the atmosphere, although it is present with about the same or higher amount in rocks and building material [101]. The highest  $\gamma$ -line in this series is the prominent peak at 2614.5 MeV from  $^{208}\text{Tl}$ . However, some  $\alpha$ -emitters

are present in the progenies of  $^{220}\text{Rn}$  and have to be taken into account for low-background experiments:  $^{216}\text{Po}$  (6.78 MeV),  $^{212}\text{Bi}$  (6.05 MeV, 6.09 MeV) and  $^{212}\text{Po}$  (8.79 MeV). A detailed overview of the Thorium series is given in Appendix B.

In the course of the total background estimation for COBRA [86], upper limits on background indices were calculated by projecting the measured background spectrum from the demonstrator (see Section 4.4) to a Monte-Carlo simulation for a large-scale experiment. Next to contaminations in the detector's holder structure, background from the  $^{232}\text{Th}$  and  $^{238}\text{U}$  series in the Glyptal lacquer is a major component for the large-scale set-up. The assumptive activities of contamination and the resulting background rates are summarized in Table 4.2. These results indicate that activities of  $^{232}\text{Th}$  and  $^{238}\text{U}$  in the order of 0.1 mBq/kg are sufficient to reach background rates generated by contaminations in the detector's passivation material below  $10^{-3}$  counts/keV/kg/a. As depicted in Section 3.1.4, this is achievable with liquid scintillator as ultrapure environment for the CdZnTe detectors.

Another important aspect is the shielding and veto capability of liquid scintillator with respect to background originating from the detector's holder structure. Alpha and beta particles arising from the Delrin and transversing the liquid scintillator will deposit energy and can be efficiently vetoed. Only ionizing particles penetrating the detectors through the bearing surface to the holder structure are not visible.



**Table 4.2:** Calculated background rate in a large-scale COBRA experiment generated by contaminations from the  $^{232}\text{Th}$  and  $^{238}\text{U}$  series in the Glyptal 1201 lacquer. The quoted activities are upper limits determined from the background spectrum of the demonstrator at the LNGS laboratory. With the current background level of the demonstrator, an upper background index of  $61.11 \times 10^{-3}$  counts/keV/kg/a resulting from the Glyptal lacquer is expected by Monte-Carlo simulation. Taken from [86].

Intrinsic contamination	Activity [mBq/kg]	Background [ $10^{-3}$ counts/keV/kg/a]
$^{232}\text{Th}$	30.6	$7.4 \pm 0.3$
$^{228}\text{Th}$	13.3	$1.48 \pm 0.09$
$^{224}\text{Ra}$	11.4	$1.33 \pm 0.08$
$^{220}\text{Rn}$	7.6	$0.85 \pm 0.05$
$^{216}\text{Po}$	0.95	$0.068 \pm 0.005$
$^{212}\text{Bi}$	0.19	$(9.1 \pm 0.9) \cdot 10^{-3}$
$^{212}\text{Po}$	0.19	$(4.2 \pm 0.6) \cdot 10^{-3}$
$^{208}\text{Tl}$	0.19	$< 3.6 \cdot 10^{-4}$
$^{238}\text{U}$	30.0	$7.3 \pm 0.3$
$^{234}\text{U}$	17.4	$3.2 \pm 0.2$
$^{230}\text{Th}$	21.5	$4.3 \pm 0.2$
$^{226}\text{Ra}$	22.4	$4.1 \pm 0.2$
$^{222}\text{Rn}$	33.6	$6.0 \pm 0.3$
$^{218}\text{Po}$	7.0	$0.8 \pm 0.05$
$^{214}\text{Bi}$	1.4	$< 0.006$
$^{214}\text{Po}$	1.4	$0.056 \pm 0.006$
$^{210}\text{Po}$	58.8	$8.2 \pm 0.5$
Surface contamination	Activity [mBq/cm <sup>2</sup> ]	Background [ $10^{-3}$ counts/keV/kg/a]
$^{222}\text{Rn}$	$2.5 \cdot 10^{-5}$	$7.1 \pm 0.2$
$^{210}\text{Po}$	$1.8 \cdot 10^{-5}$	$6.2 \pm 0.2$
$\Sigma$		$< 61.11$

### 4.2.2 Neutron Induced Background and Neutron Detection

As neutrons carry no charge they cannot interact in matter by means of the coulomb force, which is the dominant energy loss mechanism for charged particles. Neutrons can travel through many centimeters of matter without any type of interaction and thus without being visible to a detector. In a very simple perception, neutrons can be divided into slow neutrons and fast neutrons on the basis of their energy. The dividing line is often set to 0.5 eV, the so-called  $^{113}\text{Cd}$  cutoff energy [89]. Slow neutrons with an energy of 0.025 eV are called thermal neutrons.

The  $^{113}\text{Cd}$  cutoff energy is chosen in such a way, as the total cross section of neutron reactions with  $^{113}\text{Cd}$  drops drastically with neutron energies higher than 0.5 eV, see Figure 4.1. The capture of thermal neutrons on  $^{113}\text{Cd}$  is a potential background for the COBRA experiment, as  $^{113}\text{Cd}$  is contained with 12 % abundance in natural Cadmium. In the  $^{113}\text{Cd}(n, \gamma)^{114}\text{Cd}$  reaction, gamma rays with an overall energy of about 9 MeV are produced. These  $\gamma$ -particles can mimic signal events in COBRA's region of interest. A very good neutron shield is therefore necessary for the COBRA experiment.

Typical reactions for neutron absorption or detection are (n, p), (n,  $\alpha$ ) and (n, fission) reactions. Except for some (n, fission) reactions, the cross sections for these reactions drop off with increasing neutron energy. A moderation of fast neutrons to slow neutrons is therefore desirable to allow for neutron capture reactions. The most efficient moderator is Hydrogen, as neutrons can lose up to all their energy in elastic scattering collisions with Hydrogen nuclei. These recoil nuclei can pick up a detectable amount of energy from neutron collisions, e.g. in a scintillator detector.

For heavier nuclei than Hydrogen, neutrons can transfer their energy only partially via elastic scattering. However, for fast neutrons with sufficiently high energies, inelastic scattering can take place, leading to nuclei elevated to excited states. By emitting gamma rays, these nuclei quickly de-excite.

Isotopes often used to absorb or detect neutrons in (n,  $\alpha$ ) reactions are  $^{10}\text{B}$  and  $^6\text{Li}$ .  $^{10}\text{B}$  is often used, as its natural abundance of 19.8 % in Boron is already relatively high and enriched  $^{10}\text{B}$  is readily available. When thermal neutrons induce the  $^{10}\text{B}(n, \alpha)^7\text{Li}$  reaction,



94 % of all reactions have a Q-value of 2.310 MeV and leave  $^7\text{Li}$  in its excited state. The remaining 6 % have a Q-value of 2.792 MeV and decay into the ground state. The thermal neutron cross section for the  $^{10}\text{B}(n, \alpha)^7\text{Li}$  reaction is 3840 barns. With increasing neutron energy, the cross section drops proportional to the reciprocal of the neutron velocity over much of the energy range.

The  $^6\text{Li}(n, \alpha)^3\text{H}$  reaction,



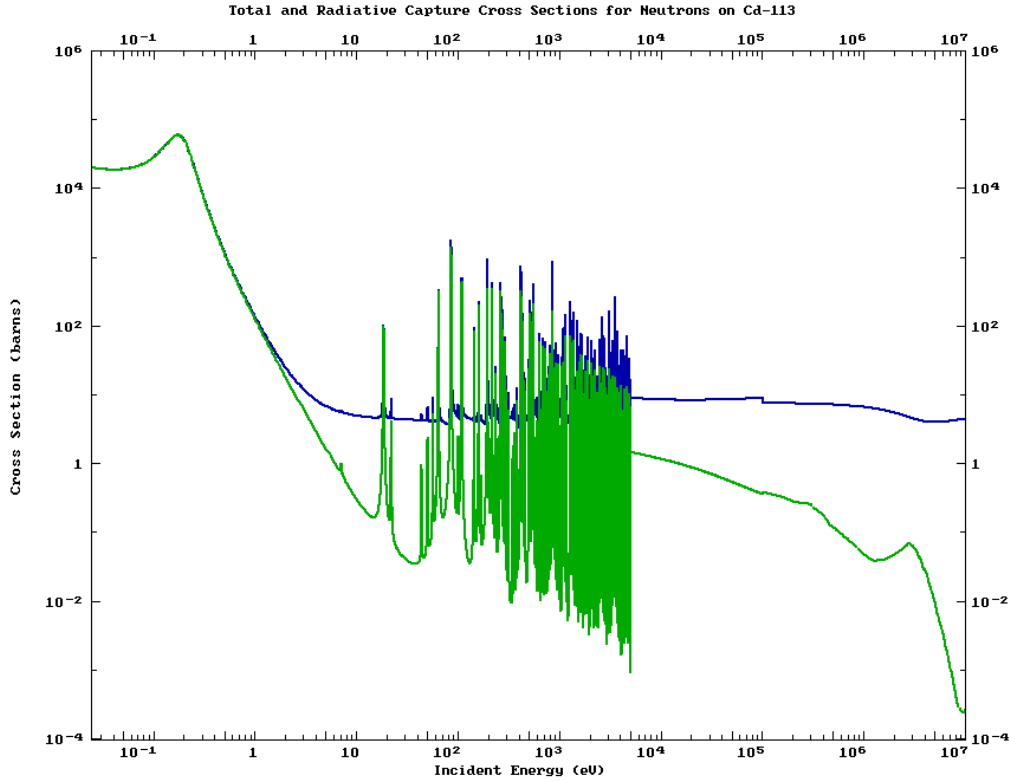


**Figure 4.1:** Total (blue) and radiative capture (green) cross sections for neutrons on  $^{113}\text{Cd}$ . Generated with data from the ENDF/B-VII.1 database [91]. Due to the high cross sections for capture on  $^{113}\text{Cd}$  and the subsequent gamma cascade, thermal neutrons are a potential background for the COBRA experiment. As the cross section for radiative capture drops drastically with neutron energies higher than the so-called  $^{113}\text{Cd}$  cutoff at 0.5 eV, neutrons are roughly divided in slow and fast neutrons.

proceeds only to the ground state with a Q-value of 4.780 MeV. For an incoming low energy neutron, the produced alpha particle has an energy of 2.050 MeV, the triton has an energy of 2.730 MeV, and both particles are oppositely directed. The thermal neutron cross section for this reaction is with 940 barns considerably lower than for the  $^{10}\text{B}(n, \alpha)^7\text{Li}$  reaction, except for a resonance region around 250 keV, see Figure 4.2.  $^6\text{Li}$  has a natural abundance of 7.40 % and is widely available.

Another isotope for the detection of thermal neutrons with proportional counters is  $^3\text{He}$ . Although its thermal neutron cross section is with 5330 barns significantly higher than the  $^{10}\text{B}$ 's cross section, its relatively high cost is a limiting factor. Like for  $^6\text{Li}$  and  $^{10}\text{B}$ , the cross section drops linearly for increasing neutron energies, see Figure 4.2. If the  $^3\text{He}(n, p)^3\text{H}$  reaction,



is induced by slow neutrons, the produced particles are oppositely directed with energies of 0.573 MeV for the proton and 0.191 MeV for the triton. The Q-value of

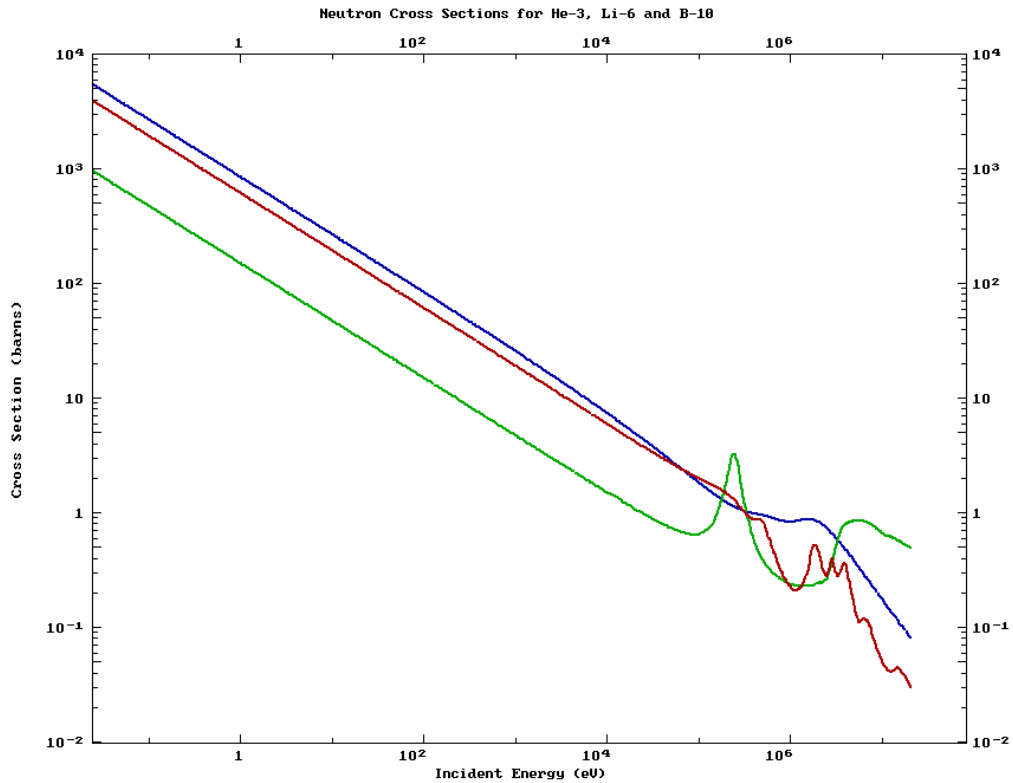


**Figure 4.2:** Cross sections for the reactions  ${}^3\text{He}(n,p){}^3\text{H}$  (blue),  ${}^{10}\text{B}(n,\alpha){}^7\text{Li}$  (red) and  ${}^6\text{Li}(n,\alpha){}^3\text{H}$  (green). Generated with data from the ENDF/B-VII.1 database [91]. For a wide range of energies, the cross sections drop linearly for increasing neutron energies.

this reaction is 0.764 MeV.

With fission cross sections in the order of  $\sim 3000$  barns, also  ${}^{235}\text{U}$  and  ${}^{239}\text{Pu}$  are used as basis for thermal and slow neutron detectors, see Figure 4.3. As the Q-values of the fission reactions are in the order of 200 MeV, detectors based on these reactions can give output pulses that are orders of magnitude larger than those induced from reactions discussed previously.

Detectors using  ${}^{238}\text{U}$  or  ${}^{237}\text{Np}$  are only sensitive to fast neutrons, as the fission cross sections for  ${}^{238}\text{U}$  and  ${}^{237}\text{Np}$  increase sharply to  $\sim 1$  barn with neutron energies higher than  $\sim 500$  keV, see Figure 4.4. These detectors are called threshold detectors.

For a large-scale COBRA experiment, a 100 mm thick layer made of doped Polyethylene (PE) is planned as neutron absorber in the shield [86]. A doping with 5% of  ${}^{10}\text{B}$  is favored. A more sophisticated method is the application of a neutron absorber instrumented with an active veto to reduce background originating from radioisotopes or muons. Liquid or plastic scintillators equipped with photomultiplier tubes might be a superior solution to shield against thermal neutrons, as already discussed in Section 3.1.5.

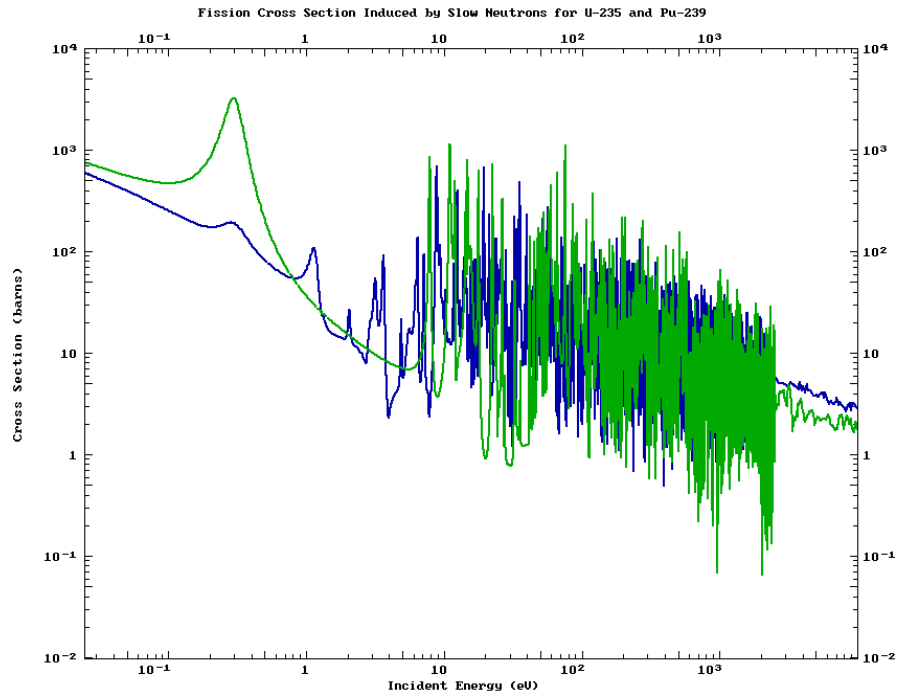


**Figure 4.3:** Fission cross sections induced by slow neutrons for  $^{235}\text{U}$  (blue) and  $^{239}\text{Pu}$  (green). Generated with data from the ENDF/B-VII.1 database [91].

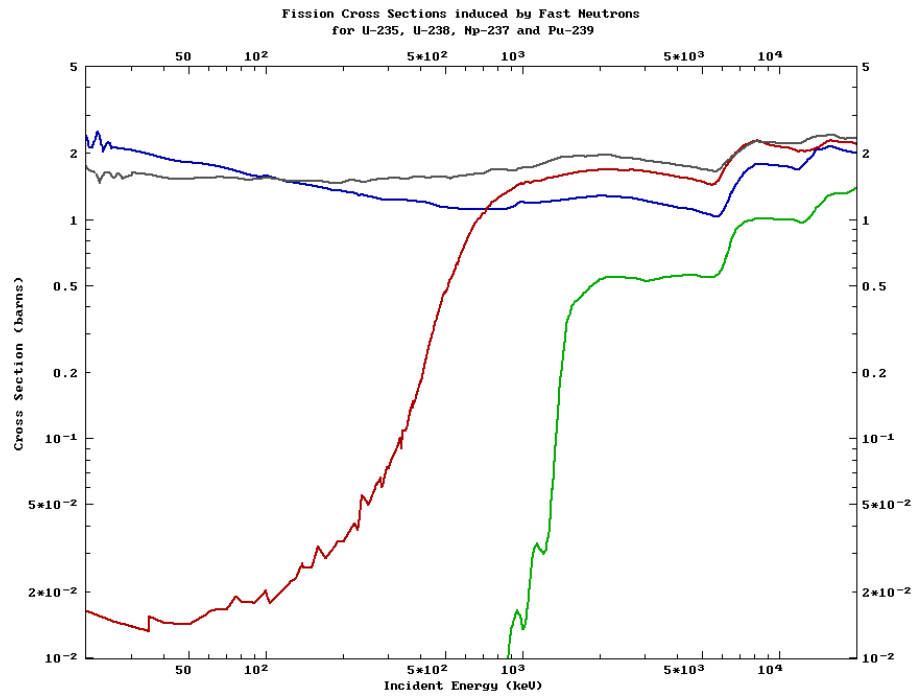


**Figure 4.4:** Fission cross sections induced by fast neutrons for  $^{235}\text{U}$  (blue),  $^{239}\text{Pu}$  (black),  $^{238}\text{U}$  (green) and  $^{237}\text{Np}$  (red). Generated with data from the ENDF/B-VII.1 database [91]. As almost no fission is induced on  $^{238}\text{U}$  and  $^{237}\text{Np}$  by neutrons with energies below  $\sim 500$  keV, these isotopes are used to build so-called threshold detectors.

### 4.2.3 Cosmogenic Radioisotopes

The hadronic component of cosmic rays can produce radionuclides in the detectors or in shielding materials during storage at sea level or during transport in air. These cosmogenic activated isotopes can reach radioactivity levels higher than the contamination by natural decay chains. Hence, detectors and shielding materials should not be stored for long periods at the Earth's surface.

In underground laboratories however, fast muons can produce particle showers of protons, neutrons and pions with a volume of several cubic meters. The production rate of cosmogenic radioisotopes has therefore to be carefully studied for all materials near to the detectors. Especially in copper, often used as the innermost shield material, shorter-living radioisotopes like  $^{56}\text{Co}$ ,  $^{57}\text{Co}$ ,  $^{58}\text{Co}$  and  $^{60}\text{Co}$  are produced.

### 4.2.4 Neutrino Accompanied Double Beta Decay

An unavoidable background for every neutrinoless double beta decay experiment is the neutrino accompanied double beta decay ( $2\nu\beta\beta$ ). As the endpoint energy of the neutrino accompanied decay is the Q-value of the decay, a number of  $2\nu\beta\beta$  events will always show up in the region of interest for the  $0\nu\beta\beta$  decay.

The fraction  $F$  of  $2\nu\beta\beta$  events in the ROI can be approximated by [102]

$$F = \frac{aQ}{m_e} \left( \frac{\Delta E}{Q} \right)^6, \quad (4.4)$$

where  $\Delta E$  is the FWHM energy resolution. The coefficient  $a$  depends slightly on resolution and is 5 at 10% FWHM, 7 at 5% FWHM and 8.5 at 1% FWHM. The  $0\nu\beta\beta$  signal (S) to  $2\nu\beta\beta$  background (B) ratio can then be expressed as

$$\frac{S}{B} = \frac{m_e}{aQ} \left( \frac{Q}{\Delta E} \right)^6 \frac{T_{1/2}^{2\nu}}{T_{1/2}^{0\nu}}. \quad (4.5)$$

From this expression one can see, that there are two possibilities to reduce the  $2\nu\beta\beta$  background: First of all the choice of an isotope with a long  $2\nu\beta\beta$  decay half-life reduces the number of background events during measurement (see Table 2.3). Secondly, the energy resolution is crucial to separate  $0\nu\beta\beta$  from  $2\nu\beta\beta$ . As the region of interest is normally defined as a  $1\sigma$  FWHM region around the Q-value, a very good energy resolution minimizes the ROI and lessens the background events originating from  $2\nu\beta\beta$  decay.

## 4.3 CdZnTe as Material for Semiconductor Detectors

$\text{Cd}_{1-x}\text{Zn}_x\text{Te}$  is a wide-bandgap semiconductor material produced by compounding small amounts ( $x \sim 0.1$ ) of ZnTe to CdTe. Due to its high average atomic number of about 49, it has a good stopping power for  $\gamma$ -rays and high-energy charged

particles. Hence, it is an excellent material for ionizing radiation detectors. A difficulty for the COBRA experiment is the available dimension of CdZnTe crystals for detector production. Currently the largest detectors commercially available measure  $2 \times 2 \times 1.5 \text{ cm}^3$  and weigh about 36 g. A large scale detector array for a  $0\nu\beta\beta$  decay search in the order of 400 kg consists of more than 10000 detectors.

### 4.3.1 Semiconductor Properties

In a crystalline semiconductor material, the periodic lattice forms allowed energy bands for electrons. Any electron within the material must be confined to one of these energy bands. The lower band is called the valence band and corresponds to the outer-shell electrons that are integrated to distinct lattice sites within the crystal. The band situated higher than the valence band is called the conduction band. Electrons in this band are responsible for the electrical conductivity of the material. Valence and conduction band are separated by the so-called bandgap, the size of which determines whether the material is a semiconductor or an insulator. The energy bands are de facto regions of discrete energy levels, which are so closely spaced that they can be regarded as a continuum. In the bandgap however no allowed energy levels are present at all. Usually materials with a bandgap energy  $E_g$  larger than 5 eV are considered as insulators, whereas semiconductors have typically bandgap energies of size  $\sim 1 \text{ eV}$ . Dependent from the amount  $x$  of Zn, the bandgap energy of CdZnTe ranges from 1.53 eV ( $\text{Cd}_{0.96}\text{Zn}_{0.04}\text{Te}$ ) to 1.64 eV ( $\text{Cd}_{0.8}\text{Zn}_{0.2}\text{Te}$ ) [89].

In absence of thermal excitation or any other ionization within the crystal, the valence band of a semiconductor is completely filled and the conduction band is completely empty. When passing the detector material, high-energy particles ionize atoms by lifting so-called primary electrons from the valence band to the conduction band. Dependent on the energy of these primary electrons, secondary ionization of atoms can occur. Primary and secondary electrons may lose energy via bremsstrahlung photons, which in turn can ionize atoms in the material through photoelectric absorption, Compton scattering or pair production. These excitation processes not only promote electrons to the conduction band, but they leave a gap in the valence band named hole. Energy deposition in a semiconductor always leads to the equal number of holes and electrons, the electron-hole pairs. If an electric field is applied to a semiconductor, an electric current constitutes from two sources: the movement of electrons in the conduction band and the movement of holes in the valence band. In contrast, the current in metallic conductors is carried out by electrons only.

The energy needed by the primary particle to produce an electron-hole pair is often called the ionization energy  $\epsilon$ . It is experimentally observed that  $\epsilon$  is largely independent of energy and type of the incident radiation [89]. This allows for the prediction of the number of electron-hole pairs created by the incident energy of the

radiation, if the primary particle and secondary radiation is fully stopped inside the active volume of the detector. Nevertheless, detector calibration using a radiation type that is identical to the one involved in the measurement is recommended if precise energy values are needed. The ionization energy is also temperature-dependent. For most semiconductor detector materials the value of  $\epsilon$  increases with decreasing temperature.

A big advantage of semiconductor detectors is the small amount of ionization energy needed to create electron-hole pairs compared to scintillation detectors or gas-filled detectors. In typical semiconductor materials values for  $\epsilon$  roughly range from 3 to 5 eV, for  $\text{Cd}_{0.9}\text{Zn}_{0.1}\text{Te}$   $\epsilon$  is 4.64 eV [103]. As in typical gases the average energy to produce an ion-pair is around 30 eV, the number of charge carriers for a given deposited energy is  $\sim 10$  times higher in semiconductor detectors than in gaseous detectors. This has two valuable effects on the obtainable energy resolution: The energy resolution at low energies is often limited by electronic noise in the readout chain and an increased number of charges per energy deposition leads to a better signal to noise ratio. On the other hand the statistical fluctuation per energy deposition is reduced as the total number of electron-hole pairs is increased. This aspect is often limiting the achievable energy resolution for medium and high radiation energy.

### 4.3.2 Intrinsic Charge Carriers

Some thermal energy is always shared by the electrons of the lattice, if the temperature is nonzero. Therefore, it is possible that an electron from the valence band gains sufficient thermal energy to be raised to the conduction band and begins to drift through the crystal. On the other hand, electrons and holes recombine at any time and under stable conditions an equilibrium concentration of electron-hole pairs is persistent.

The concentration  $n_i$  of electron-hole pairs through thermal excitation in an intrinsic semiconductor (without dopants) is given by

$$n_i = CT^{3/2} e^{-\frac{E_g}{2kT}} \quad (4.6)$$

where  $T$  is the absolute temperature,  $k$  the Boltzmann constant and  $C$  a characteristic proportionality constant of the semiconductor material. The probability of thermal excitation depends mostly on the ratio of the bandgap energy  $E_g$  to the absolute temperature. Is the bandgap energy in the order of  $\sim 1$  eV, an electrical conductivity high enough for the material to be classified as a semiconductor is caused by thermal excitation. As the equilibrium concentration  $n_i$  of electron-hole pairs is a strong function of temperature, it decreases if the material is cooled.

A big advantage of CdZnTe detectors, compared to some other semiconductor materials like germanium, is the possibility of operation at room temperatures. With absence of a cryogenic environment, handling and preparation of the detectors is highly simplified. Nevertheless, cooling the detectors moderately from room



temperature to about 278 K enhances the energy resolution of CdZnTe detectors significantly [104].

### 4.3.3 Charge Transport and Trapping

When a particle deposits energy in a semiconductor detector, equal numbers of electron and holes are created along the particle track within a few picoseconds. If an electric field  $E$  is present in the detector, both charge carriers drift in opposite directions. For low and moderate values of  $E$ , the drift velocity  $\nu_h$  for holes and  $\nu_e$  for electrons is proportional to the applied field:

$$\begin{aligned}\nu_h &= \mu_h \cdot E \\ \nu_e &= \mu_e \cdot E\end{aligned}\tag{4.7}$$

with  $\mu_h$  being the mobility for holes and  $\mu_e$  the mobility for electrons. For higher electric field values the drift velocity increases more slowly with the field until a saturation velocity in the order of  $10^7 \text{ cm s}^{-1}$  is reached.

Electrons and holes drift under the influence of the applied field through the detector until they are collected at an electrode or recombine. Some impurities inside the crystal like gold, zinc or cadmium can introduce energy levels near the middle of the bandgap energy. Charge carriers can be trapped in these impurities and are immobilized for a period of time that can be sufficiently long to prevent the carriers from contributing to the measured pulse. Other types of impurities act as recombination centers, causing charge carriers to annihilate. The mean hole lifetime  $\tau_h$  and the mean electron lifetime  $\tau_e$  are characteristic quantities for the recombination or the capture of charge carriers in semiconductor materials.

The mobility-lifetime product  $\mu\tau_h$  for holes and  $\mu\tau_e$  for electrons is a common figure of merit for detector materials. For CdZnTe  $\mu\tau_h$  is approximately two orders of magnitude lower than  $\mu\tau_e$ . The contribution of the hole motion to the signal is therefore dependent from the position inside the detector where the energy deposition took place.

Important physical properties for Cd<sub>0.9</sub>Zn<sub>0.1</sub>Te compared to the semiconductor materials Germanium and Silicon can be found in Table 4.3.

### 4.3.4 Pulse Formation

As soon as an incident particle deposits its energy into the detector crystal, electrons and holes are produced. When an electric field is applied to electrodes on the detector, the electrons move to the anode and the holes to the cathode. This motion of charge carriers instantaneously induces a charge on the electrodes and the developing output pulse can be read out. This pulse development ends when the last of the charge carriers arrive at the electrodes or when all charge carriers

**Table 4.3:** Physical properties of  $\text{Cd}_{0.9}\text{Zn}_{0.1}\text{Te}$ , Ge and Si. Values taken from [103] and from [89]. All temperature-dependent values are given at 300 K, except for the ionization energy of Ge, which is given at 77 K.

Material	$\text{Cd}_{0.9}\text{Zn}_{0.1}\text{Te}$	Ge	Si
Atomic numbers	48, 30, 52	32	14
Average atomic number	49.1	32	14
Density ( $\text{g}/\text{cm}^3$ )	5.78	5.32	2.33
Bandgap energy $E_g$ (eV)	1.572	0.665	1.115
Electron mobility $\mu_e$ ( $\text{cm}^2/\text{Vs}$ )	$10^3$	3900	1350
Electron lifetime $\tau_e$ (s)	$3 \times 10^{-6}$	$> 10^{-3}$	$> 10^{-3}$
Hole mobility $\mu_h$ ( $\text{cm}^2/\text{Vs}$ )	50 to 80	1900	480
Hole lifetime $\tau_h$ (s)	$10^{-6}$	$10^{-3}$	$2 \times 10^{-3}$
$\mu\tau_e$ ( $\text{cm}^2/\text{V}$ )	$(3 \text{ to } 5) \times 10^{-3}$	$> 1$	$> 1$
$\mu\tau_h$ ( $\text{cm}^2/\text{V}$ )	$5 \times 10^{-5}$	$> 1$	$\sim 1$
Ionization energy $\epsilon$ (eV)	4.64	2.96	3.62

are captured or recombined. The time evolution and the shape of the pulse can therefore provide useful information on the location of radiation interaction.

The induced charge on the electrodes due to the motion of charge carriers in a detector can be calculated using the Shockley-Ramo theorem [105, 106]. The instantaneous current  $i$  induced on a given electrode is equal to

$$i = q\vec{v} \cdot \vec{E}_0 \quad (4.8)$$

where  $q$  is the charge of the carrier,  $\vec{v}$  is its velocity and  $\vec{E}_0$  is the so-called weighting field. The same principal can be used to state that the induced charge  $Q$  on the electrode is the product of the charge of the carrier and the difference in the weighting potential  $\varphi_0$  from the beginning to the end of the carrier path:

$$Q = q\Delta\varphi_0 \quad (4.9)$$

The weighting potential is not the actual electric potential in the detector, but allows for determination of the charge on the electrodes induced by the motion of holes and electrons. The drift path of holes and electrons through the detector has still to be determined by the actual electric field lines.

To find the weighting potential  $\varphi_0$  it is necessary to solve the Laplace equation for every detector geometry, with some artificial boundaries: The voltage of the electrode of interest is set to unity while the voltages on all other electrodes is set to zero. If a carrier drifts through the full gradient of the weighting potential, its full charge  $q$  is deposited at the electrode:

$$\Delta Q = q(\varphi_{0,max} - \varphi_{0,min}) = q(1 - 0) = q. \quad (4.10)$$

As described in Section 4.3.3, CdZnTe has a poor mobility-lifetime product for holes. Hence, the hole signal is dependent on the interaction location and often completely lost when the incident ionization took place near the anode. Therefore, techniques are developed to reject the sensitivity of the measured pulse to the hole contribution of the signal. Two of these so-called single polarity charge sensing configurations are coplanar grid (CPG) detectors and pixelated detectors.

### Coplanar Grid CdZnTe Detectors

The working principle of a CPG detector is similar to the Frisch grid in gas detectors [107]. Only the movement of the electrons inside the detector is used to read out the charge information. The design was invented by P. N. Luke [108] and uses two anode strips in the form of closely interleaved combs instead of a planar anode. The two anode strips are electrically isolated from each other. One anode is kept on ground potential and named collecting anode (CA), while the other anode, named the non-collecting anode (NCA), is kept at a fraction of the cathode bias voltage. The voltage between CA and NCA is called grid bias (GB), the voltage between cathode and CA is called high voltage (HV). A diagram and a photograph of CPG detectors used in the COBRA experiment are shown in Figure 4.5. Figure 4.6 shows the calculated weighting potential of this detector type.

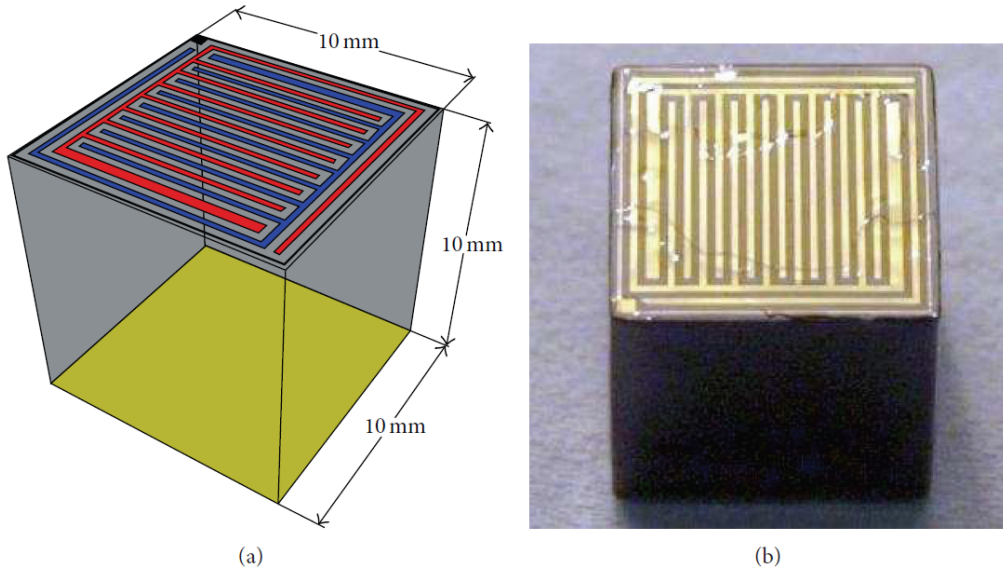


**Figure 4.5:** (a) Diagram of a CPG detector. The anode grid is indicated in blue and red, while the cathode is indicated in yellow. (b) Photograph of a typical CPG detector with a volume of  $1 \text{ cm}^3$ . Taken from [23].

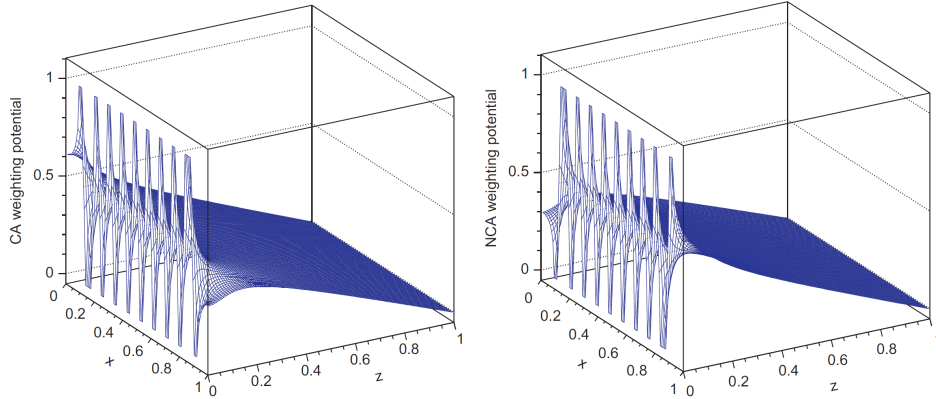


**Figure 4.6:** Diagrams calculated from the electrode geometry for the weighting potentials along a cross section of a CPG detector. The anode grids are on the left side in each figure. The left figure shows the CA weighting potential and the right figure the NCA weighting potential. Taken from [109].

The spacing of the CPG design is chosen such that the weighting potential far from the anodes is linear and a moving electron induces equal charge on both CA and NCA over the majority of its path. At distances in the order of the strip spacing (usually  $\sim 300 \mu\text{m}$ ) the electron induces more charge on the CA and the charge induction on the NCA is reduced. The difference between the two anode signals is proportional to the total charge induced. The equal contribution from the drift through the bulk cancels and therefore the difference signal is independent from the interaction point of the primary ionization. To obtain the deposited energy  $E$  in the detector, a weighting factor  $w$  has to be applied to the difference of the two signal amplitudes  $CA$  and  $NCA$  of the corresponding anodes:

$$E \propto CA - w \cdot NCA. \quad (4.11)$$

The weighting factor is a first order correction for electron trapping and capture.  $w$  has to be determined for every detector separately and depends on the quality of the detector material. Also,  $w$  varies with the HV and GB applied to the detector and can be obtained by optimizing the energy resolution of  $\gamma$ -spectra from calibration sources. To obtain the deposited energy in a CPG detector using Equation 4.11, the readout of both anodes with only one peak-sensing analog to digital converter (ADC) is sufficient. In this case, the subtraction of CA and NCA signals can be carried out by integrated circuits in the readout electronics.

With the recording of the full CA and NCA pulse shape with fast analog to digital converters (FADCs), one can furthermore derive the location of interaction along the electric field lines, the so-called interaction depth  $z$  [110]:

$$z = \frac{CA + NCA}{CA - NCA}. \quad (4.12)$$

A more elaborated formula taking electron trapping and capture in CdZnTe de-

tectors into account was developed within the collaboration [111] and is used in the COBRA analysis software:

$$z = \lambda \cdot \ln \left( 1 + \frac{1}{\lambda} \frac{CA + NCA}{CA - NCA} \right), \quad \lambda = \frac{1 + w}{1 - w}. \quad (4.13)$$

Electron trapping and capture are corrected by the factor  $\lambda$ . Again, the weighting factor  $w$  has to be determined for every detector separately.

Another feature of pulse shape analysis is the discrimination of radiation produced by  $\alpha$ -particles on the lateral surface of CdZnTe detectors due to distortions in the CA and NCA signal [109]. This is important for background reduction, as with Equation 4.13 only the determination of the interaction depth  $z$  is possible. A full 3D information with  $x$ ,  $y$  and  $z$  coordinates can't be obtained with this method. A typical event in a CPG detector recorded with FADCs is shown in Figure 4.7.

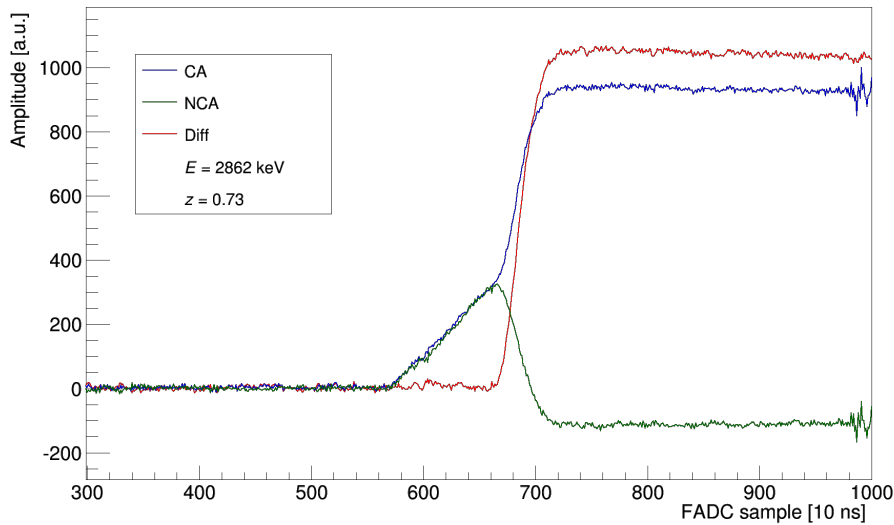


**Figure 4.7:** Pulse shape of a typical 2.8 MeV gamma interaction recorded with two FADCs with a sampling rate of 100 MHz. The CA (blue line) and NCA (green line) are recorded, while the red line depicts the calculated difference pulse between CA and NCA. When the charge carriers drift through the detector bulk between samples 560 and 660, the CA and NCA pulses rise uniformly and the difference pulse is almost zero.

A big advantage of the CPG technology is the fact, that every detector has to be instrumented only with two readout cables to the anodes and one HV cable to the cathode. Hence, the readout electronics can be separated from the detectors. This is important for the operation in a low background environment. On the other hand, the CPG design limits the obtainable energy resolution compared to other techniques like pixelated detectors.

### Pixelated CdZnTe Detectors

Similar to the CPG layout is the principle of a pixelated anode. Here, the anode is segmented into many small contacts, whose signals are read out separately. The working principle is the so-called small pixel effect: Moving electrons in the bulk far away from the anode induce very little charge in many pixels. This is due to the fact that every pixel appears to be roughly the same size from the point of view of the charge carrier. When moving to the proximity of the anode side, the terminal pixel increases in size as  $1/r^2$  and the induced charge on this pixel increases fast. In contrast, the other pixels increase only briefly in size, before shrinking quickly before the electrons impinge the terminal pixel. Very little charge is deposited in these surrounding pixels.

A result of the small pixel effect is that a charge carrier mostly contributes only to the signal of one pixel at the end of its drift path. The weighting potential in pixelated detectors rises sharply, so that even a better energy resolution than in CPG detectors can be achieved. Again, the deposited charge is nearly independent from the interaction depth.

As each electron in a homogeneous electric field drifts straight to the nearest pixel, the topology of a multi-pixel event can be projected as a 2D image. With a small pixel pitch in the order of a few 100  $\mu\text{m}$ , this feature allows for direct particle identification, as a projection on the pixels show significant differences for incident  $\alpha$ -,  $\beta$ - or  $\gamma$ -radiation. The choice between pixel pitch and energy resolution is a compromise: On the one hand, smaller pixel pitches result in tracks with a higher spatial resolution and hence a better particle identification. On the other hand, charge sharing between neighboring pixels limits the achievable energy resolution and therefore bigger pixel pitches are favored. In addition, increased diffusion of moving electrons in the detector bulk at higher drift lengths limits the detector thickness, track resolution and reasonable pixel pitch. Currently, the COBRA collaboration is investigating detector systems with a pixel pitch of 55  $\mu\text{m}$ , 110  $\mu\text{m}$  and 220  $\mu\text{m}$ . The volume of the used CdTe detectors is currently limited to about 0.2  $\text{cm}^3$ . A comprehensive overview can be found in [112]. Modifications to the ASIC<sup>1</sup> of these detector systems allow for obtaining three dimensional trajectories [113].

A disadvantage of pixelated detectors is the complexity and power consumption, as every pixel requires a separate amplification and signal shaping circuit. Therefore, a readout ASIC has to be placed near the detectors, which is undesirable with respect to low background. Furthermore, data analysis and data storage become more difficult compared to CPG detectors.

---

<sup>1</sup> ASIC: Application-Specific Integrated Circuit

## 4.4 COBRA Demonstrator at the LNGS

The COBRA R&D demonstrator is located at the Laboratori Nazionali del Gran Sasso (LNGS) underground laboratory in central Italy. The LNGS laboratory consists of three halls, each about 100 m long and 20 m wide, which are connected by service tunnels. Support facilities like a mechanical workshop, a chemical laboratory and offices are located at an overground area. The laboratory hosted and hosts a variety of notable experiments in the field of astroparticle and nuclear astrophysics which require a low background environment. Other experiments searching for neutrinoless double beta decay located at the LNGS are GERDA and CUORE, see Section 2.6. Since 2011 the COBRA experiment is placed in the hut of the former Heidelberg-Moscow Double Beta Decay Experiment.

Located under 1400 m of dolomite rock, the LNGS laboratory has an overburden equivalent to about 3800 mwe (meter water equivalent). Compared to the surface, the muon flux is reduced by about six orders of magnitude and the neutron flux is reduced by three orders of magnitude. With a comparatively low content of Uranium and Thorium in the Gran Sasso mountain, the LNGS offers very good conditions for low background experiments. An artistic scheme of the COBRA demonstrator at the LNGS is shown in Figure 4.8.

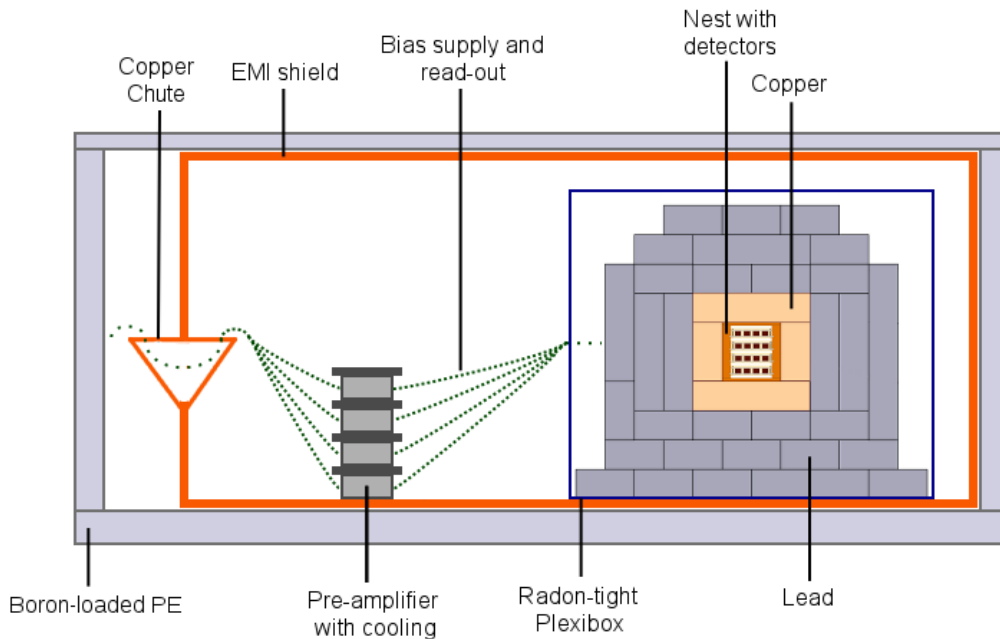


**Figure 4.8:** Artistic scheme of the COBRA demonstrator at the LNGS. Taken from [86].

### 4.4.1 Detector Build-up

The current demonstrator array consists of 64 CPG detectors, each measures about  $1 \times 1 \times 1 \text{ cm}^3$  and has a mass of about 5.8 g. They are arranged in four layers

with 16 detectors each. The holder structure for the layers consists of thermoplastic polyoxymethylene (POM) which is produced by DuPont with the trade name Delrin. Delrin was chosen because it is radiopure and little material is needed to construct the holders. The four detector holders are inserted into a carrier made of copper, the so-called copper nest. The dimensions of the nest are  $150 \times 150 \times 150 \text{ mm}^3$ .

The anodes of the CPG detectors are read out with cables embedded in a polymer film, called Kapton cables. Kapton is Polyimide film produced by DuPont. The high density of signal traces in Kapton cables allows for the readout of all 32 anodes in one layer while still having proper access to the detectors. The solder pads of the Kapton cables are connected with gold wires and LS200 conductive lacquer to the CPG anodes.

For distribution of the high voltage, RG178 coaxial cables are used in the current set-up. These cables are also connected via gold wire and LS200 lacquer to the cathode side of the detectors.

#### 4.4.2 Radiation Shield

The shield around the detector build-up essentially consists of three layers: a neutron shield made of borated Polyethylene (PE) followed by a lead castle and an inner layer of copper against  $\gamma$ -radiation.

##### Neutron Shield

A shield against neutrons is very important due to the large cross section of thermal neutron capture in  $^{113}\text{Cd}$ , see Section 4.2.2. The outermost part of the radiation shield therefore consists of 7 cm Polyethylene doped with  $^{10}\text{B}$ . The high content of Hydrogen in PE moderates neutrons to lower energies.  $^{10}\text{B}$  has a very high cross section for  $^{10}\text{B}(n,\alpha)^7\text{Li}$  capture reaction. After capturing the thermal neutron, the  $\alpha$  decay from  $^{11}\text{B}$  can go to the ground state or first excited state of  $^7\text{Li}$  [89]. In the latter case a  $\gamma$ -particle with 477.6 keV is released, which is not able to penetrate through the inside lead castle. The  $\alpha$ -particle is instantly stopped in the PE.

As muons have a high cross section for the production of neutrons in lead, the neutron shield has to be the inner part when the detectors are operated at locations with small overburden or at the surface. As the muon flux in the LNGS laboratory is reduced by about six orders of magnitude compared to the surface, the COBRA demonstrator has the neutron shield as the outermost part.

##### Lead Castle

Although the Q-value of the decay of  $^{116}\text{Cd}$  is above the highest significant  $\gamma$ -line of  $^{208}\text{Tl}$  from the Thorium decay chain, a good shield is desirable to investigate physics processes beneath 2.6 MeV. Furthermore, the  $\beta$  decay of  $^{214}\text{Bi}$  from the



Uranium decay chain produces  $\gamma$ -lines up to 3.27 MeV. Although these lines have a small probability, eight lines occur in the region between 2.7 MeV and 2.9 MeV, being roughly the ROI of COBRA. They can become a serious background source for a large-scale experiment. Due to its high density and high nuclear charge, lead has a high attenuation coefficient for  $\gamma$ -radiation.

The central part of the radiation shield consists of a  $60 \times 60 \times 60 \text{ cm}^3$  lead castle providing at minimum 20 cm of lead in every direction. The castle is build with lead layers of different grades of radiopurity, the innermost layer consists of 5 cm high-purity lead with a  $^{210}\text{Pb}$  activity  $< 3 \text{ Bq/kg}$ .  $^{210}\text{Pb}$  is part of the Uranium decay chain and can practically not be separated from the lead ore. Therefore, radiopure lead is very expensive, as it has to be ancient lead or from a mine with very low Uranium contamination.

### Copper Shield

The innermost part of the radiation shield consists of a 5 cm copper layer. It shields the detectors from radiation leaving the lead, especially intrinsic and muon-induced  $\gamma$ -radiation. Compared to lead, copper has a lower attenuation coefficient for  $\gamma$ -radiation, a higher cross section for neutron capture and a higher production rate of radionuclides by cosmic ray activation. For experiments in underground laboratories with a high overburden, the activation is insignificant. But the long-living cosmogenic isotopes produced at the surface during storage have to be considered.

On the other hand, copper can be produced with high purity [101] and is easier to machine than lead. This makes copper the preferential material for the innermost part of the COBRA radiation shield.

### Nitrogen Flushing

As explained in Section 4.2.1, all natural decay chains have intermediate Radon progenies, which can diffuse out of building materials and rock. The activity from Radon depends on the Uranium and Thorium content in the surroundings, but it is normally in the order of  $\sim 10 \text{ Bq/m}^3$  [101].  $^{220}\text{Rn}$  from the Thorium chain has a short half-life of 55.6 s compared to  $^{222}\text{Rn}$  from the Radium series with a half-life of 3.8 days and therefore the effect from  $^{220}\text{Rn}$  on the background is comparatively small. In addition,  $^{222}\text{Rn}$  has a long-living progeny,  $^{210}\text{Pb}$ , which can hardly be removed when stuck to the detector's or holder's surface.

To prevent Radon from diffusing into the set-up, the lead castle is surrounded by a Polycarbonate (PC) box. This box is antistatic coated and sealed with rubber foam. The feedthroughs for readout and HV cables as well as for Teflon tubes to insert calibration sources are constructed such that exchange of air is minimized.

Furthermore, the COBRA demonstrator is constantly flushed with gaseous Nitrogen. The Nitrogen is evaporated from liquid Nitrogen in a dewar outside the COBRA hut. It is then filtered with a charcoal filter and guided through Teflon

tubes into the set-up. The Nitrogen evaporation rate is manageable through a heating device in the bottom of the dewar. The evaporation system is permanently monitored to ensure a constant flushing of the detectors with Nitrogen.

#### 4.4.3 EMI Shield

A shield against electromagnetic interference (EMI) is needed for the COBRA demonstrator, as the preamplifiers are very sensitive. Electromagnetic disturbances can mimic physics events or introduce disturbing noise especially on the unshielded cables from the detectors to the preamplifiers and inside the preamplifiers themselves. An EMI shield made of steel plates encloses the detector array and the preamplifier boxes to suppress these disturbances [114]. To run the cables outside the EMI, a copper chute is implemented. All cables are uninsulated fed through a bath of copper to define a common electrical ground for all components of the set-up.

#### 4.4.4 Readout Electronics

For low background experiments it is desirable to separate the electronics from the detectors. Therefore the preamplifiers are located outside the radiation shield but close to the Polycarbonate box to shorten cable lengths. The charge sensitive preamplifier modules currently used in COBRA are CR-110 preamplifiers from Cremat. For the COBRA demonstrator, preamplifier boxes housing a printed circuit board (PCB) for 32 of these modules are used. As every detector needs two preamplifier channels for CA and NCA, one preamplifier box is needed for every detector layer and in total four are in operation. Grid bias and high voltage are also distributed by the preamplifier boxes, but have to be supplied externally.

The signals from the preamplifiers are transferred outwards the EMI and neutron shield using differential signalling on CAT6 cables. This allows for long distances in the order of 25 m between the preamplifiers and linear amplifiers without introducing perturbing noise. The differential linear amplifiers are used to convert the detector signals into single ended (SE) signals and adjust the amplification to the input range of the analog to digital converters. The linear amplifiers can magnify the detector signals by a factor of 0.5 up to  $\sim 90$ . Preamplifier boxes and linear amplifiers were designed and constructed by the TU Dortmund, a comprehensive summary is given in [115].

The detector signals are finally recorded by Struck SIS 3300 FADCs, previously used in the AMANDA experiment. FADCs allow for the recording of the whole pulse shape of both CA and NCA, and not only for the absolute signal amplitude like in peak sensing ADCs. This is valuable for the rejection of electromagnetic disturbances and background from physics events via pulse shape analysis as explained in Section 4.3.4. Furthermore, the weighting factor  $w$  does not have to be applied manually in the readout chain before data-taking, but can be determined

in the post-processing of the data. This digital processing of detector signals improves the achievable energy resolution. A comprehensive overview of the design and implementation of the data acquisition (DAQ) is given in [116].

#### 4.4.5 Preamplifier Cooling Unit

As the preamplifiers produce a great amount of heat and the 7 cm thick PE shield acts as a thermal insulation, thermal noise is induced in the readout electronics and the achievable energy resolution of the CdZnTe detectors is reduced. Therefore, an active cooling system was designed and installed in the course of this work. This system consists of a Julabo FL 601 recirculating water cooler, which is placed outside the COBRA hut and controlled remotely via RS232. Depending on the desired temperature, the Julabo FL 601 offers a refrigeration capacity from 0.2 kW at  $-20^{\circ}\text{C}$  to 0.6 kW at  $20^{\circ}\text{C}$ . Up to 8 l of coolant can be pumped with a flow rate of  $231\text{m}^{-1}$  at 1 bar [117].

The cooled water is pumped into the set-up through the copper chute via insulated flexible tubes. A distribution unit partitions the flow into equal parts on four cooling plates made of aluminum, see Figure 4.9. The preamplifier boxes and cooling plates are alternately stacked into a tower, with a cooling plate being the top. A fifth connection at the distribution unit is available but not yet used, e.g. for the installation of a cooling plate for the lead castle.

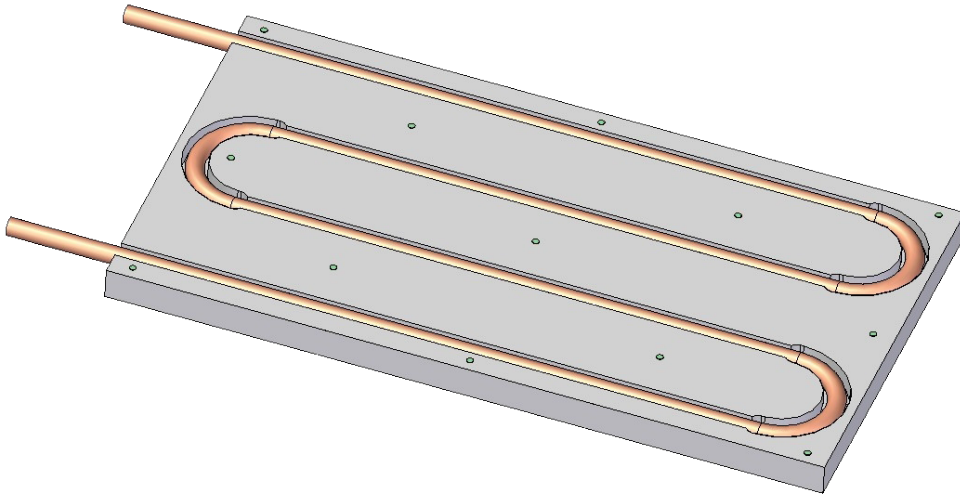


**Figure 4.9:** Cooling plate designed and manufactured at the Universität Hamburg. The plate with dimension  $(330 \times 180 \times 15)$  mm consists of aluminum. The cover plate not shown in this figure is attached with 13 screws to the cooling plate. The inner pipe consists of copper with 8 mm diameter.

The cooling of CdZnTe detectors to moderate temperatures of about  $5^{\circ}\text{C}$  mostly improves the low energy threshold and the resolution of low energy  $\gamma$ -lines

[104]. Especially the investigation of  $^{113}\text{Cd}$   $\beta$  decay into  $^{113}\text{In}$ , see Section 4.4.6, will profit from the installation of the cooling unit at the demonstrator set-up.

#### 4.4.6 Current Status

Since November 2013 the COBRA demonstrator is equipped with 64 detectors in four layers. An exposure rate of approximately 2.6 kg·d per layer and month is collected, leading to a total exposure of about 1 kg·a at the end of 2015. The data shown in this section was recorded from 2011 to 2014 and contains the complete dataset of all four installed layers. The accumulated exposure is 223.28 kg·d, see Table 4.4.

**Table 4.4:** Accumulated exposure recorded at the COBRA demonstrator from September 2011 to December 2014.

Year	Exposure [kg·d]
2011	7.03
2012	50.89
2013	64.14
2014	101.22
$\Sigma$	223.28

The LNGS 2011 to 2014 data is shown in Figure 4.10 as a 2D plot with the interaction depth  $z$  on the y-axis and the energy  $E$  on the x-axis. In this so-called  $z$ - $E$ -plot, the logarithmic color coded scale on the right indicates the number of entries per bin. Per definition, the anodes are at  $z = 0$  and the cathode is at  $z = 1$ . Unphysical events are suppressed with the `flag_bad_pulse` cut applied to the dataset, see Section 5.4.1.

In Figure 4.10, accumulations of energy depositions are identifiable, contributing with a substantial number to the LNGS background spectrum. Due to the low background environment of the COBRA demonstrator compared to laboratories at the surface, these background contributions are not observable in measurements presented in Section 6.5.

Energy depositions independent from the interaction depth are visible as vertical lines in Figure 4.10. The low-energy range up to 300 keV is dominated by the decay of  $^{113}\text{Cd}$  into  $^{113}\text{In}$ .  $^{113}\text{Cd}$  has a natural abundance of 12.2 % and its  $\beta$  decay with a half-life of  $7.7 \cdot 10^{15}$  years has a Q-value of 316 keV. Also, two  $\gamma$ -lines are slightly visible: At 511 keV from annihilation and at 1460.8 keV from electron capture of  $^{40}\text{K}$  into  $^{40}\text{Ar}$ .

Figure 4.10 also shows horizontal features from energy depositions at certain interaction depths. At the cathode ( $z = 1$ ) two regions with higher statistics are

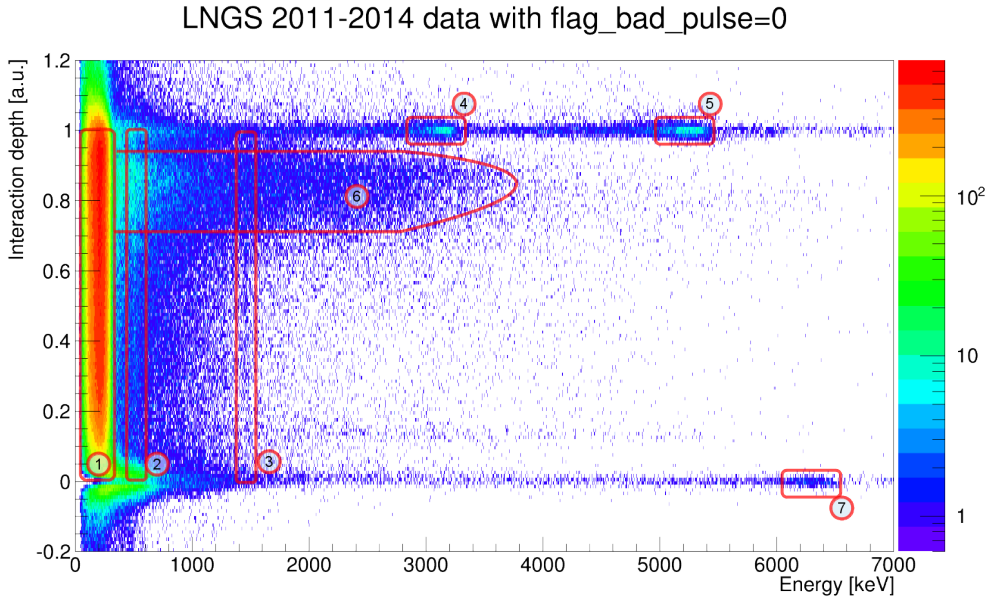


**Figure 4.10:**  $z$ - $E$ -plot for the 2011 to 2014 LNGS dataset with the `flag_bad_pulse` cut applied to suppress unphysical events. The numbered background sources are explained in more details in the text: 1)  $\beta$  decay of  $^{113}\text{Cd}$ , 2)  $\gamma$ -line from annihilation, 3)  $\gamma$ -line from  $^{40}\text{K}$  EC, 4) + 7)  $\alpha$  decay of  $^{190}\text{Pt}$ , 5)  $\alpha$  decay of  $^{210}\text{Po}$ , 6) hump region most likely due to Radon progenies on the Delrin holder structure.

observable. The first originates from the  $\alpha$  decay of  $^{190}\text{Pt}$  into  $^{186}\text{Os}$  with a  $Q$ -value of 3249 keV. Platinum is part of the cathode material and although  $^{190}\text{Pt}$  has a natural abundance of only 0.01 % and its half-life is  $6.5 \cdot 10^{11}$  years, this decay is clearly visible in the  $z$ - $E$ -plot. The second region with higher statistics originates from the  $\alpha$  decay of  $^{210}\text{Po}$  into  $^{206}\text{Pb}$ . The  $^{210}\text{Po}$  contamination could be due to a contamination with Radon, as it is part of the Uranium decay chain, see Section 4.2.1 and Appendix A. The intermediate grandmother nuclide  $^{210}\text{Pb}$  has a half-life of 22.3 years and settles down on surfaces, especially if they are statically charged.

In the region of  $0.8 < z < 1$  a broad hump with energies up to roughly 4 MeV is observable. This hump is not fully understood yet, but could be due to the Radon progenies  $^{210}\text{Bi}$  and  $^{210}\text{Po}$  deposited on the Delrin support structure.

At the anodes reconstruction distortions appear. When energy is deposited near to the anodes, created holes can be absorbed at the NCA instead of drifting to the cathode. As the calculated energy is doubled in this case, the corresponding peak from the  $\alpha$  decay of  $^{190}\text{Pt}$  is observable at energies up to 6.5 MeV. To account for this effect, the region with  $z < 0.2$  has to be omitted in the search of neutrinoless double beta decay.

## 4.5 Toward a Large Scale COBRA Experiment

To develop a strategy for a large scale experiment with a background rate in the order of  $10^{-3}$  counts/keV/kg/a and a  $^{116}\text{Cd}$  half-life sensitivity of at least  $2 \cdot 10^{26}$  years, the COBRA collaboration is investigating the operation of larger CdZnTe detectors. Detectors with a size of  $2.0 \times 2.0 \times 1.5 \text{ cm}^3$  and a weight of approximately 36 g are commercially available. These detectors offer a better surface-to-volume ratio and a higher detection efficiency compared to the  $1 \text{ cm}^3$  detectors in the current demonstrator at the LNGS. Currently the operation of the  $6 \text{ cm}^3$  detectors with a quad-CPG readout (see Figure 4.11) is favored, as multisite events are expected to be more efficiently detected.

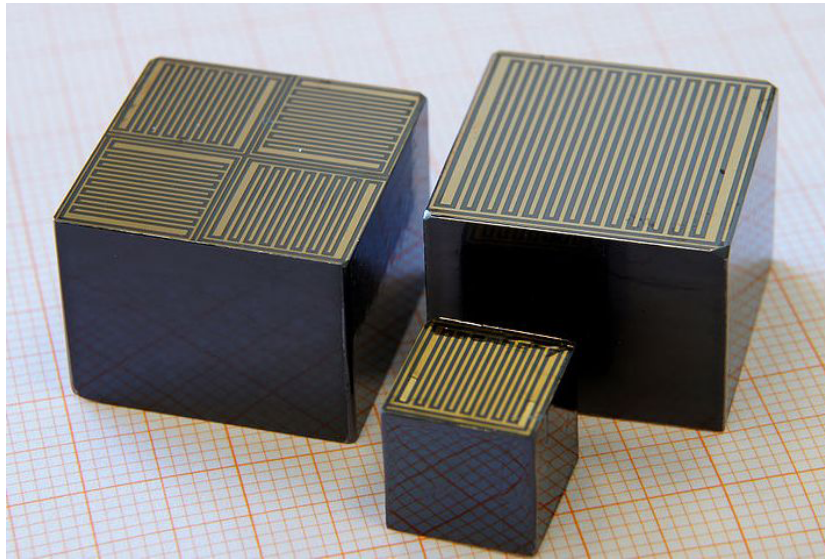


**Figure 4.11:** Photograph of the  $6 \text{ cm}^3$  detectors in comparison to a  $1 \text{ cm}^3$  detector. The quad-CPG layout of the upper left detector is currently preferred for a large scale set-up.

Instead of the current  $4 \times 4$  layer, the basic unit for a large scale experiment is planned as a module with  $3 \times 3$  detectors. Eight detector modules will be placed on a module carrier and eight module carriers next to each other form a detector layer, see Figure 4.12. With 20 layers and 11520 detectors in total, a mass of 414.7 kg is obtained. Instead of FADCs, the detector readout will be performed with a highly integrated DAQ using ASICs and FPGAs<sup>2</sup>. The construction of a basic module prototype with nine detectors and ASIC/FPGA readout system is underway and first tests are performed. A shield for the large scale COBRA set-up has already been designed [86].

To reach the desired background rate of  $10^{-3}$  counts/keV/kg/a, a substantial fraction of background events in the current demonstrator set-up, see Section 4.4.6, has to be suppressed. Especially the number of  $\alpha$ -particles in the lacquer and on the

<sup>2</sup>FPGA: Field Programmable Gate Array

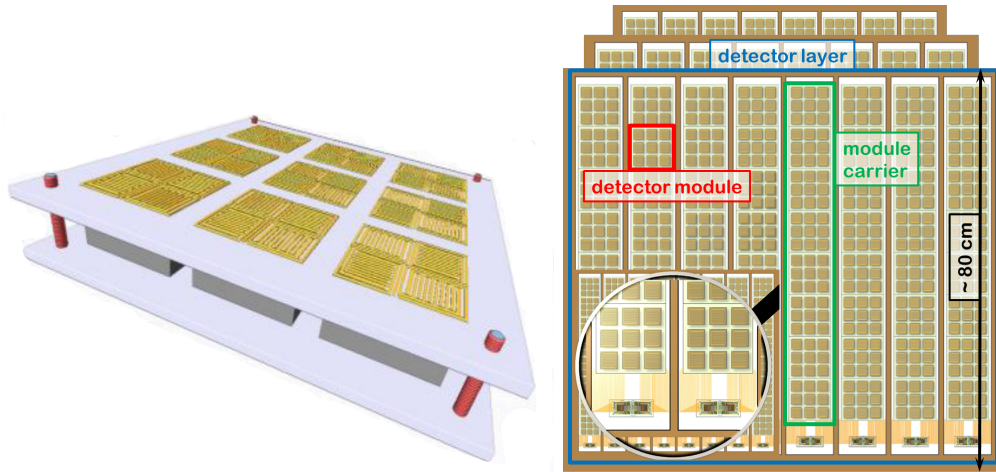


**Figure 4.12:** Artistic scheme of a detector module housing nine quad-CPG detectors of  $6\text{ cm}^3$  size (left) and principal layout for the intended detector build-up of a large scale experiment (right).

Delrin holders has to be reduced [86]. The operation of CdZnTe detectors without lacquer in a high purity liquid scintillator environment can efficiently minimize or veto the contribution of  $\alpha$ -emitters in the proximity to the detectors. In addition, the attenuation and capture of neutrons entering the set-up is possible with liquid scintillator, leading to a further background reduction. The principal suitability of liquid scintillator as an environment for the operation of CdZnTe detectors is demonstrated in the Chapters 5 and 6.

However, for the application of liquid scintillator as surrounding environment for the CdZnTe detectors, tests exceeding the work in this thesis have to be performed. Especially, the durability of recently considered components like ASICs and FPGAs is important. Also, a concept for the collection of scintillation light inside an array of about 10000 detectors has to be developed. Here the application of wavelength-shifting fiber optics could be reasonable. Possible read-out devices are for example multichannel PMTs like in the target tracker of the OPERA experiment [118] or avalanche photo diodes like in the NOvA experiment [75]. Currently, the application of liquid scintillator is not considered in the plans for a large scale set-up, making modifications in the holder structure and the shield design necessary.

As already explained in Section 4.4.5, the energy resolution and the low energy threshold of CdZnTe detectors can be improved with a moderate cooling to roughly  $5^\circ\text{C}$ . With a circulation system, the liquid scintillator could be used as a coolant for a large scale set-up. By removing the heat produced by the ASICs, the CdZnTe detectors could be operated in a very stable environment. For the application of liquid scintillator, also a liquid handling and purification system has to be developed.





## Chapter 5

# Design, Construction and Simulation of the Set-Up

To test the behavior and operation of CdZnTe semiconductor detectors in liquid scintillator, a test set-up was designed and assembled at the Universität Hamburg. The design has to meet several requirements:

- The set-up has to be lightproof and liquid-tight
- All materials have to be insensitive to solvents
- The operation of one to eight detectors must be possible
- Two photomultiplier tubes are needed to read out the scintillation light
- A read-out chain similar to the COBRA demonstrator at LNGS is desirable
- A liquid handling system is needed to exchange the liquid scintillator

Design, construction and commissioning of the test set-up took place in several steps, mostly to implement the gained experience and to improve the set-up. The most challenging parts were the cable feedthroughs for the high voltage and the read-out cables. Next to the litz wire, also the shield of the cables has to be impermeable to the liquid scintillator. In the course of the designing phase of the set-up, many materials were tested with respect to their stability and performance in liquid scintillator. Finally, to better understand the measurements presented in Chapter 6, a Monte Carlo simulation was set up.

During design and construction, the CdZnTe detectors were stored without lacquer for approximately three years in the scintillator. The successful operation of these detectors in the measurement period presented in Chapter 6 shows the applicability of liquid scintillator for a long-term experiment.

## 5.1 Material Compatibility Tests

The material compatibility tests were performed in two stages: In a first stage, the samples were immersed for about three months in liquid scintillator to rule out incompatibilities and to start the construction of the mechanical components. However, a period of three months is not sufficient to decide whether a specific material is usable in a large scale and long term experiment. Therefore, the compatibility tests were re-evaluated after 66 months.

Test tubes or small flasks were used to immerse the materials in liquid scintillator. The remaining air in the test tubes or flasks was blown out with nitrogen to prevent oxidation of the scintillator. The samples were locked and stored under a fume hood at room temperature. To accelerate the aging and the chemical reactions of the materials with liquid scintillator, higher temperatures are desirable for further tests.

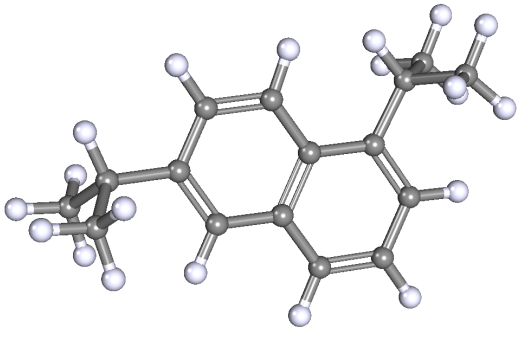
### 5.1.1 Choice of Liquid Scintillators

Two liquid scintillator mixtures were tested with respect to material compatibility. LAB was chosen, as it is relatively safe, cheap and nonhazardous (see Section 3.1.3). Therefore, it is very popular among current liquid scintillator experiments. To also test solutes with respect to material compatibility, 10 g/l PPO and 40 mg/l bis-MSB were added to the LAB.

Due to the small risks of health hazard, liquid handling of LAB should be carried out under an air exhaust. To avoid operation of the test set-up under an air exhaust in the construction phase, the liquid scintillator OptiScint HiSafe produced by PerkinElmer [119] was chosen for first leakage tests and tests of the PMTs. The performance of OptiScint HiSafe was so convincing, that it was used to obtain all results from the test set-up in the course of this work. It has an excellent HMIS rating of 0 with respect to health hazard. Hence, standard safety equipment like protection goggles and gloves is sufficient for the handling of the scintillator.

PerkinElmer describes OptiScint HiSafe as DIN-based liquid scintillator with the CAS number 38640-62-9. DIN stands for Diisopropylnaphthalene and the CAS number covers all ten structural isomers. Hence, the precise composition of the scintillator is unknown. Two of the isomers, namely 1,3- and 2,6-Diisopropylnaphthalene, are solid at room temperature, the remaining eight, namely 1,2-, 1,4-, 1,5-, 1,6-, 1,7-, 1,8-, 2,3-, and 2,7-Diisopropylnaphthalene, are liquid at room temperature. The liquid mixture of the DIN isomers is colorless, nonodorous and has a flash point well above 100 °C. Chemical and physical properties are summarized in Table 5.1.

**Table 5.1:** Chemical and physical properties of OptiScint HiSafe. The picture shows the isomer 1,6-Diisopropylnaphthalene (CAS 51113-41-8). Values taken from the Material Safety Data Sheet.

	
Name	Diisopropylnaphthalene
Short name	DIN
Product name	OptiScint HiSafe
Formula	$C_{16}H_{20}$
CAS	38640-62-9
Density	0.96 kg/l
Flash point	140 °C
HMIS Rating	
Health hazard	0
Flammability	1
Physical hazard	0

### 5.1.2 Choice of Materials

As all liquid scintillators are based on benzene compounds, liquid scintillator in general is a solvent. Where possible, stainless steel is used as material for the set-up, as it is solvent-resistant. The most crucial parts of the set-up with respect to solubility are sealing materials like O-rings. But also materials for the detector holder, cable feedthroughs and flexible tubes have to be tested, as well as HV cables and insulated and bare optical fibers. Finally, suitable adhesives including silver conductive glue have to be found for the operation in liquid scintillator.

Materials considered for O-Rings are Fluoroelastomers (FKM), Polytetrafluoroethylene (PTFE) and Polymerized Siloxane (Silicone). For the detector holder structure Polyoxymethylene (POM) is of special interest, as it is also used in the COBRA demonstrator. Furthermore, Polymethyl Methacrylate (PMMA) and Polyimide fibers are tested.

For the CPG detectors in COBRA, the combed-shaped anodes and the cathode

are connected with the readout and HV cables by using silver conduction glue [116]. This glue only provides the electrical connection, but no mechanical support. Hence, three additional glues are tested: 'Der Alleskleber' and 'Hart' produced by UHU as well as the instant adhesive Superglue 15 produced by Wiko.

For the anode readout and the HV supply, miniature cables of type SM 50 were tested. They are described in Section 5.2.2.

### 5.1.3 Results

The samples were evaluated only qualitatively and not quantitatively. Qualitative criteria for the applicability of a specific material were:

- discoloration and swelling of the sample
- elasticity, flexibility and tensile strength of the sample
- solubility of the sample in liquid scintillator
- discoloration and turbidity of the liquid scintillator

The results for both scintillators, OptiScint HiSafe and the LAB mixture, are identical and no deviation was found. A compilation of the outcome is given in Table 5.2.

After three months of immersion, no discoloration or turbidity of the liquid scintillator was found for the FKM O-rings. Hence, this material was chosen for the sealing rings, as it is more elastic than PTFE. However, after 66 months a slight discoloration is visible in both scintillators, but the FKM rings do not lose their elasticity or flexibility. This observation agrees with [85].

Silicone seems to lose elasticity and flexibility even after a short period in liquid scintillator. However, no discoloration or turbidity is observable even after 66 months.

For PTFE no discoloration or turbidity of the liquid scintillator is visible after 66 months of immersion. Therefore, PTFE was chosen as material for flexible tubes. O-rings made of or coated with PTFE are the favorite choice for a long-term experiment.

For the adhesives, only UHU 'Der Alleskleber' gets soft and brittle after immersion in liquid scintillator. UHU 'Hart' and Superglue 15 stay solid. Also the silver conduction glue is not soluble, as shown in Figure 5.1.

To construct the detector holder structure, all investigated materials are usable. For POM, PMMA and Polymide fibers the liquid scintillators show no discoloration. Also the SM 50 cables show no degradation and are suitable for anode readout and HV supply. Finally, bare optical fibers endure the immersion as well. Only the insulator of the optical fibers is soluble and should not be plunged in liquid scintillator.

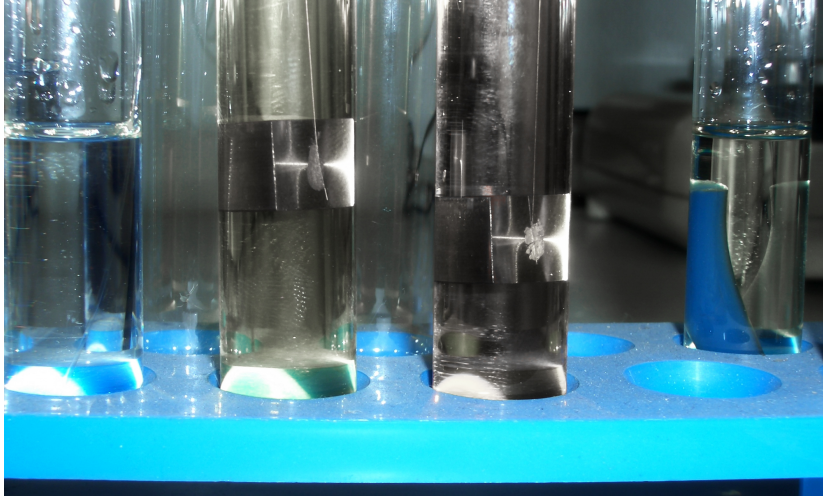


**Figure 5.1:** The solubility of silver conduction glue was investigated with  $1\text{ cm}^3$  brass cubes bonded to a  $45\text{ }\mu\text{m}$  diameter gold-plated tungsten wire. After 66 months of immersion in OptiScint HiSafe (right) or the LAB mixture (left) the cubes are still attached to the wires and the silver conduction glue is not dissolved.

## 5.2 Design of Mechanical Components

To fulfill the criteria mentioned in the introduction of this chapter, most parts of the mechanical components consist of stainless steel, namely the operation and storage vessels and parts of the connector system. For sealings and O-rings, FKM is chosen, in particular Viton produced by DuPont. For a long-term experiment, PTFE O-rings are favored. All flexible tubes are made of PTFE, namely Teflon produced by DuPont. In addition, Polyimide fibers, so called Nylon fibers made by DuPont, and POM, namely Delrin produced by DuPont, are used for the detector holder.

Prior to the production, all mechanical components were designed using the CAD (computer-aided design) program Solid Edge developed by Siemens PLM. An overview of the set-up is shown in Figure 5.2. The main parts are described in detail in the following sections and the belonging CAD drawings can be found in Appendix D.

### 5.2.1 Operation Vessel

The tank housing the CdZnTe detectors during operation in liquid scintillator is called the operation vessel. It is a cylindrical tube made of stainless steel with a wall thickness of 2 mm. The inner diameter is 110 mm and the height is 120 mm, resulting in a volume of 1.14 l.

Both ends of the vessel are closed by flanges and tightened with six screws. The flanges are also made of stainless steel and are sealed against the vessel with FKM O-rings of 125 mm diameter. Both flanges have a bore of 51 mm diameter

**Table 5.2:** Compilation of results from material compatibility tests performed for the test set-up at the Universität Hamburg. All materials were immersed in a LAB/PPO/bis-MSB scintillator mixture as well as in OptiScint HiSafe produced by PerkinElmer. Short-term stability refers to a period of months, while long-term refers to a period of years of immersion in liquid scintillator.

Material	Short Name	Stability	
		short-term	long-term
O-rings:			
Fluoroelastomers	FKM	✓	×
Polytetrafluoroethylene	PTFE	✓	✓
Polymerized Siloxane	Silicone	×	×
Holder:			
Polymide fibers		✓	✓
Polyoxymethylene	POM	✓	✓
Polymethyl methacrylate	PMMA	✓	✓
Adhesives:			
UHU 'Der Alleskleber'		×	×
UHU 'Hart'		✓	✓
Instant adhesive	Superglue 15	✓	✓
Silver conduction glue	LS200	✓	✓
Misc.:			
HV cable	SM 50	✓	✓
Optical fiber		✓	✓
Insulated optical fiber		×	×

in their center to insert the PMTs into the operation vessel. CAD drawings of the upper flange are shown in Figure D.4 in Appendix D.

To control the liquid level inside the vessel, a transparent PTFE tube is installed parallel to the vessel. The tube is connected to a delivery pipe at the lower flange and a U-shaped pipe at the upper flange. Both pipes are made of stainless steel. During filling and emptying the operation vessel with liquid scintillator, the liquid level is observable through the PTFE tube. During operation of PMTs this tube is masked with a black foil to prevent light coming inside the vessel. Detailed CAD drawings of the operation vessel are shown in Figure D.5 in Appendix D.

To increase the amount of photons detected by the PMTs, VM2000 reflector foil produced by 3M is used to cover the inside of the operation vessel. This foil has a reflectivity of 98.5% for optical photons and additionally shifts photons from the ultraviolet range into the optical range [120].

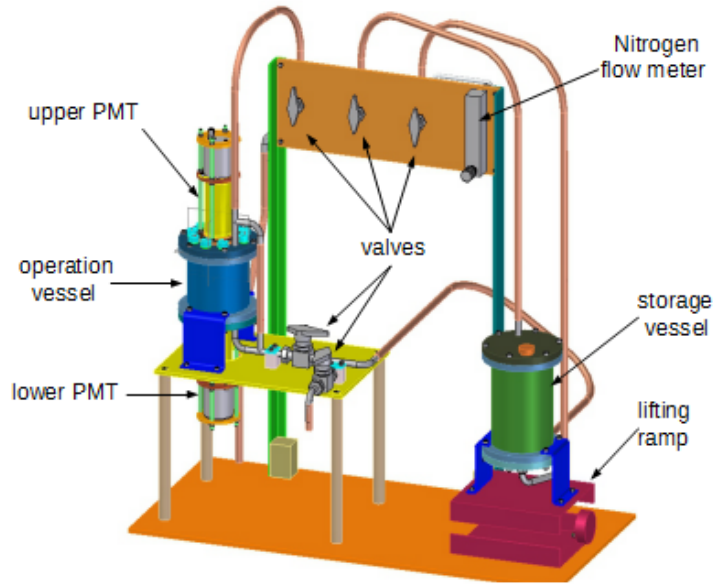


**Figure 5.2:** Overview of the set-up. The mechanical components were designed with the CAD program Solid Edge.

### 5.2.2 Cable Feedthroughs

The most crucial part of the operation vessel is the sealing of the SM50 readout cables produced by Habia and the construction of satisfactory cable feedthroughs. The miniature SM50 coaxial cables have 1 mm outer diameter and an impedance of  $50\ \Omega$ . The dielectric is made of PTFE and the sheath consists of Fluorinated Ethylene Propylene (FEP). Only the inner conductor (litz wire) with 0.16 mm diameter is used to connect the detectors to the preamplifiers. The outer conductor is only connected to the preamplifiers shield, but not connected to the detectors or the detector holder. In total, three different versions of the feedthroughs were constructed and tested.

In version 1, the readout cables were directly guided through the upper flange and sealed with small O-rings of 4 mm outer and 1.1 mm inner diameter. The O-rings were pressed with a pressure plate in orthogonal direction against the cables to ensure an appropriate sealing. This version had two drawbacks: Firstly, with this technique the number of feedthroughs was limited due to finite space on the upper flange. Secondly, a sealing with adhesive between inner conductor and isolation was not successful and the liquid scintillator crawled inside the cables into the preamplifier box.

In version 2, the feedthroughs were completely redesigned and a new upper

flange with nine boreholes of 12 mm diameter was produced. In every bore a PTFE plug was pressed, containing three small boreholes for pin contacts. Every plug contained two pins for the CA and NCA readout and one pin for the high voltage supply. The plugs were designed such that an interchange between readout and HV pins was not easily possible. However, the HV pin and the anode readout were very close and a leakage current occurred.

To better isolate the HV supply, new PTFE plugs were designed for version 3. They have the same diameter like version 2, so that no new flange had to be produced. The new plugs are separated for anode readout and high voltage, containing two and one pin, respectively. Eight plugs are sufficient for four detectors, the ninth plug is spare. The plugs have a sinking on the outer side for better isolation and a solid coupling to the attached cables. On the inner side the plugs have a shroud to prevent leakage currents between the pins and the vessel.

CAD drawings of all three versions are shown in Figures D.1, D.2 and D.3 in the Appendix.

### 5.2.3 PMT Support Structure

Both flanges of the operation vessel have a 52 mm diameter bore in their center for insertion of the PMTs, see Section 5.2.1. The PMTs used in the test set-up have a length of 126 mm and a diameter of 51 mm and are described in more detail in Section 5.5.

To prevent the liquid scintillator leaking from the operation vessel, the PMTs are sealed with FKM O-rings of 61 mm outer diameter. As the glass housing of the PMTs is very fracturable, the O-rings are not pressed in orthogonal direction against the PMTs. Instead, O-shaped stainless steel rings press the O-rings in parallel direction against the flanges.

To hold the PMTs in place, four thread bars are screwed into the flanges next to the PMT bores. The PMT bases are fixed with screw nuts to the thread bars, ensuring a stable attachment of the PMTs. This mounting has the big advantage that the penetration depth of the PMTs into the operation vessel can be steplessly adjusted. CAD drawings of the PMT support structure are shown in Figure D.4 and D.5 in Appendix D.

### 5.2.4 Storage Vessel and Liquid Handling

To store the liquid scintillator, a second vessel made of stainless steel is used. It has the same diameter and similar flanges like the operation vessel, but a height of 180 mm and thus a volume of 1.71 l. Storage and operation vessel are attached side by side on a steel plate.

To pump the liquid scintillator to the operation vessel and back, the storage vessel is mounted on a lifting ramp. Both vessels are connected via a flexible



PTFE tube. By lifting up the storage vessel, the liquid scintillator flows into the operation vessel. A valve prevents unintentional pumping of the scintillator.

To purify the scintillator, a gas system for flushing with gaseous Nitrogen is attached to the storage vessel. The Nitrogen is used to replace Oxygen from the set-up and prevent the scintillator from oxidation. During liquid handling, a constant Nitrogen flux is applied to prevent intrusion of air into the vessels. The flux is adjustable via a flow meter. A shower head installed at the lower flange generates small Nitrogen bubbles for flushing out Oxygen. A CAD drawing of the storage vessel is shown in Figure D.6 in Appendix D.

### 5.2.5 Detector Holder

The detector holder consists of four stainless steel thread bars, similar to the PMT support structure, and two O-shaped stainless steel rings. The O-shaped rings have an inner diameter of 70 mm, an outer diameter of 100 mm and are 2 mm thick. They have four equidistant bore holes, where the thread bars are fixed each with two screw nuts.

The detectors are mounted on a Delrin plate, which is clipped into the four thread bars in the center of the holder structure. Delrin is chosen here, as it is also used at the COBRA demonstrator at the LNGS laboratory (see Section 4.4.1). The CdZnTe detectors are glued with the adhesive UHU 'Hart' to the Delrin plate, which also offers cut-outs to connect high voltage and read-out wires. This construction allows for the replacement of different Delrin plates and the flexible installation of one, four or eight detectors. A photograph of the detector holder with four installed detectors connected to the feedthroughs of the upper flange is shown in Figure 5.3.

Two different Delrin plates were used during commissioning and operation of this set-up, both designed and produced at the TU Dortmund. The first plate was designed for a single CdZnTe detectors, while the second plate can carry four detectors.

The detector holder is placed into four bores at the lower flange of the operation vessel. These bores ensure a fixed position at the center of the vessel with the Delrin plate exactly above and below the PMTs. However, dismantling the holder is easily possible, as only the upper flange has to be unfastened from the vessel.

## 5.3 EMI Shield

To prevent electromagnetic interference (EMI) from disturbing the readout of the detectors, a shielding box made of steel plates was constructed. The box has the dimensions  $1.2\text{ m} \times 1.0\text{ m} \times 0.6\text{ m}$  and thus a volume of  $0.72\text{ m}^3$ . It is big enough to house both vessels and the gas system.

The steel plates have a thickness of 3 mm and are welded together, except

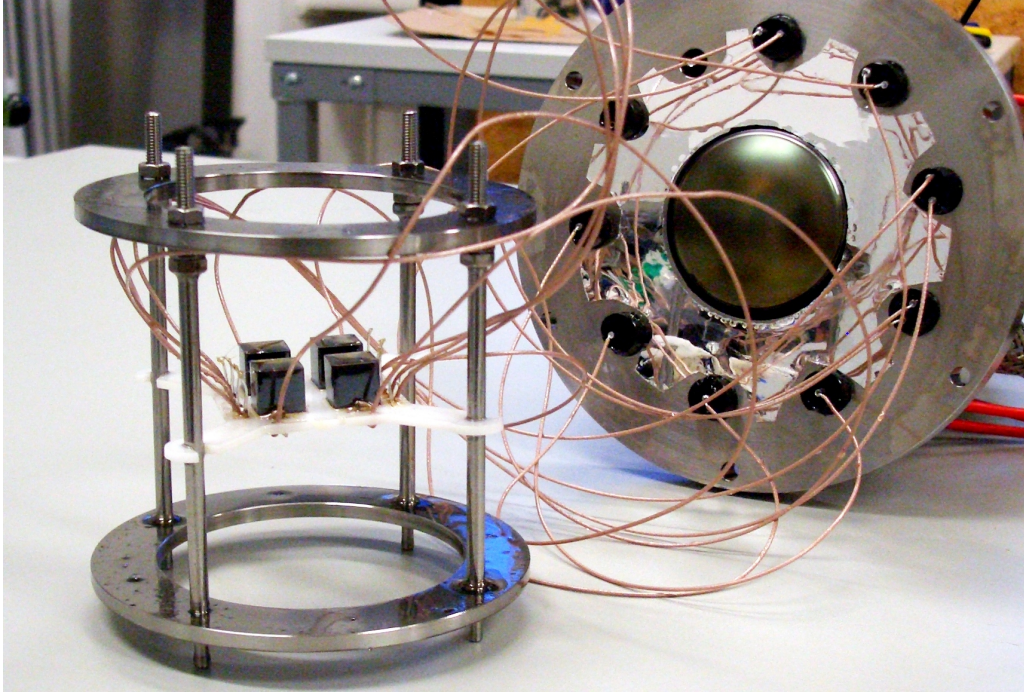


**Figure 5.3:** Photograph of the detector holder with four detectors installed, all connected with SM50 cables to the feedthroughs of the upper flange. The detectors are glued to a Delrin plate using UHU 'Hart'.

for two parts: The front plate with dimensions  $1.2\text{m} \times 1.0\text{m}$  can be separated, allowing for accessibility to the vessels, PMTs and electronics. With 24 wingnuts the front plate is easily fastened to the EMI box. On the back of the box, a plate with dimensions  $0.2\text{m} \times 1.0\text{m}$  is also not welded to the box and can be separated or exchanged. This plate houses the feedthroughs for signal and voltage supply cables as well as for the Nitrogen flushing. Both plates are connected via sealing tape to the box to guarantee the electrical connection needed to efficiently suppress electromagnetic interferences.

## 5.4 Readout Electronics, DAQ and Data Processing

To attain comparable results, the readout electronics and the DAQ system are very similar to the COBRA demonstrator at the LNGS, see Section 4.4.4. A sketch of the components and their wiring is depicted in Figure 5.4.

A preamplifier box designed and produced by the TU Dortmund is placed near to the operation vessel, to allow as short readout cables as possible. The box houses eight CR-110 preamplifiers and distributes the grid bias and the high voltage. As every detector needs two preamplifier channels for the CA and NCA, this preamplifier box is sufficient to operate up to four detectors.

A mesh wire is used to shield the  $\sim 50\text{cm}$  long cables connecting the

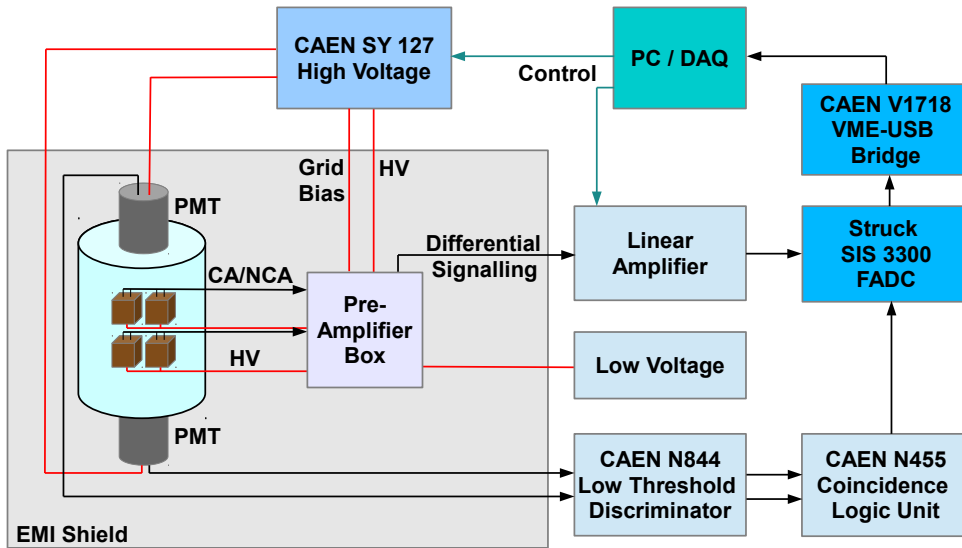


**Figure 5.4:** Sketch of the components used as readout electronics and DAQ at the set-up in Hamburg. The preamplifier box is placed near to the operation vessel inside the EMI shield to allow as short readout cables as possible. The box delivers the high voltage as well as the grid bias to the detectors. To operate the eight CR-110 preamplifiers, a low voltage supply is necessary. High voltage and grid bias are supplied by a CAEN SY 127 device which is adjustable via RS232 from a PC.

The detector CA and NCA pulses are amplified and converted into differential signals inside the preamplifier box and fed outside the EMI shield using CAT 6 Ethernet cables. After amplification with a NIM-housed linear amplifier, the pulses are converted into single-ended signals and transferred via LEMO cables to a VME-based Struck SIS 3000 with eight FADC channels in total. Using a VME-USB bridge, the data is finally stored on a PC.

The PMTs high voltage is also supplied by the CAEN SY 127. The PMT signals are fed outside the EMI shield with LEMO cables into a CAEN N844 discriminator and afterward into a CAEN N455 Coincidence Logic Unit. The coincidence or AND signal is also recorded by the SIS 3000 FADC, providing a time stamp to reject simultaneous events in the detectors and the liquid scintillator.

feedthroughs in the upper flange and the preamplifier box. The mesh wire is connected thoroughly at the box and the operation vessel to shield electromagnetic interference penetrating the EMI box. The detector signals are transferred from the preamplifier box outwards the EMI box using differential signaling on CAT6 cables. At the feedthrough plate, the CAT6 cables are stripped and the cables' shield is connected to the EMI box.

Linear amplifiers designed by the TU Dortmund and constructed at the Universität Hamburg convert the detector signals into single-ended signals. Also an amplification factor to adjust the signal height to the input range of the ADCs is tunable via Ethernet. Finally, Struck SIS 3300 FADCs are used to record the whole pulse shape of both the CA and NCA.

To obtain signals produced in the liquid scintillator, the LEMO signal cables from the PMTs are also fed through the feedthrough plate at the back of the EMI box. Using a CAEN N844 Low Threshold Discriminator, the analog signals are converted into NIM signals when an adjustable threshold is exceeded. With a CAEN N455 Coincidence Logic Unit an AND signal of both PMTs is created and fed to the FADC. This signal provides a very good time information if events in the liquid scintillator generate enough light for both PMTs to create a measurable signal.

One Struck SIS 3300 module houses eight FADC channels in total, providing a very good timing alignment of about 10ns among the channels. If the timing information from the PMTs should be logged, only the signals from three detectors can be recorded. Six FADC channels are then used for the detectors CA and NCA signals, while one channel records the PMT veto signal.

For trigger generation, a particular firmware for spectroscopy applications is available for the Struck SIS 3300. Here, the trigger is activated via a moving average window if steps arise within the signal pulse. Minimum pulse height and polarity for the trigger are configurable for every channel. In the current set-up, the trigger is only activated on the CA channels.

The input signal for every channel is sampled and digitized continuously by the FADC. After activation of the trigger by an appropriate signal pulse, the FADC proceeds the sampling for an adjustable number of samples. Afterward, the FADC switches to a new data buffer waiting for the next event, while the triggered pulse is read out and stored. Hereby, next to post-trigger also pre-trigger information is recorded, providing a sufficient number of baseline samples for the energy determination of every recorded signal pulse. The DAQ software framework used within the COBRA collaboration is called Data-Acquisition and Control Environment (DAQCorE) [116].

The raw signal pulses are stored in so-called ROOT files. ROOT is an object-oriented program developed by CERN and written in C++. It was originally designed for the analysis of large amounts of data in particle physics, but is also used in other fields like astronomy.

Within COBRA, the pulse-shape processing of the stored raw signal pulses is carried out with the software package Multiple-Analysis Toolkit for the COBRA Experiment (MAnTiCORE) [116]. The processed files are again stored as ROOT files and contain information like deposited energy and reconstructed interaction depth. To process the stored data, MAnTiCORE has to be configured with a settings file, the so-called ROOTRC file. The ROOTRC file contains general settings for the initialization, the assignment of the detectors to the different FADC channels, detector specific calibration parameters and weighting factors.

### 5.4.1 Data Cleaning Cuts and Pulse Shape Analysis

Due to the recording of the pulse-shapes with FADCs for every triggered event, complex offline pulse-shape analysis (PSA) for background reduction and rejection of non-physical events is possible. For the data recorded at the LNGS, a set of optimized cuts is already implemented into MAnTiCORE. The most important cuts for data cleaning and PSA are explained in this Section.

The trigger for event-recording is activated when steps arise within the signal pulse at a minimum CA pulse height. The height for CA pulses is not only dependent on the deposited energy, but also on the drift of electrons inside the detectors. For events near the cathode ( $z \sim 1$ ), the drift distance is very long and less energy is needed to activate the trigger than for near anode events. Hence, the trigger threshold for events with small energies is highly depth dependent. To account for this, the `flag_above_threshold` cut can be used to remove below threshold events. This cut is used, if an exposure independent from the interaction depth is needed to calculate event rates.

As mentioned before, the recording of the pre-trigger and post-trigger baselines for the CA and NCA channels enables the determination of the interaction depth  $z$  with Equation 4.13. For the data recorded at the LNGS, only events with  $0.2 < z < 0.97$  are used to calculate half-life limits. This  $z$ -cut removes most of the background originating from  $\alpha$ -events at the anodes and cathodes.

To identify background events on the four detector sides apart from anode and cathode, a PSA cut has recently been developed [109]. These lateral surface events (LSE) are identified due to nonuniformities in the weighting potential. If for a given detector side the outside rail of the co-planar grid is the CA, events at this side show a characteristic early rise time (ERT). Events at a side with the NCA being the outside grid rail show a dip in the difference pulse below the baseline (DIP). The LSE cut rejects point-like energy depositions on the four surface sides of the detectors and thus reduces the background originating from  $\alpha$ -events. In addition, a PSA cut to distinguish multi-site events (MSE) from single-site events (SSE) was recently implemented in MAnTiCORE.

To identify unphysical events like disturbances by EMI, the cut `flag_bad_pulse` is used. This cut uses many parameters in the PSA, like limits on the expected

rise time, variations in the pre- and post-trigger baseline noise and a reconstructed energy with non-negative value. This cut does not account for the interaction depth, thus events reconstructed outside the physical meaningful region  $0 < z < 1$  are not affected when this flag is used.

## 5.5 Photomultiplier Tubes

The PMTs used in this set-up are of type 9829B produced by ET Enterprise [121], its data sheet can be found in Appendix C. This PMT is designed for liquid scintillation counting and low level light detection. The domed window is made of borosilicate glass and is transparent roughly between 280 nm and 600 nm. The bialkali photocathode has a quantum efficiency of 30 % at 300 nm.

The electrons emitted at the photocathode are multiplied with 12 BeCu dynodes. The nominal high voltage is 1600 V, resulting in a nominal gain of  $6 \times 10^6$ . However, the PMTs can be operated with high voltages up to 1900 V.

The PMT's diameter is 51 mm if no mu-metal shield against electromagnetic disturbances is applied. The height from the domed window to the voltage divider connectors is 126 mm, the height of the type 628A voltage dividers is 50 mm.

For calibration and monitoring the PMTs with respect to gain-stability, the implementation of a LED system into the operation vessel is in principal possible. For the characterization of the PMTs with respect to gain and dark current, an optical test set-up with a suitable LED was constructed and put in operation [122].

## 5.6 Calibration Sources

To properly calibrate the energy scale of the CdZnTe detectors, gamma radiation in an energy region as large as possible is used for calibration. For the COBRA demonstrator at the LNGS laboratory,  $^{22}\text{Na}$  and  $^{228}\text{Th}$  are used for this purpose. These two calibration sources are in principal available at the Universität Hamburg, but due to the short half-life of the isotopes sources with sufficient activity are not on hand. Instead,  $^{137}\text{Cs}$ ,  $^{60}\text{Co}$  and  $^{152}\text{Eu}$  are used.

The most important isotope to calibrate the CdZnTe detectors in this set-up is  $^{137}\text{Cs}$ , which undergoes a  $\beta$  decay with a decay energy of 1.176 MeV and a half-life of 30.07 years into  $^{137}\text{Ba}$ . With a relative intensity of 85.1 %, a gamma ray with an energy of 661.657 keV is emitted. This gamma line is used to determine the best operation parameters, namely high voltage and grid bias, for every detector. This procedure is described in Chapter 6.1.

Another important isotope to characterize semiconductor detectors in general, is  $^{60}\text{Co}$ . The full peak efficiency and peak to Compton ratio are quality criteria for  $\gamma$ -radiation detectors and often defined with the gamma lines of this isotope.  $^{60}\text{Co}$  undergoes a  $\beta$  decay with a decay energy of 2.824 MeV and a half-life of 5.27 years into  $^{60}\text{Ni}$ . Mainly two gamma rays are emitted, namely at 1173.237 keV

with a relative intensity of 99.9736 % and at 1332.501 keV with a relative intensity of 99.9856 %.

Another popular calibration source is  $^{152}\text{Eu}$ , due to its convenient half-life of 13.54 years and wide range of gamma energies produced in its decays.  $^{152}\text{Eu}$  decays with a branching ratio of 72.1 % via electron capture into  $^{152}\text{Sm}$  and with a branching ratio of 27.9 % via  $\beta^+$  decay into  $^{152}\text{Gd}$ .

**Table 5.3:** Compilation of the most prominent  $\gamma$ -lines emitted by  $^{152}\text{Eu}$  [89]. The  $\gamma$ -lines originate either from  $\beta^+$  decay into  $^{152}\text{Gd}$  (labeled with  $\beta^+$ ) or from electron capture into  $^{152}\text{Sm}$  (labeled with EC).

Energy [keV]	Rel. Intensity	Decay Mode
121.8	141.0	EC
244.7	36.6	EC
344.3	127.2	$\beta^+$
367.8	4.19	$\beta^+$
411.1	10.71	$\beta^+$
444.0	15.00	EC
488.7	1.984	EC
586.3	2.24	$\beta^+$
678.6	2.296	$\beta^+$
688.7	4.12	EC
778.9	62.6	$\beta^+$
867.4	20.54	EC
964.0	70.4	EC
1005.1	3.57	EC
1085.8	48.7	EC
1089.7	8.26	$\beta^+$
1112.1	65.0	EC
1212.9	6.67	$\beta^+$
1299.1	7.76	EC
1408.0	100.0	EC
1457.6	2.52	EC

$^{152}\text{Eu}$  provides plenty of  $\gamma$ -lines to calibrate semiconductor detectors, a compilation of the most prominent  $\gamma$ -lines is listed in Table 5.3. Unfortunately the energy resolution of the CdZnTe detectors used in this set-up is only sufficient to discriminate three to four gamma lines and use them in the calibration procedure, see Section 6.2.1.

As already mentioned, at the LNGS laboratory two other calibration sources are used.  $^{22}\text{Na}$  decays with a branching ratio of 89.8 % via  $\beta^+$  decay into  $^{22}\text{Ne}$ .

Next to the two 511 keV gammas from positron annihilation, a gamma with an energy of 1274.53 keV is emitted.

Next to  $^{22}\text{Na}$ ,  $^{228}\text{Th}$  is used as calibration source.  $^{228}\text{Th}$  is a progeny of  $^{232}\text{Th}$  in the Thorium series and decays with a half-life of 1.9131 years into  $^{224}\text{Ra}$  via  $\alpha$  decay. With a half-life of approximately 100 hours the subsequent decay chain ends with  $^{208}\text{Pb}$ , see Appendix B. The main isotope for calibration purposes is the beta decaying  $^{208}\text{Tl}$  with a  $\gamma$ -line at 2614.5 MeV. A list of prominent  $\gamma$ -lines in the subsequent decay chain of  $^{228}\text{Th}$  are listed in Table 5.4.

**Table 5.4:** Compilation of prominent  $\gamma$ -lines emitted in the subsequent decay chain of  $^{228}\text{Th}$ . The relative intensities are not comparable among different isotopes, as the decay chain is split up into different branches. Scaled emission probabilities can be found in Appendix B.

Energy [keV]	Rel. Intensity	Decay Mode
241.0	4.10	$^{224}\text{Ra} \xrightarrow{\alpha} ^{220}\text{Rn}$
238.6	100.0	$^{212}\text{Pb} \xrightarrow{\beta} ^{212}\text{Bi}$
300.1	7.57	$^{212}\text{Pb} \xrightarrow{\beta} ^{212}\text{Bi}$
727.3	10.27	$^{212}\text{Bi} \xrightarrow{\beta} ^{212}\text{Po}$
1620.5	2.32	$^{212}\text{Bi} \xrightarrow{\beta} ^{212}\text{Po}$
277.4	6.36	$^{208}\text{Tl} \xrightarrow{\beta} ^{208}\text{Pb}$
510.8	22.80	$^{208}\text{Tl} \xrightarrow{\beta} ^{208}\text{Pb}$
583.2	85.20	$^{208}\text{Tl} \xrightarrow{\beta} ^{208}\text{Pb}$
763.1	1.83	$^{208}\text{Tl} \xrightarrow{\beta} ^{208}\text{Pb}$
860.6	12.53	$^{208}\text{Tl} \xrightarrow{\beta} ^{208}\text{Pb}$
2614.5	100.00	$^{208}\text{Tl} \xrightarrow{\beta} ^{208}\text{Pb}$

## 5.7 Monte Carlo Simulation

Monte Carlo (MC) simulations are often used to solve complex analytical problems. The stochastic methods rely on a large number of random samples to gain a numerical result. In the case of this set-up, calibration sources and atmospheric muons are simulated. Due to the complexity of the underlying physics processes, the analytical calculation of the expected detector response is hardly possible.



### 5.7.1 Geant4 and VENOM

To properly simulate the test set-up, the Geant4 (GEometry ANd Tracking) simulation framework [123, 124] is used. Geant4 is developed at CERN and designed to describe the passage of particles through matter. It offers models and cross sections for various particle interactions with matter. In addition, also methods for tracking, geometry, hits, etc. are provided.

Within the COBRA collaboration the simulation package VENOM has been developed and is used for most simulations regarding the set-up at LNGS and for the design of a large scale experiment. VENOM is based on Geant4 and uses its methods and models. It is frequently updated to the latest version of Geant4. Within VENOM the appropriate interaction method, initialization of parameters, data output and geometry definitions are chosen.

In principal, VENOM offers two possibilities to define the simulated geometries and materials. Firstly, it is possible to implement the MC geometry in the source code of VENOM, which has several disadvantages [115]. Secondly, it is possible to implement the geometry using the Geometry Description Markup Language (GDML), which is based on the Extensible Markup Language (XML) document structure rules.

### 5.7.2 Implementation of the Set-Up

The test set-up has been implemented into the VENOM source code in close cooperation with TU Dresden. The implementation was based on the CAD drawings produced in Hamburg and consists of the main parts of the operation vessel. Next to the steel vessels with both flanges and the bores for the PMTs, the holder structures for the detectors and PMTs as well as the Delrin plates were applied. As active detection material, liquid scintillator and PMTs are added.

For a faster modification of the simulation accounting for changes at the test set-up, a GDML implementation is performed in the course of this work. The new GDML version uses the dimensions for the operation vessel, PMTs, detector holder and Delrin plates from the implementation in the VENOM source code. In addition, the shape of calibration sources is simulated properly.

In addition to calibration sources, the simulation of muon events is possible with this MC simulation. The angular and energy dependent muon distribution used in the course of this work is given in Equation 6.7 in Section 6.6.

The implementation of the simulation in GDML offers the possibility to easily change the type of radiation being muons or a calibration source and their initial point. Also a variation of the operation vessel filling being liquid scintillator or gaseous Nitrogen is possible. A schematical drawing of the GDML implementation with the  $2 \times 2$  detector array is shown in Figure 5.5.

In case of the CdZnTe detectors, the processes leading to the detector output signal described in Section 4.3 are not yet implemented in VENOM. Instead, only

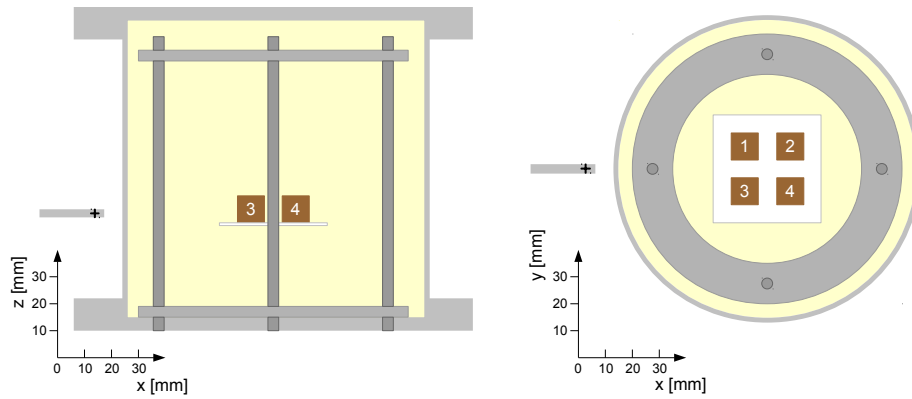


**Figure 5.5:** Side view (left) and top view (right) of the set-up implemented in VENOM using GDML. For a clear arrangement, some parts are not shown, including the PMTs and the PMT holder. Parts made from steel are shown in gray, Delrin in white and liquid scintillator in yellow. The numbered detectors are shown in brown. The point-like origin of simulated gammas inside the  $^{137}\text{Cs}$  calibration source is marked with a black cross.

the deposited energy inside the active detector volume is stored. To make the simulations comparable to measurements, the data is smeared according to the energy resolution of the detectors used in the set-up, see Figure 5.6.

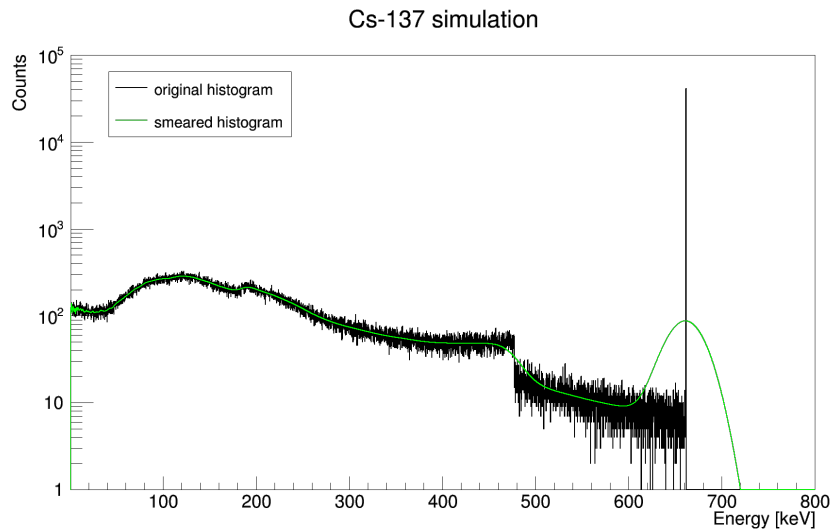


**Figure 5.6:** Original (black) and smeared (green) spectra of a  $^{137}\text{Cs}$  simulation.

## Chapter 6

# Measurements and Comparison to Simulations

To make general statements about the feasibility of operating CdZnTe detectors in liquid scintillator, the data collected by three CPG detectors is evaluated. The fourth detector operated in liquid scintillator has a poor energy resolution and is omitted in the analysis. Instead, one of its FADC channel is used to record the timing information from the PMTs as a veto against external radiation depositing energy in the liquid scintillator.

The data shown in this chapter was collected with the three remaining detectors in the period of December 2014 to February 2015. Next to calibration periods, mostly the background spectrum in the laboratory was measured during this time. Previously, the optimal working point for every detector was determined. Energy resolution and weighting factor were reevaluated with every calibration.

To better understand the collected data, the MC simulations explained in Section 5.7 are compared to measurements with a  $^{137}\text{Cs}$  calibration source. To use the liquid scintillator as a veto against external radiation, a coincidence time of  $50\ \mu\text{s}$  is chosen to define events in the detectors and the scintillator as simultaneous. Hereby, events depositing energy in the scintillator can be rejected from the laboratory background spectrum. The collected data of events with and without simultaneous events in the scintillator veto are analyzed taking the standard data cleaning cuts and pulse shape analysis introduced in Section 5.4 into account.

### 6.1 Detector Working Points

As described in Section 4.3.4, the optimal weighting factor has to be determined for every CPG detector to gain an appropriate energy resolution. The weighting factor depends on the high voltage and grid bias applied. In the course of this work,  $w$  is determined by the irradiation of the detectors with a  $^{137}\text{Cs}$  source emitting gammas of  $661.7\ \text{keV}$ . The determination of  $w$  is performed in the course of the regular

calibration campaigns presented in Section 6.2.1. The method explained in this section was developed at the TU Dresden for the CPG detector characterization procedure of the LNGS layers three and four.

The working point for every combination of HV and GB under investigation is found by plotting the uncalibrated raw amplitudes of the CA signals against the NCA signals. A linear fit on the full energy line yields  $w$  for the weighted difference signal  $CA - w \cdot NCA$ .

To obtain the energy resolution for every  $w$ , the full energy line of the resulting  $^{137}\text{Cs}$  spectrum is fitted to the function

$$y(x) = A \cdot e^{-\frac{x-\mu}{2\sigma_{lr}}} + a \cdot x + b, \quad \text{with } \sigma_{lr} = \begin{cases} \sigma_l & \text{for } x < \mu, \\ \sigma_r & \text{for } x > \mu. \end{cases} \quad (6.1)$$

$y(x)$  describes a two sided Gaussian with the normalization factor  $A$ , the mean value  $\mu$  and the standard deviation  $\sigma_{lr}$  together with a linear background approximation  $a \cdot x + b$ . For some detectors the full energy peak is strongly asymmetrical. This is taken into account with the differentiation into a left and a right handed standard deviation,  $\sigma_l$  and  $\sigma_r$  respectively. The standard deviation for the whole peak is then given by  $\sigma_{lr} = (\sigma_l + \sigma_r)/2$ .

In general, the detector resolution is given using the relative full width half maximum (FWHM) value of the peak. To be independent from the energy scale, the absolute FWHM (aFWHM) is divided by the fitted mean value  $\mu$  of the peak:

$$\begin{aligned} \text{FWHM} &= \frac{\text{aFWHM}}{\mu} \\ \text{aFWHM} &= 2\sqrt{2 \ln 2} \sigma_{lr} \approx 2.355 \sigma_{lr}. \end{aligned} \quad (6.2)$$

To find the optimal working point for every detector, the fitted FWHM is plotted against different values of  $w$ . A parabolic function is found with a minimum of FWHM for the best weighting factor. This procedure has to be repeated for every set of HV and GB and finally the minimum value of the FWHM can be obtained. The values for  $w$  are written in the ROOTRC file, which is used for the pulse-shape processing of the stored raw signal pulses in MAnTiCORE.

Unfortunately, detector 4 is performing very poorly and the fit with Equation 6.1 is hardly possible for any HV and GB combination due to a very high energy resolution of at least 15% FWHM. Therefore, the detector is rejected from further analysis and the corresponding channels of the FADC are used to collect the timing information of the veto. For the remaining three detectors, the achieved FWHM with the corresponding  $w$ , HV and GB are summarized in Table 6.1. In comparison to the CdZnTe CPG detectors used at the COBRA demonstrator, all three detectors have a large FWHM. To make statements about the general feasibility of operating CdZnTe in liquid scintillator, the poor energy resolution is not an issue. Nevertheless, locating  $\gamma$ -ray peaks in the background spectrum measured in the laboratory is challenging with these detectors.

**Table 6.1:** Optimal working point for the three detectors of the set-up. Due to its poor performance, detector 4 is omitted in the analysis.

	FWHM	$w$	HV	GB
Detector 1	6.5 %	0.47	600 V	20 V
Detector 2	6.4 %	0.90	600 V	20 V
Detector 3	7.3 %	0.43	600 V	20 V

## 6.2 Calibration and Time Stability

During the data taking period from December 2014 to February 2015, several calibration campaigns were performed. As  $^{137}\text{Cs}$  is one of the gamma emitters used for calibration, also the determination of the working points described in Section 6.1 were repeated. To check the stability of data taking, the data rate was monitored throughout the measurement.

### 6.2.1 Calibration Parameters

The calibration of the CPG detectors is performed by using three different  $\gamma$ -ray emitters:  $^{137}\text{Cs}$ ,  $^{60}\text{Co}$  and  $^{152}\text{Eu}$ . From  $^{152}\text{Eu}$ , only the  $\gamma$ -lines at 344.3 keV, 778.9 keV, 964.0 keV and 1408.0 keV are usable. The two prominent lines at 1085.8 keV and 1112.1 keV are too closely spaced and too close to the Compton edge of the 1408.0 keV line, to separate them using the detectors of this set-up. Thus, in total seven  $\gamma$ -lines between 344.3 keV and 1408.0 keV are available for calibrations.

The position  $\mu_i$  in terms of ADC channels  $n$  for every gamma line  $i$  is determined by a fit with a superposition of a two-sided Gaussian function and a linear background approximation as shown in Equation 6.1. The  $\mu_i$ 's are then plotted against the known gamma energy and a linear fit is applied. The energy calibration fit is described with two parameters: The offset  $p_0$  and the slope of the linear function  $p_1$ :

$$E = p_0 + p_1 \cdot n. \quad (6.3)$$

As the offset  $p_0$  is normally very small, the stability of the detectors with respect to the energy scale is expressed in terms of the slope  $p_1$ . In Figure 6.1 the linear function slopes for the three detectors obtained in the calibrations performed between December 2014 and February 2015 are shown. During this period the slopes are stable and no large deviations are traceable.

After calibration, the obtained parameters  $p_0$  and  $p_1$  are written into the ROOTRC file. This file is used in MAnTiCORE to simultaneously reproduce and calibrate the deposited energy stored in raw signal pulses of a measurement.

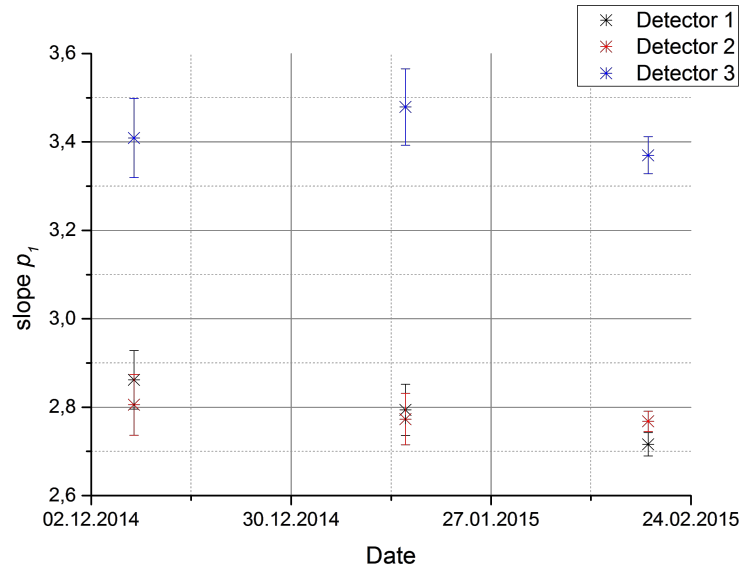


**Figure 6.1:** Slope  $p_1$  of the linear calibration function obtained between December 2014 and February 2015 for all three detectors. Large deviations are not observable.

### 6.2.2 Data Rate

Another criterion for the stability of data taking is the rate of events. The background measurement in the laboratory was performed in so-called runs with a duration of 2 hours. For the period between December 2014 and February 2015 the file size was monitored continuously. Most files have a size of 19 MB to 21 MB, all files with a size larger than 26 MB are rejected due to noise on the signal pulses. In addition, all aborted and uncompleted runs are rejected. The number of recorded events per run is shown in Figure 6.2.

The periods with no entries are mainly due to calibration campaigns or crashes of the DAQ. In normal operation the data rate per run is very stable with approximately 8500 events in total. Also the ratio of events flagged as good events and bad events is constant, except for some runs around 28/12/2015 with an exceeding number of bad events. The reason for this is unknown, but could be due to a source of external noise affecting the data-taking.

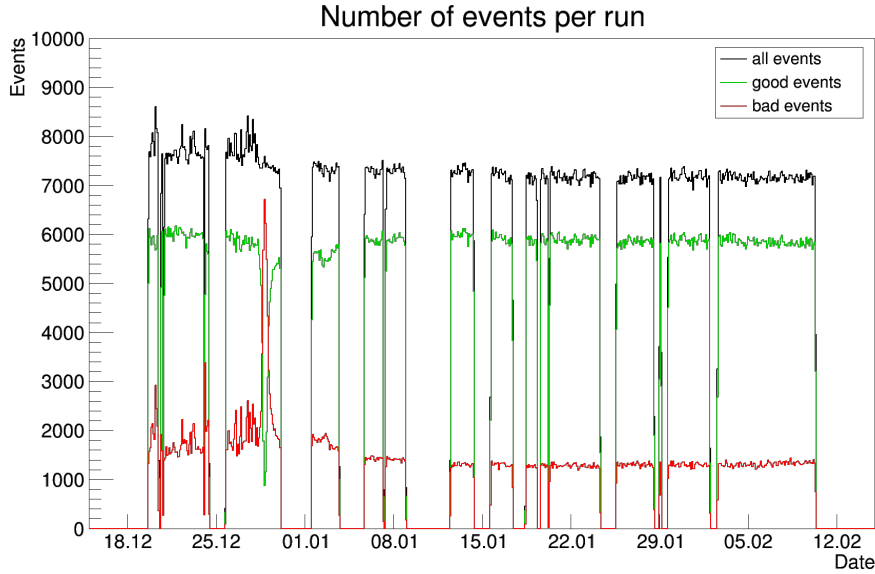


**Figure 6.2:** Number of recorded events per run in the period from December 2014 to February 2015.

### 6.3 Coincidence Time for Veto

For data acquisition of this set-up, the software DAQCorE is configured to store 1024 samples of every recorded signal pulse. This corresponds to a pulse-length of  $10.24 \mu\text{s}$ . The trigger is set only to the CA signal channels of the FADC and the trigger position is fixed to the sample 640. Hence, for every pulse 640 samples before and 384 samples after the trigger criterion applied are recorded.

To define events in the detectors and the liquid scintillator as simultaneous, a coincidence time  $\Delta t$  has to be specified.  $\Delta t$  has to meet two demands: On the one hand, the coincidence time has to be long enough to compensate for time differences between the detector and veto signals. These differences can arise from the drift of the charge carriers in the CdZnTe detectors and PMTs, time delays in the electronics and cables or the light propagation in the liquid scintillator. On the other hand, the coincidence time should be kept as small as possible to avoid random coincidences. Taking these two criteria into account, a  $\Delta t$  of  $50 \mu\text{s}$  is reasonable. If energy is deposited simultaneously within  $\Delta t$  in the scintillator veto and in one or more detectors, the event is called scintillator veto event (SVE).

To test this hypothesis, a measurement with a  $^{137}\text{Cs}$  source and activated veto was performed. Normally, the veto signal is not recorded at measurements with calibration sources, because more than 90 % of all events originating from a  $^{137}\text{Cs}$  source are triggered by the scintillator veto, see Figure 6.3. This makes the matching of simultaneous events computationally intensive.

For the  $^{137}\text{Cs}$  full energy deposition at  $661.7 \text{ keV}$  in the CPG detector, no veto signal from the scintillator veto is expected, except for random coincidences.

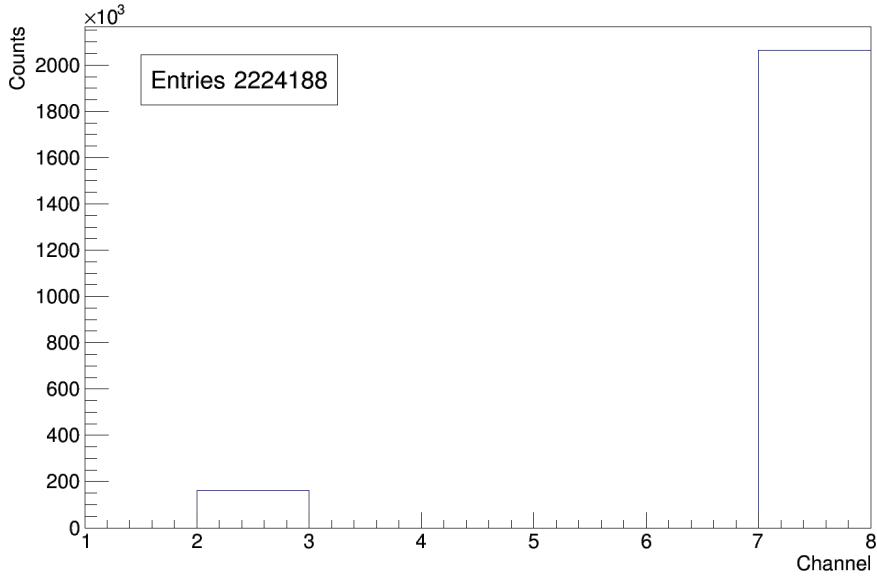


**Figure 6.3:** Number of triggered events per channel within a  $^{137}\text{Cs}$  calibration run of half an hour. In total, 2224188 events meet the trigger criterion. For detector 1 with its CA recorded on channel 2, the trigger is activated less than 200000 times. Most events are triggered by the scintillation veto recorded on channel 7.

Hence, a low-activity  $^{137}\text{Cs}$  source with 115 kBq is used for the determination of the best veto time. In Figure 6.4, a  $^{137}\text{Cs}$  measurement with detector 1 is shown. In the region between 610 keV and 713.4 keV, 87% of all events survived the veto criterion of  $\Delta t = 50 \mu\text{s}$ .

The determination of vetoed events in the region between 610 keV and 713.4 keV is repeated for other values of  $\Delta t$  with the same measurement. Here,  $\Delta t$  is varied between  $1 \mu\text{s}$  and 10 ms, see Figure 6.5. In the range between  $1 \mu\text{s}$  and  $500 \mu\text{s}$  the variation of the veto time has no effect. Above  $\Delta t = 500 \mu\text{s}$ , the number of vetoed events increases due to random coincidences. The  $^{137}\text{Cs}$  spectra for the different  $\Delta t$  are shown in Appendix E.

As the variation of  $\Delta t$  has no effect on  $N_{\text{veto}}$  within a range from  $10 \mu\text{s}$  to  $500 \mu\text{s}$ ,  $\Delta t = 50 \mu\text{s}$  is chosen for the analysis described in the upcoming sections. This is roughly the fivefold of the recorded pulse length and compensates for possible time differences in the readout chains. Also,  $50 \mu\text{s}$  are not too long to produce an exceeding number of random coincidences.



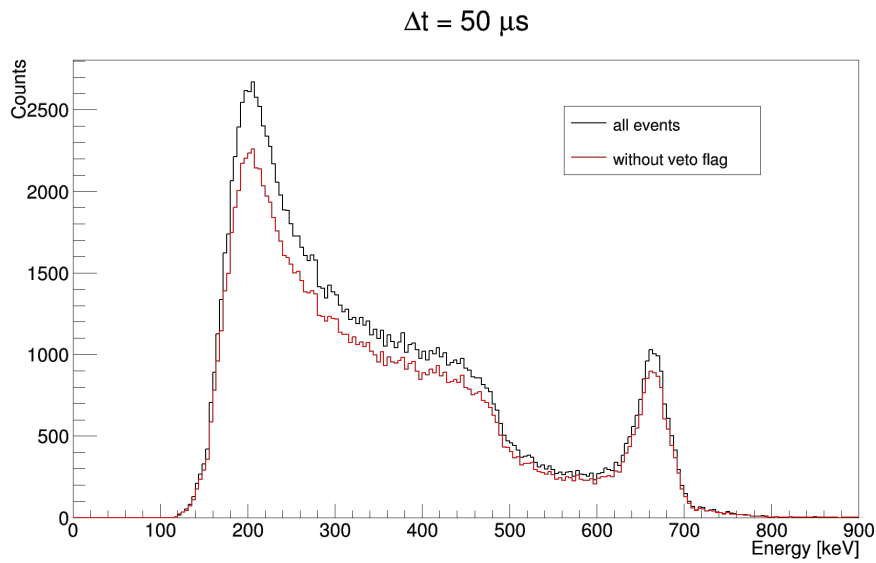


**Figure 6.4:** Spectra for a  $^{137}\text{Cs}$  measurement performed with detector 1 with no veto applied (black) and with a veto time of  $50 \mu\text{s}$  (red). 12.95 % of all events in the region between 610 keV and 713.4 keV do not survive the veto criterion of  $\Delta t = 50 \mu\text{s}$ .

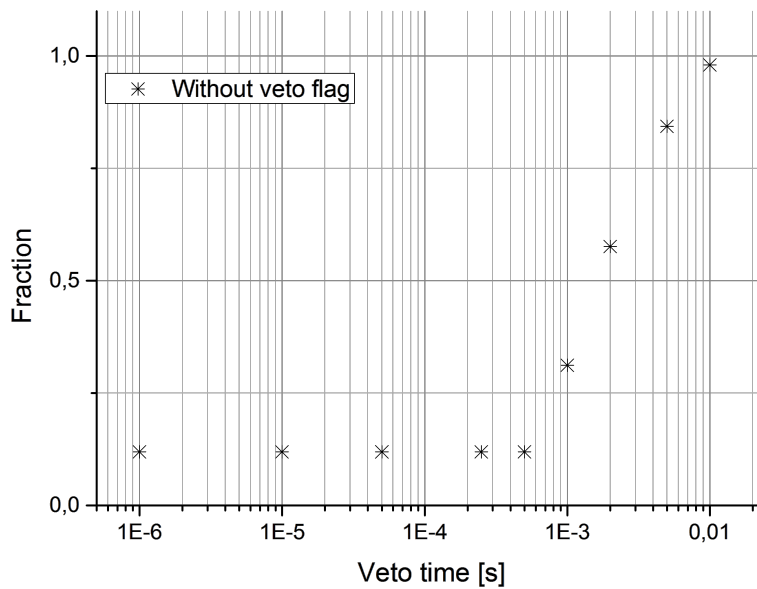


**Figure 6.5:** Fraction of vetoed events plotted against  $\Delta t$ . The fraction increases above  $\Delta t = 500 \mu\text{s}$  due to random coincidences.

## 6.4 Comparison of $^{137}\text{Cs}$ Measurement and Simulation

To better understand the performance of the detectors operated in liquid scintillator, several calibrations with  $^{137}\text{Cs}$  are simulated. As described in Section 5.7.2, the decay of  $^{137}\text{Cs}$  is simulated outside the operation vessel in a small steel tube with the dimensions of the actual calibration source. To check for the correct implementation of the liquid scintillator in VENOM, the simulations are also performed with Nitrogen as surrounding medium and compared to the corresponding measurements. Also the size of the implemented detectors can be varied, starting with a size of  $1\text{ cm}^3$  according to the actual detector size. For every simulation  $2.5 \cdot 10^9$  events are generated and the simulated spectra are smeared with a Gaussian distribution of 7% FWHM.

The simulations are compared to measurements with detector 1 of the set-up. Two calibration runs for 16.5 hours each are performed in liquid scintillator and in Nitrogen. For both measurements the calibration source is screwed into the same position with respect to the operation vessel.

The results of the simulations compared to the measurements are shown in Figure 6.6. The general shape of the measured calibration spectra is reflected by the simulations: Due to the lower density of Nitrogen compared to liquid scintillator, the full energy peak (FEP) at 661.7 keV is higher in the measurements performed in Nitrogen. Also the shapes of the spectra at the Compton edge around 450 keV and in the lower energy Compton continua between 200 keV and 300 keV are described properly by the simulations.

However, the ratios between the FEP values and the Compton continua, the so-called peak to Compton ratios (P/C), are not reflected by the simulations. The peak to Compton ratio is often used to characterize detectors, because it takes the detection efficiency and the energy resolution into account. A higher efficiency detector has more counts in the full energy photopeak, and with better resolution, the photopeak is narrower resulting in an increased number of peak channel counts. For  $^{60}\text{Co}$ , the P/C is the number of counts in the peak channel of the 1332 keV line compared to the average of counts in the spectrum ranging from 1040 keV to 1096 keV. Analogous, the P/C for  $^{137}\text{Cs}$  is defined as the number of counts in the peak channel at 661.7 keV versus the average of counts in the spectrum ranging from 358 keV to 382 keV [89].

In Figure 6.7 the simulation of  $^{137}\text{Cs}$  in liquid scintillator is scaled to fit the Compton edge of the corresponding measurement. The simulation is in very good agreement with the shape of the measurement in the Compton spectrum from 200 keV to 600 keV. Also the shape of the Compton spectrum measured in Nitrogen is in quite good agreement with its simulation. The simulation of  $^{137}\text{Cs}$  in Nitrogen is scaled with the same factor and also shown in this Figure. However, both measurements yield a much lower P/C than expected from the simulations.

An overestimation of the peak to Compton ratio in the simulation compared

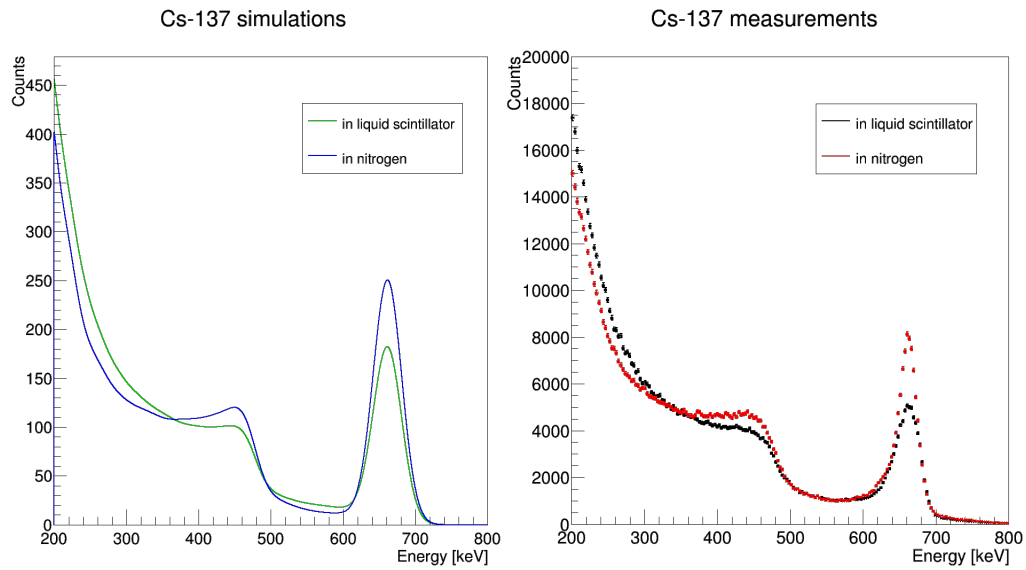


**Figure 6.6:** Comparison of  $^{137}\text{Cs}$  simulations in liquid scintillator and Nitrogen (left) with the corresponding measurements (right). The number of simulated events respectively the measuring time are identical to allow comparison of the spectra. Besides the P/C, the simulations reflect in general the shapes of the measured spectra.

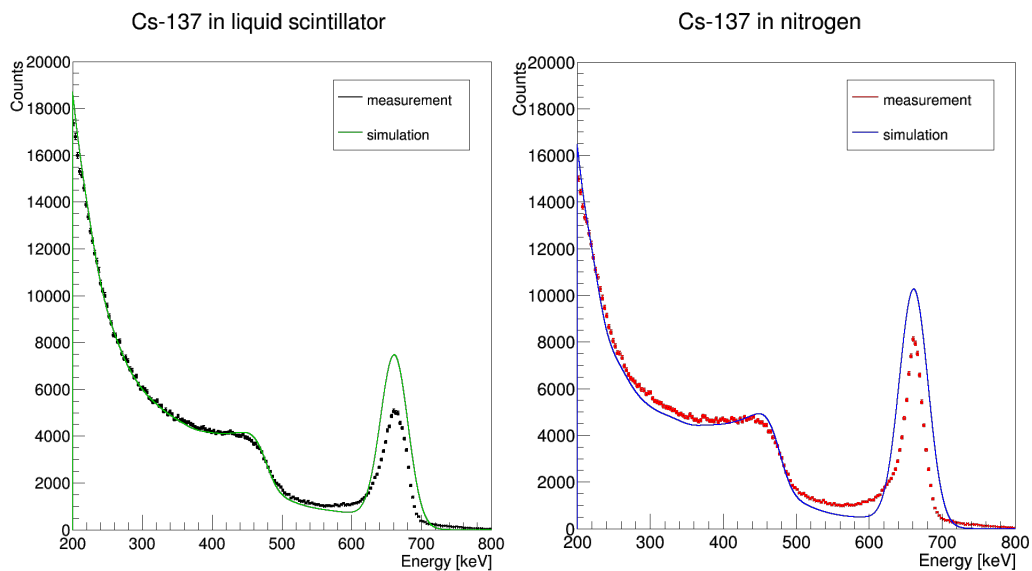


**Figure 6.7:** Comparison of  $^{137}\text{Cs}$  simulations with measurements in liquid scintillator (left) and Nitrogen (right). The simulation with liquid scintillator is scaled to fit the Compton edge of the corresponding measurement. The simulation with Nitrogen is scaled with the same factor.

to the measurement can in general be caused by two reasons: The size of the simulated detectors is too large or detector effects leading to an inferior FEP detection efficiency are not accurately considered. The latter case can not be investigated, as the simulation performed with Geant4 only yields the deposited energy in the detectors and not the physical formation of the signal pulses. To account for detector effects in the charge transport and pulse formation processes described in Section 4.3, only the energy deposition in the simulation can be smeared with a Gaussian distribution to fit to the detectors energy resolution.

A too large size of the simulated detectors could be due to dead layers in the CdZnTe crystals. To account for this, the simulations are repeated with different detector sizes from 6 mm edge length to 11 mm edge length. This corresponds to crystal volumes from  $0.22 \text{ cm}^3$  to  $1.33 \text{ cm}^3$ , respectively. The spectra can be found in Figure 6.8 and the peak to Compton ratios are summarized in Table 6.2.

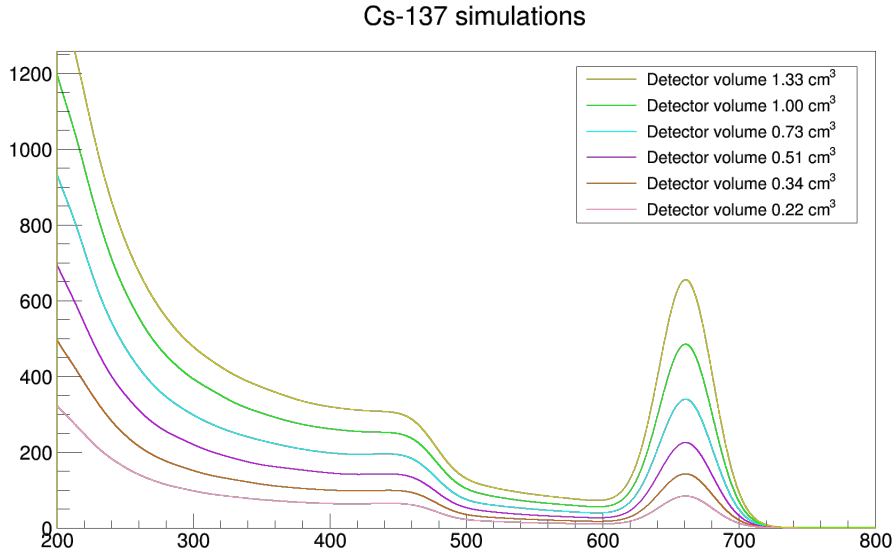


**Figure 6.8:** Comparison of  $^{137}\text{Cs}$  simulations in liquid scintillator for different sizes of the implemented detector crystals from  $0.22 \text{ cm}^3$  to  $1.33 \text{ cm}^3$ .

Only the simulation with a  $0.22 \text{ cm}^3$  CdZnTe detector provides a P/C comparable to the measurement. Therefore, possible dead layers in the crystal can not explain the measured P/C and an extensive simulation of the processes inside the detectors resulting in the measured pulse-shapes is needed to better understand this issue.

**Table 6.2:** Comparison of peak to Compton ratios for different simulated detector sizes. For every simulation  $2.5 \cdot 10^9$  events are generated. The Compton value is the average bin value between 358 keV and 382 keV.

Edge length	Volume	Peak value	Compton value	P/C
11 mm	1.33 cm <sup>3</sup>	654.79	345.88	1.89
10 mm	1.00 cm <sup>3</sup>	484.68	281.74	1.72
9 mm	0.73 cm <sup>3</sup>	339.43	214.37	1.58
8 mm	0.51 cm <sup>3</sup>	224.94	156.66	1.44
7 mm	0.34 cm <sup>3</sup>	142.23	106.85	1.33
6 mm	0.22 cm <sup>3</sup>	83.72	68.94	1.21

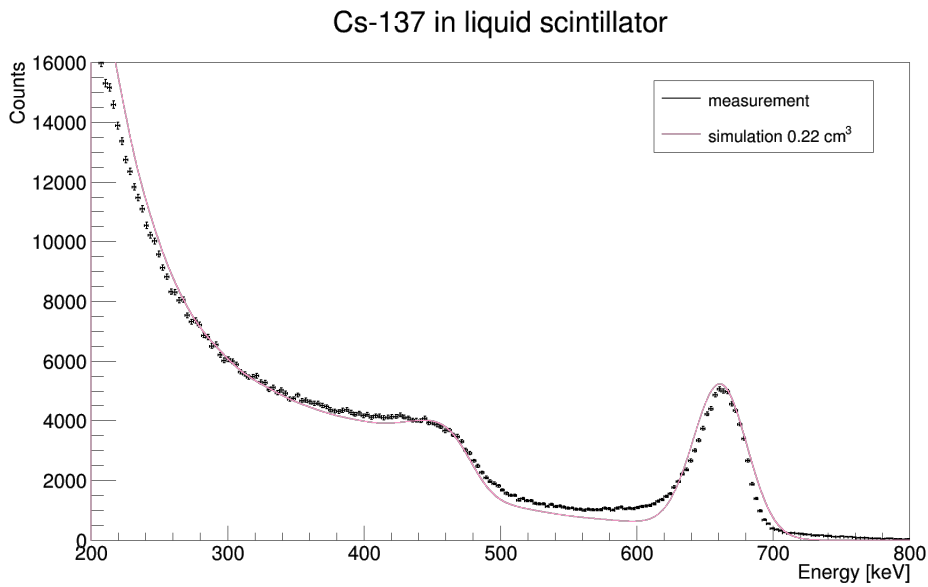


**Figure 6.9:** Comparison of  $^{137}\text{Cs}$  simulations with detectors of 6 mm edge length to a measurement performed in liquid scintillator.

## 6.5 Veto Performance in the ROI of COBRA

The measurement of the laboratory background spectrum was performed from December the 19th 2014 to February the 10th 2015. Prior to this measurement, the detectors were stored for approximately three years without lacquer in the scintillator. During this time, the design, construction and commissioning of the set-up took place. The successful operation of CdZnTe detectors after years of immersion demonstrate the applicability of liquid scintillator for a long-term and large scale COBRA experiment.

As already shown in Figure 6.2, the measuring periods were interrupted for calibration runs and special measurements presented in the previous sections. For the measurement presented in this and the following section, 449 runs with a duration of two hours each are analyzed. This corresponds to a measuring time of 0.1025 years. With the total mass of the three detectors of 17.3 g, an exposure of 0.649 kg·d is collected.

The complete dataset is split up into two separate subsets: Events depositing energy in the scintillator veto and in one or more of the detectors within  $\Delta t$  of 50  $\mu$ s are flagged as scintillator veto events (SVEs). The remaining events in the detectors with no simultaneous veto are referred to as no veto events (NVEs).

As already depicted in Section 4.4.6, 2D plots are often chosen to represent at once the interaction depth  $z$  on the y-axis and the energy  $E$  on the x-axis in the following sections. This representation is referred to as  $z$ - $E$ -plot. Per definition, the anodes are at  $z = 0$  and the cathode is at  $z = 1$ . The logarithmic color coded scale on the right of each  $z$ - $E$ -plot indicates the number of entries per bin. For clarity, the scales have the same range when two or more  $z$ - $E$ -plots are compared.

In Figure 6.10 the background spectrum up to 6 MeV with all events compared to the spectrum of NVEs is shown. Only one prominent  $\gamma$ -line is visible, a peak at 1460 keV originating from the decay of  $^{40}\text{K}$ . At energies above 2.4 MeV, a significant number of events is removed with the application of the scintillator veto. In the region from 3 MeV to 4 MeV, where no prominent  $\gamma$ -lines are expected, roughly a factor of  $0.97 \pm 0.02$  of all events is discarded. In principal, this value should also be achievable around the Q-value of  $^{116}\text{Cd}$  with the absence of the  $\gamma$ -line from the  $^{208}\text{Tl}$  decay at 2.6 MeV. Events from this decay would be strongly suppressed in the ROI of COBRA, if the detectors had an energy resolution of 3.5 % FWHM or better.

The energy spectra with all events and NVEs are shown in Figure 6.11 as a  $z$ - $E$ -plot. Again the decrease of events at energies above 2.4 MeV is clearly visible, when SVEs are removed. At the anode ( $z = 0$ ) and cathode ( $z = 1$ ) reconstruction distortions appear, causing events with  $z < 1$  and  $z > 1$ . The distortions and structures shown in Figure 6.11 are studied in Section 6.6. Compared to the spectrum from the demonstrator at the LNGS (see Section 4.4.6), regions with significant higher statistics originating from  $\alpha$  decays at the anode or cathode are

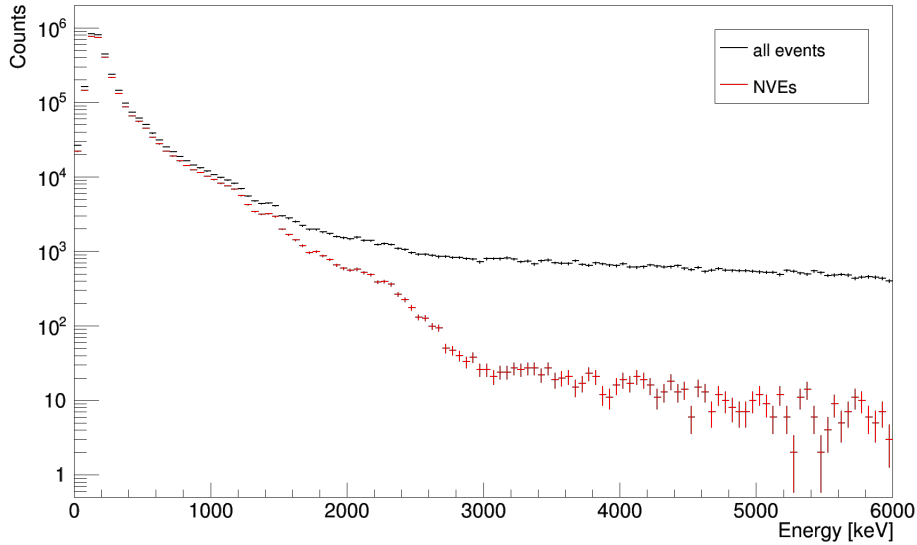


**Figure 6.10:** Spectra for all events (black) and NVEs (red) with energies up to 6 MeV. A notable decrease of events in the NVE spectrum is visible for energies above 2.4 MeV. For energies above 3 MeV, no prominent  $\gamma$ -lines are expected in the spectrum and the scintillator veto reduces the number of events by roughly 97%.

not identifiable in the NVE dataset. On the one hand, the existing dataset has not enough statistics for the observation of  $\alpha$  decays from  $^{190}\text{Pt}$ , which is intrinsic to the anode and cathode material. On the other hand, strong  $\alpha$ - or  $\beta$ -emitters are not apparent in the liquid scintillator used in this set-up.

The ROI is defined for this analysis as the  $\pm 1\sigma$  region around the Q-value of  $^{116}\text{Cd}$  at 2813.5 keV. For the average detector resolution in the course of this work the ROI ranges from 2718 keV to 2910 keV. Within the ROI, the complete dataset contains  $3171 \pm 56$  events. If the interaction depth is restricted to the physical meaningful values ranging from 0 to 1,  $1728 \pm 42$  events remain, corresponding to an background index of  $(5063 \pm 122)$  counts/keV/kg/a. This restriction defines the  $z$ -cut in the scope of the work. The  $z$ -cut removes in particular SVEs with  $z > 0$ , this will be explained in Section 6.6.

The NVE dataset contains  $154 \pm 12$  events in the ROI. Applying the  $z$ -cut,  $114 \pm 11$  events remain and the corresponding background index is  $(334 \pm 31)$  counts/keV/kg/a. Hence, the scintillator veto reduces the background index for  $z$  ranging from 0 to 1 in the ROI by more than one order of magnitude, namely by a factor of  $0.93 \pm 0.05$ . In Figure 6.12 the  $z$ - $E$ -plot is shown for all events in the ROI before and after discarding the SVEs. The pulse-shapes of some randomly chosen events surviving these two cuts are shown in Figure 6.13.

Applying the standard analysis cuts explained in Section 5.4 in addition to the  $z$ -cut, the number of events in the ROI within the NVE dataset is further

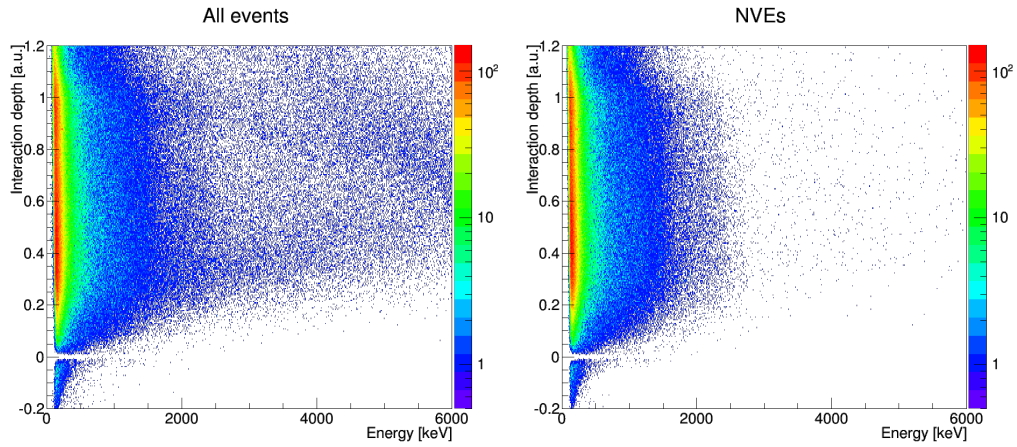


**Figure 6.11:** Spectra of all events (left) and NVEs (right) as a  $z$ - $E$ -plot. As in Figure 6.10, a decrease of events in the NVE spectrum is visible for energies above 2.4 MeV.

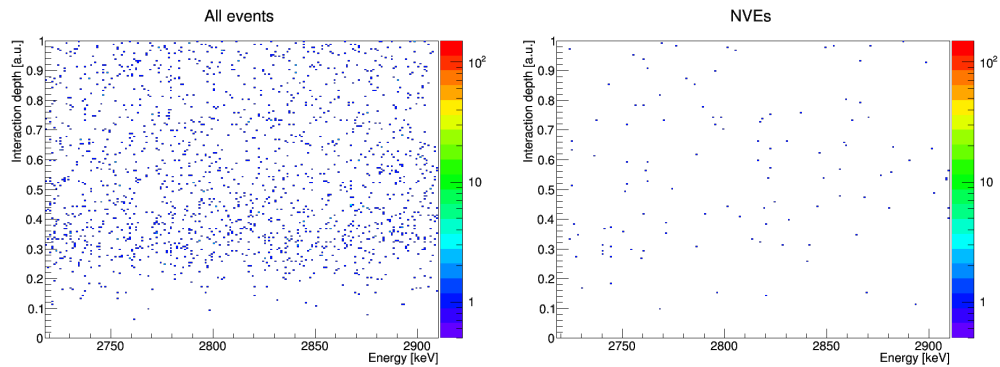


**Figure 6.12:** Remaining events in the ROI for the full spectrum (left) and NVEs (right) as a  $z$ - $E$ -plot. As additional cut,  $z$  is restricted to values from 0 to 1. In this region for  $z$  and  $E$ , the SVE flag removes approximately 93% of all events.

decreased. The cut `flag_bad_pulse` refuses additional 6 events and has a minor impact on the background index. In contrast, the LSE and `flag_MSE` cuts have a huge impact. The `flag_MSE` cut spares only  $10 \pm 3$  events and the LSE cut removes all events from the dataset. All events shown in Figure 6.13 are affected by these two cuts. The reason for this is not exactly known, but these cuts are especially developed for the pulse-shapes recorded at the LNGS. Hence, the LNGS pulse shape analysis cuts are not applicable to this dataset without adjustments.

The number of events surviving the foresaid cuts and the corresponding background indices are summarized in Table 6.3.



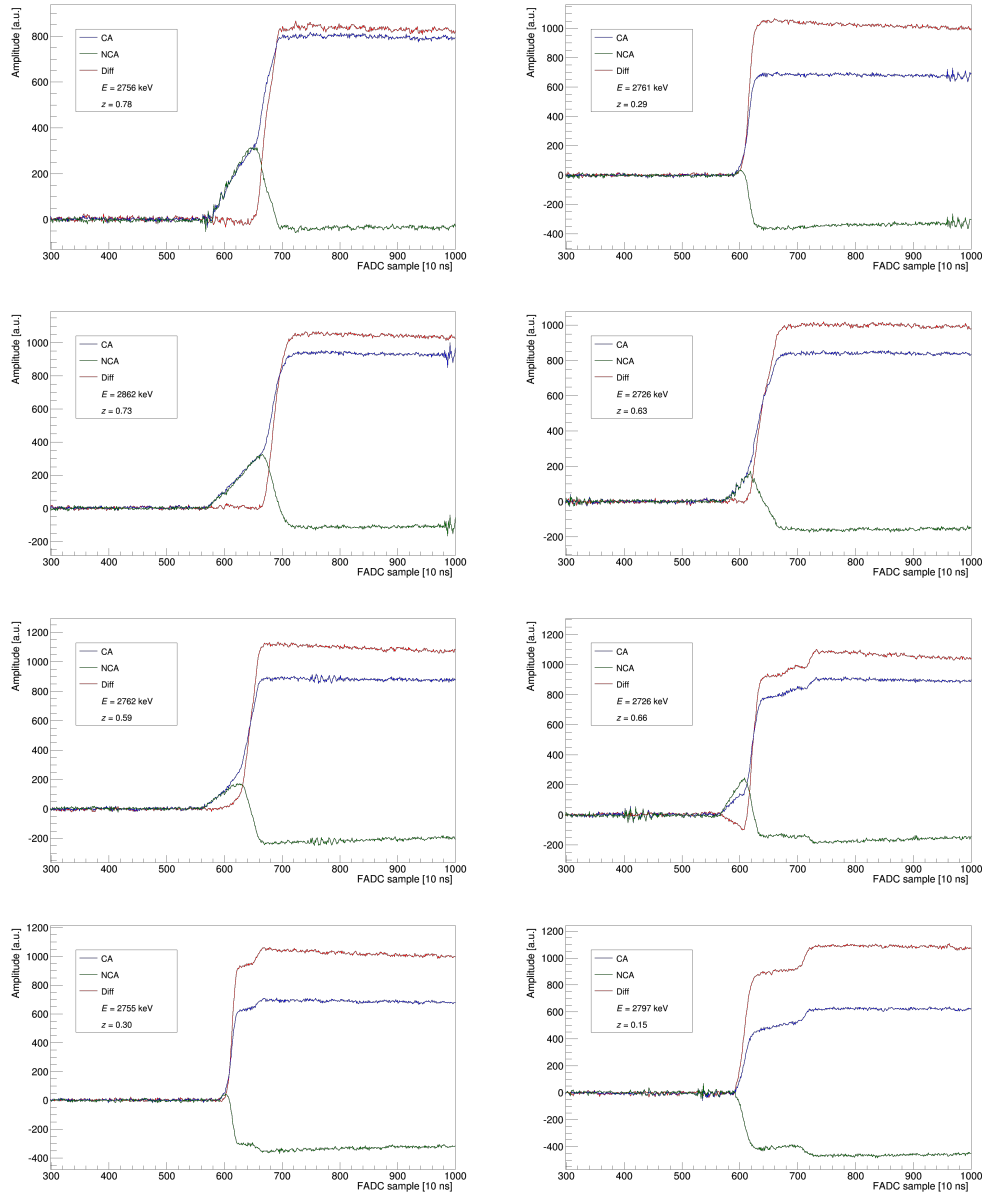


**Figure 6.13:** A selection of randomly chosen NVEs after application of the  $z$ -cut. The CA signal is shown in blue, the NCA signal in green and the difference pulse in red. The first five events are typical SSEs. The pulse shape of the last three events show characteristics of MSEs. The calculated Energy  $E$  and interaction depth  $z$  are given for every event.

**Table 6.3:** The number of events in the ROI surviving the different analysis cuts. The corresponding background indices  $B$  are calculated with an exposure of 0.649 kg·d.

Cuts applied	Number of events	$B$ [counts/keV/kg/y]
no cuts	$3171 \pm 56$	$9291 \pm 165$
$z$ -cut	$1728 \pm 42$	$5063 \pm 122$
NVE	$154 \pm 12$	$451 \pm 36$
$z$ -cut + NVE	$114 \pm 11$	$334 \pm 31$
$z$ -cut + NVE + flag_bad_pulse	$108 \pm 10$	$316 \pm 31$
$z$ -cut + NVE + flag_MSE	$10 \pm 3$	$29 \pm 9$
$z$ -cut + NVE + LSE	0	0

## 6.6 Characterization of Scintillator Veto Events

If no strong  $\alpha$  or  $\beta$  emitters are present in the liquid scintillator or the Delrin holder, the SVEs with energies above 2.6 MeV are due to charged cosmic ray particles. At sea level, muons are the most numerous charged particles with a mean energy of approximately 4 GeV. They are produced at a height of typically 15 km, when protons from the primary cosmic radiation react with protons and neutrons in the upper atmosphere and produce charged pions and kaons.

While charged kaons decay in (charged) pions or muons and the corresponding neutrinos, charged pions decay quasi solely in muons and the corresponding neutrinos:

$$\pi^+ \rightarrow \mu^+ + \nu_\mu \quad (6.4)$$

$$\pi^- \rightarrow \mu^- + \bar{\nu}_\mu. \quad (6.5)$$

At sea level, the angular distribution of muons with energies of  $\sim 3$  GeV is proportional to  $\cos^2 \theta$ . The integral intensity is approximately  $70 \text{ m}^{-2} \text{ s}^{-1} \text{ sr}^{-1}$  for vertical muons with momenta above 1 GeV, which corresponds roughly to  $1 \text{ cm}^{-2} \text{ s}^{-1}$  in case of horizontal detectors. The energy and angular dependent muon flux can be approximated with some minor restriction by the formula [125]

$$\frac{dN_\mu}{dE_\mu d\Omega} \approx \frac{0.14 \cdot E_\mu^{-2.7}}{\text{cm}^2 \text{ s sr GeV}} \quad (6.6)$$

$$\cdot \left( \left( 1 + \frac{1.1 \cdot E_\mu \cos \theta}{115 \text{ GeV}} \right)^{-1} + \left( 1 + \frac{1.1 \cdot E_\mu \cos \theta}{850 \text{ GeV}} \right)^{-1} \right), \quad (6.7)$$

where the first term corresponds to the contribution from pion decay and the second term from kaon decay, respectively.

For charged particles, the so called linear stopping power or mean rate of energy loss  $-dE/dx$  along a track through matter is described by the Bethe formula [89]:

$$-\frac{dE}{dx} = \frac{4\pi e^4 z^2}{m_e v^2} \cdot N \cdot Z \cdot \left[ \ln \left( \frac{2m_e v^2}{I} \right) - \ln \left( 1 - \frac{v^2}{c^2} \right) - \frac{v^2}{c^2} \right], \quad (6.8)$$

where  $v$  and  $ze$  are the particle velocity and charge. The permeated matter is described by the number density  $N$ , the atomic number  $Z$  and the mean excitation energy  $I$ . To describe the energy loss of electrons in matter, this formula has to be modified to account for radiative energy loss (bremsstrahlung) and Coulomb interactions.

The mean rate of energy loss has a broad minimum around  $\beta\gamma = 3.0$  to  $3.5$ , depending on the traversed matter. Most cosmic ray muons have energy loss rates close to this minimum and are called minimum-ionizing particles. The most important values for minimum-ionizing particles traversing Cd, Zn or Te are given in Table 6.4.

**Table 6.4:** Values for the mean energy loss of minimum-ionizing particles using the Bethe formula for Cd, Zn and Te [126, 127].

Element	Symbol	Z	A	$\rho$ [g/cm <sup>3</sup> ]	I [eV]	-dE/dx [MeV/cm]
Zinc	Zn	30	65.39	7.133	330.0	10.07
Cadmium	Cd	48	112.411	8.560	469.0	11.04
Tellurium	Te	52	127.60	6.240	485.0	7.656

Assuming that the mean energy loss per atom for compounds or mixtures of materials is additive, the stopping power of CdZnTe can be calculated using the so called Bragg-Kleemann rule [89]:

$$\left( \frac{dE}{dx} \right)_{\text{CdZnTe}} = \rho_{\text{CdZnTe}} \quad (6.9)$$

$$\cdot \left[ \frac{w_{\text{Cd}}}{\rho_{\text{Cd}}} \left( \frac{dE}{dx} \right)_{\text{Cd}} + \frac{w_{\text{Zn}}}{\rho_{\text{Zn}}} \left( \frac{dE}{dx} \right)_{\text{Zn}} + \frac{w_{\text{Te}}}{\rho_{\text{Te}}} \left( \frac{dE}{dx} \right)_{\text{Te}} \right], \quad (6.10)$$

with  $w_i$  representing the atomic fraction of the corresponding material. For the CdZnTe detectors used in the COBRA collaboration, the manufacturer states a Zinc concentration of 3.5% to 6% [104]. Measurements performed by the collaboration yield mean Zinc concentrations in the range from 5.4% to 5.8%. For a Zinc concentration of 5.6% and  $\rho_{\text{CdZnTe}}$  from Table 4.3, the mean energy loss  $\langle E \rangle$  of minimum-ionizing particles in CdZnTe is  $7.28 \text{ MeV cm}^{-1}$ .

In Figure 6.14 the deposited energy in all three detectors during the laboratory measurement presented in Section 6.5 as a  $z$ - $E$ -plot for two datasets: In the upper figure only the NVEs are plotted, in the lower figure the SVEs are shown. In

both figures reconstruction distortion at the cathode side are apparent. However, the distortions are different for the two datasets, as the distortion for the SVEs is distributed over nearly the whole energy range unlike in the case of the NVEs dataset. This indicates problems in the  $z$  reconstruction for muons and will be addressed later in this section.

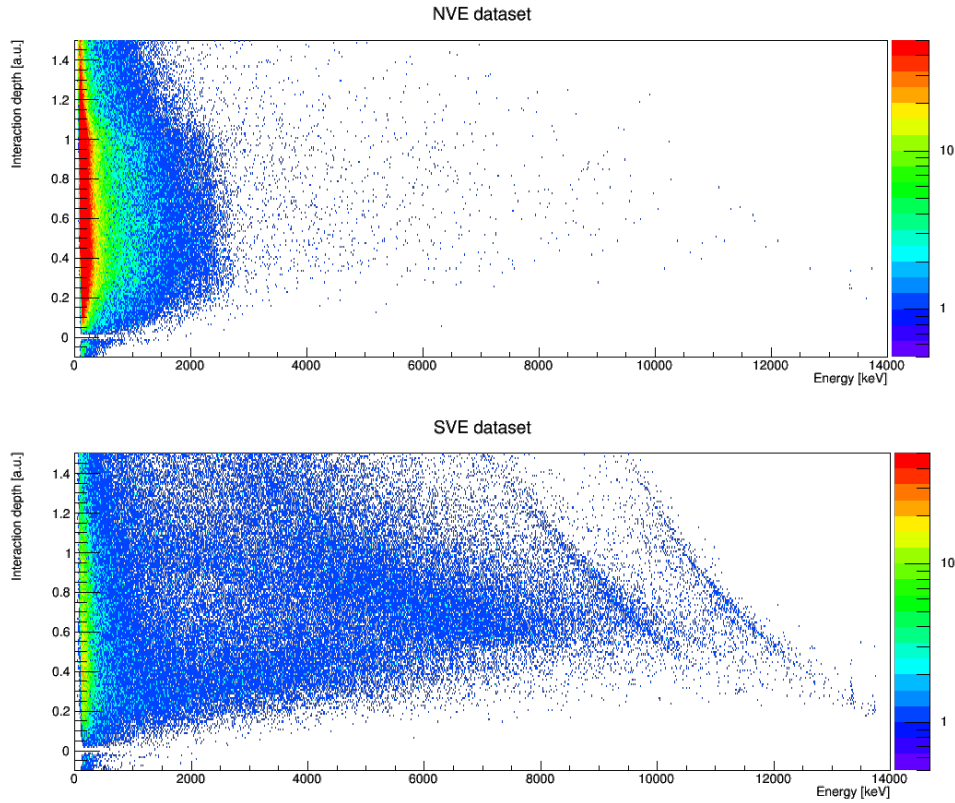


**Figure 6.14:**  $z$ - $E$ -plot for NVEs (top figure) and SVEs (bottom figure). In both datasets reconstruction distortions at the cathode side ( $z > 1$ ) are visible. In particular for the SVEs high  $z$  values are calculated over a broad energy range. Also two hyperbolic curves due to saturation effects in the FADCs are observable in the SVE dataset.

To describe the energy deposition of cosmic ray muons passing the detectors, a simple model is applied grouping the muons into five categories (see Figure 6.15):

1. Fully traversing: Entering at the anode and exiting at the cathode
2. Fully inclined traversing: Entering and exiting through opposite sides
3. Top entry: Entering at the anode and leaving through a side surface
4. Bottom exit: Entering through a side surface and exiting at the cathode
5. Inclined traversing: Entering and exiting through adjacent sides

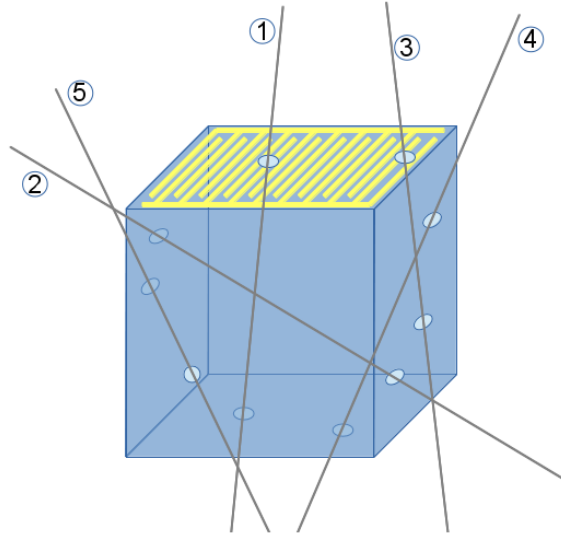


**Figure 6.15:** Schematic drawing of the five categories of muon passage through the detectors: Fully traversing (1), fully inclined traversing (2), top entry (3), bottom exit (4) and inclined traversing (5).

Assuming the detectors are cubes with edge length  $d$ , the covered distance in the detector  $s$  for fully traversing muons is  $d < s < \sqrt{3}d$ . For CdZnTe detectors with edge lengths of 1 cm, the deposited energy  $E_{\text{dep}} = s \cdot \langle E \rangle$  ranges from 7.28 MeV to 12.61 MeV. As the calculated interaction depth is an energy-weighted depth for non point-like energy depositions,  $z$  is 0.5 for fully traversing muons.

Muons with angles from  $54.7^\circ$  to  $90.0^\circ$  with respect to the vertical can produce fully inclined tracks in the detectors. Entering the detector through a side and exiting it at the opposite side, they also deposit energy in the range from 7.28 MeV to 12.61 MeV. For diagonal traversing muons with angles close to  $54.7^\circ$  the calculated interaction depth is also 0.5, but with higher angles closer to the horizontal the muons can intersect the detectors at any  $z$  values closer to 0 and 1. However, as the angular distribution is proportional to  $\cos^2 \theta$  with respect to the vertical, the number of muons falls off for increasing  $\theta$ .

Top entry muons penetrate the detectors at the anode side and leave the detectors through a side surface at a height  $h < z = 1$ , with  $h = 0$  cm at the anode and  $h = 1$  cm at the cathode. Assuming nearly vertical muons with a very small angle  $\theta$ , the covered distance is  $s \approx h$  and they are called minimal top entry muons. They deposited energy of  $E_{\text{dep}} \approx h \cdot \langle E \rangle$  and their calculated interaction depth is  $z = \frac{h}{2\text{cm}} \approx \frac{E_{\text{dep}}}{2\text{cm} \cdot \langle E \rangle} < 0.5$  with  $h$  given in cm. In a  $z$ - $E$ -plot, they form a clustered line from  $[0 \text{ MeV}, 0]$  to  $[7.28 \text{ MeV}, 0.5]$  with the slope  $0.0687 \text{ MeV}^{-1}$ , see Figure 6.16. Top entry muons with larger angles can deposit energies up to  $E_{\text{dep}} = \sqrt{2d^2 + h^2} \cdot \langle E \rangle$ , but their interaction depth is also  $z = \frac{h}{2\text{cm}}$ .

Basically, bottom exit muons can be treated analogously. They enter the detec-

tors at a height  $h > z = 0$  through a side surface and leave the detectors through the cathode. Assuming again nearly vertical muons with very small angle, the covered distance is  $s \approx 1 - h$ , the deposited energy is  $E_{\text{dep}} \approx (1 - h) \cdot \langle E \rangle$  and the calculated interaction depth is  $z = 1 - \frac{1-h}{2\text{cm}} \approx 1 - \frac{E_{\text{dep}}}{2\text{cm} \cdot \langle E \rangle} > 0.5$ . These minimal bottom exit muons form a clustered line from [0 MeV, 1] to [7.28 MeV, 0.5] with the slope  $-0.0687 \text{ MeV}^{-1}$ . Also, bottom exit muons with larger angles can deposit energies up to  $E_{\text{dep}} = \sqrt{2d^2 + h^2} \cdot \langle E \rangle$  with an interaction depth  $z = \frac{1-h}{2\text{cm}}$ .

In a  $z$ - $E$ -plot, minimal top entry and minimal bottom exit muons form a triangle of clustered events with its tip at [7.28 MeV, 0.5]. Only a fraction of inclined traversing muons can deposit energy in the area enclosed by this triangle, all other categorized muons mentioned before deposit energy on the contour or outside of the triangle. A graphic representation for the energy deposition versus the interaction depth for the before mentioned five muon categories is given in Figure 6.16.

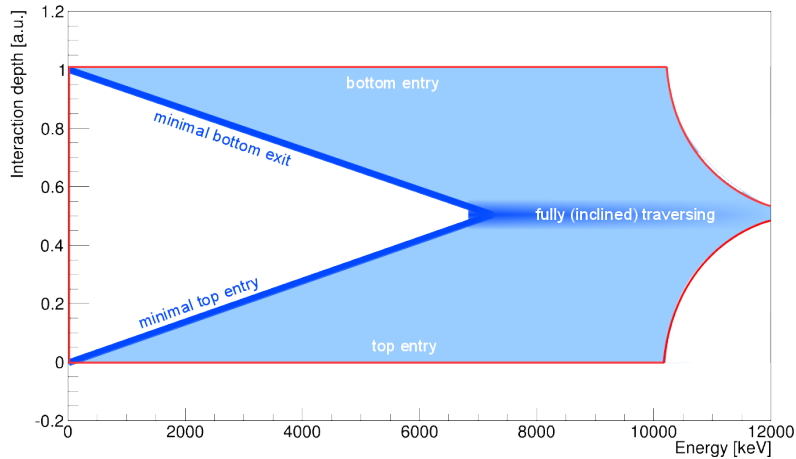


**Figure 6.16:** Graphical representation of the energy deposition versus the interaction depth for the five muon categories explained in the text. In principal, muons can deposit energy at any point in the red bordered area. Inside the white triangle, only inclined traversing muons can occur. Nearly vertical traversing muons deposit their energy on the dark blue lines.

The SVE dataset in Figure 6.14 shows regions with clearly accumulated amounts of entries. As the structure of these entries arises from the overlay of three detector spectra, the display of single detector spectra is reasonable and shown in Figure 6.17. Every single detector spectrum shows in general similar but not identical regions with accumulated entries. Nevertheless, the general scheme of energy deposition shown in Figure 6.16 is visible for every single detector. The formation of the characteristic triangle in every detector shows that the model for the passage of muons through the detectors is reasonable.

The hyperbola shaped clusters at high energies are most likely due to saturation

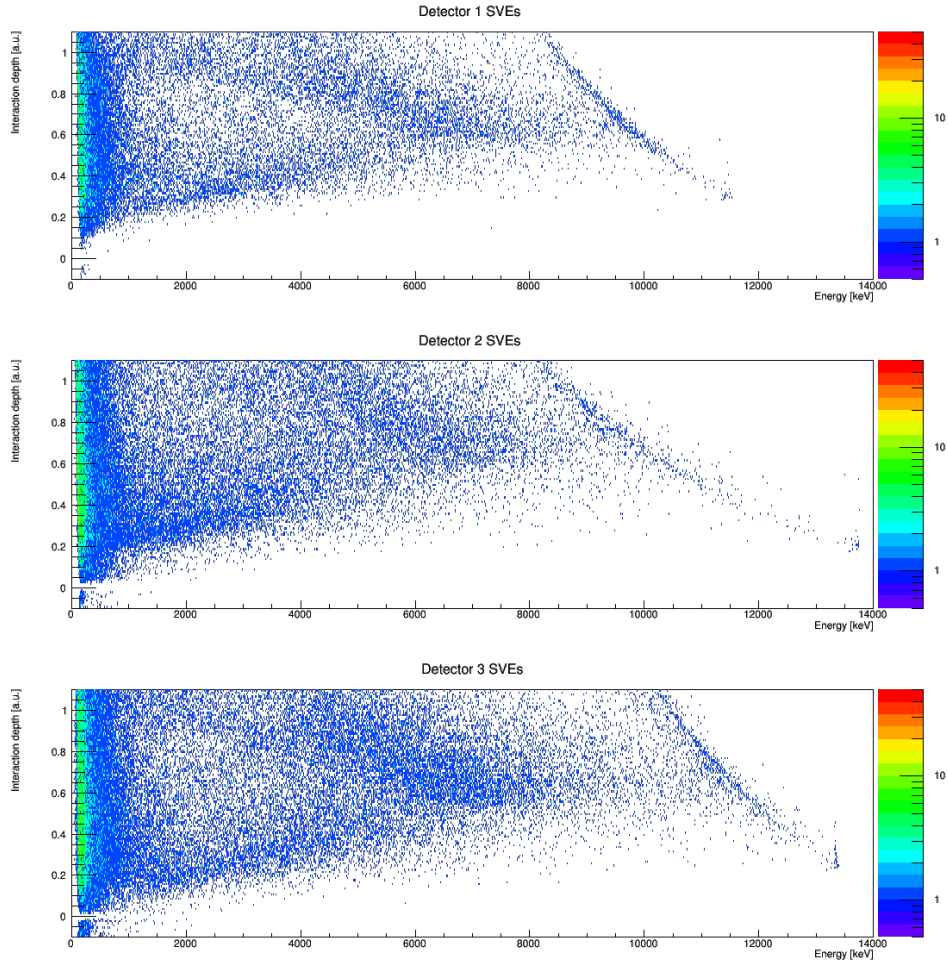


**Figure 6.17:** The SVE spectrum as shown in Figure 6.14 separated for every single detector. The triangular shaped entries predicted by the model of traversing muons shown in Figure 6.16 is visible in every detector.

effects in the FADCs. If  $CA_{\max}$  is the maximal recordable amplitude of the CA signal in the corresponding FADC channel, the maximum reconstructed energy  $E_{\max}$  can be calculated using Equations 4.11 and 4.12:

$$E_{\max}(z) = \frac{2 \cdot CA_{\max}}{z + 1}. \quad (6.11)$$

This formula describes accurately the saturation effects shown in Figure 6.17. The saturation curves for detector 1 and 2 are very similar, as their calibration parameters are similar, see Figure 6.1. In contrast, the calibration slope  $p_1$  for detector 3 is a factor  $\sim 1.2$  higher, resulting in a saturation curve at higher energies.

In comparison to the typical pulse-shapes originating from events without scintillation veto shown in Figure 6.13, the pulse-shapes generated by muons shown in Figure 6.18 have a much longer rise and fall time on the CA and NCA. This is

due to the continuous charge collection of events with energy depositions along a lengthy track in  $z$  direction.

All events from the SVE dataset show a noise pattern during the rise time on both the CA and NCA, which is not present in the dataset with removed SVEs. Therefore, it seems likely that this noise is due to electromagnetic interference generated by the acceleration of electrons in the PMTs. As this pattern is hardly observable in the difference pulse, the noise is symmetrically induced on the CA and NCA. The duration of the noise pattern ranges roughly from 60 ns to 120 ns, which is in good agreement with the transit time value of 41 ns given by the manufacturer (see Appendix C) and considering afterpulses and a non-delta distribution of the incoming light.

An additional EMI shield to prevent noise from the PMTs on the signal cables inside the operation vessel is not possible without a completely revised construction or alternative readout devices for the scintillation light. However, as the energy and interaction depth are calculated by the baselines before and after rise and fall of CA and NCA respectively, this noise pattern has an insignificant influence on the calculation of  $E$  and  $z$ .

In addition, a small undulation is visible especially in the difference pulse, independent from the noise generated by the PMTs. This hints to an unconstant energy deposition along the muon tracks. The undulation could also be caused by the drift of the generated electrons inside the detector to different rails of the coplanar grid. But as the muon flux is proportional to  $\cos^2 \theta$ , only a small number of muons pass the detectors perpendicular to the anode rails generating electrons that drift to multiple rails. Therefore, the number of small undulations shown in the pulse-shapes of Figure 6.18 are more likely explainable by an unconstant energy deposition from the muons.



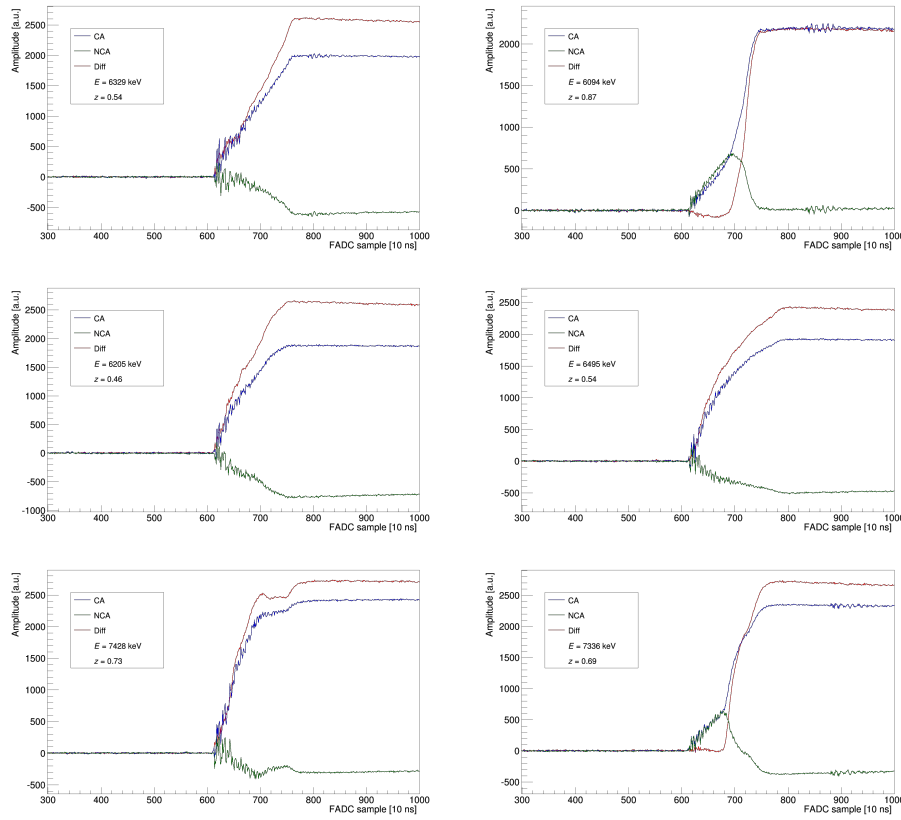


**Figure 6.18:** A selection of randomly chosen SVEs in the  $z$  range from 0 to 1. In contrast to the pulse-shapes from the NVE dataset shown in Figure 6.13, symmetrical noise pattern originating from the PMTs on both the CA and NCA are observable.

As already seen in Figure 6.14, the reconstruction of the interaction depth  $z$  produces remarkable distortions with a multitude of entries with  $z > 1$ . Similar to Figure 6.17, the SVEs separated for every detector are shown for a wide range of  $z$  in Figure 6.19. For every detector a parabolic band of clustered events parallel to the saturation curve is observable. In total,  $\sim 33\%$  of all SVEs are reconstructed outside the physical meaningful range of  $0 < z < 1$ .

In Figure 6.20 some typical muon events for  $z > 0$  are shown. In these examples mainly the NCA signal is responsible for the faulty reconstruction of both the energy and interaction depth. Since the NCA signal does not completely decline as in the pulse-shapes shown in Figures 6.13 and 6.18, the interaction depth is reconstructed to higher values and the energy is calculated to lower values. To obtain  $z$  values between 0 and 1, the NCA post-trigger baseline has to reach values equal to or less than zero, see Equation 4.12. This explains the observable band structures of muon events in Figure 6.19. But also the CA signals show edges and dips during the rise time, indicating disturbances in the electric field when muons traverse the detector.

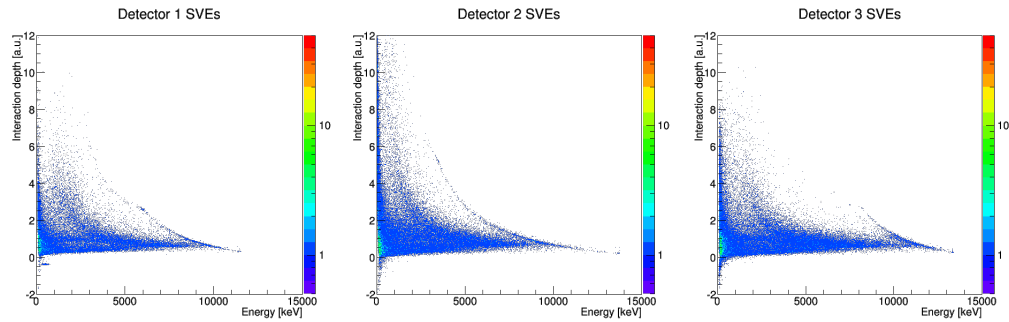


**Figure 6.19:** The SVE single detector spectra shown for a wide range of  $z$ . In total  $\sim 33\%$  of the SVEs are reconstructed outside the range of  $0 < z < 1$ . A hyperbolic band structure parallel to the saturation curve is observable for every detector. These bands most likely originate from the incomplete decline of NCA pulses leading to miscalculated values of  $z$  and  $E$ .

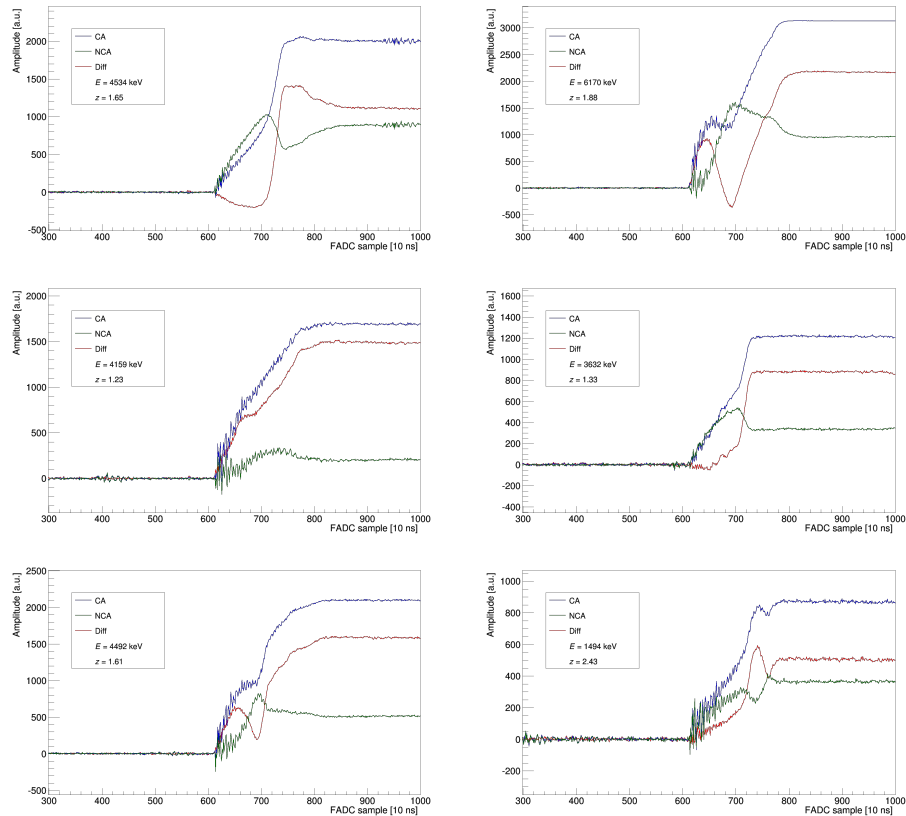


**Figure 6.20:** A selection of randomly chosen SVEs with a reconstructed  $z$  above 1. The CA signal is shown in blue, the NCA signal in green and the difference pulse in red.

Due to the distortions shown in Figure 6.19, the comparison of Monte Carlo simulations to the measured SVE spectrum is not easily possible. Also the saturation of the CA pulses in the FADCs cannot be addressed by the simulation. For the muon simulation the spectral shape given in Equation 6.7 is used. A comparison of the Monte Carlo simulation to the SVE spectrum of all three detectors is shown in Figure 6.21. The scaling of the simulation is chosen such it fits to the low energy region up to 2 MeV of the measured spectrum as good as possible.

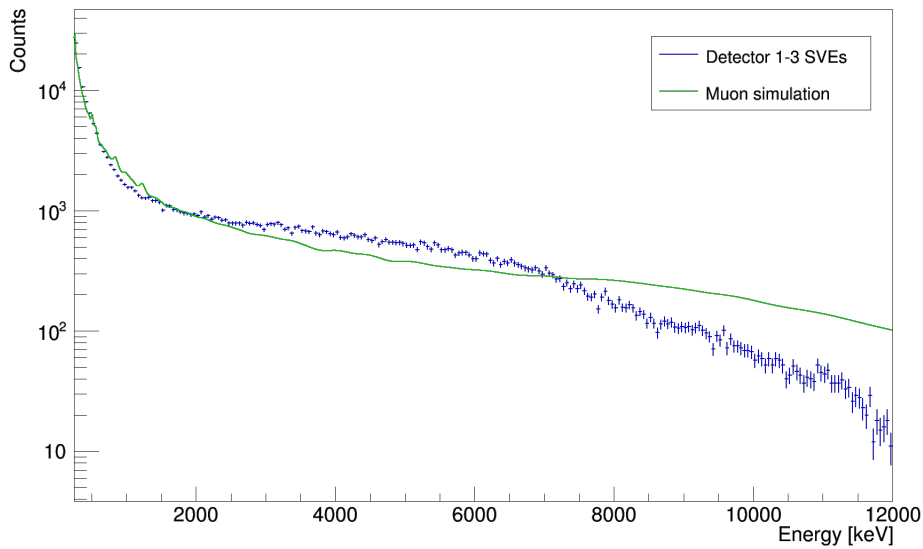


**Figure 6.21:** Comparison of the SVE spectrum of all three detectors to the simulated MC spectrum.

As can be seen in Figure 6.17, the saturation begins at  $z = 1$  for detectors 1 and 2 roughly at 9 MeV and for detector 3 roughly at 11 MeV. This is also visible in Figure 6.21, where the simulation overestimates the measured spectrum for energies larger than 7.5 MeV. For the energy range between 2.5 MeV and 7.5 MeV, the simulation underestimates the measured spectrum. This could be caused by the distortions of the NCA pulses leading to lower calculated values for  $E$  and higher values for  $z$ .

Like in Section 6.5, the standard analysis cuts presented in Section 5.4 are applicable to the SVE dataset. The outcome of the `flag_bad_pulse` cut applied on the SVE data is shown in Figure 6.22. More than 51 % of all events are rejected by this cut, especially for events with energies above 1 MeV. The reason for this was already shown in Figure 6.18. The noise pattern on the rising and falling CA and NCA pulses generated by the PMTs is responsible for the event rejection by this cut. As this issue is not avoidable without a completely modified construction of the operation vessel, the refusal of only unphysical events with the `flag_bad_pulse` cut is not possible for the existing set-up and dataset. Unfortunately, an efficiency

estimation for the `flag_bad_pulse` cut on the SVE dataset is not feasible.

The noise pattern on the CA and NCA pulses generated by the PMTs has also a major effect on the identification of lateral surface events. The applied cuts identifying DIP and ERT events are very sensitive to disturbances during the rise and fall of the CA and NCA signals. Therefore, most of the muon events with the PMT noise pattern are misleadingly interpreted as LSE, see Figure 6.23.

The effect of the `flag_MSE` cut on the SVE data is shown in Figure 6.24. In this plot all events flagged as multi-site events are shown. The effect of the `flag_MSE` cut for different energy thresholds is summarized in Table 6.5. Most of the muons depositing at least 1 MeV of energy are identified as MSE. For energies above 2 MeV, even  $\sim 97\%$  of all muons are identified as multi-site events.

**Table 6.5:** Fraction of MSE in the SVE dataset. The `flag_MSE` cut identifies nine out of ten muons depositing energy of at least 1 MeV as multi-site events. For muon energies above 2 MeV, only  $\sim 3\%$  of all events are identified as single-site events. The restriction to  $z$  values between 0 and 1 has only a small impact on the efficiency of the `flag_MSE` cut.

Energy range	Fraction of MSE for all $z$	Fraction of MSE for $0 < z < 1$
all energies	$0.412 \pm 0.001$	$0.411 \pm 0.002$
0.0 MeV to 0.5 MeV	$0.176 \pm 0.001$	$0.189 \pm 0.001$
0.5 MeV to 1.0 MeV	$0.760 \pm 0.007$	$0.759 \pm 0.008$
1.0 MeV to 1.5 MeV	$0.861 \pm 0.011$	$0.888 \pm 0.015$
1.5 MeV to 2.0 MeV	$0.926 \pm 0.013$	$0.928 \pm 0.019$
above 2.0 MeV	$0.967 \pm 0.005$	$0.973 \pm 0.006$

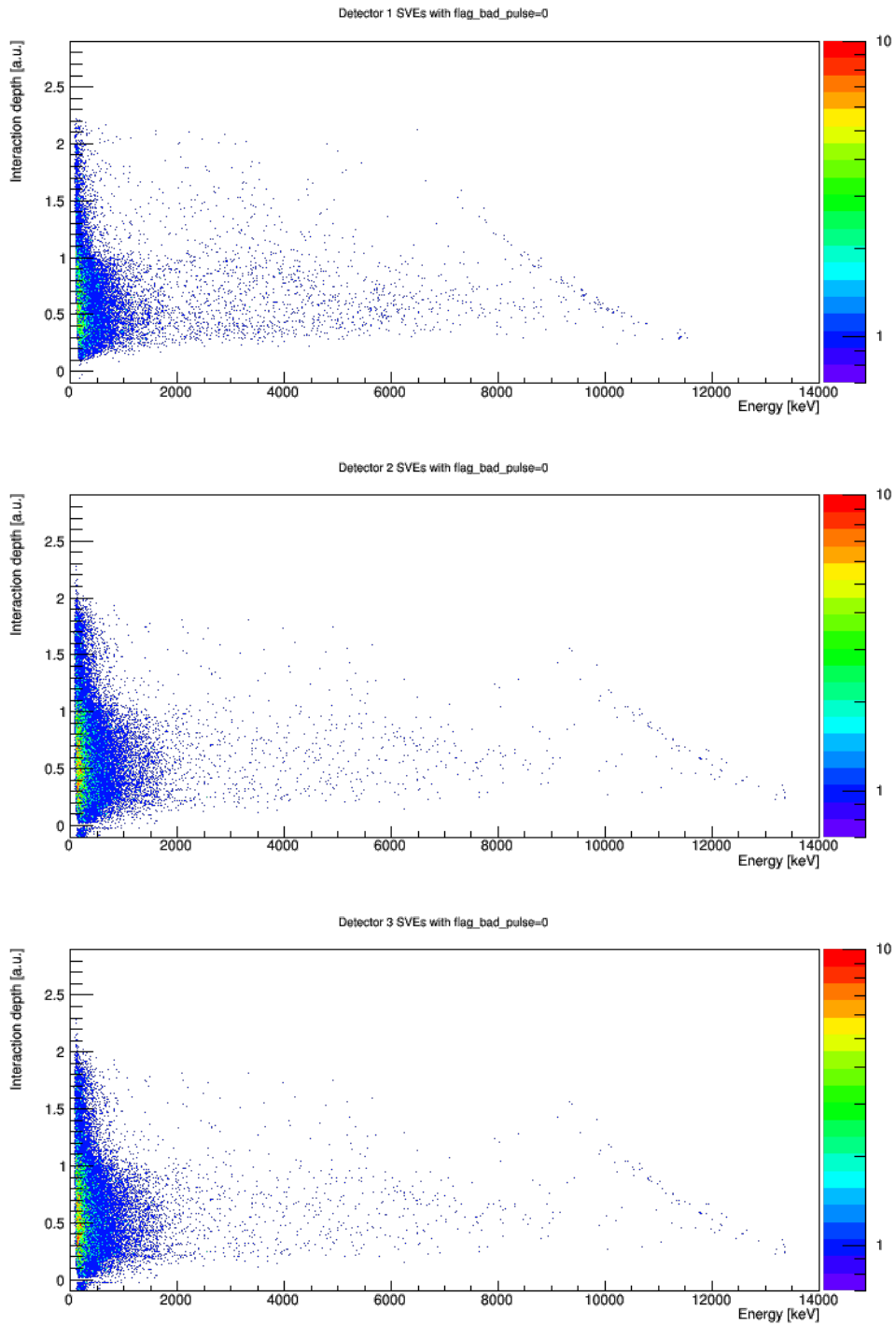


**Figure 6.22:** The SVE single detector spectra as shown in Figure 6.17, but only with events passing the flag\_bad\_pulse cut. This cut removes 51.4% of all events, especially events with energies above 1 MeV.

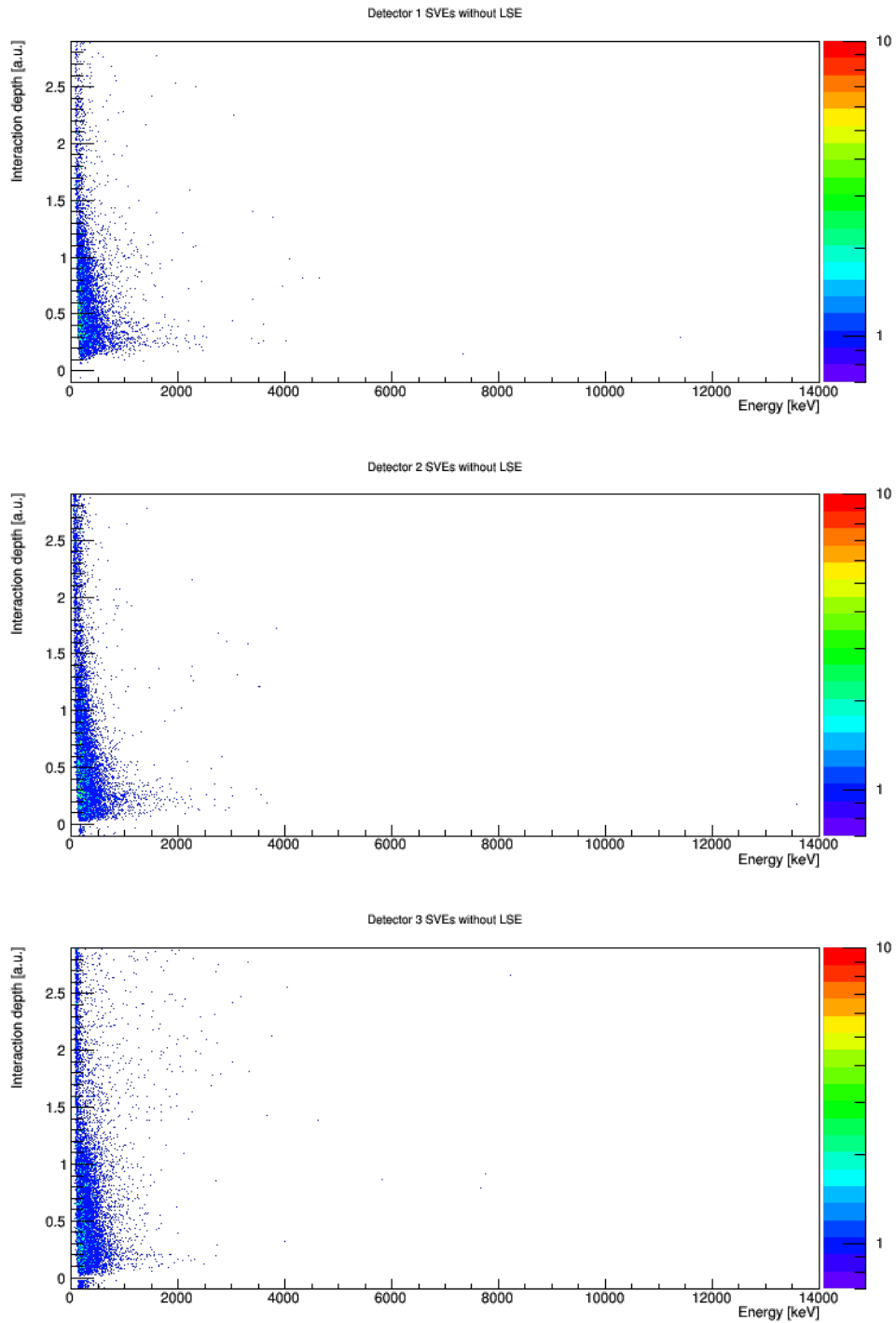


**Figure 6.23:** The SVE single detector spectra as shown in Figure 6.17, but only with events not flagged as LSE. Due to the noise on the CA and NCA pulses during their rise time, this cut misleadingly interprets muons as surface events.

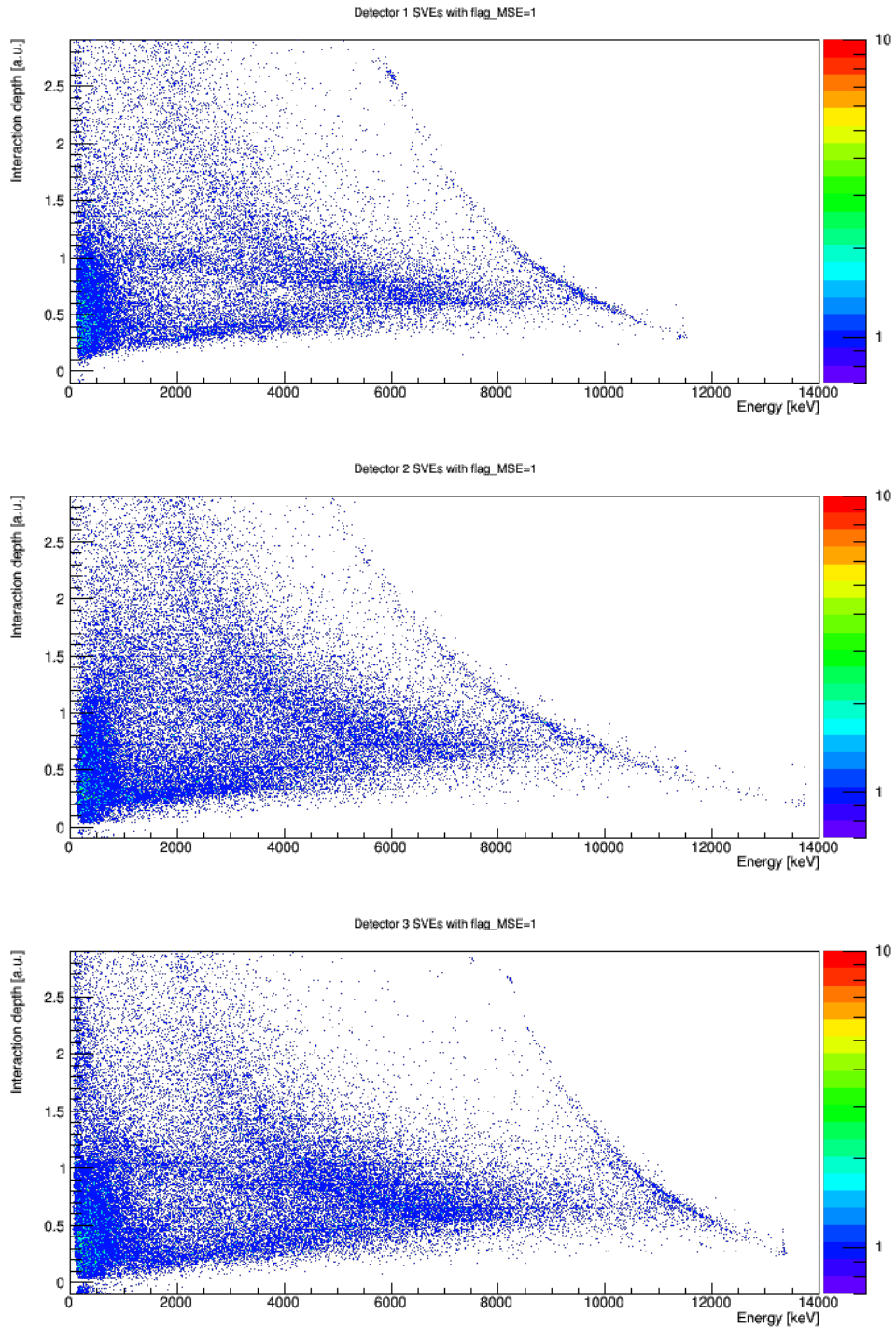


**Figure 6.24:** The SVE single detector spectra as shown in Figure 6.17, but only with events flagged as MSE. This cut removes about 40 % of all events, especially events with energies below 1 MeV.





## Chapter 7

# Summary and Outlook

This thesis describes the design and construction of a test set-up for CdZnTe semiconductor detectors immersed in liquid scintillator. The operation of CdZnTe detectors after years of immersion is demonstrated. Data taken with this set-up in the measurement period from December 2014 to February 2015 is analyzed. The background reduction capabilities of the liquid scintillator veto and cosmic ray muons are studied. The results from the test set-up are compared to Monte Carlo simulations.

Events originating from the Delrin holder structure and from the Glyptal lacquer applied on the CdZnTe detectors generate a large part of the background at the current COBRA demonstrator at the LNGS underground laboratory. With regard to a large scale COBRA set-up, the background index has to be reduced significantly to a level of  $10^{-3}$  counts/keV/kg/a to reach the desired half-life sensitivity of  $2 \cdot 10^{26}$  years for the neutrinoless double beta decay of  $^{116}\text{Cd}$ . This requires the operation of the detectors in a very clean environment and liquid scintillator is an excellent option as a high purity passivation material.

Prior to the design of the test set-up, extensive compatibility tests have been performed to identify appropriate materials. Stainless steel is chosen for the construction of the operation and storage vessels, the connecting tubes are made of Teflon. The examined glue UHU 'Hart', the instant adhesive Superglue 15 and the silver conduction glue LS200 are not soluble and hence usable in liquid scintillator. Also materials already used in the COBRA demonstrator like the SM50 high voltage cables and Delrin for the detector holders are suitable for the operation in liquid scintillator. Only the O-rings made of Viton are not entirely insoluble and should be replaced by O-rings made of or coated with Teflon for a long-term experiment.

The core of the test set-up consists of four CdZnTe detectors of size  $1\text{ cm}^3$  mounted on a holder made of stainless steel and Delrin, which is placed in the center of the operation vessel. During design, construction and commissioning of the set-up, the unpainted detectors were already stored in liquid scintillator

for three years. The design of the feedthroughs for the high voltage supply and anode readout is an important aspect for the successful operation of the detectors, as they have to be liquid-tight, insolvable and shielded against electromagnetic disturbances. The scintillation light is read out with two photomultiplier tubes in the upper and lower flange of the vessel. The veto signal is generated by a logical AND circuit from the PMT signals and recorded together with the detectors anode signals by an FADC.

Due to the FADC-based full pulse shape recording of the detectors, the calculation of the interaction depth between anode and cathode is possible. This allows for the rejection of background events and the acquisition of typical muon pulse shapes in combination with the liquid scintillator veto. A software cut already implemented in the COBRA analysis framework identifies roughly 97 % of all cosmic ray muons as multi-site events. However, a significant fraction of cosmic muons cause unexpected signals on the non-collecting anodes, leading to miscalculations for the energy and interaction depth. This detector behavior has to be further investigated.

In total 0.649 kg·d of data, acquired in the measurement period from December 2014 to February 2015, are analyzed with respect to the background reduction capabilities of the liquid scintillator veto. In the region of interest for the COBRA experiment around 2813.5 keV, the veto discards a factor of  $0.93 \pm 0.05$  of all energy depositions in the detectors. About 7 % of the background events remain, reducing the background index by more than one order of magnitude to  $(334 \pm 31)$  counts/keV/kg/a. Due to the average energy resolution of only 6.7 % FWHM, the remaining background in the CdZnTe detectors mostly consists of  $\gamma$ -radiation from the  $^{208}\text{Tl}$  decay at 2.6 MeV. For energies between 3 MeV and 4 MeV, the veto actually discards  $0.97 \pm 0.02$  of all background events. This background reduction of nearly two orders of magnitude is supposed to be achievable with the current set-up and CdZnTe detectors of 3.5 % FWHM energy resolution or better.

Toward a concept for a large scale experiment with over 10000 detectors and a source mass of roughly 400 kg, results from the COBRA demonstrator set-up are taken into account. Especially  $\alpha$ -contaminations on the support structure and in the lacquer have to be significantly reduced. Liquid scintillator as replacement for the lacquer and as a high purity environment can veto and shield external radiation from the detectors. This application would also allow for the moderation and capture of neutrons, further reducing the background. The operating ability of the CdZnTe detectors after several years of immersion demonstrates the applicability of liquid scintillator for a long-term COBRA experiment.

Currently, the use of liquid scintillator is not incorporated in the plans for a large scale experiment. To account for this, the design of the holder structures and the shield has to be modified. Also, the durability of components recently considered for the  $6\text{ cm}^3$  detectors has to be studied. Especially the reliability of ASICs and FPGAs in liquid scintillator is important. In addition, a concept

for the light collection inside an array consisting of about 10000 detectors has to be developed. Here, the use of wavelength-shifting fiber optics collecting the scintillation light and guiding it to multichannel PMTs or avalanche photo diodes is a promising solution. Furthermore, purification and liquid handling systems have to be developed. The application of liquid scintillator used as a refrigerant allows in addition for the cooling of the CdZnTe detectors, leading to better energy resolution and low energy threshold.

## Appendix A

# Uranium Decay Chain

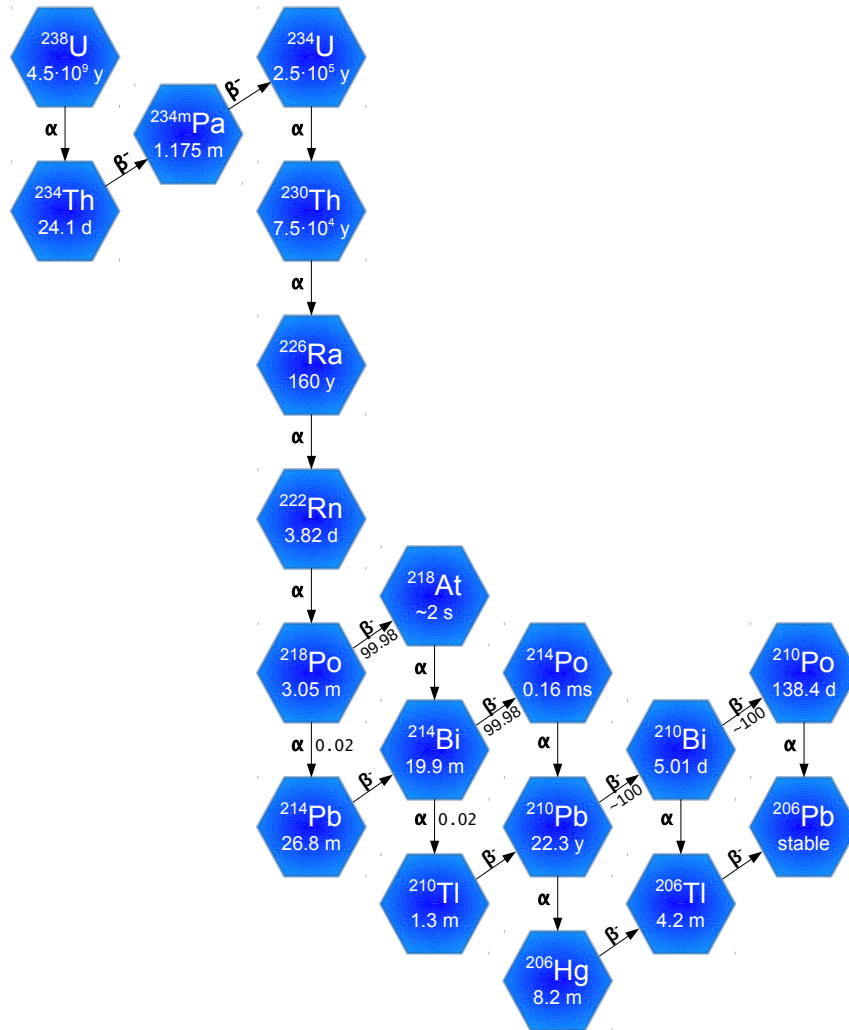


**Figure A.1:** Illustration of Uranium decay chain starting with  $^{238}\text{U}$  and ending in  $^{206}\text{Pb}$ . All values taken from Table A.1.

**Table A.1:** Overview of the Uranium decay chain. For each decay the half-life of the isotope, the branching ratio and the energy of emitted  $\alpha$ -,  $\beta$ - and  $\gamma$ -rays is shown [128].  $^{206}\text{Hg}$  and  $^{206}\text{Tl}$  are shown in Figure A.1 but not listed in this table, as their mother nuclides have a very low branching ratio for the  $\alpha$ -decays.

half-life	isotopes decay branch [%]	$\alpha$ -decay energy [MeV] (branch [%])	$\beta$ -decay energy [MeV] (branch [%])	$\gamma$ -decay energy [keV] (emiss. prob. [%])
4.468 · 10 <sup>9</sup> y	$^{238}_{92}\text{U}$ 100 ↓ $\alpha$	$\alpha$ : 4.197 (77) $\alpha$ : 4.147 (23)		$\gamma$ : 49.55 (0.062)
24.1 d	$^{234}_{90}\text{Th}$ 100 ↓ $\beta$		$\beta$ : 0.199 (72.5) $\beta$ : 0.104 (17.8) $\beta$ : 0.060 (7.1)	$\gamma$ : 92.37 (2.42) $\gamma$ : 63.28 (4.1) $\gamma$ : 92.79 (2.39)
1.175 m	$^{234m}_{91}\text{Pa}$ 100 ↓ $\beta$		$\beta$ : 2.29 (98.4) $\beta$ : 1.53 (0.62) $\beta$ : 1.25 (0.74)	$\gamma$ : 766.37 (0.316) $\gamma$ : 1001.03 (0.839)
2.45 · 10 <sup>5</sup> y	$^{234}_{92}\text{U}$ 100 ↓ $\alpha$	$\alpha$ : 4.775 (72.5) $\alpha$ : 4.723 (27.5)		$\gamma$ : 53.20 (0.123)
7.538 · 10 <sup>4</sup> y	$^{230}_{90}\text{Th}$ 100 ↓ $\alpha$	$\alpha$ : 4.688 (76.3) $\alpha$ : 4.621 (23.4)		$\gamma$ : 67.67 (0.38)
1600 y	$^{226}_{88}\text{Ra}$ 100 ↓ $\alpha$	$\alpha$ : 4.784 (94.5) $\alpha$ : 4.601 (5.55)		$\gamma$ : 186.10 (3.51)*
3.8235 d	$^{222}_{86}\text{Rn}$ 100 ↓ $\alpha$	$\alpha$ : 5.490 (99.9) $\alpha$ : 4.987 (0.08)		
3.05 m	$^{218}_{84}\text{Po}$ 0.018 99.98	$\alpha$ : 6.002 (100)		
~2 s	$\beta \swarrow \searrow \alpha$ $^{218}_{85}\text{At}$ $^{214}_{82}\text{Pb}$		$\beta$ : 0.73 (40.5)	$\gamma$ : 295.21 (18.15)
26.8 m	$\alpha \searrow \swarrow \beta$		$\beta$ : 0.67 (46)	$\gamma$ : 241.98 (7.12)* $\gamma$ : 351.92 (35.1)
19.9 m	$^{214}_{83}\text{Bi}$ 0.021 99.979 $\alpha \swarrow \searrow \beta$		$\beta$ : 3.275 (19.9) $\beta$ : 1.88 (7.18) $\beta$ : (17.5) $\beta$ : (8.26) $\beta$ : 1.51 (16.9) $\beta$ : 1.02 (16.9)	$\gamma$ : 609.32 (44.6)* $\gamma$ : 768.36 (4.76)* $\gamma$ : 1120.29 (14.7)* $\gamma$ : 1238.11 (5.78)* $\gamma$ : 1764.49 (15.1)* $\gamma$ : 2204.21 (4.98)*
1.3 m	$^{210}_{81}\text{Tl}$ $^{214}_{84}\text{Po}$	$\alpha$ : 7.687 (100)		
164.3 $\mu\text{s}$	$\beta \searrow \swarrow \alpha$			
22.3 y	$^{210}_{82}\text{Pb}$ ~100 ↓ $\beta$		$\beta$ : 0.063 (19) $\beta$ : 0.017 (81)	$\gamma$ : 46.54 (4.24)
5.013 d	$^{210}_{83}\text{Bi}$ ~100 ↓ $\beta$		$\beta$ : 1.161 (99)	
138.4 d	$^{210}_{84}\text{Po}$ 100 ↓ $\alpha$	$\alpha$ : 5.305 (99)		
stable	$^{206}_{82}\text{Pb}$			



## Appendix B

# Thorium Decay Chain

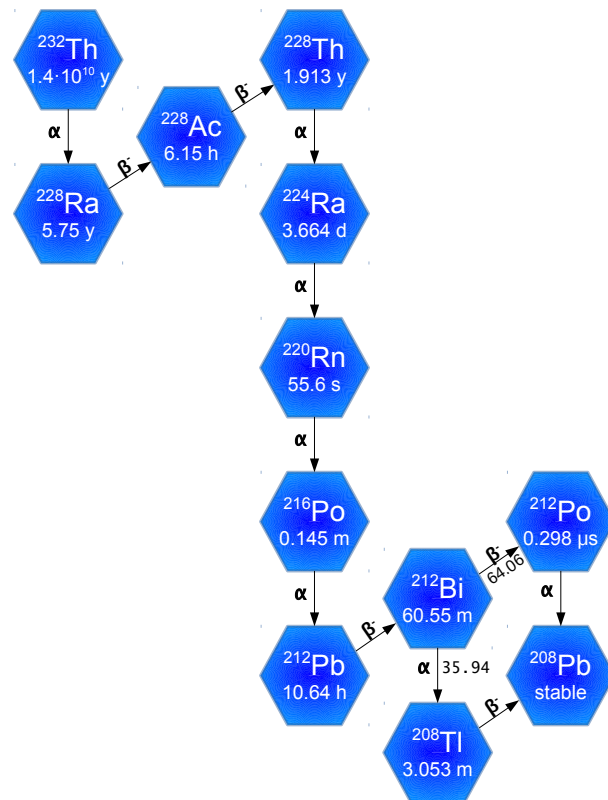


**Figure B.1:** Illustration of Thorium decay chain starting with  $^{232}\text{Th}$  and ending in  $^{208}\text{Pb}$ . All values taken from Table A.1.

**Table B.1:** Overview of the Thorium decay chain. For each decay the half-life of the isotope, the branching ratio and the energy of emitted  $\alpha$ -,  $\beta$ - and  $\gamma$ -rays is shown [128].

half-life	isotopes decay branch [%]	$\alpha$ -decay energy [MeV] (branch [%])	$\beta$ -decay energy [MeV] (branch [%])	$\gamma$ -decay energy [keV] (emiss. prob. [%])
1.405·10 <sup>10</sup> y	<sup>232</sup> <b>Th</b> 90 100 ↓ $\alpha$	$\alpha$ : 4.012 (77.9) $\alpha$ : 3.954 (22.1)		$\gamma$ : 63.81 (0.27)
5.75 y	<sup>228</sup> <b>Ra</b> 88 100 ↓ $\beta$		$\beta$ : 0.039 (60) $\beta$ : 0.015 (40)	
6.15 h	<sup>228</sup> <b>Ac</b> 89 100 ↓ $\beta$		$\beta$ : 2.18 (10) $\beta$ : 1.70 (11.6) $\beta$ : 1.11 (31.0)	$\gamma$ : 338.32 (11.3) $\gamma$ : 968.97 (16.2)* $\gamma$ : 911.21 (26.6)*
1.9131 y	<sup>228</sup> <b>Th</b> 90 100 ↓ $\alpha$	$\alpha$ : 5.423 (71.1) $\alpha$ : 5.340 (28.2) $\alpha$ : 5.221 (0.44)		$\gamma$ : 84.37 (1.22) $\gamma$ : 215.99 (0.28)
3.664 d	<sup>224</sup> <b>Ra</b> 88 100 ↓ $\alpha$	$\alpha$ : 5.685 (94.9) $\alpha$ : 5.449 (5.1)		$\gamma$ : 240.99 (4.1)
55.6 s	<sup>220</sup> <b>Rn</b> 86 100 ↓ $\alpha$	$\alpha$ : 6.288 (99.9) $\alpha$ : 5.747 (0.11)		$\gamma$ : 549.73 (0.11)
0.145 s	<sup>216</sup> <b>Po</b> 84 100 ↓ $\alpha$	$\alpha$ : 6.778 (100)		
10.64 h	<sup>212</sup> <b>Pb</b> 82 100 ↓ $\beta$		$\beta$ : 0.569 (12) $\beta$ : 0.331 (83) $\beta$ : 0.159 (5)	$\gamma$ : 300.09 (3.25) $\gamma$ : 238.63 (43.5)
60.55 m	<sup>212</sup> <b>Bi</b> 83 35.94 64.06 $\alpha \swarrow \searrow \beta$	$\alpha$ : 6.089 (27.1) $\alpha$ : 6.050 (69.9)	$\beta$ : 2.248 (86.6) $\beta$ : 1.521 (6.8)	$\gamma$ : 1620.74 (1.5)* $\gamma$ : 727.33 (6.7)
3.053 m 0.298 $\mu$ s	<sup>208</sup> <b>Tl</b> <sup>212</sup> <b>Po</b> 81 84 $\beta \searrow \swarrow \alpha$	$\alpha$ : 8.785 (100)	$\beta$ : 1.80 (51) $\beta$ : 1.52 (21.7) $\beta$ : 1.29 (22.8) $\beta$ : 1.52 (3.1)	$\gamma$ : 583.19 (30.6)* $\gamma$ : 860.56 (4.5)* $\gamma$ : 510.77 (8.2) $\gamma$ : 2614.53 (35.8)*
stable	<sup>208</sup> <b>Pb</b> 82			



## Appendix C

# ET Enterprise 9829B Photomultiplier Tube



# 51 mm (2") photomultiplier 9829B series data sheet

## 1 description

The 9829B is a 51 mm (2") diameter, end window photomultiplier with a thin domed window, sandblasted for enhanced cathode sensitivity, blue-green sensitive bialkali photocathode and 12 BeCu dynodes of linear focused design for good linearity and timing. The 9829QB is a variant for applications requiring uv sensitivity.

## 2 applications

- liquid scintillation counting
- photon counting of bio- and chemi-luminescent samples
- low light level detection

## 3 features

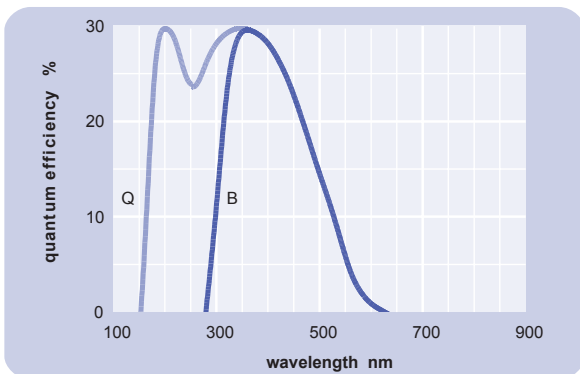
- good SER

## 4 window characteristics

	9829B borosilicate	9829QB* fused silica
spectral range**(nm)	290 - 630	160 - 630
refractive index (n <sub>s</sub> )	1.49	1.46
K (ppm)	300	<10
Th (ppb)	250	<10
U (ppb)	100	<10

\*note that the sidewall contains graded seals of high K content  
\*\*wavelength range over which quantum efficiency exceeds 1% of peak

## 5 typical spectral response curves

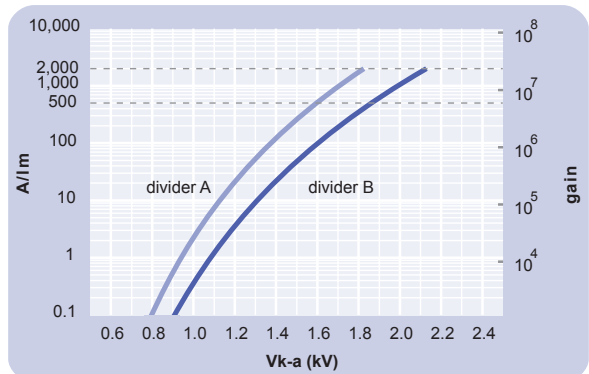


## 6 characteristics

	unit	min	typ	max
<b>photocathode: bialkali</b>				
active diameter	mm		46	
quantum efficiency at peak	%		30	
luminous sensitivity	μA/lm		85	
with CB filter		9.5	12.5	
with CR filter			2	
<b>dynodes: 12LFBBeCu</b>				
<b>anode sensitivity in divider A:</b>				
nominal anode sensitivity	A/lm		500	
max. rated anode sensitivity	A/lm		2000	
overall V for nominal A/lm	V		1600	1900
overall V for max. rated A/lm	V		1800	
gain at nominal A/lm	x 10 <sup>6</sup>		6	
<b>dark current at 20 °C:</b>				
dc at nominal A/lm	nA		3	10
dc at max. rated A/lm	nA		12	
dark count rate	s <sup>-1</sup>		300	
<b>pulsed linearity (-5% deviation):</b>				
divider A	mA		50	
divider B	mA		150	
<b>rate effect (I<sub>a</sub> for Δg/g=1%):</b>				
	μA		1	
<b>magnetic field sensitivity:</b>				
the field for which the output decreases by 50 %				
most sensitive direction	T x 10 <sup>-4</sup>		1	
<b>temperature coefficient:</b>	% °C <sup>-1</sup>		± 0.5	
<b>timing:</b>				
single electron rise time	ns		2	
single electron fwhm	ns		3	
single electron jitter (fwhm)	ns		2.2	
multi electron rise time	ns		3.2	
multi electron fwhm	ns		4.5	
transit time	ns		41	
<b>weight:</b>	g		130	
<b>maximum ratings:</b>				
anode current	μA			100
cathode current	nA			100
gain	x 10 <sup>6</sup>			25
sensitivity	A/lm			2000
temperature	°C	-30		60
V (k-a) <sup>(1)</sup>	V			2800
V (k-d1)	V			500
V (d-d) <sup>(2)</sup>	V			450
ambient pressure (absolute)	kPa			202

<sup>(1)</sup> subject to not exceeding max. rated sensitivity <sup>(2)</sup> subject to not exceeding max rated V(k-a)

## 7 typical voltage gain characteristics



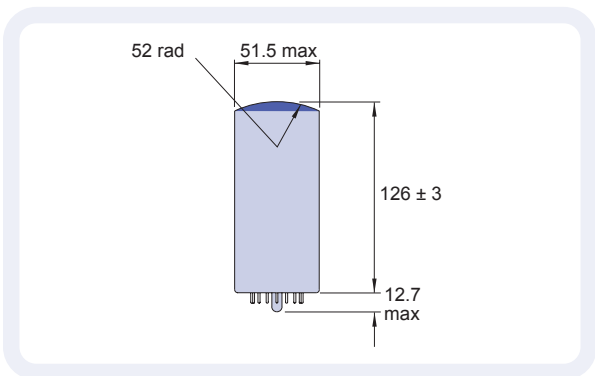
### 8 voltage divider distribution

	k	d <sub>1</sub>	d <sub>2</sub>	.....	d <sub>8</sub>	d <sub>9</sub>	d <sub>10</sub>	d <sub>11</sub>	d <sub>12</sub>	a	
A	300V	R	.....	R	R	R	R	R	R	R	Standard
B	300V	R	.....	R	R	1.25R	1.5R	2R	3R		High Pulsed Linearity

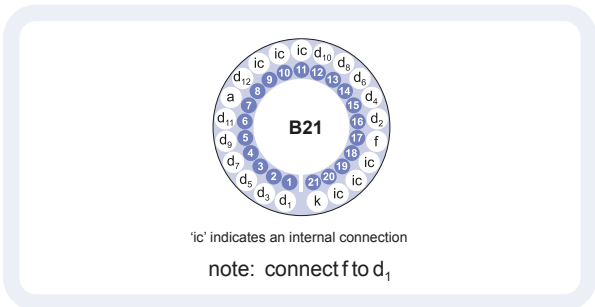
note: focus connected to d<sub>1</sub>

Characteristics contained in this data sheet refer to divider A unless stated otherwise.

### 9 external dimensions mm



### 10 base configuration (viewed from below)



Our range of B21 sockets, available for this series, includes versions with or without a mounting flange, and versions with contacts for mounting directly onto printed circuit boards.

### 11 handling instructions

The window of this pmt has been specially cleaned to give maximum efficiency. It should not be touched with fingers or allowed to come into contact with oil or grease. The window can be cleaned with isopropyl alcohol to remove oil deposits.

### 12 ordering information

The 9829B meets the specification given in this data sheet. You may order **variants** by adding a suffix to the type number. You may also order **options** by adding a suffix to the type number. You may order product with **specification options** by discussing your requirements with us. If your selection option is for one-off order, then the product will be referred to as 9829A. For a repeat order, **ET Enterprises** will give the product a two digit suffix after the letter B, for example B21. This identifies your specific requirement.

**9829**

**window variants**

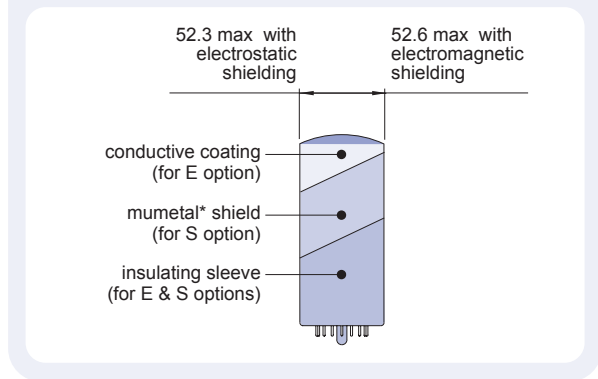
- Q** fused silica

**options**

- E** electrostatic shielding see drawing below
- S** electromagnetic shielding see drawing below
- M** supplied with spectral response calibration

**specification options**

- B** as given in data sheet
- A** single order to selected specification
- Bnn** repeat order to selected specification



### 14 voltage dividers

The standard voltage dividers available for these pmts are tabulated below:

	k	d <sub>1</sub>	d <sub>2</sub>	d <sub>3</sub>	.....	d <sub>8</sub>	d <sub>9</sub>	d <sub>10</sub>	d <sub>11</sub>	d <sub>12</sub>	a
C628A	3R	R	R	.....	R	R	R	R	R	R	
C628B	3R	R	R	.....	R	1.25R	1.5R	2R	3R		
C628C	300 V	R	R	.....	R	R	R	R	R		
C628D	300 V	R	R	.....	R	1.25R	1.5R	2R	3R		

note: focus connected to d<sub>1</sub>

R = 330 kΩ

\*mumetal is a registered trademark of Magnetic Shield Corporation

**ET Enterprises Limited**  
45 Riverside Way  
Uxbridge UB8 2YF  
United Kingdom  
tel: +44 (0) 1895 200880  
fax: +44 (0) 1895 270873  
e-mail: sales@et-enterprises.com  
web site: www.et-enterprises.com

**ADIT Electron Tubes**  
300 Crane Street  
Sweetwater TX 79556 USA  
tel: (325) 235 1418  
toll free: (800) 521 8382  
fax: (325) 235 2872  
e-mail: sales@electron tubes.com  
web site: www.electrontubes.com

choose accessories for this pmt on our website

an ISO 9001 registered company

The company reserves the right to modify these designs and specifications without notice. Developmental devices are intended for evaluation and no obligation is assumed for future manufacture. While every effort is made to ensure accuracy of published information the company cannot be held responsible for errors or consequences arising therefrom.



© ET Enterprises Ltd, 2010  
DS\_9829B Issue 8 (21/09/10)

## Appendix D

# Technical CAD Drawings

To efficiently produce the mechanical components in the workshop of the Universität Hamburg, the set-up was designed in close cooperation with the division Technische Entwicklung und Betrieb (TEB). All CAD drawings shown in this section are provided by Jutta Pelz.

### Cable Feedthroughs

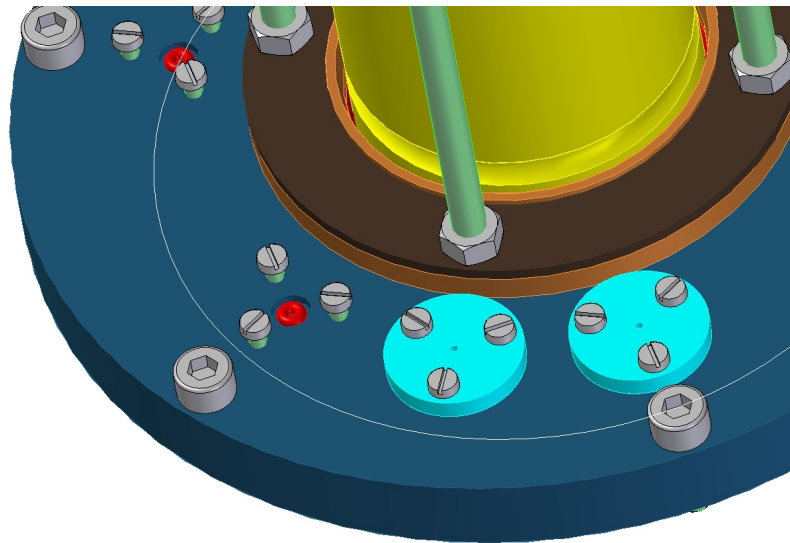


**Figure D.1:** In version 1 of the cable feedthroughs the SM 50 cables were sealed with FKM O-rings of 1 mm inner diameter (red). To ensure an appropriate sealing the O-rings were pressed with a pressure plate (turquoise) in orthogonal direction against the cables.

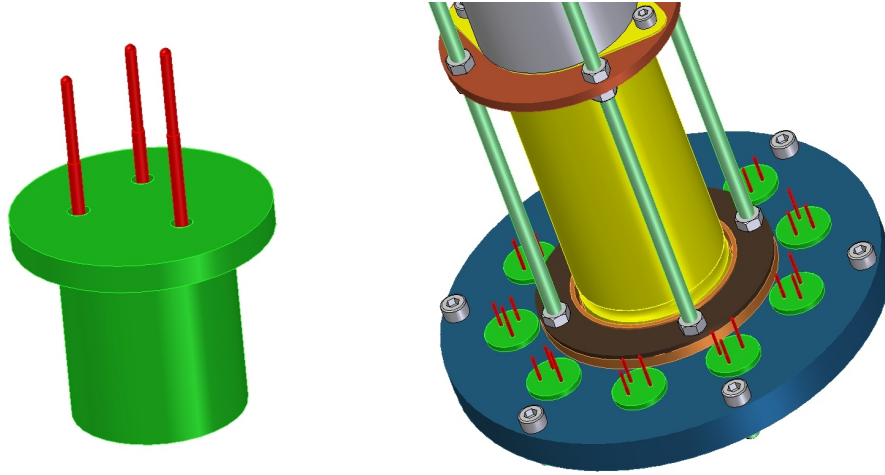


**Figure D.2:** In version 2 of the cable feedthroughs the upper flange (right) contains nine bore holes. In each hole, a PTFE plug (left) is pressed, containing two pins for the CA and NCA readout and one pin for the high voltage supply. The plugs were designed such that an interchange between readout and HV pins was not easily possible. However, the HV pin and the anode readout were very close and a leakage current occurred.

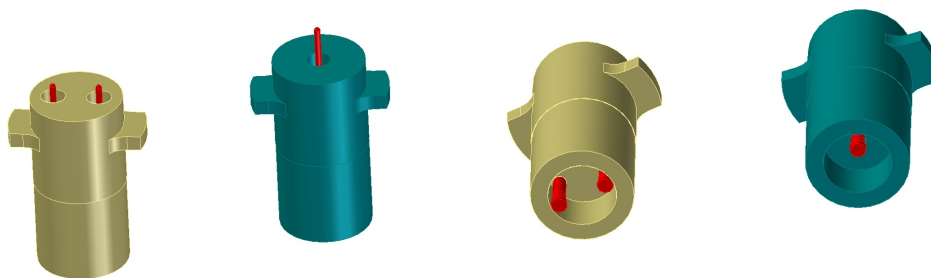


**Figure D.3:** PTFE plugs of version 3 of the cable feedthroughs, top view on the left, bottom view on the right. The plugs for anode readout contain two pins and are depicted in yellow, the plugs for HV supply contain one pin and are shown in turquoise. They have the same diameter like version 2, so that no new flange had to be produced.

### Operation Vessel

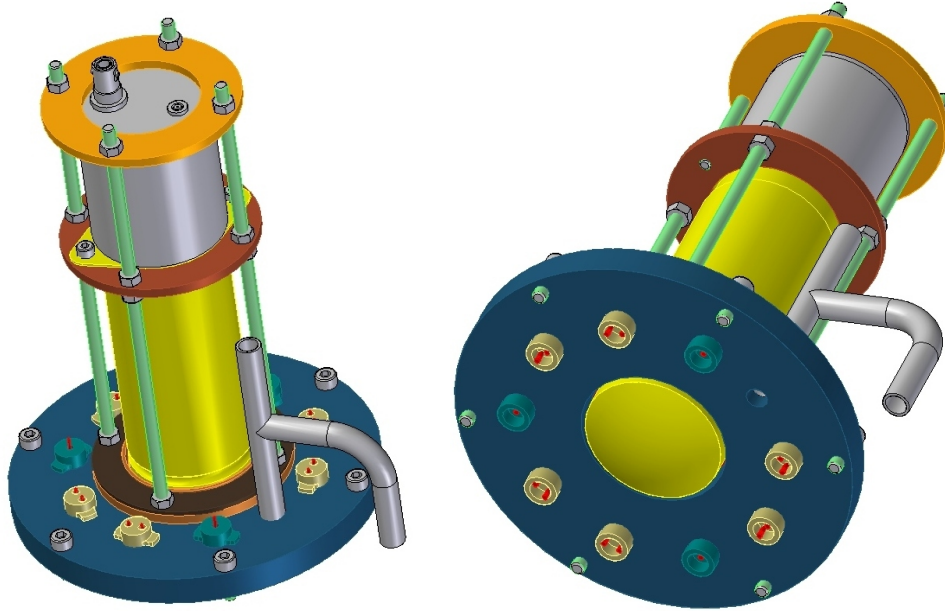


**Figure D.4:** View on the upper flange with PMT support structures and installed PMT from above (left) and below (right). On top of the support structure, a high voltage connector and a LEMO connector to read out the PMT are integrated. In this drawing, the cable feedthroughs of version 3 are implemented.

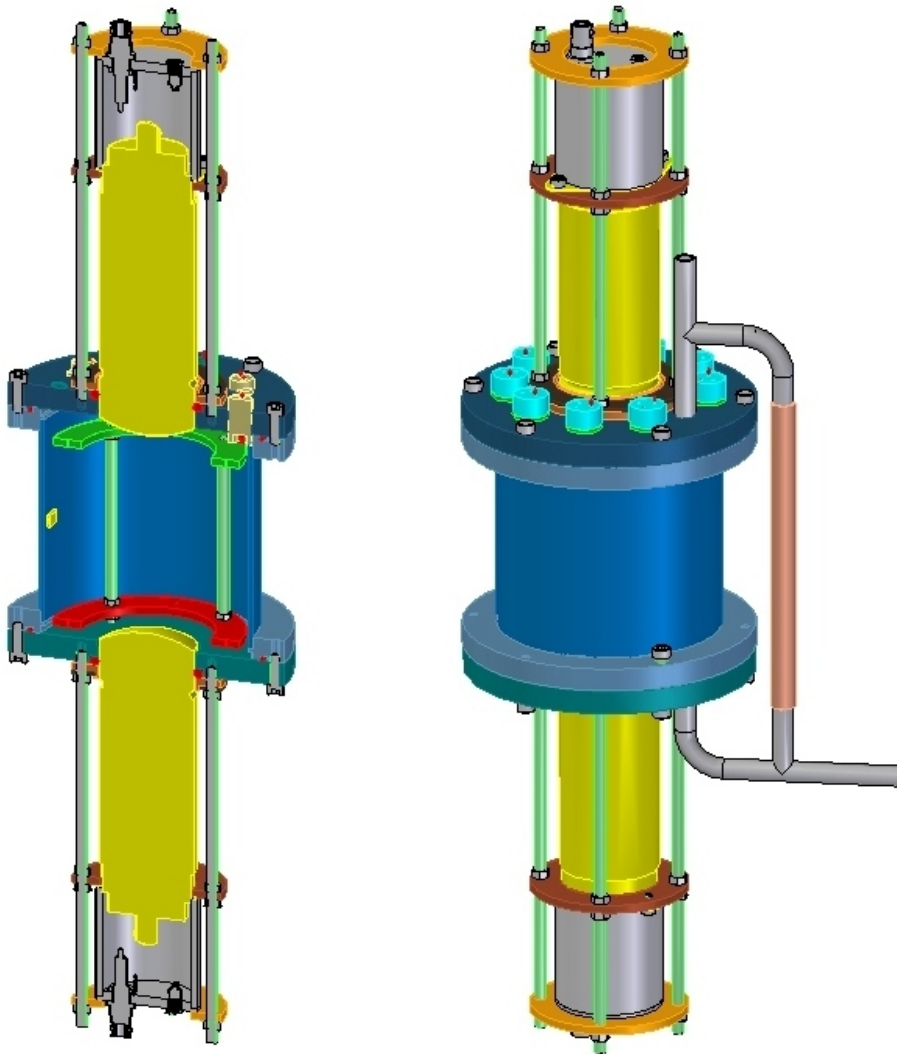


**Figure D.5:** Cross-sectional view (left) and exterior view (right) of the operation vessel. The detector holder is designed such that as much light as possible can reach the PMTs (depicted in yellow). The support structures hold the PMTs in place and ensure the liquid-tight sealing to the tank. To control the liquid level, a transparent PTFE tube is installed in parallel to the operation vessel.

### Storage Vessel

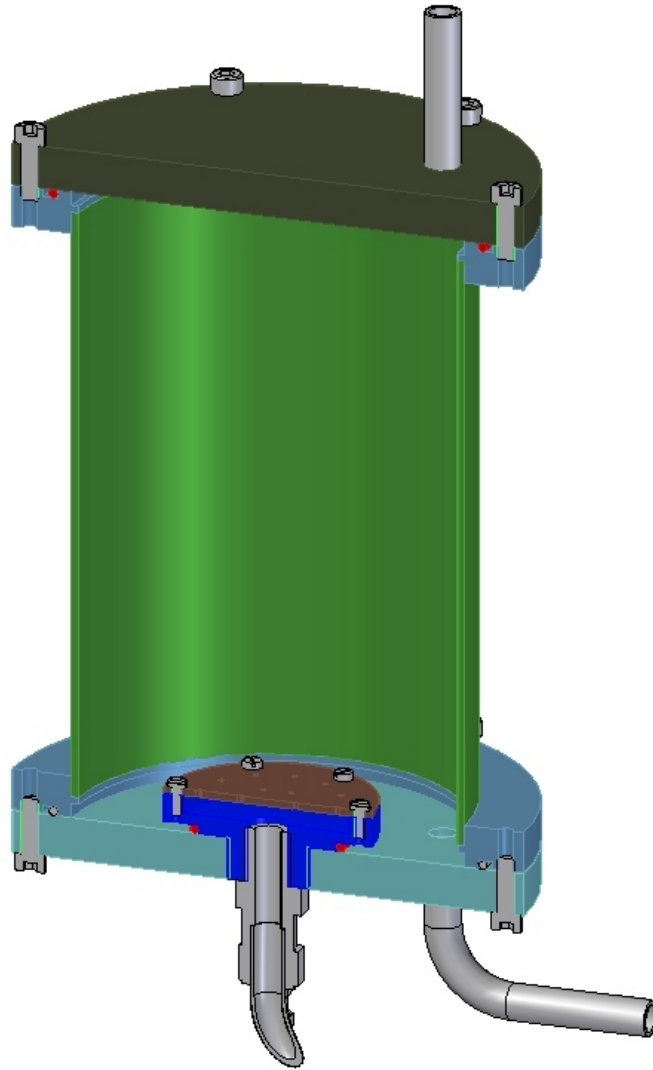


**Figure D.6:** Cross-sectional view of the storage vessel. To flush the liquid scintillator with Nitrogen bubbles, a shower head is installed inside the vessel. From the upper flange, the Nitrogen is guided via a flexible PTFE tube to an exhaust valve to prevent Oxygen from attaining into the set-up. With a second connection in the bottom flange, the liquid scintillator is guided to the operation vessel by using a lifting ramp.



# Appendix E

## Veto Time

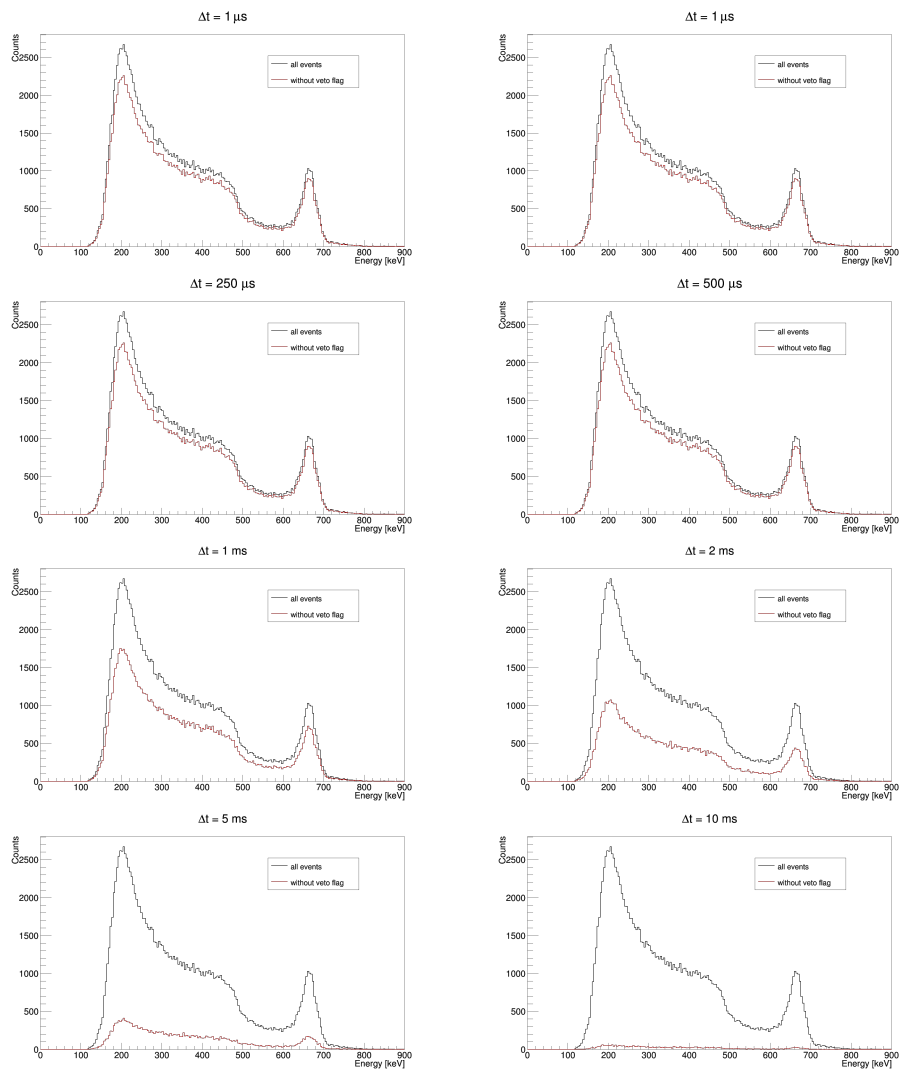


Figure E.1: Spectrum of a  $^{137}\text{Cs}$  measurement of detector 1 for different veto times  $\Delta t$ .



# List of Figures

2.1	Mass chain for $A = 116$ . . . . .	18
2.2	Feynman diagram for $2\nu\beta\beta$ decay . . . . .	18
2.3	Feynman diagram for $0\nu\beta\beta$ decay . . . . .	20
2.4	Feynman black box diagram for $0\nu\beta\beta$ decay . . . . .	21
2.5	Allowed regions for $m_{\beta\beta}$ as a function of the lightest neutrino mass	23
2.6	Nuclear matrix elements $M^{0\nu}$ for several isotopes . . . . .	25
2.7	Half-lives $T_{1/2}^{0\nu}$ calculated with different nuclear structure approaches	25
2.8	Allowed regions of $m_{\beta}$ as a function of the lightest neutrino mass .	32
2.9	2D distribution of the number of effective neutrinos $N_{eff}$ and total neutrino mass $\sum m_i$ using Planck and WMAP data . . . . .	34
3.1	Mesomerism of Benzene . . . . .	37
3.2	$\pi$ -electronic energy levels for aromatic molecules . . . . .	38
3.3	Cross sections for neutron capture on $^{157}\text{Gd}$ , $^{155}\text{Gd}$ and H . . . . .	48
4.1	Cross sections for total and radiative neutron capture on $^{113}\text{Cd}$ . .	59
4.2	Cross sections for $^3\text{He}(n, p)^3\text{H}$ , $^{10}\text{B}(n, \alpha)^7\text{Li}$ and $^6\text{Li}(n, \alpha)^3\text{H}$ . . . .	60
4.3	Fission cross sections induced by slow neutrons for $^{235}\text{U}$ and $^{239}\text{Pu}$	61
4.4	Fission cross sections induced by fast neutrons for $^{235}\text{U}$ , $^{238}\text{U}$ , $^{237}\text{Np}$ and $^{239}\text{Pu}$ . . . . .	61
4.5	Diagram and photograph of a CPG detector . . . . .	67
4.6	Weighting potentials of CPG detectors . . . . .	68
4.7	Typical gamma interaction pulse shape . . . . .	69
4.8	Artistic scheme of the COBRA demonstrator at the LNGS . . . . .	71
4.9	Scheme of cooling plate for the preamplifier cooling unit . . . . .	75
4.10	$z$ - $E$ -plot for the 2011 to 2014 LNGS dataset . . . . .	77
4.11	COBRA detectors for large scale set-up . . . . .	78
4.12	Artistic schemes for COBRA large scale set-up . . . . .	79
5.1	Solubility of silver conduction glue . . . . .	85
5.2	CAD drawing for the mechanical components of the liquid scintilla- tor test set-up . . . . .	87
5.3	Photograph of the detector holder with four detectors installed . .	90

5.4	Overview on readout Electronics and DAQ of the test set-up . . . . .	91
5.5	Implementation of the test set-up in VENOM . . . . .	98
5.6	Original and smeared spectra of a $^{137}\text{Cs}$ simulation . . . . .	98
6.1	Stability of calibration parameters . . . . .	102
6.2	Stability of data taking . . . . .	103
6.3	Number of triggered events per channel . . . . .	104
6.4	Spectra for a $^{137}\text{Cs}$ calibration with and without veto . . . . .	105
6.5	$N_{veto}$ for different $\Delta t$ . . . . .	105
6.6	Comparison of $^{137}\text{Cs}$ simulations and measurements in liquid scintillator and Nitrogen . . . . .	107
6.7	Comparison of $^{137}\text{Cs}$ simulations with measurements in liquid scintillator and Nitrogen . . . . .	107
6.8	Comparison of $^{137}\text{Cs}$ simulations for different different detector sizes . . . . .	108
6.9	Comparison of $^{137}\text{Cs}$ simulations and measurement with a detector of 6 mm edge length . . . . .	109
6.10	Energy spectra for all events compared to no veto events . . . . .	111
6.11	$z$ - $E$ -plot comparison of all events and no veto events . . . . .	112
6.12	$z$ - $E$ -plot comparison of all events and no veto events in the ROI . . . . .	112
6.13	Selection of randomly chosen no veto events . . . . .	113
6.14	$z$ - $E$ -plot comparison for no veto events and SVEs . . . . .	116
6.15	Schematic drawing of muon passage through a detector . . . . .	117
6.16	Graphical representation for the energy deposition of muons . . . . .	118
6.17	Single detector veto event spectrum . . . . .	119
6.18	Selection of randomly chosen vetoed events . . . . .	121
6.19	Single detector vetoed event spectra for a wide range of $z$ . . . . .	122
6.20	Selection of randomly chosen vetoed events with $z > 1$ . . . . .	122
6.21	Comparison of vetoed events spectrum to simulation . . . . .	123
6.22	Single detector vetoed events spectra with flag_bad_pulse cut . . . . .	125
6.23	Single detector vetoed events spectra with LSE cut . . . . .	126
6.24	Single detector vetoed events spectra with flag_MSE cut . . . . .	127
A.1	Illustration of Uranium decay chain . . . . .	132
B.1	Illustration of Thorium decay chain . . . . .	135
D.1	CAD drawings of the cable feedthroughs, version 1 . . . . .	140
D.2	CAD drawings of the cable feedthroughs, version 2 . . . . .	141
D.3	CAD drawings of the cable feedthroughs, version 3 . . . . .	141
D.4	CAD drawings of the upper flange . . . . .	142
D.5	CAD drawings of the operation vessel . . . . .	143
D.6	CAD drawings of the storage vessel . . . . .	144
E.1	$^{137}\text{Cs}$ spectra for different veto times $\Delta t$ . . . . .	145

# List of Tables

2.1	Neutrino oscillation parameters . . . . .	14
2.2	Selection of double beta decay isotopes . . . . .	17
2.3	Compilation of $2\nu\beta\beta$ decay half-lives . . . . .	19
2.4	Compilation of double $\beta^+$ decay isotopes . . . . .	19
2.5	Compilation of nuclear matrix elements $M^{0\nu}$ . . . . .	24
3.1	Chemical and physical properties of Pseudocumene and Dodecane. . . . .	42
3.2	Chemical and physical properties of PXE and LAB . . . . .	43
3.3	Chemical and optical properties of PPO and pTP . . . . .	43
3.4	Chemical and optical properties of bis-MSB and POPOP . . . . .	44
3.5	Chemical and optical properties of PMP . . . . .	44
4.1	Decay modes, natural abundance and Q-values . . . . .	54
4.2	Calculated background rate in a large-scale COBRA experiment . . . . .	57
4.3	Physical properties of CdZnTe, Ge and Si . . . . .	66
4.4	Accumulated exposure recorded at the COBRA demonstrator . . . . .	76
5.1	Chemical and physical properties of OptiScint HiSafe . . . . .	83
5.2	Compilation of material compatibility tests . . . . .	86
5.3	Compilation of $\gamma$ -lines emitted by $^{152}\text{Gd}$ . . . . .	95
5.4	Compilation of $\gamma$ -lines emitted in decay chain of $^{228}\text{Th}$ . . . . .	96
6.1	Detector working points . . . . .	101
6.2	Comparison of P/C for different detector sizes . . . . .	109
6.3	Summary of background indices for different analysis cuts . . . . .	114
6.4	Mean energy loss of minimum-ionizing particles in Cd, Zn and Te . . . . .	115
6.5	Fraction of MSE in the SVE dataset . . . . .	124
A.1	Uranium decay chain . . . . .	133
B.1	Thorium decay chain . . . . .	136



# Bibliography

- [1] Y. Fukuda et al. Evidence for oscillation of atmospheric neutrinos. *Phys.Rev.Lett.*, 81:1562–1567, 1998. DOI: 10.1103/PhysRevLett.81.1562.
- [2] Q. R. Ahmad et al. Direct evidence for neutrino flavor transformation from neutral current interactions in the Sudbury Observatory. *Phys.Rev.Lett.*, 89:011301, 2002. DOI: 10.1103/PhysRevLett.89.011301.
- [3] N. Schmitz. *Neutrino physics*. Teubner Verlag, Stuttgart, 1997.
- [4] H. Weyl. Electron and Gravitation. 1. (In German). *Z.Phys.*, 56:330–352, 1929. DOI: 10.1007/BF01339504.
- [5] E. Majorana. Teoria simmetrica dell elettrone e del positrone. *Nuovo Cim.*, 14:171–184, 1937. DOI: 10.1007/BF02961314.
- [6] R. Davis Jr. Attempt to detect the antineutrinos from a nuclear reactor by the  $\text{Cl}^{37}(\text{anti-}\nu, e)\text{A}^{37}$  reaction. *Phys.Rev.*, 97:766–769, 1955. DOI: 10.1103/PhysRev.97.766.
- [7] R. Davis Jr. and D. S. Harmer. Solar neutrinos. 1964.
- [8] S. Bilenky. *Introduction to the Physics of Massive and Mixed Neutrinos*. Lecture Notes in Physics. Springer, 2010. 9783642140426.
- [9] K. Zuber. *Neutrino Physics*. Series in High Energy Physics, Cosmology and Gravitation. Routledge Chapman & Hall, 2nd Edition, 2011.
- [10] T. Asaka, S. Blanchet, and M. Shaposhnikov. The nuMSM, dark matter and neutrino masses. *Phys.Lett.*, B631:151–156, 2005. DOI: 10.1016/j.physletb.2005.09.070.
- [11] T. Asaka and M. Shaposhnikov. The nuMSM, dark matter and baryon asymmetry of the universe. *Phys.Lett.*, B620:17–26, 2005. DOI: 10.1016/j.physletb.2005.06.020.
- [12] M. Anelli et al. A facility to Search for Hidden Particles (SHiP) at the CERN SPS. 2015. e-Print arXiv:1504.04956.

- [13] S. Alekhin et al. A facility to Search for Hidden Particles at the CERN SPS: the SHiP physics case. 2015. e-Print arXiv:1504.04855.
- [14] C. Athanassopoulos et al. Evidence for anti-muon-neutrino to anti-electron-neutrino oscillations from the LSND experiment at LAMPF. *Phys.Rev.Lett.*, 77:3082–3085, 1996. DOI: 10.1103/PhysRevLett.77.3082.
- [15] A. A. Aguilar-Arevalo et al. Event Excess in the MiniBooNE Search for  $\bar{\nu}_\mu \rightarrow \bar{\nu}_e$  Oscillations. *Phys.Rev.Lett.*, 105:181801, 2010. DOI: 10.1103/PhysRevLett.105.181801.
- [16] D. V. Forero, M. Tortola, and J. W. F. Valle. Neutrino oscillations refitted. *Phys.Rev.*, D90(9):093006, 2014. DOI: 10.1103/PhysRevD.90.093006.
- [17] Benjamin W. Lee and Robert E. Shrock. Natural Suppression of Symmetry Violation in Gauge Theories: Muon - Lepton and Electron Lepton Number Nonconservation. *Phys.Rev.*, D16:1444, 1977. DOI: 10.1103/PhysRevD.16.1444.
- [18] J. Beringer et al. Review of Particle Physics (RPP). *Phys.Rev.*, D86:010001, 2012. DOI: 10.1103/PhysRevD.86.010001.
- [19] C. F. von Weizsäcker. Zur theorie der kernmassen. *Zeitschrift für Physik*, 96(7-8):431–458, 1935. DOI: 10.1007/BF01337700.
- [20] H. A. Bethe and R. F. Bacher. Nuclear physics a. stationary states of nuclei. *Rev. Mod. Phys.*, 8:82–229, Apr 1936. DOI: 10.1103/RevModPhys.8.82.
- [21] E. Segré. *Nuclei and Particles: An Introduction to Nuclear and Subnuclear Physics*. Benjamin-Cummings Pub Co, 1977.
- [22] B. Schwingenheuer. Status and prospects of searches for neutrinoless double beta decay. *Annalen Phys.*, 525:269–280, 2013. DOI: 10.1002/andp.201200222.
- [23] J. Ebert et al. Current Status and Future Perspectives of the COBRA Experiment. *Adv.High Energy Phys.*, 2013:703572, 2013. DOI: 10.1155/2013/703572.
- [24] J. H. K. Timm. *Thesis currently in preparation*. PhD Thesis, Universität Hamburg, 2015.
- [25] M. Goeppert-Mayer. Double beta-disintegration. *Phys. Rev.*, 48:512–516, Sep 1935. DOI: 10.1103/PhysRev.48.512.
- [26] A. P. Meshik, C. M. Hohenberg, O. V. Pravdivtseva, and Ya. S. Kapusta. Weak decay of Ba-130 and Ba-132: Geochemical measurements. *Phys.Rev.*, C64:035205, 2001. DOI: 10.1103/PhysRevC.64.035205.



- [27] F. Boehm and P. Vogel. *Physics of massive neutrinos*. Cambridge University Press, 1992.
- [28] G. Racah. On the symmetry of particle and antiparticle. *Nuovo Cim.*, 14:322–328, 1937. DOI: 10.1007/BF02961321.
- [29] W. H. Furry. On transition probabilities in double beta-disintegration. *Phys.Rev.*, 56:1184–1193, 1939. DOI: 10.1103/PhysRev.56.1184.
- [30] F. Simkovic, J. Vergados, and A. Faessler. Few active mechanisms of the neutrinoless double beta-decay and effective mass of Majorana neutrinos. *Phys.Rev.*, D82:113015, 2010. DOI: 10.1103/PhysRevD.82.113015.
- [31] J. Schechter and J. W. F. Valle. Neutrinoless Double beta Decay in SU(2) x U(1) Theories. *Phys.Rev.*, D25:2951, 1982. DOI: 10.1103/PhysRevD.25.2951.
- [32] F. Simkovic. Theory of neutrinoless double beta decay - A brief review. *Phys.Part.Nucl.Lett.*, 10:623–632, 2013. DOI: 10.1134/S154747711307008X.
- [33] D. V. Forero, M. Tortola, and J. W. F. Valle. Global status of neutrino oscillation parameters after Neutrino-2012. *Phys.Rev.*, D86:073012, 2012. DOI: 10.1103/PhysRevD.86.073012.
- [34] A. de Gouvea et al. Neutrinos. 2013. e-Print arXiv:1310.4340.
- [35] F. Simkovic. Matrix Elements for Neutrinoless Double Beta Decay. *Nucl.Phys.Proc.Suppl.*, 229-232:160–164, 2012. DOI: 10.1016/j.nuclphysbps.2012.09.026.
- [36] R. G. Winter. Double K Capture and Single K Capture with Positron Emission. *Phys.Rev.*, 100:142–144, 1955. DOI: 10.1103/PhysRev.100.142.
- [37] M.I. Krivoruchenko, F. Simkovic, D. Frekers, and A. Faessler. Resonance enhancement of neutrinoless double electron capture. *Nucl.Phys.*, A859:140–171, 2011. DOI: 10.1016/j.nuclphysa.2011.04.009.
- [38] H.V. Klapdor-Kleingrothaus, I.V. Krivosheina, A. Dietz, and O. Chkvorets. Search for neutrinoless double beta decay with enriched Ge-76 in Gran Sasso 1990-2003. *Phys.Lett.*, B586:198–212, 2004. DOI: 10.1016/j.physletb.2004.02.025.
- [39] H.V. Klapdor-Kleingrothaus and I.V. Krivosheina. The evidence for the observation of  $0\nu\beta\beta$  decay: The identification of  $0\nu\beta\beta$  events from the full spectra. *Mod.Phys.Lett.*, A21:1547–1566, 2006. DOI: 10.1142/S0217732306020937.

- 
- [40] M. Agostini et al. Results on neutrinoless double beta decay of  $^{76}\text{Ge}$  from GERDA Phase I. *Phys.Rev.Lett.*, 111:122503, 2013. DOI: 10.1103/PhysRevLett.111.122503.
- [41] E. Aguayo et al. The Majorana Demonstrator. 2011. e-Print arXiv:1109.6913.
- [42] M. Pedretti. CUORE and CUORE-0 status: Toward a next-generation neutrinoless double beta decay experiment. *Nucl.Phys.Proc.Suppl.*, 235-236:261–266, 2013. 10.1016/j.nuclphysbps.2013.04.020.
- [43] K. Alfonso et al. Search for Neutrinoless Double-Beta Decay of  $^{130}\text{Te}$  with CUORE-0. 2015. e-Print arXiv:1504.02454.
- [44] E. Andreotti et al. Double-beta decay of  $^{130}\text{Te}$  to the first  $0^+$  excited state of  $^{130}\text{Xe}$  with CUORICINO. *Phys.Rev.*, C85:045503, 2012. DOI: 10.1103/PhysRevC.85.045503.
- [45] L. Sibley. SNO+: Physics program and status update. *AIP Conf.Proc.*, 1604:449–455, 2014. DOI: 10.1063/1.4883464.
- [46] V. Lozza. Scintillator phase of the SNO+ experiment. *J.Phys.Conf.Ser.*, 375:042050, 2012. DOI: 10.1088/1742-6596/375/1/042050.
- [47] A. Gando et al. Measurement of the double-beta decay half-life of  $^{136}\text{Xe}$  with the KamLAND-Zen experiment. *Phys.Rev.*, C85:045504, 2012. DOI: 10.1103/PhysRevC.85.045504.
- [48] K. Asakura et al. Results from KamLAND-Zen. 2014. e-Print arXiv:1409.0077.
- [49] M. Auger et al. The EXO-200 detector, part I: Detector design and construction. *JINST*, 7:P05010, 2012. DOI: 10.1088/1748-0221/7/05/P05010.
- [50] N. Ackerman et al. Observation of Two-Neutrino Double-Beta Decay in  $^{136}\text{Xe}$  with EXO-200. *Phys.Rev.Lett.*, 107:212501, 2011. DOI: 10.1103/PhysRevLett.107.212501.
- [51] J. B. Albert et al. An improved measurement of the  $2\nu\beta\beta$  half-life of  $^{136}\text{Xe}$  with EXO-200. *Phys.Rev.*, C89:015502, 2014. DOI: 10.1103/PhysRevC.89.015502.
- [52] M. Auger et al. Search for Neutrinoless Double-Beta Decay in  $^{136}\text{Xe}$  with EXO-200. *Phys.Rev.Lett.*, 109:032505, 2012. DOI: 10.1103/PhysRevLett.109.032505.
- [53] M. Danilov et al. Detection of very small neutrino masses in double beta decay using laser tagging. *Phys.Lett.*, B480:12–18, 2000. DOI: 10.1016/S0370-2693(00)00404-4.

- [54] T. Brunner et al. A setup for Ba-ion extraction from high pressure Xe gas for double-beta decay studies with EXO. *Nucl.Instrum.Meth.*, B317:473–475, 2013. DOI: 10.1016/j.nimb.2013.05.086.
- [55] N. Yahlali et al. NEXT: Neutrino experiment with high pressure xenon gas TPC. *Nucl.Instrum.Meth.*, A617:520–522, 2010. DOI: 10.1016/j.nima.2009.10.076.
- [56] R. Arnold et al. Probing New Physics Models of Neutrinoless Double Beta Decay with SuperNEMO. *Eur.Phys.J.*, C70:927–943, 2010. DOI: 10.1140/epjc/s10052-010-1481-5.
- [57] P. Guzowski. Results of NEMO-3 and Status of SuperNEMO. *PoS, EPS-HEP2013:517*, 2013.
- [58] L. Simard. The NEMO-3 results after completion of data taking. *J.Phys.Conf.Ser.*, 375:042011, 2012. DOI: 10.1088/1742-6596/375/1/042011.
- [59] Ch. Kraus et al. Final results from phase II of the Mainz neutrino mass search in tritium beta decay. *Eur.Phys.J.*, C40:447–468, 2005. DOI: 10.1140/epjc/s2005-02139-7.
- [60] V. M. Lobashev. The search for the neutrino mass by direct method in the tritium beta-decay and perspectives of study it in the project KATRIN. *Nucl.Phys.*, A719:153–160, 2003. DOI: 10.1016/S0375-9474(03)00985-0.
- [61] E.W. Otten and C. Weinheimer. Neutrino mass limit from tritium beta decay. *Rept.Prog.Phys.*, 71:086201, 2008. DOI: 10.1088/0034-4885/71/8/086201.
- [62] J. Angrik et al. KATRIN design report. 2004.
- [63] J. A. Formaggio. Project 8: Using Radio-Frequency Techniques to Measure Neutrino Mass. *Nucl.Phys.Proc.Supl.*, 229-232:371–375, 2012. DOI: 10.1016/j.nuclphysbps.2012.09.058.
- [64] E. Andreotti et al. MARE, Microcalorimeter Arrays for a Rhenium Experiment: A detector overview. *Nucl.Instrum.Meth.*, A572:208–210, 2007. DOI: 10.1016/j.nima.2006.10.198.
- [65] P. C.-O. Ranitzsch et al. Development of metallic magnetic calorimeters for high precision measurements of calorimetric  $^{187}\text{Re}$  and  $^{163}\text{Ho}$  spectra. *Journal of Low Temperature Physics*, 167(5-6):1004–1014, 2012. DOI: 10.1007/s10909-012-0556-0.
- [66] P. A. R. Ade et al. Planck 2015 results. XXIV. Cosmology from Sunyaev-Zeldovich cluster counts. 2015. e-Print arXiv1502.01597.

- [67] G. Mangano, G. Miele, S. Pastor, and M. Peloso. A Precision calculation of the effective number of cosmological neutrinos. *Phys.Lett.*, B534:8–16, 2002. DOI: 10.1016/S0370-2693(02)01622-2.
- [68] P. A .R. Ade et al. Planck 2013 results. XVI. Cosmological parameters. 2013. e-Print arXiv:1303.5076.
- [69] A. Gando et al. Constraints on  $\theta_{13}$  from a Three-Flavor Oscillation Analysis of Reactor Antineutrinos at KamLAND. *Phys.Rev.*, D83:052002, 2011. DOI: 10.1103/PhysRevD.83.052002.
- [70] Y. Abe et al. Improved measurements of the neutrino mixing angle  $\theta_{13}$  with the Double Chooz detector. *JHEP*, 1410:86, 2014. DOI: 10.1007/JHEP10(2014)086.
- [71] F. P. An et al. Spectral measurement of electron antineutrino oscillation amplitude and frequency at Daya Bay. *Phys.Rev.Lett.*, 112:061801, 2014. DOI: 10.1103/PhysRevLett.112.061801.
- [72] J. K. Ahn et al. Observation of Reactor Electron Antineutrino Disappearance in the RENO Experiment. *Phys.Rev.Lett.*, 108:191802, 2012. DOI: 10.1103/PhysRevLett.108.191802.
- [73] G. Bellini et al. Final results of Borexino Phase-I on low energy solar neutrino spectroscopy. *Phys.Rev.*, D89:112007, 2014. DOI: 10.1103/PhysRevD.89.112007.
- [74] G. Bellini et al. Neutrinos from the primary proton-proton fusion process in the Sun. *Nature*, 512(7515):383–386, 2014. DOI: 10.1038/nature13702.
- [75] D. S. Ayres et al. The NOvA Technical Design Report. 2007. FERMILAB-DESIGN-2007-01.
- [76] Pubchem database maintained by the national center for biotechnology information (ncbi), a component of the national library of medicine, which is part of the united states national institutes of health (nih), 2014. [Online; accessed January 2nd 2015].
- [77] J. B. Birks. The Theory and practice of scintillation counting. 1964.
- [78] Sigma-Aldrich Co. LLC. Material safety data sheet for pseudocumene, version 5.2, revision date 16.10.2014, 2014. [Online; accessed January 2nd 2015].
- [79] Sigma-Aldrich Co. LLC. Material safety data sheet for dodecane, version 5.2, revision date 13.06.2014, 2014. [Online; accessed January 2nd 2015].
- [80] M. C. Johnson. *Scintillator purification and study of light propagation in a large liquid scintillation detector*. PhD Thesis, Princeton University, 1998.

- [81] Dixie Chemical Company Inc. Material safety data sheet for pxe, version from june 28, 2012, 2012. [Online; accessed January 2nd 2015].
- [82] CEPESA Quimica Becancour. Material safety data sheet for lab, version from january 26, 2007, 2007. [Online; accessed January 2nd 2015].
- [83] T. A. DeVol, D. K. Wehe, and G. F. Knoll. Evaluation of wavelength shifters for spectral separation of barium fluoride emissions. *Nucl.Instrum.Meth.*, A348:156–162, 1994. DOI: 10.1016/0168-9002(94)90854-0.
- [84] R. C. Fernow. *Introduction to Experimental Particle Physics*. Cambridge University Press, 1986. 9780511622588. Cambridge Books Online.
- [85] T. Marrodan Undagoitia et al. Spectroscopy of electron-induced fluorescence in organic liquid scintillators. *Eur.Phys.J.*, D57:105–110, 2010. DOI: 10.1140/epjd/e2010-00004-1.
- [86] N. Heidrich. *Monte Carlo-Based Development of a Shield and Total Background Estimation for the COBRA Experiment*. PhD Thesis, Universität Hamburg, 2014.
- [87] G. Alimonti et al. A large scale low-background liquid scintillation detector: The counting test facility at Gran Sasso. *Nucl.Instrum.Meth.*, A406:411–426, 1998. DOI: 10.1016/S0168-9002(98)00018-7.
- [88] G. Alimonti et al. The liquid handling systems for the Borexino solar neutrino detector. *Nucl.Instrum.Meth.*, A609:58–78, 2009. DOI: 10.1016/j.nima.2009.07.028.
- [89] G. F. Knoll. *Radiation detection and measurement*. Wiley, New York, NY, 4th Edition, 2010.
- [90] W. Beriguete et al. Production of a gadolinium-loaded liquid scintillator for the Daya Bay reactor neutrino experiment. *Nucl.Instrum.Meth.*, A763:82–88, 2014. DOI: 10.1016/j.nima.2014.05.119.
- [91] M. B. Chadwick et al. Endf/b-vii.1 nuclear data for science and technology: Cross sections, covariances, fission product yields and decay data. *Nuclear Data Sheets*, 112(12):2887 – 2996, 2011. Special Issue on ENDF/B-VII.1 Library. DOI: 10.1016/j.nds.2011.11.002.
- [92] C. Aberle et al. Large scale Gd-beta-diketonate based organic liquid scintillator production for antineutrino detection. *JINST*, 7:P06008, 2012. DOI: 10.1088/1748-0221/7/06/P06008.
- [93] F. P. An et al. Improved Measurement of Electron Antineutrino Disappearance at Daya Bay. *Chin.Phys.*, C37:011001, 2013. DOI: 10.1088/1674-1137/37/1/011001.

- [94] S. Abe et al. Precision Measurement of Neutrino Oscillation Parameters with KamLAND. *Phys.Rev.Lett.*, 100:221803, 2008. DOI: 10.1103/PhysRevLett.100.221803.
- [95] A. Gando et al. Limit on Neutrinoless beta beta Decay of Xe-136 from the First Phase of KamLAND-Zen and Comparison with the Positive Claim in Ge-76. *Phys.Rev.Lett.*, 110(6):062502, 2013. DOI: 10.1103/PhysRevLett.110.062502.
- [96] J. N. Bahcall, M.H. Pinsonneault, and S. Basu. Solar models: Current epoch and time dependences, neutrinos, and helioseismological properties. *Astrophys.J.*, 555:990–1012, 2001. DOI: 10.1086/321493.
- [97] B. Aharmim et al. Combined Analysis of all Three Phases of Solar Neutrino Data from the Sudbury Neutrino Observatory. *Phys.Rev.*, C88:025501, 2013. DOI: 10.1103/PhysRevC.88.025501.
- [98] S. Biller. SNO+ with Tellurium. 2014. e-Print arXiv:1405.3401.
- [99] M. Hirsch, K. Muto, T. Oda, and H.V. Klapdor-Kleingrothaus. Nuclear structure calculations of beta+ beta+, beta+ / EC and EC / EC decay matrix elements. *Z.Phys.*, A347:151–160, 1994. DOI: 10.1007/BF01292371.
- [100] N.I. Rukhadze et al. New limits on double beta decay of Cd-106. *Nucl.Phys.*, A852:197–206, 2011. DOI: 10.1016/j.nuclphysa.2011.01.006.
- [101] G. Heusser. Low-radioactivity background techniques. *Ann.Rev.Nucl.Part.Sci.*, 45:543–590, 1995. DOI: 10.1146/annurev.ns.45.120195.002551.
- [102] S. R. Elliott and P. Vogel. Double beta decay. *Ann.Rev.Nucl.Part.Sci.*, 52:115–151, 2002. DOI: 10.1146/annurev.nucl.52.050102.090641.
- [103] P. Russo. *Ionizing Radiation Detectors for Medical Imaging*, chapter 3: Detectors for digital radiography, pages 53–124.
- [104] J.V. Dawson, C. Montag, C. Reeve, J.R. Wilson, and K. Zuber. An Investigation on Cooling of CZT Co-Planar Grid Detectors. *Nucl.Instrum.Meth.*, A599:209–214, 2009. DOI: 10.1016/j.nima.2008.11.013.
- [105] W. Shockley. Currents to conductors induced by a moving point charge. *J. Appl. Phys.*, 9:635–635, 1938. DOI: 10.1063/1.1710367.
- [106] S. Ramo. Currents induced by electron motion. *Proceedings of the IRE*, 27(9):584 – 585, 1939. DOI: 10.1109/JRPROC.1939.228757.
- [107] O. Frisch. *British Atomic Energy Report, BR-49*, 1944.

- [108] P. N. Luke. Single-polarity charge sensing in ionization detectors using coplanar electrodes. *Applied Physics Letters*, 65(22):2884–2886, 1994. DOI: 10.1063/1.112523.
- [109] M. Fritts et al. Pulse-shape discrimination of surface events in CdZnTe detectors for the COBRA experiment. *Nucl.Instrum.Meth.*, A749:27–34, 2014. DOI: 10.1016/j.nima.2014.02.038.
- [110] Z. He, G. F. Knoll, D. K. Wehe, and J. Miyamoto. Position-sensitive single carrier cdznte detectors. *Nuclear Instruments and Methods in Physics Research Section A: Accelerators, Spectrometers, Detectors and Associated Equipment*, 388:180 – 185, 1997. DOI: 10.1016/S0168-9002(97)00318-5.
- [111] M. Fritts et al. Analytical model for event reconstruction in coplanar grid CdZnTe detectors. *Nucl.Instrum.Meth.*, A708:1–6, 2013. DOI: 10.1016/j.nima.2013.01.004.
- [112] T. Michel, T. Gleixner, J. Durst, M. Filipenko, and S. Geisselsöder. The Potential of Hybrid Pixel Detectors in the Search for the Neutrinoless Double-Beta Decay of  $^{116}\text{Cd}$ . *Adv.High Energy Phys.*, 2013:105318, 2013. DOI: 10.1155/2013/105318.
- [113] M. Filipenko, T. Gleixner, G. Anton, and T. Michel. 3D Particle Track Reconstruction in a Single Layer Cadmium-Telluride Hybrid Active Pixel Detector. 2014.
- [114] T. Neddermann. *Material screening by means of low-level gamma ray spectrometry with the Dortmund Low Background HPGe Facility*. PhD Thesis, TU Dortmund, 2014.
- [115] T. Köttig. *Sensitivity studies of CdZnTe semiconductor detectors for the COBRA experiment*. PhD Thesis, TU Dortmund, 2012.
- [116] O. Schulz. *Exploration of new data acquisition and background reduction techniques for the COBRA experiment*. PhD Thesis, TU Dortmund, 2011.
- [117] JULABO GmbH. Product data sheet fl601, 2015. [Online; accessed May 18th 2015].
- [118] R. Acquafredda et al. The OPERA experiment in the CERN to Gran Sasso neutrino beam. *JINST*, 4:P04018, 2009. DOI: 10.1088/1748-0221/4/04/P04018.
- [119] PerkinElmer Inc. Data sheet for optiscint hisafe, 2015. [Online; accessed February 17th 2015].
- [120] M. Knapp. *Design, Simulation und Aufbau des GERDA-Myonvetos*. PhD Thesis, Universität Tübingen, 2009.

- 
- [121] ET Enterprises Limited. Data sheet, 2015. [Online; accessed January 2nd 2015].
- [122] V. Braunert. Photomultiplierkalibration am COBRA-Experiment. 2013.
- [123] M. Asai. Geant4-a simulation toolkit. *Trans.Amer.Nucl.Soc.*, 95:757, 2006.
- [124] J. Allison et al. Geant4 developments and applications. *Nuclear Science, IEEE Transactions on*, 53(1):270–278, Feb 2006. DOI: 10.1109/TNS.2006.869826.
- [125] K. A. Olive et al. Review of Particle Physics. *Chin.Phys.*, C38:090001, 2014. DOI: 10.1088/1674-1137/38/9/090001.
- [126] Particle Data Group. Atomic and nuclear properties of materials for more than 300 materials, 2014. [Online; accessed March 23 2015].
- [127] D. E. Groom, N. V. Mokhov, and S. I. Striganov. Muon stopping power and range tables 10-MeV to 100-TeV. *Atom.Data Nucl.Data Tabl.*, 78:183–356, 2001. DOI: 10.1006/adnd.2001.0861.
- [128] W. Wahl. *Radionuklid-Handbuch für den Anwender in der Spektrometrie im Strahlenschutz und der Medizin*. ISuS Publikationen, 2007.